Graphene Oxide – Towards A Comprehensive Characterization Scheme

A THESIS
SUBMITTED TO THE FACULTY OF
UNIVERSITY OF MINNESOTA
BY

Issam Ismail

IN PARTIAL FULFILLMENT OF THE REQUIREMENTS

FOR THE DEGREE OF

DOCTOR OF PHILOSOPHY

Christopher W. Macosko

September 2015

Acknowledgements

This work owes a huge debt to a large number of people for making it possible. First, I would like to thank my parents Mohammad and Maha Ismail, family and fiancée Samah Ismail for fueling my strength and motivation to see this endeavor through to completion; everything I do is for you. Secondly, I would like to thank my advisor, Dr. Christopher W. Macosko for his faith in me and for investing a huge amount of time in my personal development. He was like a second parent for me in the States and had patience with my sometimes trying ways for which I will forever be grateful. Thirdly, I would like to thank all the outstanding individuals that I have had the opportunity to work with, including Drs. Ahmed Abdala, Saeed Al Hasan, Benjamin Stottrup, Andreas Stein, Michael Tsapatsis, Joseph Zasadzinski, Andre Mkhoyan and many others. Moreover, I would like to thank the Macosko group members as well as the group members of all the professors I had the privilege of working with, who have all shown me nothing but support. I would also like to thank Charfac personnel, particularly Dr. Bing Luo, for the patience and kindness they showed in teaching me characterization techniques such as X-ray photoelectron spectroscopy, infrared and raman spectroscopy. I would also like to thank all the gifted researchers with whom I got connected through my work, including Drs. Jan Vermant, Jiaxing Huang, Matteo Pasquali and Erik Hobbie, from whom the ideas in this thesis benefited greatly.

I would like to thank my esteemed committee members, both in the past and present, who have shown interest in my work, including Drs. Edward Cussler, Satish Kumar and Wayne Gladfelter. I would also like to thank the institutions that supported me through my work, including the Abu-Dhabi-Minnesota Institute for Research Excellence (ADMIRE) program, the University of Minnesota, the Petroleum Institute, MASDAR Institute, the University of Waterloo and Augsburg College. I have a sizeable debt towards the undergrad students who have given me their time, dedication and considerable resourcefulness, especially Cain Valtierrez, Jeremy Vandenberg, Karthik Sankar and Sunny Dhaliwal. At the end, I would like to encourage each and every friend, family member and acquaintance that encouraged me on this journey. To each and every person listed above, I owe you a debt of everlasting and undying gratitude.

Abstract

Graphene oxide (GO) is a near-2D material derived via oxidation of graphite and exploited in nanocomposites and optoelectronics. Following a literature review, the modified Tour-Dimiev (MTD) method was singled out for making GO, with the introduction of modifications tailored towards producing large sheets by starting with a large graphite size, tuning the oxidation conditions, employing temperature control and a modified wash routine. The product was characterized using wide-angle x-ray diffraction, x-ray photoelectron and Raman spectroscopy, revealing near completeness of graphite conversion, high oxygen content of GO and a comparable degree of defects to literature reports on the same. We imaged MTD-GO via fluorescence quenching microscopy (FQM) and atomic force microscopy (AFM). We compared the analytical capabilities of the image analysis software ImageJ with MATLAB, introducing several MATLAB subroutines to mitigate image analysis issues. We image-analyzed MTD-GO, concluding that GO size and thickness are statistically uncorrelated and described by lognormal and normal distributions respectively. We demonstrated that AFM captures small particles better than FQM, and that these two techniques can be combined to obtain a complete picture of polydisperse sample size distributions.

Next, we modeled polydisperse dilute dispersions of oblate spheroids and discs in shear, uniaxial and biaxial extension using microhydrodynamic models found in the literature. We used the shear model to fit experimental shear data on a number of serially diluted sheet dispersions to obtain the dimensions and distributions thereof. The systems analyzed were MTD-GO, commercial GO before and after sonication, and a literature dataset on aqueous layered double hydroxides. Finally, we conducted novel Langmuir trough experiments with MTD-GO to understand the mechanisms surrounding the air-water interfacial assembly of GO. We were able to successfully transfer our films from the air-water interface onto a simple and versatile substrate such as surface-treated glass. We correlated film morphology *in situ* using Brewster Angle Microscopy and *ex situ* through FQM imaging of Langmuir-Blodgett-coated glass slides, to the pressure-area isotherm. We established that film packing occurs at low surface pressures. Finally, we showed that GO shows weak, pH-dependent intrinsic surface activity.

Table of Contents

List of Tables

List of Figures

Chapter 1: Introduction

1.1 Background and Motivation

Ever since graphene was produced by the scotch-tape method by Geim and Novoselov (2004), the scientific community has developed interest in this new material which has opened doors to 2D material physics. Such investigations had been previously thought to be impossible due to thermodynamic instability of 2D structures, as theoretically proposed by Lifshitz and Lifshitz (1980). Graphene as a network of sp^2-hybridized, honey-comb layers of carbon was successfully isolated from graphite, and is considered to be the potential building blocks for other carbon nanostructures such as buckyballs and carbon nanotubes as shown in **Figure 1-1** from Geim and Novoselov (2007). Graphene rapidly found its way in numerous applications as a result of its unique properties (**Table 1-1**), as described by authors such as Bunch (2008), Nair et al.. (2008) and Zhang et al. (2005).

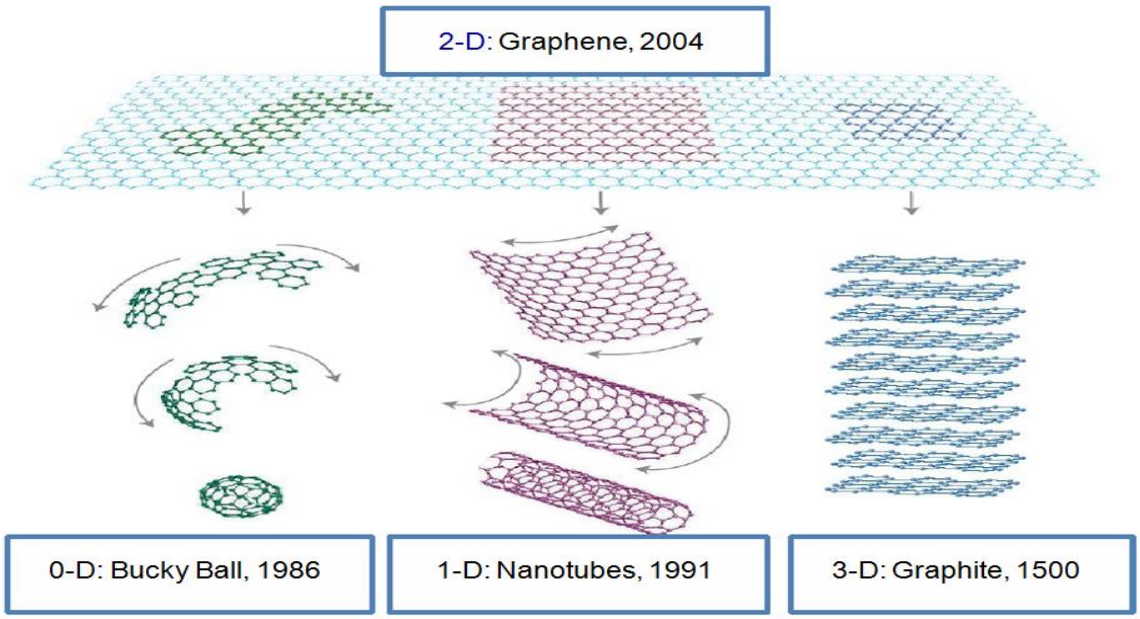

Figure 1-1. Artistic depiction of graphene as the building block for different types of materials reproduced from Geim and Novoselov (2007).

Table 1-1. Summary of physico-chemical properties of graphene from Rao et al. (2009), Geim (2009), Allen et al.. (2010), Pumera (2010) and Kim et al.. (2010).

Graphene Properties	
Young Modulus	1 TPa
Strength	~100-1000 GPa (~100-1000x steel)
Electrical Conductivity	~10^b S/m
Surface Area	2600 m^2/g
Light Absorbance	2.37 % per layer (transparent monolayers)

The exceptional properties of graphene were exploited in numerous applications , explored by Rao et al.. (2009), Geim (2009) Allen et al.. (2010), Pumera (2010) and Kim et al.. (2010), ranging from conducting electrodes, ultracapacitors and integrated circuits to solar cells, biosensors, nanocomposites and transparent devices. The Thomson Reuters Global Research Report by Adams and Pendelbury (2011) on materials science and technology in June 2011 cites 5000 publications on graphene in the first half of 2011, far higher than other active nanomaterial research areas such as metallo-organic frameworks and nanofibre scaffolds. To highlight one such growing area of application for graphene, there has been significant progress in the usage of graphene for fabricating transparent conductors for LCD screens and solar cells by authors such as Bae et al. (2010 and Li et al. (2009) . Graphene is viewed by Kaner and Wassei (2010) as a potential replacement for indium-doped tin oxide (ITO), the market standard for transparent conductors. Reasons include graphene's higher flexibility, chemical stability and lower density, together with the cost of indium (>$1000/kg) and expenses in depositing ITO (reactive sputtering, etc.).

This growing interest in graphene has created a need for reliable mass production routes. Epitaxial growth, chemical vapor deposition (CVD), scotch-tape exfoliation and sonication of graphite all provide pristine graphene but at relatively small yields as noted by Li et al.. (2006), Stankovich et al.. (2007) and Wang et al.. (2009). Kaner and Wassei (2010) elucidate the problems in some of the recent graphene production methods. In response to these low yield techniques, the following top-down three-step process was developed by authors such as Stankovich et al.. (2007) as a commercially viable alternative to mass-produce graphene: 1) - oxidation of graphite to graphite oxide,

followed by, 2) - sonication-based exfoliation to graphene oxide (GO), and 3) - subsequent reduction to chemically reduced graphene (CRG) or thermally reduced graphene (TRG) using reducing agents or heat respectively. A summary of the oxidation process is depicted in **Figure 1-2** from Garg et al.. (2014). This process, while scalable, is difficult to control in terms of graphene quality without considerable efforts to purify and characterize the GO via techniques like AFM. There is room for improvement in terms of standardization of the synthesis and characterization of this precursor, and so these areas, especially characterization, will be the focus of this thesis.

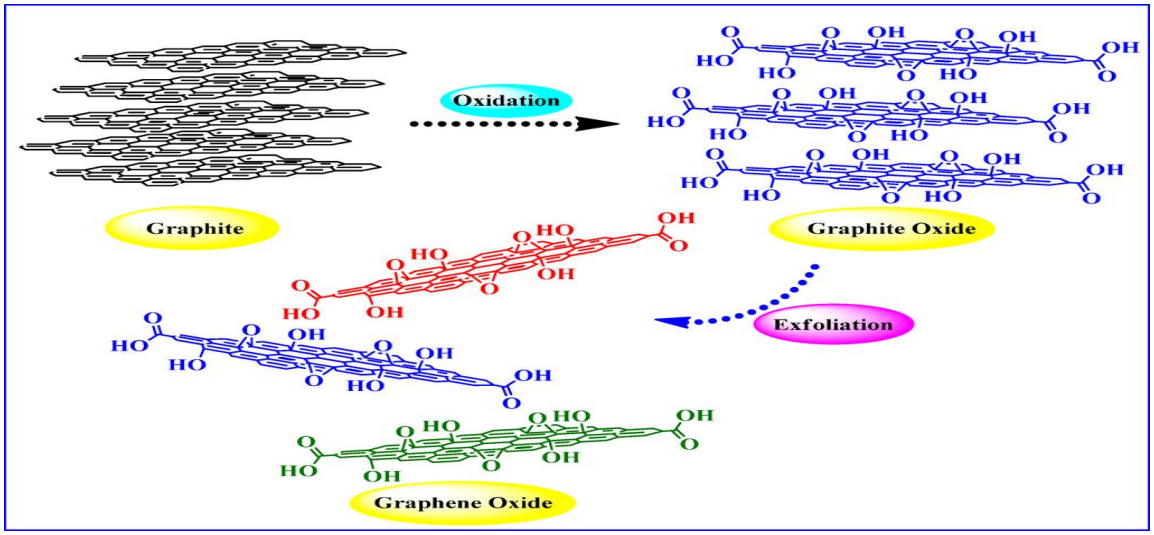

Figure 1-2. Chemical schema for the oxidation and exfoliation of graphite resulting in GO as depicted by Garg et al.. (2014)

1.2 Objectives

The aim of this work is to improve the production and characterization of graphene oxide (GO). The goal of our improvements is to work towards producing and characterizing the GO such that it may be reliably reproduced for use in GO-based graphene coatings for applications such as transparent conducting films. To achieve this end, we focus on: 1) - producing GO at as large a size as possible given lab conditions, 2)- suggesting reliable and efficient characterization tools by which the quality of a general GO sample can be comprehensively assessed in the lab. Novel approaches are introduced wherever possible to aid with the accomplishment of both of these objectives, with the added target of achieving generality in the suggested characterization methods to kindred colloidal and

nanoparticle systems of sheets and oblate spheroids (e.g. clay vermiculite, zeolite nanosheets, graphene, and double-layered hydroxides). To date, there is little colloidal literature addressing the problems of sheet and oblate spheroidal particle systems, especially compared to the more common spherical, fiber and prolate spheroidal geometries.

As a result, we will present a comprehensive scheme, starting from a critical literature review of common GO synthetic routes, adopting one of these techniques to the purpose of producing ultralarge GO sheets for applications such as optoelectronics and hybrid materials. We then introduce a characterization scheme for GO. Finally, we observe the behavior of these GO sheets at the air-water interface in Langmuir monolayers and submonolayers, in order to understand how they could be used for applications such as thin films for optoelectronics or hybrid films. A more detailed overview of the work done is presented in the following subsection.

1.3 Thesis Overview

This thesis deals with two fundamental aspects pertaining to GO: 1)- synthesis, especially tailored towards the preparation of ultralarge sheets, and 2)- characterization schema to understand the properties of GO.

Chapter 2 provides a comparative review of the four common GO synthetic routes. The review starts with a scientometric analysis of these methods over the last few years, followed by a presentation of an accurate comparison among these experimental procedures and their results as reported in the concerning literature. The final section recommends a synthesis procedure to produce large GO sheets.

Chapter 3 discusses the use of a modification of the Tour synthetic method (which we chose to call the modified Tour-Dimiev method) to produce ultralarge GO sheets. Our proposed improvements resolve current inefficiencies in the GO production and purification process, while producing very large GO sheets, reaching ~200 microns, with above 90% yield of monolayers.

Chapter 4 focuses on the characterization of GO particle dimensions by direct imaging. First we present an overview of the coating recipes optimized for GO and the subsequent

imaging protocols used for Fluorescence-Quenching Microscopy (FQM) and Atomic Force Microscopy (AFM). The chapter also reviews the problems commonly encountered with image analysis for particle systems like GO and proposes the software tools used to analyze the obtained images. With these solutions introduced, automation in characterizing distributions of nanoparticles has been realized in order to complement our rheological studies. Imaging results are presented in subsequent chapters.

In Chapter 5, we review models for rheology of dilute dispersions of oblate spheroids and sheets, including shear rheology, uniaxial and biaxial extensional rheology. We introduce a rigorous method to account for the rheology of a polydisperse system of general distribution characteristics and simulations showing the sensitivity analysis of the introduced models to changes in the system-descriptive parameters. This approach allows us to characterize the size distribution for potentially any oblate spheroidal/sheet system of interest; we demonstrate this using Gaussian, bimodal and lognormal models to simulate distributions.

Chapter 6 presents shear rheology experimental results from aqueous dispersions of GO to test the viability of the proposed models in Chapter 5. We begin with analyzing a commercial samples of GO, comparing it before and after sonication, followed by analysis of a lab-synthesized, highly polydisperse Tour GO sample, and finally, analysis of a shear rheology dataset found in literature for aqueous dispersions of double-layered hydroxides, to demonstrate the flexibility of the proposed technique to other particle systems than GO. The rheology results are compared, wherever possible, to sizing results from other characterization methods, such as FQM and AFM.

Chapter 7 examines the interfacial behavior of Tour GO at the air-water interface (a somewhat vaguely-understood phenomenon cited by some researchers in the literature) using a number of novel step-strain and Small Amplitude Oscillatory Shear (SAOS) experiments couple with Brewster Angle Microscopy (BAM) and FQM imaging to understand the behavior of what appear to be Langmuir submonolayers and monolayers of GO trapped at the air-water interface.

Chapter 8 summarizes the conclusions and future research directions that could be undertaken with GO, based on the results of the preceding sections.

Chapter 2: Literature Review on Graphene Oxide Synthesis

As described in the previous chapter, graphene oxide (GO) is an intermediary product formed during the oxidation of 3D stacks of graphite flakes in the top-down synthesis of 2D sheets of graphene, a material of increasing interest to both the scientific and industrial communities on account of the unique physicochemical properties offered by its 2D structure. The production of GO is thus one of the key routes towards the commercial production of graphene. In order to pave the way for the synthesis and characterization work suggested for GO in the following chapters, a greater understanding of the material being synthesized is necessary. The following review will thus start with describing the four main synthetic routes used to produce GO. This will be followed with a scientometric comparison of these four methods in the field over the last few years. The review will then present a comparison between the experimental procedures and results of these different methods as reported in the literature. Finally, it will recommend the synthesis procedure used in the next chapter.

2.1 Common Graphite Oxidation Methods

In this part of the review, we highlight the three GO synthesis methods of Staudenmaier (1898), Hummers (1958) and Tour (2010). These three methods capture the majority of the historical progress in the GO synthesis field and remain the most commonly-used synthetic routes to-date for making GO. These methods have become more popular after the recent discovery of graphene in 2004.

The goal of any top-down, graphite-based chemical synthesis of graphene is to exfoliate the graphene sheets that make up the original graphite material. The immediate problem with exfoliation of the graphene sheets is that it is only slightly dispersible in most organic and aqueous solvents. The idea is then to chemically modify these graphene sheets to lower the surface interaction energy between the sheets and the common solvent (such as water) to make the sheets more dispersible. The different methods below mainly

focus on different chemical routes to modify and oxidize the graphene sheets before the exfoliation steps.

2.1.1 Brodie Method

Graphite oxide was first synthesized by chemist Benjamin C. Brodie (1859) of Oxford using a mixture of potassium chlorate and fuming nitric acid to oxidize graphite; the former acts primarily as the oxidizing agent, while the latter helps with the intercalation of the graphite to expand the galleries and aid oxidation. Brodie (1859) reported on the yield of "paper-like foils" with a thickness of 0.05 mm. His initial report on the subject – which we mention for completeness - fueled numerous successful attempts to reproduce his results in safer, quicker and more efficiently scalable ways.

2.1.2 Staudenmaier Method

The Staudenmaier method (**Figure 2-1**), developed by Staudenmaier (1898), uses sulphuric acid in addition to fuming nitric acid as reagents (primarily as intercalating agents). Besides generating a smaller quantity of gas (NO_x) during the reaction, the introduction of concentrated sulphuric acid to the recipe made it possible to run a continuous reaction without the need to add fuming nitric acid during the reaction, giving it a practical advantage over the Brodie method. The method calls for the acid volume ratio to be 1:4 between nitric and sulphuric acid. The acid mixture is cooled by an ice bath to near 0˚C. Under vigorous stirring, graphite is then added to the acid, 4.37 g for every 100 ml. 1:11 weight equivalence graphite to oxidant is employed. The oxidant is added slowly while the ice bath is maintained. Reaction is left for 96 hours to complete. Purification is achieved by a 5% HCl wash followed by multiple DI water washes to remove sulphate and chloride impurities. The resultant slurry is dried at 60˚C in a vacuum oven to recover the product. Staudenmaier's efforts in refining this procedure allow GO to be synthesized in a safer manner than the Brodie synthesis. While toxic gasses are still created, there is a lower risk of explosion during this reaction; this is one reason why the Brodie method is not in common use for the academic or commercial

production of GO. It is also a reason for the more widespread use of the Hummers method compared to the Staudenmaier method, as discussed below.

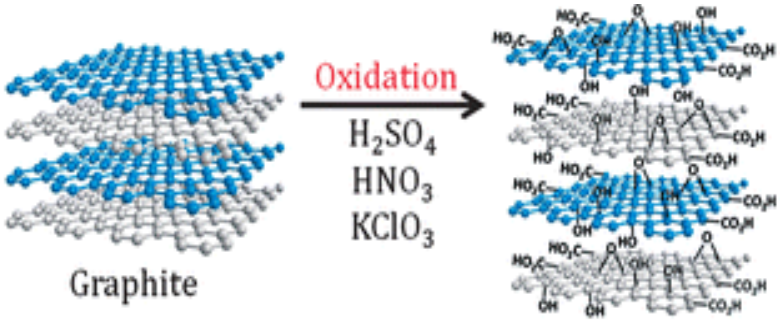

Figure 2-1. Schematic for the Staudenmaier GO synthesis as shown by Goh et al.. (2011)

2.1.3 Hummers Method

This method (**Figure 2-2**) was developed by Hummers (1958), over half a century after the method of Staudenmaier. The process uses sulphuric acid as the intercalating agent and replaces the fuming nitric acid used by Staudenmaier with sodium nitrate. This method also replaces potassium dichlorate with potassium permanganate as the oxidant. 0.5 weight equivalence of sodium nitrate is added to the sulphuric acid and graphite; the latter is typically chosen to be of 325 mesh size in classical preparations, as this is a small enough size to ensure minimal diffusion limitations as well as completeness and uniformity of oxidative treatment. 1 g graphite is added per 23 ml of sulphuric acid. The resultant mixture is held at 0˚C and 3 weight equivalences of potassium permanganate are added such that the temperature of the mixture never exceeds 20˚C during addition. The reaction is then allowed to occur at 35±3˚C for 30 minutes. The mixture is thereafter observed to thicken, evolve small amounts of gas and form a gray paste.

Water is then added to the mixture to quench it such that the acid is diluted threefold. The reaction temperature temporarily increases to 98˚C (boiling) and is held there for 15 minutes. The suspension is then diluted to the required concentration and dilute hydrogen peroxide added to reduce the remaining potassium permanganate, resulting in a bright yellow solution. Product washing is typically done via filtration such that pH approaches neutrality, a process which could take days, especially towards the last few

washes as the GO can at times gel and agglomerate, clogging up filters. At the end of the wash, the solid may be dried *in vacuo* at 40-70^{o}C with or without desiccating agent (typically phosphorus pentoxide at 40˚C), or by freeze-drying. These improvements introduced by Hummers mostly eliminated the toxic gasses evolved in the Brodie and Staudenmaier methods, leaving this method a good candidate for GO production.

Figure 2-2. Schematic for the Hummers synthesis for GO, as depicted by Sharma et al.. (2014):

2.1.4 Tour Method

The Tour method (**Figure 2-3**) is a recent 2010 innovation by Marcano et al.. (2010). The main change over the Hummers method is the addition of the chelating agent H_3PO_4, coupled with the omission of $NaNO_3$. The acid is used in a 9:1 ratio H_2SO_4: H_3PO_4. $KMnO_4$is added in 1:6 wt to the graphite. The reaction exotherm is allowed to evolve naturally, after which the reaction is brought to 50˚C for 12 hours under stirring, and finally, the reaction is quenched with ice and concentrated H_2O_2. Washes are performed using centrifugation and filtration in water, HCl and ethanol. The GO suspension is then filtered over a membrane with 0.45 um pore size, and the solid obtained vacuum-dried. 100-mesh graphite from Sigma-Aldrich was used by Tour. GO from this technique tends to be oxygen-enriched and larger than average, so it gels easily and becomes difficult to wash regardless of technique used (filtration, centrifugation, dialysis), presumably the rationale behind Tour's choice of a relatively small starting graphite size.

The chelating agent is claimed by Tour and Kosynkin (2012) to bind to the graphitic surface at certain locations, for e,g.: where the oxidant action has resulted in the

formation of vicinal –OH groups. This chelation is claimed to protect the surface against subsequent conversion of these vicinal hydroxyls (by dehydrogenation) into vicinal oxygen groups which, in turn, could later evolve as ozone and result in the formation of undesirable surface defect sites from which cracks could propagate through the sheets and lead to fragmentation. For this reason, the Tour method is claimed by Marcano et al. (2010) to produce larger than average sheets compared to the other two.

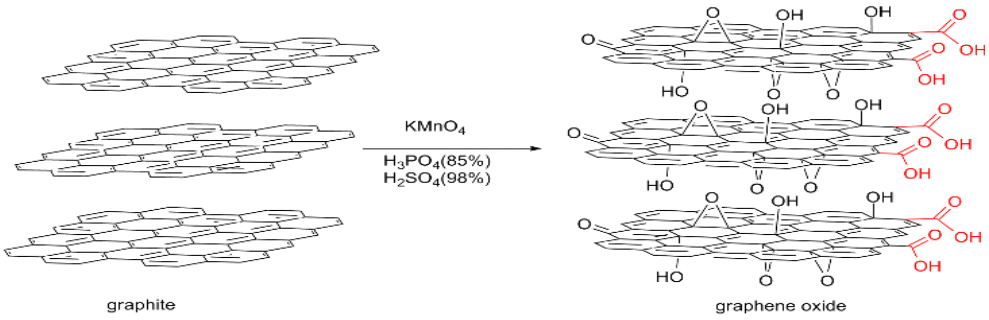

(a)

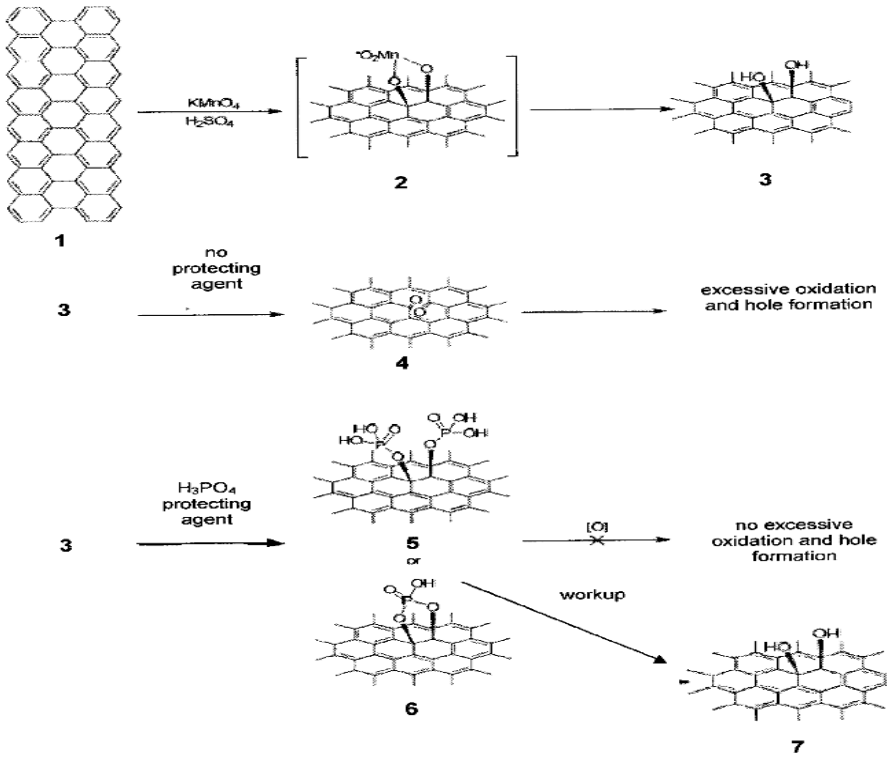

(b)

Figure 2-3.(**a)** Tour method reaction and conditions as depicted by Zuo et al. (2013), and (b) mechanism of the Tour method by Tour and Kosynkin (2012) depicting how the chelating agent (phosphoric acid) protects the surface from excessive oxidation and hole formation.

2.2 Scientometric Trends

Now that we have examined the physical differences between GO synthesis techniques we will look at the current usage of the techniques in the field. The Scopus database was used to study the recent usage history of the four main GO synthetic routes: the methods of Brodie, Staudenmaier, Hummers and Tour. **Figure 2-4** shows a comparison of usage between these techniques since 2007. The methods of Brodie and Staudenmaier have not seen an increase in usage over the past few years, indicating that researchers are migrating away from these to the Hummers and Tour methods, which is justifiable in light of the reaction hazards associated with the former methods, as well as the literature results from the next subsection which compares the products from these four methods.

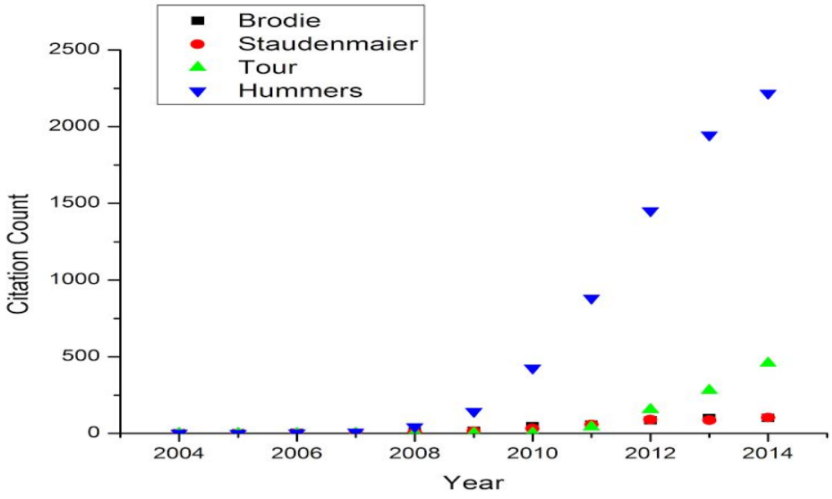

Figure 2-4. Citation trends in GO literature since 2007 (isolation of pristine graphene) from Scopus database.

Figure 2-4 also shows that the Hummers method is the dominant chemical route for producing GO, while the Tour method seems to be gaining increasing attention. A more careful examination of the trends in the Hummers and Tour publications from **Figure 2-4** reveals the trends shown in **Figure 2-5**. We can see that the annual rate of usage of the Hummers method is decreasing and approaching zero, while the annual usage of the Tour method is still positively accelerating. This trend may indicate a developing preference by researchers to use the Tour method for making GO, and will thus be used as one of the motivations to focus on the latter as the method of choice for making GO in this work.

It is understandable why the Tour method might be gaining such attention; making ultralarge GO which is oxygen-enriched (and thus easily water-dispersible) might be advantageous for a number of applications, including coatings for anti-corrosion and optoelectronics, catalytic membranes, adsorption, etc. As will be shown in the comparative discussion on synthetic methods, there are other reasons for wanting to adopt the Tour method to make GO, such as reduced metallic waste during the synthesis and lower degree of defects in the product GO compared to other techniques such as those of Staudenmaier and Hummers. The impact of the paper of Tour et al. (2010), "Improved Synthesis of Graphene Oxide", is shown in **Figure 2-5** and explored in detail in **Figure 2-6** which follows an exhaustive review we conducted on the citing articles. It is illustrated that these articles cite Tour's paper for one of the following reasons:

1) – purely for literature review purposes,

2) – for citing a modification of the Hummers method used by Tour in his paper (i.e.: a modified Hummers method similar to the classical method), and

3) – for citing use of the improved Hummers method which is Tour's major value-added contribution to the field in his paper, a process described in the previous section which uses a protective chelating agent to guard the graphitic basal planes against breakdown during harsh oxidative treatment by Hummers oxidants, leading to large GO.

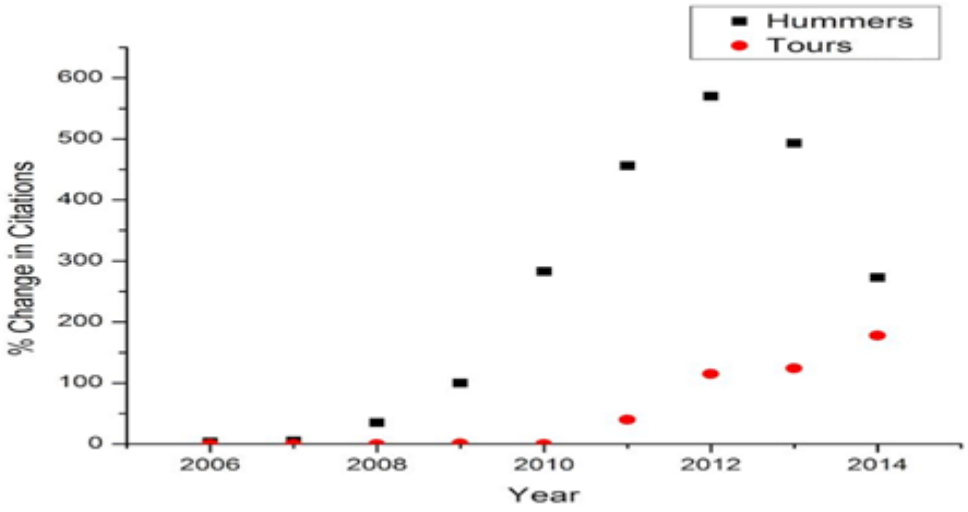

Figure 2-5. Annual increase in citations of the methods of Hummers and Tour for GO synthesis.

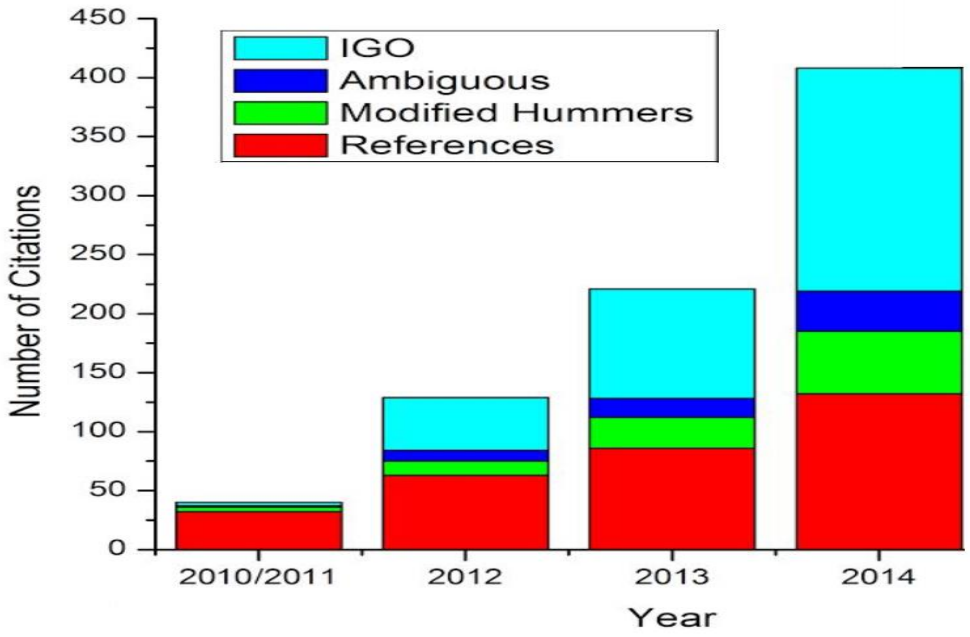

Figure 2-6. Breakdown in citation usage for the Tour et al. paper (IGO – Improved Graphene Oxide). Our review revealed that most citing papers do not use the novel technique introduced by Tour et al. but rather cite the paper for its informative value for review purposes.

We have to be careful in interpreting the growth in Tour citations shown in **Figure 2-5**; Tour's paper attracts more citations for its informative value on the general topic of GO synthesis and not necessarily indicating adapting the method for the preparation of GO. The break-down is presented below in **Figure 2-6**. Approximately 60% of the citations of the Tour paper are for the novel method while the rest of the citations are for other components of the paper. It is worth noting that this data was generated by exhaustively going through each article that cites the Tour et al. paper.

There are a few conclusions that may be drawn from the data. Firstly, the Hummers' method is still the dominant method of producing GO and will most likely continue to be for several years to come. Secondly, Tour's Improved Method is still gaining popularity with researchers in the field as it has not reached a growth cap as seen with other methods such as Brodie's or Staudenmaier's, and might well become the first choice for GO synthesis in the near future. Thirdly, most of the current citations using the Tour paper utilize it for literature review purposes, rather than for the practical synthetic value of the novel chelation-based technique introduced. This seems to indicate that there might be

certain inherent difficulties in performing or reproducing the results of the Improved Hummers method (Tour's Method). We will thus discuss next the impact of Tour's method on the characteristics and quality of the produced GO.

2.3 Comparative Review of GO Product by Method

Having established a marked increase in the number of publications on the Tour method over recent years, the purpose of this section is to give some comparative scope on the widely cited Tour paper which was published in 2010 on improved GO synthesis, versus its direct alternatives mainly that of Hummers (1958) and modified versions of the same.

Over our investigation, we found a few systematic problems that need to be addressed in the field. Primarily, the fact that many novel synthesis techniques are solely evaluated by their ability to oxidize graphite is problematic. While many researchers indicate that oxidation is the final goal, we remind our reader that the oxidation is only the means by which we achieve our goal of exfoliation. All proposed processes are capable of oxidizing graphite and the degree of oxidation can be controlled by reaction parameters, meaning that each synthesis technique is more or less the same and depends on the reaction conditions. Yet this fact is not stressed by many researchers. Secondly, there are insufficient reports on synthesis condition control, e.g.: graphite size used, temperatures, washing conditions, and stirring rate. Other literature deficiencies are related to the characterization of the particles; due to difficulties in obtaining representative morphologies, not many papers report such data. Finally, as is seen in the current discussions about the nature of oxidative groups in GO, techniques like FT-IR can lead to differing results depending on how the author chooses to interpret characterization data.

Despite these problems, we attempt to summarize the results of the comparative articles that may provide insight into differences between the products of these different synthetic techniques, with special attention to comparing the popular Hummers and Tour methods. The comparison focuses on two main areas: elemental composition (with a focus on C:O ratio) and GO sheet size. Elemental composition, especially impurity content, is particularly pertinent to sensitive fields such as optoelectronics, in which even small

doping concentrations of unwanted species can significantly affect device performance. C: O ratio is related to the degree by which the π-π conjugated network has been disrupted by oxidation as well as the degree of hydrophilicity, and can thus influence properties such as electrical conductivity of the final reduced-GO as well as compatibility with polymers in nanocomposite applications. Sheet size is also expected to affect electrical conductivity – a film composed of large rather than small sheets will contain fewer lines of contact between sheet edges per unit area and this is expected to reduce the degree of electrical resistance of a film made from big sheets of GO-derived graphene. Membrane applications, for instance, might be able to make better use of big sheets on account of their better barrier properties.

2.3.1 Elemental and Chemical Composition

Ambrosi et al.. (2014) was the only study we found that provided a systematic account of the elemental composition of different types of GO (C, H and O) as well as the major impurities coming from the synthesis and acid washes (Cl and S). In their study, the authors compare the Hummers, Staudenmaier and Tour methods, respectively. They also include an older, less popular modification of the Brodie method called the Hofmann method in their comparison. The authors of this paper also used combustive elemental analysis and inductively-coupled plasma mass spectrometry (ICP-MS) to investigate the presence of metallic and non-metallic contaminants in the product GO depending on the synthetic techniques employed. The results are summarized in **Tables 2-1** and **2-2**. **Table 2-1** results suggest that the Tour method produces the lowest C:O ratio of all GO synthesis techniques, which is consistent with the observation in Tour's original paper. The impurity content comparison in **Table 2-2.** ICP-MS comparison adapted from Ambrosi et al. (2014) of the elemental impurity content of Staudenmaier, Hummers and Tour GO, as well as the graphite for th syntheses. shows that the Tour method results in a large improvement over Hummers' method in terms of removal of potassium and manganese ions. The former in particular is a concern because it is thought to be a major contributor to GO flammability, while the latter poses a significant disposal concern from an environmental perspective both on account of its toxicity, and because it is harder to

remove via washing than other metallic impurities as observed in **Table 2-2** results. The difficulty in removing Mn is primarily because it is an elemental component of the active species which oxidizes graphite to GO, meaning that it is abundantly present in the GO reaction mixture to begin with, in addition to the difficulty associated with removing it from the graphite oxide galleries. The highly toxic Cr impurity, on the other hand, is retained more in Tour GO compared to Hummers GO, which makes the former technique less attractive in that regard. The Staudenmaier process is better than both the Hummers and Tour methods in terms of purity of GO, as observed in **Table 2-2**. Hence, any attempts to synthesize GO via the Tour method would need to focus on reducing the amount of oxidant used during the synthesis and/or improving product purity.

Table 2-1. Combustible elemental analysis of the GO produced from the methods of Staudenmaier, Hummers and Tour, adapted from Ambrosi et al. (2014).

Material	**Atomic %**					
	Cl	**S**	**N**	**O**	**C**	**H**
Graphite	-	-	-	4.42	94.03	1.55
Staudenmaier GO	0.52	1.06	-	27.09	45.92	25.41
Hummers GO	0.09	1.06	-	32.33	36.39	30.12
Tour GO	0.17	1.20	-	33.91	32.47	32.25

Table 2-2. ICP-MS comparison adapted from Ambrosi et al. (2014) of the elemental impurity content of Staudenmaier, Hummers and Tour GO, as well as the graphite for th syntheses.

Material	**Concentration (ppm)**						
	K	**Mn**	**Cr**	**Fe**	**Ni**	**Mo**	**Cu**
Graphite	130.0	3.7	11.4	128.3	6.4	59.82	1.52
Staudenmaier GO	480.2	2.5	6.6	47.6	4.9	-	3.88
Hummers GO	3400.6	5791.2	18.1	79.6	6.9	0.86	5.22
Tour GO	804.6	490.9	88.5	509.1	58.1	0.17	9.60

Moo et al. (2014) compared the Staudenmaier and Hummers methods. They used graphite flakes that were < 20 μm. The Staudenmaier reaction took 96 hours while the

Hummers method took 1 hour at 35°C with water addition occurred at a high temperature <90˚C. They report a C:O ratio of 3.30 for Hummers GO and 4.00 for Staudenmaier GO. To note, it is unknown if reactions went to completion.

Table 2-3. XPS C1 results detailing the chemical bonds formed in GO from the methods of Hummers and Staudenmaier, adapted from Moo et al.. (2014)

Material	**C1s peak distribution (%)**				
	C=C	**C-C**	**C-O**	**-C=O**	**O-C=O**
Staudenmaier GO	50.2	5.8	38.3	4.7	0.9
Hummers GO	40.1	11.3	30.3	13.1	5.3

The Staudenmaier GO, as seen in **Table 2-3**, does seem have a higher sp^2 character from the XPS results reported by Moo et al. (2014). XPS data give us a good quantitative indicator of GO surface functional groups; Fourier transform infrared spectroscopy (FT-IR) shows different groups distinctly but only qualitatively, while elemental analysis results can be complicated by the technique's inability to avoid detecting adsorbed water in the sample, as described earlier. Although the seemingly higher sp^2 character observed in XPS of Staudenmaier GO seems to indicate that the graphitic domains are better preserved using this synthetic method, Moo et al.. (2014) observe that the Staudenmaier GO is not well-exfoliated, which is a problem in terms of product quality. This observation, in turn, could partly justify the higher percent of C-C and C=C bonds in Staudenmaier GO; if the intercalation and exfoliation are poor during the synthesis, this means a smaller graphitic surface area is exposed to the oxidant action. Jia et al. (2014) reported the C:O ratio of Tour GO (shown in **Table 2-4**), based on the oxidant amount used:

Table 2-4. XPS results from Jia et al.. (2014) showing variations in the chemical bonds depending on the oxidant amount used.

Graphite: oxidant (wt)	Bonding environment and % presence on GO surface			
	-C-C- ~285.0 eV	-C-OH ~286.7 eV	-C=O/-C-O-C- ~287.0 eV	-COOH ~289.2 eV
1:5	39.9	19.3	33.1	7.7
1:7	32.4	19.9	38.0	9.8
1:10	10.6	27.0	50.3	12.2

As the amount of oxidant is increased, **Figure 2-7** suggests that we will obtain more epoxy groups and carboxylic groups until around 1:10 where the material switches from a carbon backbone structure to a largly epoxy-like base structure. These results indicate that C:O tuning can be accomplished by varying the ratio of graphite to oxidant to achieve the desirable chemical functionality of the GO surface, such that we can approach an OH-rich or an epoxy-rich surface.

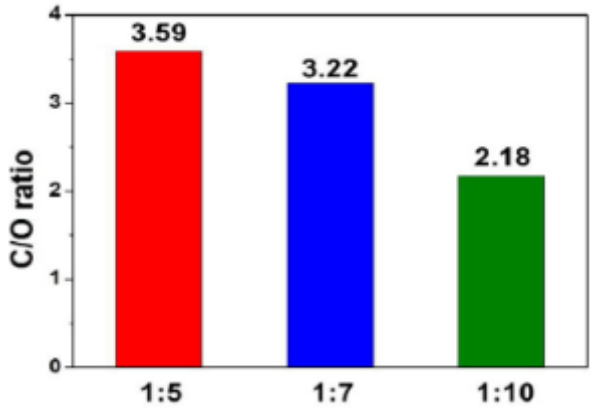

Figure 2-7. Jia et al.. (2014) C:O ratio depending on the wt ratio of graphite:oxidant employed.

2.3.2 GO size:

With regard to sheet size, it must once again be highlighted that a fair and direct one-to-one comparison is difficult due to variations in the starting materials and alterations to each method that a particular team may employ. For this reason, we present only two major examples: 1)- an attempt to make large GO (claimed 22 μm on average) using the

Tour method to oxidize 150 μm graphite for 12 hrs, and 2)- a useful comparison presented by Moghaddam and Paneri (2015) between the methods of Hummers (labeled HGO-1) and Tour (labeled MGO-1).

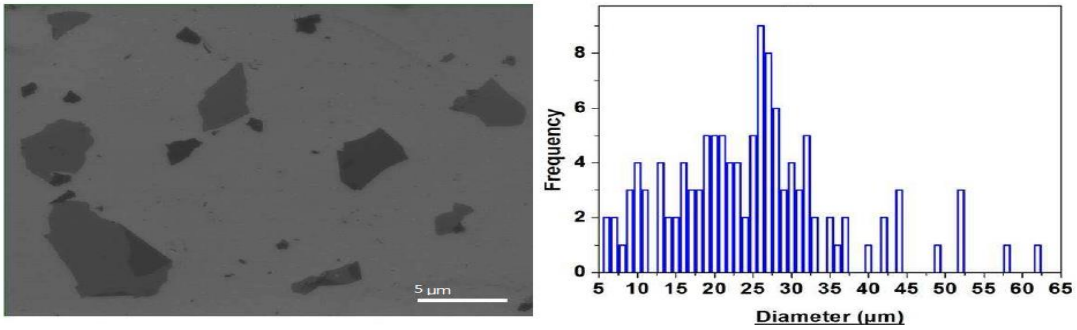

Figure 2-8. Xiang et. al.'s (2013) size characterization using SEM.

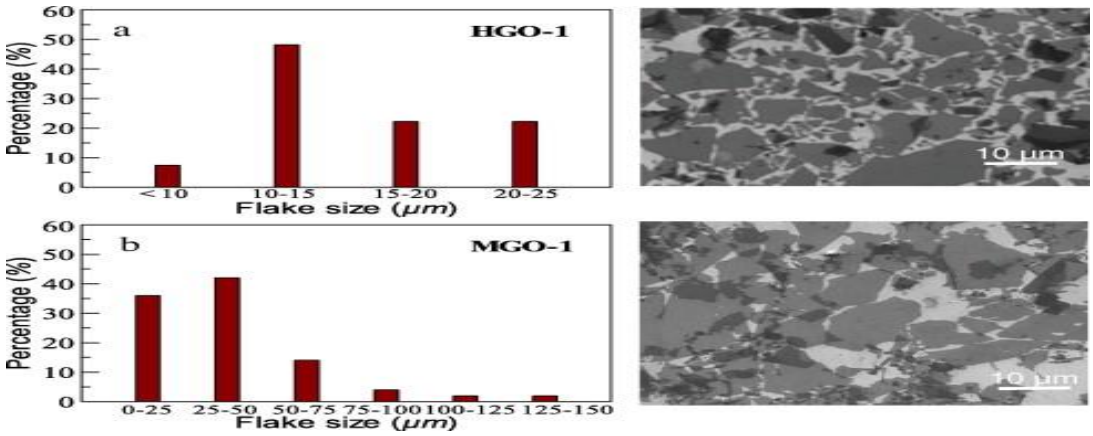

Figure 2-9. Moghaddam and Paneri (2015)'s own SEM size characterization results.

It is worthy of note that between authors and laboratories, the synthesized GO seems to take on different size characteristics; Mogaddam and Paneri had greater success in making large GO sheets using the Tour method than Xiang et al., while the Hummers GO generated by Mogaddam and Paneri does not differ much from Xiang et al.'s GO. This highlights the difficulty in comparing two GO synthetic techniques. However, we must point out that Mogaddam and Paneri used the Langmuir-Blodgett technique to coat GO for their size distribution analysis, which might have biased their results towards bigger sheets (we will review this in some detail in Chapter 7 on Langmuir-Blodgett deposition), while Xiang et al. used spin-coating.

It is also worthy of comment that none of the papers examined in the literature which claim to produce large GO used the Staudenmaier process. This could be the result of the comparatively harsher Staudenmaier oxidizing conditions which use fuming nitric acid in addition to sulphuric and permanganate, all of which are oxidants. Thus, and in the absence of a chelating agent like that used by Tour, it is expected that the Staudenmaier process produces relatively small GO compared to the Tour and Hummers methods.

To conclude this comparative review section, it seems like the Tour method produces the largest sheets of all the methods used in the literature, which gives it an advantage for modulus improvement in nanocomposites, as well as optoelectronics and barrier-based applications. The ability of this method to produce big sheets also means an expanded application window due to a wider range of accessible sheet sizes. It also seems that the Tour method, while generating larger sheets than average, is environmentally friendlier than the Hummers method both in terms of gross production of metal ions as well as in the individual cases of potassium (major contributor to GO spontaneous flammability) and manganese (toxic) ions. In addition, the absence of nitrates and nitric acid means that the Tour method releases the least amount of toxic gas (especially NO_x) of all the synthetic methods reviewed. The Tour method also increases the level of oxidation of GO compared to other synthetic techniques, making the material more hydrophilic, water-dispersible and solution-processable for coating-based applications. As we will see in the next subsection, the Tour method is able to achieve this increase in hydrophilicity while maintaining a similar degree of pristine graphitic domains in the product GO compared to the other common synthetic routes. For these reasons, we are further inclined towards using the Tour method and adapting it to our purposes to prepare ultralarge GO.

2.4 Recent Advancements in GO Synthesis

There have been other developments in the field not related directly to the Tour synthesis method. The articles reviewed below are presented as interesting and useful techniques which represent some of the most recent attempts to diversify the field of GO synthesis.

Kumar et al.. (2015) claim a new synthesis technique with long range order. Their technique relies on employing expanded graphite. This 26 hour synthesis technique reached a 41% yield. The novelty in their synthesis is that the graphite is first expanded with nitric acid for 24 hours, then grounded in a powder mixture with potassium permanganate which is dusted into a sulphuric acid bath and the end product was sonicated. Kumar et al.. (2015) stress the importance of the D/G band ratio in Raman spectrometry to indicate the quality of the produced GO. Caution should be employed here because this metric is very susceptible to non-oxidized graphite reactant. Their novel technique gave a D:G band ratio of 0.85. The product quality from this process seems inferior to that from the Tour method; the latter gives greater yield of GO (i.e.: higher conversion) and D:G ~ 0.8 as reported in a recent work by Moghaddam and Paneri (2015) , indicating fewer defects.

In the interest of producing large sheets of GO, Xufeng Zhou and Zhaoping Liu (2013) report having produced GO as large as 200 μm. Their approach consisted of the regular Hummer's based process aided by gentle shaking of 300 μm graphite powder with polymeric surfactants such as Trition-X 100. However, their methods have not been clearly elucidated for replication. Additionally, this method does not seem scalable due to the use of surfactants and long exfoliation time.

2.5 Conclusion

We conclude from this literature review that there is a need in the scientific community to reliably produce large GO sheets that preserve as much of the sp^2-graphene character as possible. Large improvements in the process have been made since Brodie first published his paper on GO synthesis. An increasing number of researchers in the past few years have been turning to the Tour method, which uses phosphoric acid as a protective chelating agent to prevent excessive oxidative damage to the graphitic surface, compared to the Staudenmaier method. In addition, the annual rate of increase in the number of citations which use the Tour method is greater than that for the Staudenmaier method and is increasing, while that for the Hummers method is decreasing. This seems to indicate a

shift in the interest of the scientific community to the Tour method, and that this method might replace that of Hummers as the future GO synthetic method of choice.

This growing interest in the Tour method was attributed to a number of reasons reviewed in the literature: 1)- it was observed to have given other researchers success in creating large area GO compared to the other methods, 2)- it is lower than the Hummers method both in terms of gross production of metal ions as well as in the individual cases of potassium (major contributor to GO spontaneous flammability) and manganese (toxic) ions, 3)- In addition, the absence of nitrates and nitric acid means that the Tour method releases the least amount of toxic gas (especially NO_x) of all the synthetic methods reviewed, and 4) the Tour method also increases the level of oxidation of GO compared to other synthetic techniques, making the GO more hydrophilic, water-dispersible and thus solution-processable for coating-based applications. As we will see in the next subsection, the Tour method is able to achieve this increase in hydrophilicity while maintaining a similar degree of pristine graphitic domains in the product GO compared to the other common synthetic routes. For these reasons, we are further inclined towards using the Tour method and adapting it to our purposes to prepare large GO. This review has thus granted us confidence in the viability of the Tour method for our research purposes as it seems to be the next evolving method for the production of GO, and we thus use it as the synthetic method of choice for the remainder of this thesis.

Chapter 3: Graphene Oxide Synthesis

In this chapter we will detail our synthesis and characterization of chemically exfoliated graphene oxide (GO). The process turns graphite flakes, which consist of tightly packed sheets of graphene, into exfoliated sheets of GO dispersed into an aqueous medium. Our work is inspired in part by a number of papers published by the Tour group, specifically: Marcano et al..'s (2010) and Dimiev and Tour (2014). The former describes the use of a protecting agent in the chemical reaction to oxidize graphite to minimize sheet defection and breakage whereas the second paper details each step of the more traditional Hummers methods. Our synthesis work is based on modifications of this recent Tour method: specifically, we introduce modifications to the starting graphite type and oxidant amount, synthesis conditions as well as the wash procedure to tailor the process towards producing big sheets. For the purposes of this chapter, we shall adopt the stages described by Dimiev and Tour (2014) and use their nomenclature, calling our method the modified Dimiev-Tour method (DTM). The first stage in the synthesis is intercalating graphite with sulphuric acid. The second stage is the chemical oxidation of graphite. The third stage involves product purification. It is in the third stage that our compound is finally exfoliated and the product is purified.

We start with 10-mesh graphite from Alfa Aesar whose flakes have been pre-sieved through a 2 mm mesh. The choice was made to start with larger graphite because this was thought to increase the likelihood of preserving large flake size in the product GO flake. This is perceived to be a practical advantage; since graphite oxidation is a top-down, making big GO sheets in this way can offer a flexible experimental window, whereby the GO can be sonicated, centrifuged and/or filtered to fractionate the required size fraction(s) for the application(s) of interest. Moreover, big sheets might be better-suited for applications such as optoelectronics and polymer nanocomposites; using big sheets results in fewer electrically insulating sheet-sheet junctions per unit area for use in optoelectronic films, while in nanocomposites, such sheets are expected to enhance mechanical properties such as stiffness per unit loading of filler. The downside to this choice of graphite is the increased time of reaction and potential increase in the amount of oxidant needed. Using a combination of optical microscopy and Raman spectroscopy

to track reaction progress, Dimiev and Tour (2014) were able to show that the reaction mainly progresses from the outside of the graphite flake inwards. The larger flake size means that there are fewer starting edges for the reaction to occur at. The centre of any given graphite flake is thus more protected from oxidation than the peripheries, and may not be well-oxidized. There also exists the possibility that using an increased time of oxidation can cause peripheral regions of a given flake to be over-oxidized. It was thus seen as important to control conditions such as oxidant loading and reaction time to ensure that the product is as homogeneous in composition as possible.

Based on the preceding discussion, the synthesis was set up using 10-mesh graphite from Alfa Aesar (starting size: 2000 μm) to achieve as big a size of GO as possible, using the chelation-protection mechanism from the Tour synthesis to minimize sheet breakdown, and optimizing the amount of oxidant used to achieve the required conversion as per the synthesis recipe described by Marcano et al. (2010) and Dimiev and Tour (2014). The washing of large area, oxygen-enriched GO from the Tour synthesis can result in severe gelling issues, rendering it difficult to filter or perform dialysis. For these reasons, washing was carefully conducted via centrifugation using solvents such as HCl acid and water. The inspiration for the washing recipe came in part from the work by Kim et al. (2010) on the subject. The following is a detailed description of the reaction setup and monitoring.

3.1 Synthesis Procedure

The first part of the synthesis is preparing the acid graphite suspension. We added 120 ml of acid to each gram of Alfa Aesar 10-mesh graphite. The acid was a 1:9 mixture of phosphoric acid (Sigma Aldrich, 85% in water) and sulphuric acid (Sigma Aldrich, 98%). Marcano et al.. (2010) claim that this added phosphoric acid acts as a protective chelating agent for the graphite and inhibitor of excessive oxidation, preserving the structural integrity of the sheets, as reviewed in the previous chapter. The graphite and acid mixture is added together to form a graphite intercalation compound (GIC). Dimiev and Tour (2014) make the claim that the compound forms instantaneously upon addition of the two components. We mixed the dispersion for a half hour using a propeller stirrer at 300 rpm;

the propeller stirrer offers the advantage of constant stirring rate regardless of changes in suspension viscosity, as opposed to a regular magnetic stirrer.

$KMnO_4$ (Sigma Aldrich) was then added slowly to the GIC to avoid an exotherm buildup that would normally increase the mixture's temperature to 35°C; by ensuring that no excessive local exotherms are experienced in the reaction mixture, we are able to minimize the chances of defect formation on the graphitic surface that could result from faster local kinetics. $KMnO_4$ was added in 4.5 weight equivalence to graphite. This amount is significantly less than the 6 wt equivalences employed by Marcano et al.. (2010). The oxidizer ratio was optimized by starting at 3 wt equivalences and slowly adding more oxidizer until the product had no significantly visible fraction of dark, unoxidized particles in the washed product (**Figure 3-2**). This was done in an attempt not to over-oxidize our product and preserve the original pristine sheet size. Upon addition of the $KMnO_4$, the dispersion changes to a dark green. The mixture was stirred at 20° C for 72 hours or till the green colour disappeared. It must be noted that on previous trials, 72 hrs was observed to be a time requirement regardless of the oxidant amount used, indicating that the limiting factor here is the graphite size rather than graphite:oxidant ratio, and thus vindicating our attempt to optimize this latter ratio. Dimiev and Tour (2014) state that the green colour is indicates the presence of MnO_4^- ions in solution. By the end of the reaction, the dispersion turned purplish gray, as observed in **Figure 3-1**.

Figure 3-1. Appearance of GO reaction mixture a) – immediately after addition of $KMnO_4$, and b) - after reaction completion

In the next stage, water is normally added to the mixture to dilute the acidic mixture. The highly exothermic dilution step could lead to GO boiling. It has been our experience that boiling the GO can lead to precipitate formation much like the base-boiling procedure reported by Dimiev and Polson (2015). This observation is supported by papers such as Bing-Bing et al.. (2014) who report degradation in the crystalline structure of GO by conducting the reaction at elevated temperatures (>30^{o}C). Instead, we have adapted our procedure by first performing a centrifugation at 5000 rpm for 20 minutes in a Beckman-Coulter centrifuge to separate most of the acid, as opposed to the Tour method were the first post-synthetic step is washing with 1M HCl acid. By first removing the acid (pH = 1) from the reaction mixture before adding the HCl acid wash, we were able to minimize the local exotherm release that would have resulted from dissociation of the concentrated sulphuric-phosphoric acid from the reaction mixture in the water from the HCl wash. This extra step decreases the chances of accidentally reducing some of the GO formed during the synthesis due to large exotherm release; as well as the chances of creating defects on the GO sheets as a result of unnecessary cycles of oxidation-reduction due to poor control over the reaction temperature. H_2O_2 was then added in small amounts until no gas evolution was observed. This step reduced the remaining permanganate ions to their colourless form. After the first centrifugation, the solution showed a bright yellow colour like peanut butter as seen in **Figure 3-2**(a). Washes were continued with 1M HCl acid till the supernatant was no longer clouded by the addition of barium chloride. All washes were performed at the same conditions listed above (5000 rpm, 20 min spins) with a slow deceleration to prevent dispersion intermixing during the deceleration stage.

The next step was a DI water wash. It is in this step that the unexfoliated graphite oxide is converted into exfoliated GO, as shown by Dimiev and Tour (2014). The washing was performed similarly to the acid washes but the centrifugation time was increased to one hour. This step is noted by a colour change to deep brown. The final dispersion colour can be noted in **Figure 3-2**(b). This dispersion seems to be biphasic after multiple washes with some of the original light yellow colour persisting. We support the exfoliation by presenting florescence microscopy results in the characterization subsection below. It is worth-mentioning that we attempted substituting HCl with DI water as the wash solvent during the first washes (i.e.: washing with water throughout), with the only observable

difference being that we needed to add one wash step to ensure that the sulphate was exchanged out completely (under the detection limit, as detected by the barium chloride test); this eliminates the need for HCl as a wash solvent during GO synthesis. After the wash completion, the product was passed through a 500 μm mesh to remove unoxidized particles. A few filtrations were required to remove undesirable dark particulates.

(a) (b)

Figure 3-2. Appearance of a) aqueous graphite oxide at the end of the synthesis after adding hydrogen peroxide, and b)- graphene oxide (GO) at the end of the wash steps

3.2 Characterization

To evaluate the quality of the GO obtained via our synthesis for preliminary quality control purposes, we used the following techniques:

- Wide-angle X-ray Diffraction (WXRD) to determine the degree of graphite conversion to GO as well as the intercalation level from the (002) d-spacing
- X-ray Photoelectron Spectroscopy (XPS) to determine the C:O ratio and functionalities present in the product GO
- Elemental analysis and Fourier Transform Infrared Spectroscopy (FTIR) to confirm said C:O ratio and functionalities
- Raman Spectroscopy to determine the degree of oxidation-induced surface defects

- Combination of Fluorescence Quenching Microscopy (FQM) and Atomic Force Microiscopy (AFM) to measure the lateral size and thickness of the GO sheets at random and generate statistics using those.

The next section describes the details of these characterizations techniques. Details of the microscopy, image acquisition and analysis are presented in Chapter 4, where special attention is given to this aspect of GO characterization. In all the characterizations that follow, the procedure followed was that each sample was run twice to ensure result consistency, with the condition of conducting a third run if a discrepancy was observed between the two measurements. In all cases, however, both of the first two trials gave similar results with no significant discrepancy, so we suffice by showing results from one run each below.

3.2.1 Wide-angle X-ray Diffraction (WXRD)

Wide-angle X-ray diffraction (WXRD) patterns were acquired on the dry GO using a PANalytical X-Pert Pro MPD X-ray diffractometer equipped with a Co source (45 kV, 40 mA, k = 1.790A°) and an X-Celerator detector. Data was collected for 2θ ranging from 5^o to 60^o in increments of 0.02^o and a dwell time of 2.0s. The dry sample was first ground into a fine powder in a porcelain crucible, before loading 50 mg onto the quartz sample holder with care to ensure that the sample formed a flat layer on the surface.

3.2.2 X-ray Photoelectron Spectroscopy (XPS)

X-ray photoelectron spectroscopy (XPS) spectra were collected using an SSX-100 instrument (Surface Science Laboratories, Inc.) equipped with a 200W high throughput bent quartz crystal monochromated Al K_α X-ray source, a hemispherical sector analyzer (HSA) and a resistive anode detector. The sample was mounted on the sample holder using double-sided carbon or aluminum tape. Care was taken to ensure the surface was fully covered with a sufficiently thick layer of the sample. The base pressure of the XPS system was 6.0×10^{-10} Torr. During the data collection, the pressure was ca. 1.0×10^{-8} Torr. The sample GO was not sufficiently conductive and a low-energy electron beam

(10 eV) was applied for charge neutralization. The X-ray spot size was 1 x 1 mm^2, which corresponded to an X-ray power of 200 W. The survey spectrum was collected using 10-16 scans at 150 eV pass energy and 1 eV/step. The high resolution spectra were collected using 50 eV pass energy and 0.1 eV/step.

The atomic percentages were calculated from the survey spectra using the ESCA HAWK software provided with the XPS system. For high resolution data, the lowest binding-energy C 1s peak (presumably, C-C/C-H peak) was set at 285.0 eV and used as the reference for all of the other elements. The curve fitting used a combination of Gaussian/Lorenzian function with the Gaussian percentages being at 80% or higher.

3.2.3 Elemental Analysis

Elemental analysis by combustion was carried out on a EuroVektor Euro EA-300 elemental analyzer by loading 1.0 mg into the sample chamber. The front furnace temperature was 980^oC. In this way the, CNHS was directly measured for the powder, with the O content determined by subtraction.

3.2.4 Fourier Transform Infrared Spectroscopy (FTIR)

A spectrometer of model Nicolet Magna - IR760 was used to obtain the FTIR spectra for GO. The GO was first dried in vacuum at 60^oC overnight and ground with potassium bromide (KBr) at a ratio of GO:KBr = 1:10 by mass. The ground powder was then packed into clear pellets and used to obtain FTIR measurements.

3.2.5 Raman Spectroscopy

An alpha 300R confocal Raman microscope equipped with a UHTS200 spectrometer and a DV401 CCD detector from WITec (Ulm, Germany) was employed to collect Raman spectra. An Ar-ion laser with a wavelength of 532 nm, a 10x lens and a power of 6 mW was used for excitation. The data was collected over 30-60s. The sample was deposited as

a powder on glass slides for the measurement and spread out using a spatula to make sure thickness remained consistent throughout. Instrument: Witec Alpha 300 R confocal Raman microscope.

3.2.6 Fluorescence Quenching Microscopy (FQM) and Atomic Force Microscopy (AFM)

As stated above, detailed procedures for coating, image acquisition and analysis are provided in Chapter 4 for both of these techniques, which are the subject of that chapter.

3.3 Results

3.3.1 X-ray Photoelectric Spectroscopy (XPS)

XPS analysis was carried out in order to find the surface composition of GO. XPS spectra results are shown in **Figure 3-3**. The deconvoluted C1s spectrum (**Figure 3-3**) shows different peak positions along the x-axis, corresponding to binding energies that are the signature of different bonding environments of the carbon and oxygen in GO. The inset of **Figure 3-3** shows that the C1s spectrum is a superposition of two strong peaks at 284.4 eV and 287.4 eV, as well as a weak peak at a binding energy of 288.8 eV. The former two peaks are signatures of C-C and C-O bonds respectively, as explained by Briggs and Beamson (1992), as well as Waltman et al. (1993). The C-O bond is thought to be the result of contributions by epoxy and OH groups which are impossible to decouple. The last major peak is the small one at 288.8 eV, thought to belong to C=O, understandably small because C=O are thought to be concentrated at the edges of the GO sheets. For Tour GO, which is thought to be bigger than average in terms of size, the ratio of edges to center is small enough that such a peak is quite small in size. The O1s peak gives rise to consistent results with the C1s peak, revealing two major peaks: a weaker C=O peak at 531.5 eV and another stronger peak at 533 eV corresponding to a combination of C-O and O-H. Once again, the comparative weakness of the C=O peak can be typically attributed to small edge-to-center ratio for the GO sheets.

Decomposition of the C^{1s} XPS spectrum into these main components indicates that the fractions of C-O and C-C bonds in GO are about 60% and 40% respectively. Analysis of XPS data by comparing the C1s and O1s normalized peak area yielded a C: O ratio of 1.70. Elemental analysis (EA) was also performed on the GO to corroborate results from XPS. A similar ratio C:O of 1.67 is also found from standard EA measurement, which indicates consisteny. This heavy degree of oxidation where more than one O atom is bonded to every two C is expected for a heavily oxidized material such as GO.

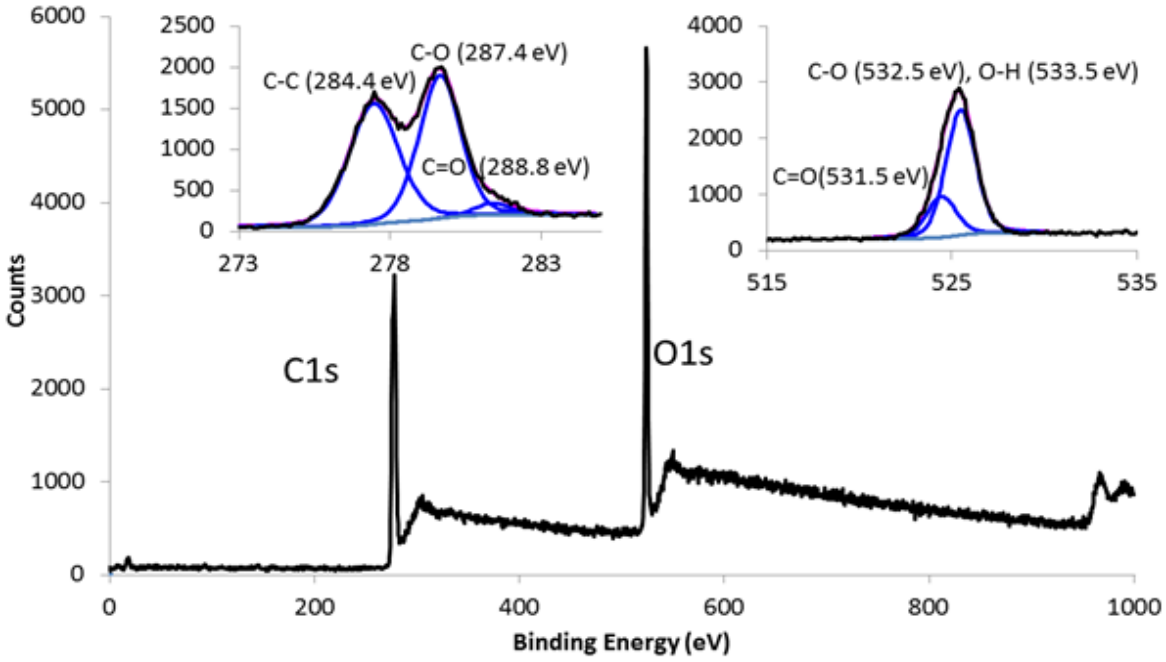

Figure 3-3. XPS spectrum for GO showing that the elemental composition is primarily C and O, with each peak deconvoluted and resolved in the insets to reveal different bonding environments

3.3.2 Wide Angle X-ray Diffraction (XRD)

WXRD characterization is typically carried out on GO for a couple of reasons:

1) - to estimate the d-spacing between GO layers, as per Bragg's law diffraction equation: ($n\lambda = 2d\sin\theta$) where, n is order of diffraction λ is the X-ray wavelength of 0.15418nm for a Cu-K-α ~1, source, and d is the (002) interlayer d-spacing between individual GO sheets. The d-spacing estimate helps provide an indication as to the degree of success of exfoliation for the GO, even though a certain amount of re-stacking is expected to occur upon the drying of GO that precedes the WXRD measurement.

2) - WXRD spectra help indicate the amount of unoxidized graphite left behind from the GO synthesis (the peak for graphite occurs at 26.5^{o}), thus providing an indicator for the completeness of the reaction. It can also act as an indicator for the presence or lack of amorphous carbon formed sometimes as an undesirable side synthetic product of; this can happens due to severe heat-shock steps during the synthesis, which we eliminated from our procedures by taking care to make gradual additions of H_2O_2 and water to the acidic reaction mixture (in the quenching and wash stages), as well as taking care to centrifuge out the acid before proceeding with washing (especially water). Amorphous carbon can manifest as characteristically unsharp, broad peaks, sometimes at 2θ as high as 43^{o}.

WXRD results are shown in **Figure 3-4**. These results indicate that the GO interlayer spacing is approximately 0.9 nm, which is close to the reported from other literature, for which the average interlayer spacing is found to be 0.9-1.1nm. This indicates successful exfoliation. The large interlayer spacing of the GO is indicative of surface decoration with functional groups such as hydroxyl and carboxyl, as well as intercalation by water molecules. Moreover, the lack of strong peaks at 26.5^{o} and elsewhere indicates that our synthesis is successful in achieving almost 100% conversion of graphite to GO, with virtually no unreacted graphite or secondary products such as amorphous carbon which could mar the quality of the product. This point is emphasized by the absence of a graphite oxide (001) peak between 10^{o} and 20^{o} (such a peak would be expected around $14\text{-}15^{o}$), indicating completeness of the exfoliation.

The small peak at 20.5^{o} might correspond to a small quantity of reduced GO (r-GO) which might have been formed during the synthesis despite our best attempts to eliminate the possibility of this occurrence. This small peak might also be the (002) graphite peak, shifted from its original position at 26.5^{o} to indicate short-range order in stacks. The small peak at 42.5^{o} might correspond to a turbostratic band of disordered carbon materials, such as amorphous carbon. Both of these peaks are expected to manifest themselves as broad, unsharp peaks due to short-range order, so the explanations for these two small peaks might not be accurate, but they are nonetheless thought to be the most likely justifications for the presence of such peaks in our spectrum. These peaks are, in any case, very small

and indicate a high degree of conversion of graphite to GO, with minimal formation of side-products.

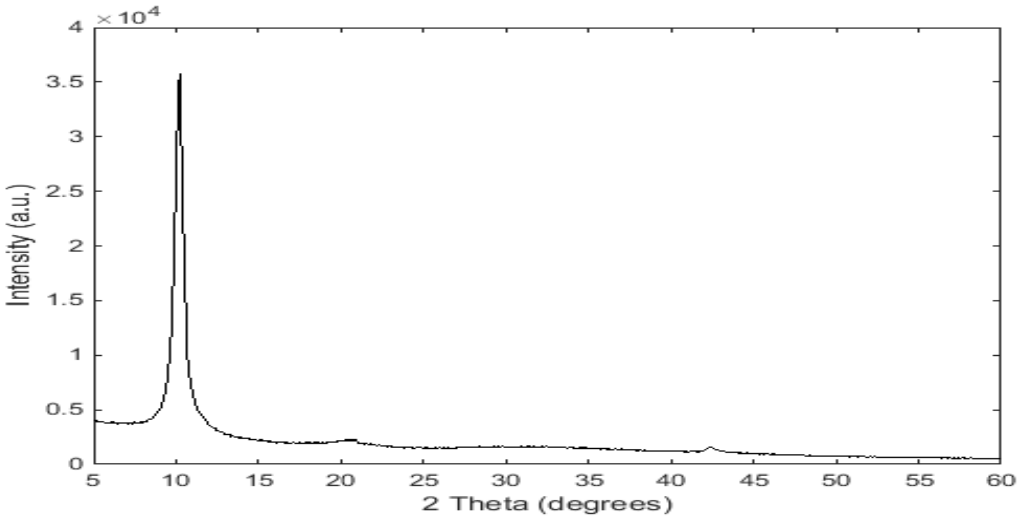

Figure 3-4. WXRD result of GO synthesized via the Tour method, showing a dominant 2θ peak at 10^{o}, corresponding to the (002) d-spacing of GO

3.3.3 Raman Spectroscopy

The results of Raman analysis of GO are shown in **Figure 3-5**. Upon carrying out peak integrations, a D: G band ratio of 2.0 was calculated. The D:G band ratio provides an indication of the degree of surface defects; the higher this ratio, the more defective the GO ratio. This is consistent with literature reports by Bing-Bing et al. (2014), and considering that the reaction was conducted for 72 hrs at 20^{o}C, this value of D: G indicates that our GO is not significantly different from that synthesized by others in the literature in terms of degree of surface defects. In fact, if anything, having gone through a 72-hr oxidation while maintaining a D:G maximum ratio of 2.0 indicates our success with reducing the potential degree of surface defects during this long synthesis by the expedient of reducing the amount of oxidant used (as described in the experimental section above), and it holds promise for future attempts to reduce GO surface defectiveness in-situ during the synthesis.

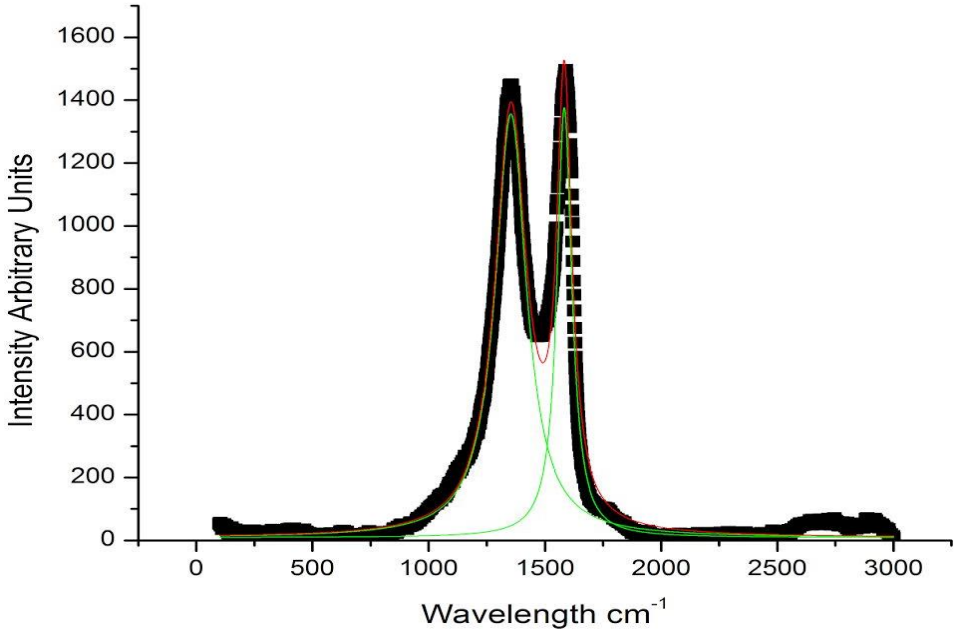

Figure 3-5. Raman spectroscopy result for lab-synthesized Tour GO in powder form

3.3.4 Fourier Transform Infrared Spectroscopy

FT-IR spectroscopy was used to identify the functional groups present in our MTD GO (Kosynkin et al., 2009), as shown in **Figure 3-6**. The qualitative presence of these groups is consistent with the observations previously obtained based on the XPS analysis of the GO. All the groups are consistently present across XPS and FTIR, with FTIR further revealing the presence of C=C and R-O-R groups. The C=C groups act as an indicator to the presence of unoxidized "pristine" graphitic islands on the surface, which is also in consistency with the D:G band ratio obtained from Raman. The presence of R-O-R groups is also consistent with our expectation that a graphitic surface is likely to contain clusters of C atoms (i.e.: R-groups) which are connected to O atoms by epoxy-linkage, yet an indicator of success in minimizing the level of surface oxidation.

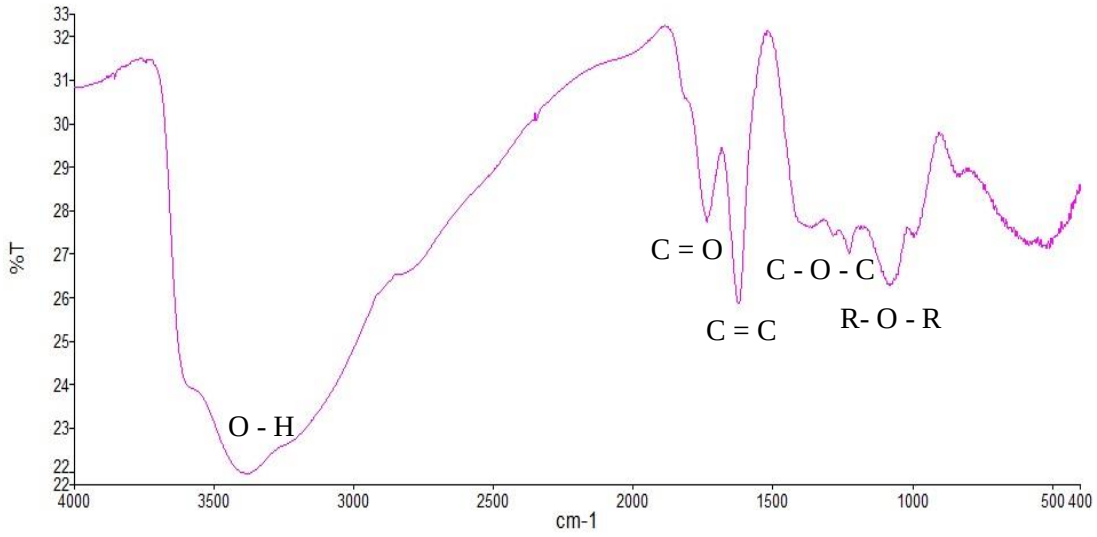

Figure 3-6. FT-IR spectrum for Tour GO with peaks corresponding to different functionalities labelled.

3.3.5 Microscopy

In this subsection, we present the microscopy results from both FQM and AFM **Figure 3-7** to convince the reader of our success in creating large, well-exfoliated GO, while we defer discussion of the detailed procedures for coating, microscopy and image analysis to Chapter 4, which deals with these characterization aspects of GO at length.

FQM and AFM preliminary imaging results are shown in **Figure 3-7** a) and b). In some instances, the sheets reached a size of 200 μm, an observation consistent with the expectation that the Tour synthesis yields larger than average GO compared to some of the other conventional synthesis techniques such as the Hummers method. Preliminarily, it can be said that our Tour synthesis is successful at creating large GO using a single-pot synthetic reaction route. Moreover, the similar contrast level revealed by sheets in the FQM image in **Figure 3-7**(a) indicates that most of the sheets are at the same level of thickness. **Figure 3-7** (c) and (d) show a contact mode AFM image from one such GO sheet selected at random from the surface, revealing the thickness of said sheet to be 1.2 nm, consistent with literature reports by Stankovich et al. (2007) on monolayer GO. This is encouraging because it indicates that our technique is successful at exfoliating GO into monolayers.

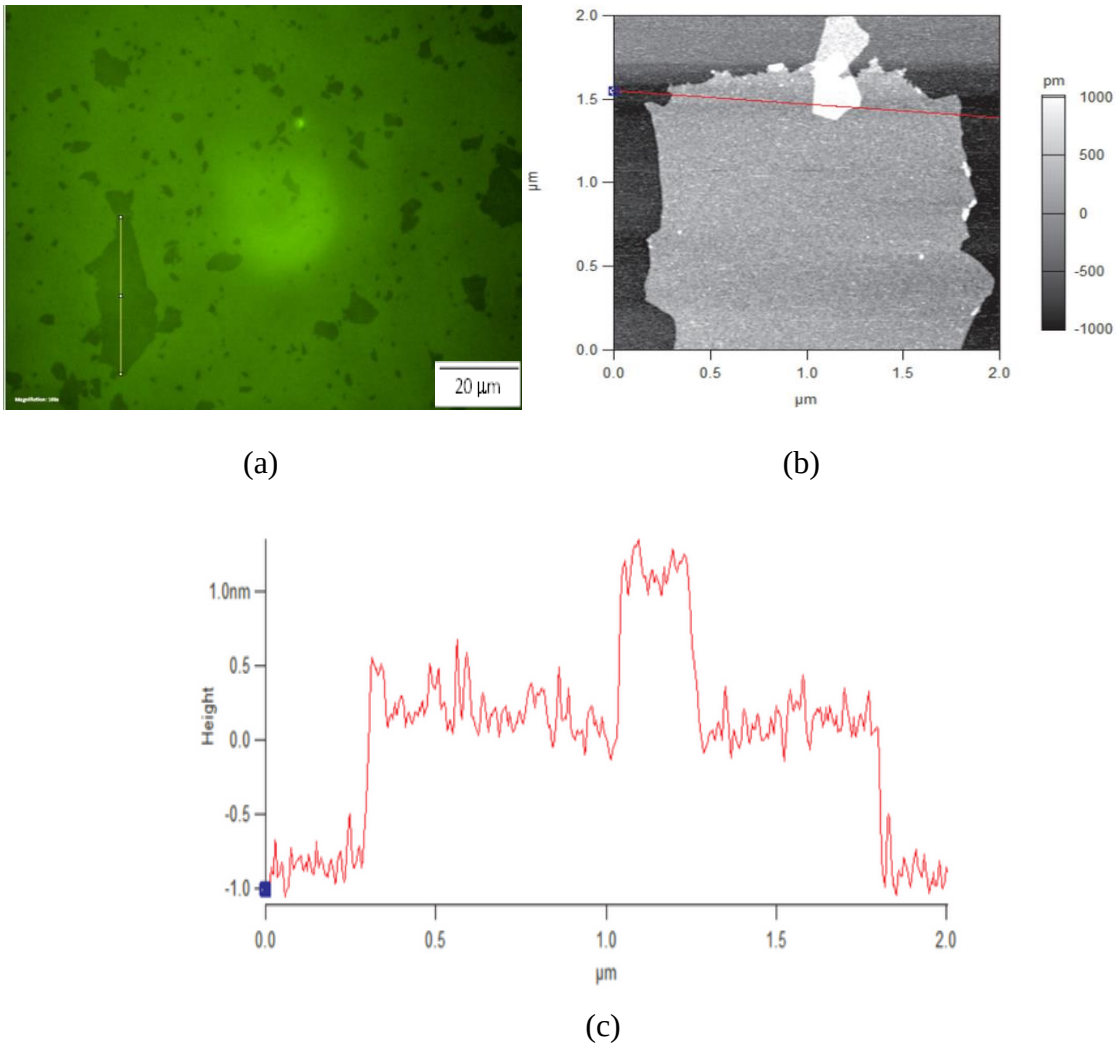

(a) (b)

(c)

Figure 3-7. (a): Fluorescence-Quenching Microscopy (FQM) image of Tour GO showing all sheets to be at the same level of contrast (and thus, thickness) albeit showing a high apparent polydispersity, (b) non-contact mode Atomic Force Microscopy (AFM) images of GO and, (c) line trace taken across one such sheet.

3.4 Conclusion

In conclusion, GO was synthesized using modifications of the Tour method tailored towards producing large GO sheets by starting with a large graphite size and using the protective chelation mechanism of the Tour method to minimize the amount of sheet breakage and degradation. The reaction oxidation conditions (graphite: oxidant amount

and reaction time) were optimized at 1:4.5 (compared to 1:6 using the Tour method) and 72 hrs respectively, by visually inspecting the disappearance of dark flakes in the product. Temperature control was used to insure reproducibility in the results and avoid unintentional reduction of the GO product. The product GO was characterized using a number of techniques: XPS revealed a higher than normal O content (expected for Tour-synthesized GO), an observation supported by elemental analysis. FT-IR qualitatively revealed the same functionalities that were discerned by XPS, indicating consistency of results. Raman spectroscopy revealed a comparable degree of surface defects to GO synthesized by similar techniques in the literature, an indication that the long oxidation time we used did not significantly increase the level of surface defects introduced to the graphite beyond what is expected following oxidation. This might be attributed to our minimization of the oxidant amount used. FQM and AFM respectively revealed the sheets to be primarily composed of monolayers and containing large sheets (>20 μm), and. All of this work significantly improves the knowledge on reproducibly making large GO sheets.

Chapter 4: Imaging and Image Analysis

Imaging of nanoparticles represents the most direct means to characterize the dimensions and polydispersity of the nanoparticles. This chapter is concerned with the coating recipes optimized for Graphene Oxide (GO) and the subsequent imaging protocols used for fluorescence-quenching microscopy (FQM) and atomic force microscopy (AFM). It also introduces the software tools used to analyze the obtained images. The tools needed to address this latter aspect of the nanoparticle imaging process are emerging slowly since image analysis is a complicated field of its own. The difficulty in this field, as observed using GO as a case study, is the result of one or more of the following problems:

1) - the inherent difficulty in coating without overlap, computationally identifying and fairly representing a population of non-spherical/circular, widely polydisperse and polymorphic nanoparticles (similar to what is typically dealt with in sheet-based systems).

2) - Edge identification difficulties with some nanoparticles render it impossible to accurately mark the boundaries of these particles and estimate their size. These difficulties stem from an occasional lack of sufficient magnitude and consistency of contrast levels in the flourecence quenching images.

3) - Issues with the coating quality – especially with FQM images – can result in the generation of some stains or scratches on the substrate surface. To automate the process as best as possible, the software tool used to analyze the particles should be able to filter these "ghost particles" out as noise and not identify and include them as part of the analysis.

4) - Images can display variations in the level of brightness and uniformity across them (especially FQM, and to a lesser extent, AFM images). The software analysis tool should also be able to filter such fluctuations out as noise.

At the end of the chapter, we will illustrate and review most of these problems that are typically encountered. We also propose our own solutions to these problems, both from the coating and MATLAB analytical perspectives. With these solutions introduced, automation in characterizing distributions of nanoparticles has been realized in order to

complement our rheological studies, and imaging results are presented in the subsequent chapters.

4.1 Experimental Imaging

4.1.1 Microscopy Techniques

Fluorescence quenching microscopy (FQM) is an imaging technique used to determine the lateral dimensions of nanoparticles that can accept electrons from donor photoactive fluorescent particles. GO contains π- π aromatic rings that allow it to accept electrons in an excited state. Kim et al.. (2015) describe this process between pyrene and GO where the excited electron in pyrene at approximately -3.2 eV can decay to -4.5 eV in GO instead of the -5.5eV ground state in pyrene. In order for this electron transfer process to occur the two systems have to be in contact through tight π- π stacking. The π- π stacking allows the band-structure of the two materials to overlap and facilitate electron transfer. The alternative decay mechanism avoids irradiation in the visible spectrum "quenching" the fluorescence.

A typical fluorescence microscope consists of a standard optical microscope with a mercury lamp. The mercury lamp provides a broad spectrum of light to excite the fluorescent species. The excess light can then be filtered out from the reflection by appropriate filters.

To obtain information about the thickness of the particles, contrast levels can be correlated with the thickness levels from atomic force microscopy. Increasing amounts of GO stacking will linearly reduce the intensity of the fluorescence. **Figure 4-1** depicts one such FQM image of Tour GO displayed in the image processing software ImageJ, with the characteristic quenching-induced contrast between sheets and surrounding background. Some of the sheets at the edges of **Figure 4-1** appear darker than those closer to the center; this could be due to increased stacking on the fringe sheets, but it could also be because of a misalignment between the mercury lamp and system optics, resulting in the image receiving an uneven level of illumination. It is for reasons such as this that AFM is more commonly used than FQM for thickness determination on such sheets.

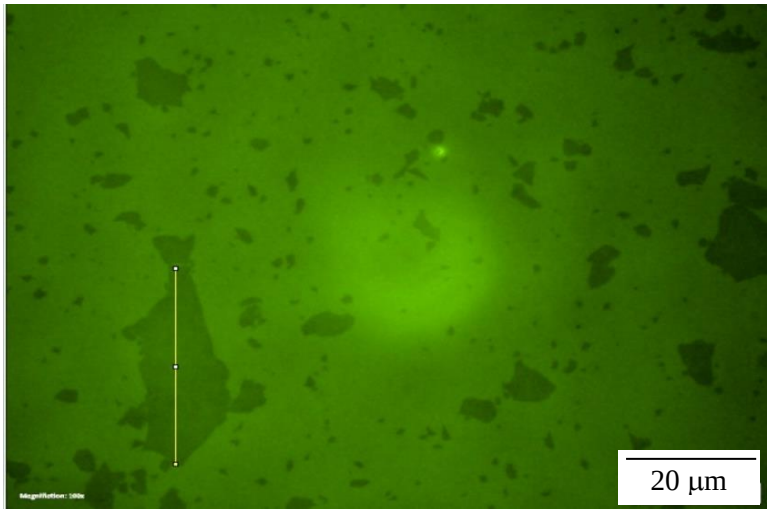

Figure 4-1. The Tour's GO lateral dimension analysis using longest traced dimension method (scale bar = 20 μm). The sheets show high degree of polydispersity.

4.1.2 Sample Preparation

For this study, the Laurel WS-650HZB spin coater was used to coat GO on freshly-cleaved, atomically smooth mica wafers for AFM, and glass slides for FQM. An additional layer of coating from a fluorescent solution was applied to the surface of the glass slides in the case of FQM. The coating was performed in using a purge of condensed dry air (CDA) to maintain a constant coating atmospheric environment.

4.1.2.1 Slide Preparation:

The standard glass microscopy slides were cleaned for two hours by bath sonication in a solution of ~ 30% H_2SO_4 after a standard cleaning in soapy water. This cleaning process makes the glass slides more hydrophilic; we presume this to be due to the attachment of hydroxyl groups to the surface of the glass slide by the treatment. Since GO particles are in an aqueous medium, the increase in hydrophilicity enhances wettability. Afterwards, the slides were rinsed with DI water and left to dry at 85° C. The mica wafers consist of an onion layer structure and can be pealed either using the scotch tape or blade technique. The scotch tape technique involves pressing a piece of scotch tape across the substrate and then peeling away to remove a layer of the onion structure, and it proved to be problematic. Only certain regions of the substrate were able to peel from the traction of

the tape, resulting in an uneven surface. Consequently, the blade technique was adopted and allowed for clean cleavage of slides. Using an X-ACTO knife made it effortless to cleave thin layers, while ensuring a uniform finish.

4.1.2.2 Coatings

There were two types of coatings used; one being a low concentration of typically 0.05-0.1 mg/ml GO suspension and the other being a dilute fluorescein solution. The dilute fluorescein solution consists of a 1% polyvinylpyrrolidone polymer (PVP, Aldrich, MW ~55,000) dissolved in ethanol (Aldrich, >99.8%) with 10 wt% sodium fluorescein salt (Aldrich, < 10% water) dissolved into solution. These types of solutions were used following the method of Huang et al. (2010). The dilute GO suspension was the primaray coating by drop casting the dispersion until ~75% of the glass slide or mica wafer area was completely covered. After the GO suspension coating has completed, the fluorescein solution was drop casted and followed the same spin coating procedure. All spin-coated samples followed a two-step procedure. Firstly, the substrates were revolved at 100 rpm for 10 s. Subsequently, they were spun at 1000 rpm for 30 s. Following the fluorescein coating, the glass microscope slides were ready for FQM imaging. For the mica slides, they were firstly dried in a vacuum oven at 40 ℃ for 6 h and then were ready for AFM imaging.

4.1.3 Fluorescent Quenching Microscopy (FQM)

The Tour method synthesizes relatively large GO sheets (~4 um) compared to the graphene oxide from Angstron (~500 nm). Since the FQM microscopy technique consists of an optical microscope with a mercury lamp (**Figure 4-2**), the technique is limited to the lens systems available to us. The 100x objective lens was the upper limit on magnification since that was the largest magnification of the lenses. The 100x lens, with a numerical aperture of 0.90, allowed for a resolution of 350 nm. As the 500 nm Angstron GO is close to this limit, the GO Angstron could not be accurately imaged with FQM (**Figure 4-3**).

Figure 4-2. Optical microscope with mercury lamp attachment (FQM). The mercury lamp add-on allows for accurate fluorescence-quenching imaging

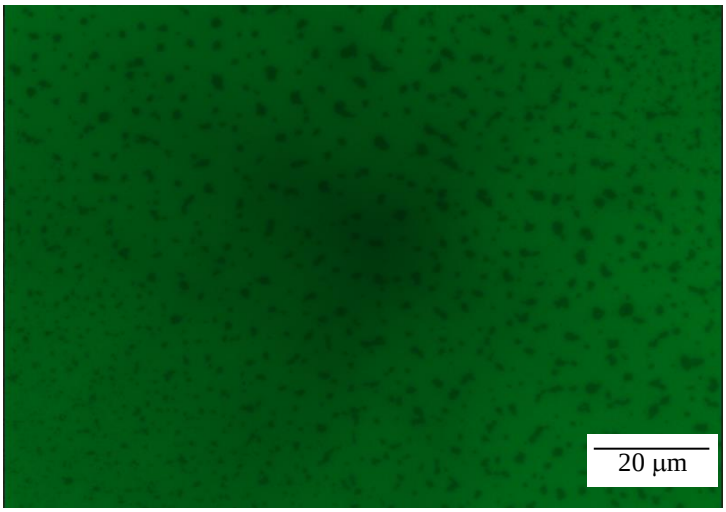

Figure 4-3. The maximum magnification on the fluorescence microscope is unable to clearly map out particles of the assumed 500 nm commercial Angstron GO batch.

On the other hand, Tour's GO sheets showed excellent particle dispersity and a size greater than our resolution capabilities creating clear and accurate FQM images (**Figure 4-4**). Moreover, the range of the measured particle size was between 0.8 and 26 μm, much higher than the resolution limit of 350 nm. However, since the range of the objective lens for the fluorescent microscope falls very near to the minimum measured particle size (0.8 μm), it is unknown if a tail of even smaller particles exist until an imaging tool of higher resolution is used, such as AFM. AFM is not only necessary to extend the polydispersity range but also to find the average thickness of GO particles.

Currently, we have used FQM imaging for lateral dimension size and AFM imaging to discern smaller particles and particle thickness but it must be stressed that for these nanoparticle systems the imaging techniques are limited by the optical wavelength of light employed. In the discussion section, we show an attempt at integrating FQM and AFM distribution data for the lab-synthesized Tour GO sample.

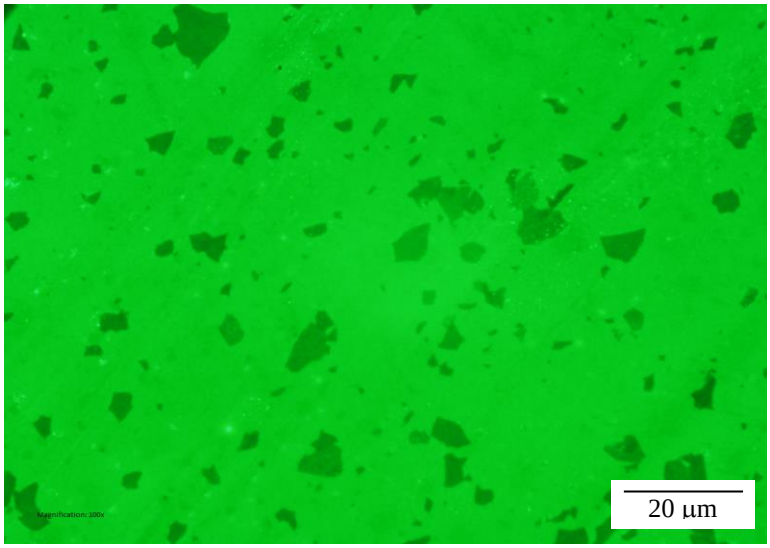

Figure 4-4. MTD-GO showing good dispersity (i.e.: each particle is observed distinctly from other particles). The GO particles are observed with an objective lens with magnification 100x.

4.1.4 Atomic Force Microscopy (AFM) and Thickness Determination

Mica-coated samples were analyzed using AFM for both the commercial and Tour lab-synthesized GO samples. AFM imaging provides not only visibly accurate GO dispersion images with good resolution at small sizes (**Figure 4-5**), but also confirmation if GO sheets are single-layered. Importantly, sheet thickness can reveal if the synthesis process has exfoliated the GO to the single-layer GO sheets. If not, then the synthesis process can be modified to increase exfoliation. All AFM images were analyzed using the software Gwyddion to measure particle thickness by tracing lines across imaged sheets.

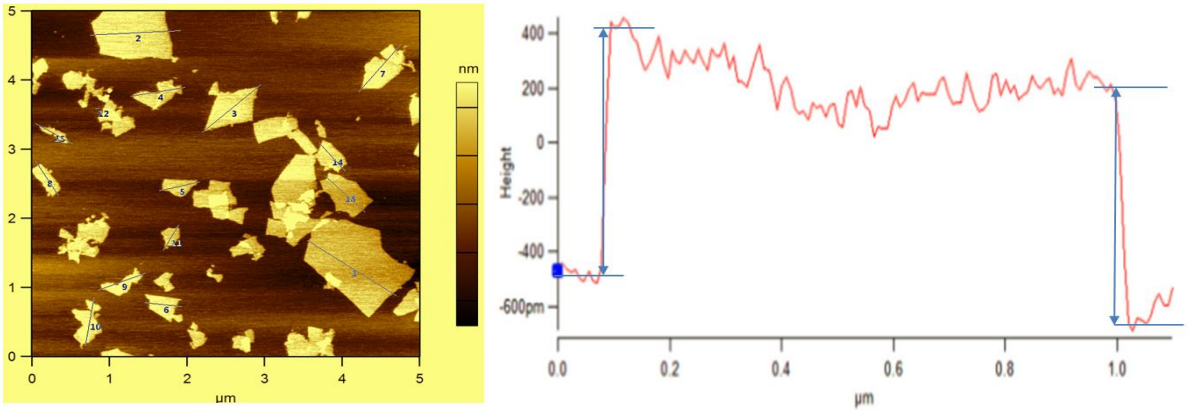

(a) (b)

Figure 4-5.(a) Non-contact mode AFM image of commercial GO. Sheet thickness is measured by taking line traces across the longest dimension of each sheet, measured by taking the difference between the sheet and background as shown in (b), which gives an estimate ~0.8 nm

GO sheet thickness was measured by taking line traces across non-contact mode AFM images. To obtain a calibration standard of sorts for z-measurements by AFM-cantilevers, freshly-cleaved mica was soaked in 40% HF acid for 5 hrs, as per the method of Nagahara et al. (1994); the HF etching a stair-like morphology with a layer spacing of ~1.0 nm (**Figure 4-6**) based on XRD measurements. Measuring the thickness of these stairs using AFM revealed an inherent uncertainty of at least ~0.2-0.3 nm in measurement, as observed from the unevenness of this morphology in **Figure 4-6**(b), where stair thickness was measured to be as high as ~1.5-2 nm/stair in places.

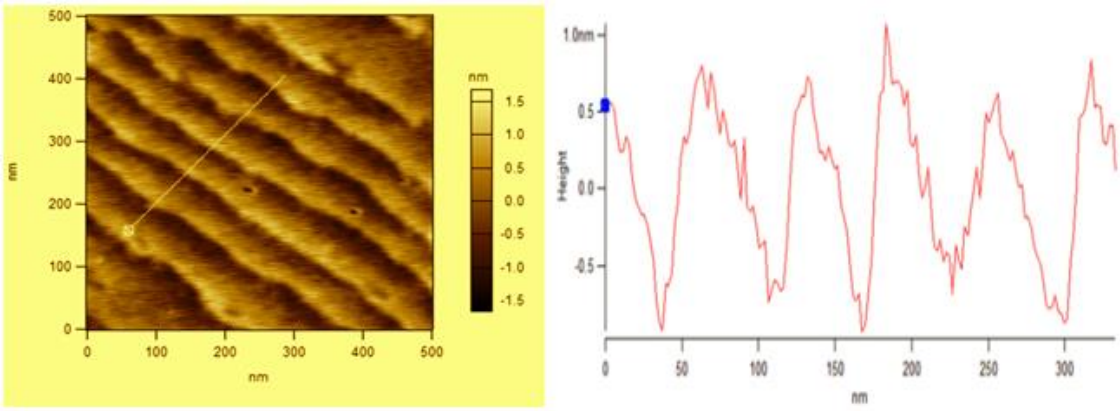

(b)

Figure 4-6.(a) AC-mode AFM of HF-treated mica showing characteristic stair pattern used to calibrate cantilevers before making any z-measurements on GO-coated mica, (b) line traces across each stair shows that the z-spacing is ~1.0-2.0 nm / stair.

4.1.5 Image Analysis

To begin with, we compare the analysis results from the imageJ and Matlab techniques for an AFM image of the commercial GO (**Figure 4-7**). Details of the code used to analyze the images are presented in Appendix A.

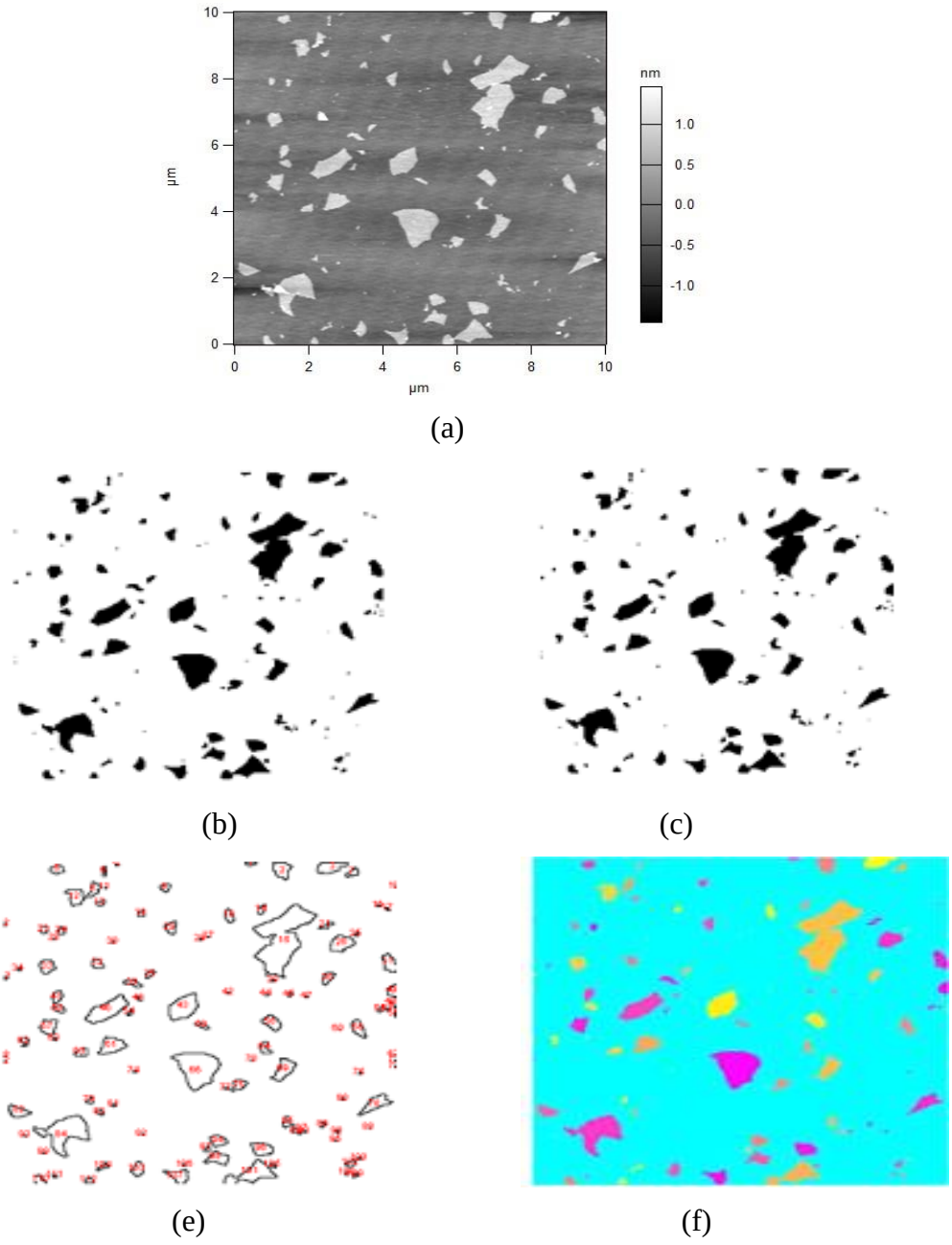

(a)

(b) (c)

(e) (f)

Figure 4-7.(a) original uniform-background AFM image of spin-coated commercial GO on freshly cleaved mica, (b) same image represented in binary form in matlab, and (c) in imageJ, (d) image analyzed in matlab, (e) analyzed image in imageJ

For these AFM images (**Figure 4-7**(a)), binary images obtained from both methods have no appreciable differences. Both of the converted images (**Figure 4-7**(b) and (c)) have likeness to each other. We also qualitatively observe that the shape and size of the detected particles are similar in analyzed images between the two algorithms employed for analyzing the particles (**Figure 4-7**(d) and (e)). The percent difference between results was calculated as follows:

$$\%\ \text{diff} = +\left(\frac{imageJ\ estimate - matlab\ estimate}{(imageJ\ estimate + matlab\ estimate)/2}\right) * 100\%$$

It was calculated that more than 50% of size estimate differences between results of matlab method and imageJ are lower than 5% for these even-background AFM images (statistics are presented in detail in Appendix A in the form of a particle-by-particle comparison table). The difference is in an acceptable range, which indicates that the improved Matlab method is valid. This is a comforting initial observation, because it indicates that our Matlab method is giving the same results that would be given for such images as imageJ. Taking ImageJ as a standard for particle image analysis against which to compare, the average difference between results of improved Matlab method and imageJ is 1% for area and 14% for perimeter.

For even background FQM images, there were no detection problems with either matlab or imageJ. One such matlab analysis result is shown in **Figure 4-8** (for the next FQM images, we will avoid showing the scale bar to help the reader follow the differences between the original and analyzed images). For this particular image, the difference between imageJ and matlab was calculated to be 8%, once again indicating consistency between the two methods, albeit lower than before, presumably because the background uniformity and background-particle contrast levels are not a sharp as in AFM images. This is still an acceptable margin of difference, however, and indicates that matlab can be used as effectively as imageJ to analyze particles from such even background FQM images.

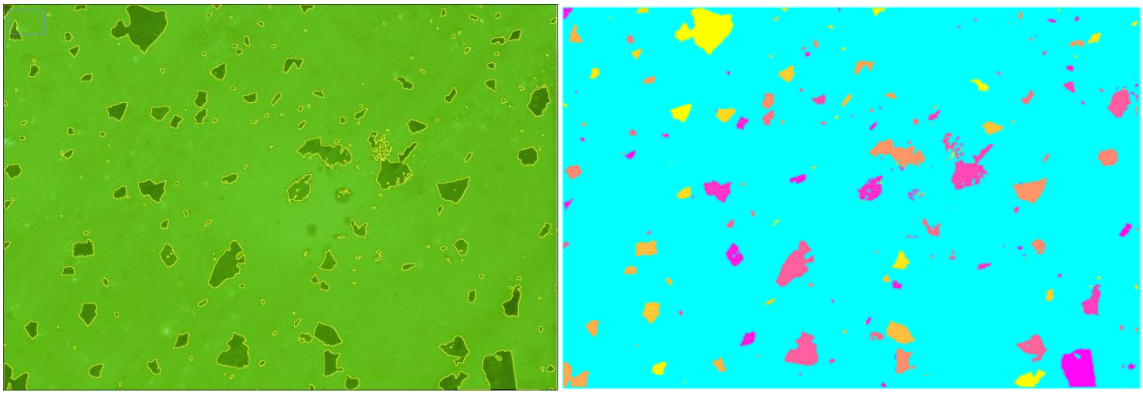

Figure 4-8. (a) FQM image of MTD GO, (b) image after Matlab processing.

The primary problem encountered in using imageJ was that of analyzing FQM images with uneven background which, due to shadowing effects and uneven contrast levels, makes it difficult to distinguish between background noises and nanoparticles for standard softwares like imageJ. The remainder of this methods section and Appendix A are thus dedicated to a discussion on the matlab routines used to deal with these issues typically encountered in the imageJ analysis of such uneven-background FQM images, using a few images to qualitatively highlight the problems and suggest solutions to them, followed by a discussion of image analysis results for MTD-GO as well as commercial GO when coated, imaged and analyzed following our proposed methods.

Figure 4-9 demonstrate the difference in particle shape and size in the analyzed image from the two methods for one such FQM image of MTD-GO. For the circled particle shown in **Figure 4-9**, the shape detected by the matlab analysis (**Figure 4-9**(d)) seems to map more closely to that of the particle observed in the original image (**Figure 4-9**(c)) than the imageJ-detected particle (**Figure 4-9**(e)). The lack of uniform contrast between the particle edge and its surrounding background leads imageJ to construct "ghost edges" in several locations which do not necessarily follow from the original image, as observed in **Figure 4-9**(e), which can lead to inaccuracies in estimating values like the particle area and especially, particle perimeter. For this reason, and considering the difference observed between imageJ in estimating particle perimeter (even in even background, high

resolution AFM images as discussed above), we choose never to rely on the particle perimeter to infer size information about the analyzed particles.

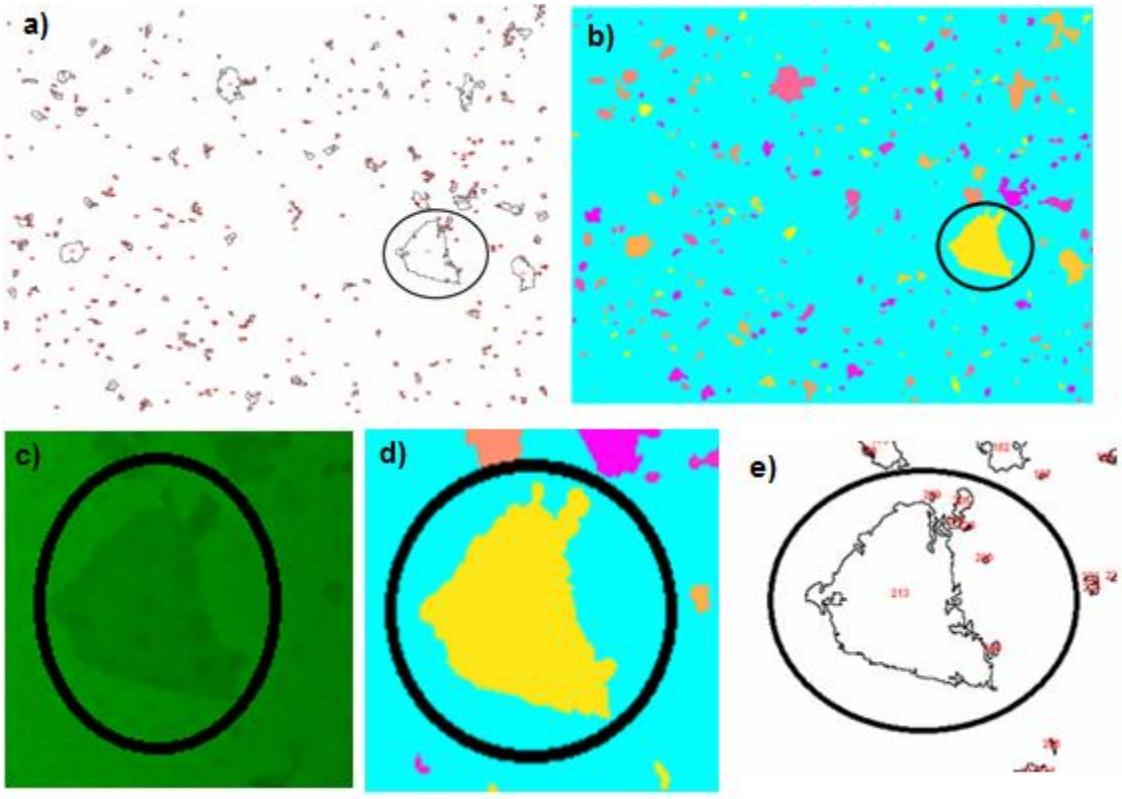

Figure 4-9. (a) FQM image of MTD GO detected in imageJ, (b) Same image after matlab post-processing, (c) circled particle from the original FQM image, (d) particle after Matlab's post-processing, and (e) imageJ particle.

Moreover, imageJ sometimes detects a lot of background noise in these FQM images (**Figure 4-10(b))** and merges noise and particles into combined objects, which can lead to inaccuracy in estimating edges, and thus perimeters and particle areas (**Figure 4-10**(c)). In matlab, by comparison, the ’Edge’ function (discussed in further detail in Appendix A) enabled us to neglect most of the background noise (**Figure 4-10**(d)) and still detect the particles closely in shape (**Figure 4-10**(e)) compared to the original image (**Figure 4-10**(a)). A difference of 33% on average (and reaching as high as 60%) was estimated in the comparison between the imageJ and matlab in analyzing this uneven-background image. This difference will not be interpreted as an error in either approach for the purpose of maintaining a fair comparison, but we instead refer the reader to **Figure 4-10**(a), (c) and (e)

to examine the closeness of the particle shapes in the analyzed images by matlab and imageJ to the original image.

ImageJ uses the Sobel method when finding edges. It returns edges at those points where the contrast gradient is maximum. Matlab uses the “Canny” method to find edges. Canny uses two thresholds to detect strong and weak edges; only when weak edges are connected to strong edges are they shown in the output. We think this latter approach is less likely to be fooled by noise and more likely to detect true edges, especially since it is our experience in image analysis that a natural particle edge often is blurred by a few pixels around a true edge, so a maximum gradient might not be the best metric to characterize the position of such an edge, as opposed to the Canny approach.

To conclude, it would appear that imageJ lacks the subroutines for filtering the images that matlab has. The matlab code capabilities come from the vast amount of open source routines that users make available in academia. ImageJ also lacks the capability to repair artificial defects in the particles it detects. For these reasons, we recommend the use of matlab for interpreting FQM images of GO of uneven background for characterization purposes similar to ours. ImageJ, on the other hand, can be used with no problems to detect particles in uniform contrast, even background images such as those obtained from AFM, and yields results that are similar to those obtained via matlab. Perimeters in particular seem to be estimated differently across techniques – due to differences in edge detection - and so might not be highly reliable in inferring particle size distributions compared to particle areas.

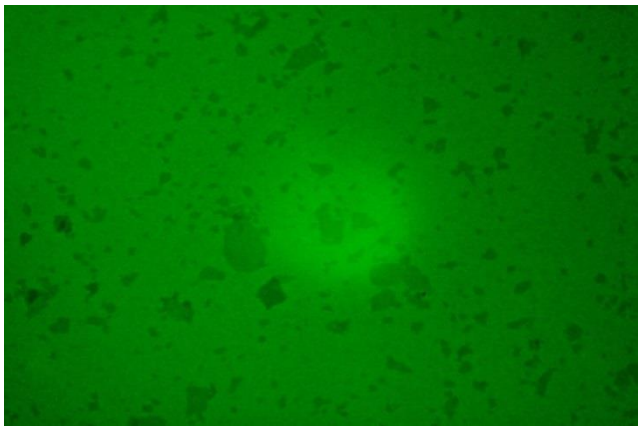

(a)

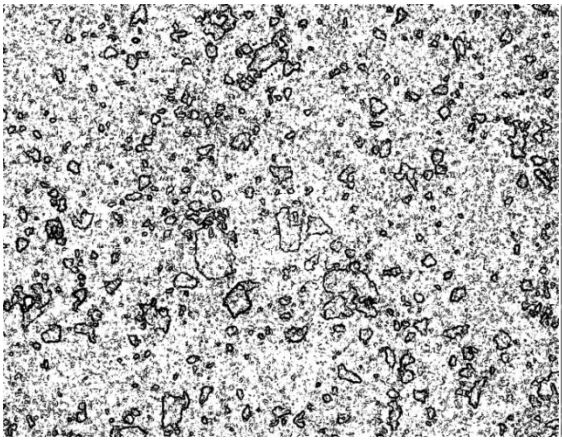

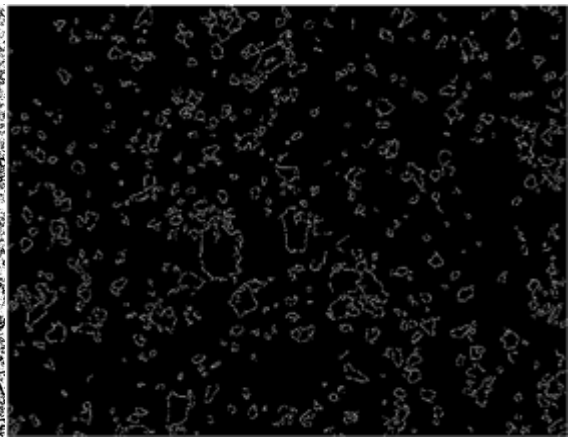

(b) (c)

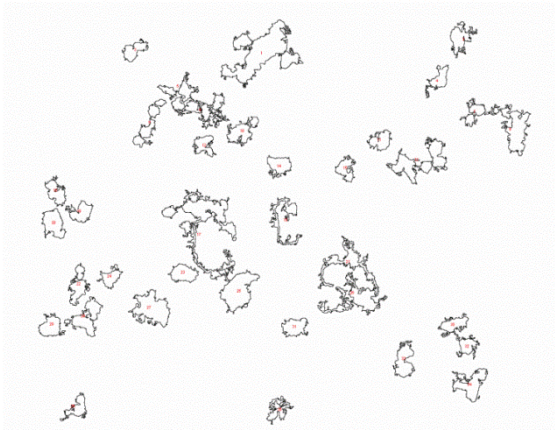

(d) (e)

Figure 4-10. (a) FQM image of MTD GO and (b) imageJ-processed image, with black spots on the background representing noise, (c) matlab-detected image, showing much lower degree of background noise a result of using the "Edge" function, (d) particles >1000 pixels are singled out in the imageJ-processed image to show that the detected particles look different from those in the original image due to background noise issues, (e) the corresponding image processed in matlab shows particles that generally shape-mimic those in the original image better than imageJ .

4.2 Results and Discussion

4.2.1 Sonicated vs Unsonicated commercial GO size distributions

To verify that our imaging and image analysis methods work, we compared the distribution statistics for a sample of commercial GO from Angstron Materials before and after sonication, as obtained using AFM images (**Figure 4-11**).

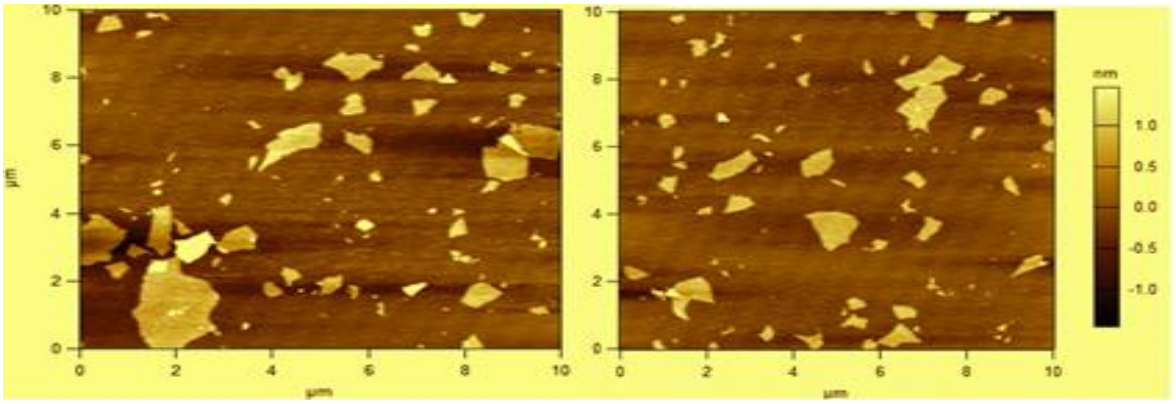

(a)

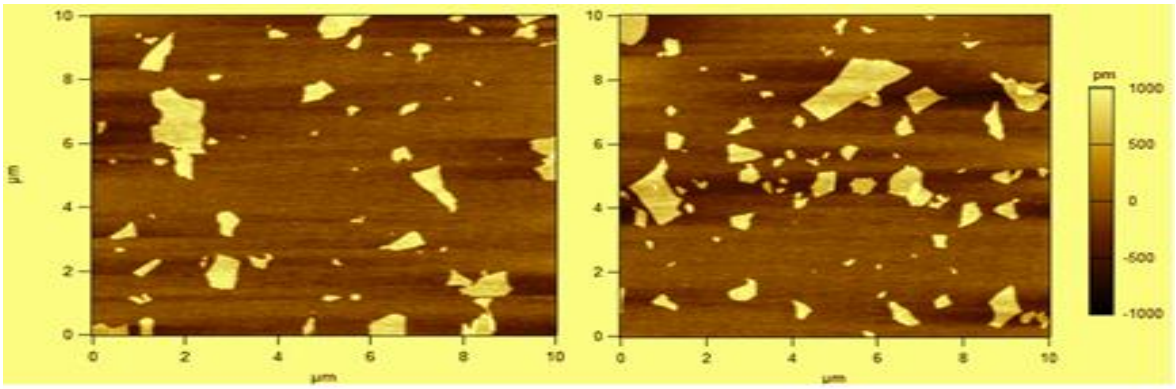

(b)

Figure 4-11. Commercial GO imaged using non-contact mode AFM on freshly-cleaved mica (a) before and (b) after 6 min of sonication

The AFM images (**Figure 4-11**) do not show a marked qualitative difference before and after sonication. However, a quantitative analysis of about 100 imaged particles per sample using ImageJ (**Figure 4-12**) indicates that the GO size distribution was changed by sonication, as expected from this energy-intensive process which can result in the breakage of some of the bigger particles and a shift in the entire distribution towards smaller sizes. This is a good indicator that our coating, imaging and image analysis

protocol is sensitive to changes in the population that are introduced by size-changing processes such as sonication, filtration or centrifugation. These imaging results will be re-examined in further detail later when we compare the results of this technique with those obtained from dispersion rheology in Chapter 6.

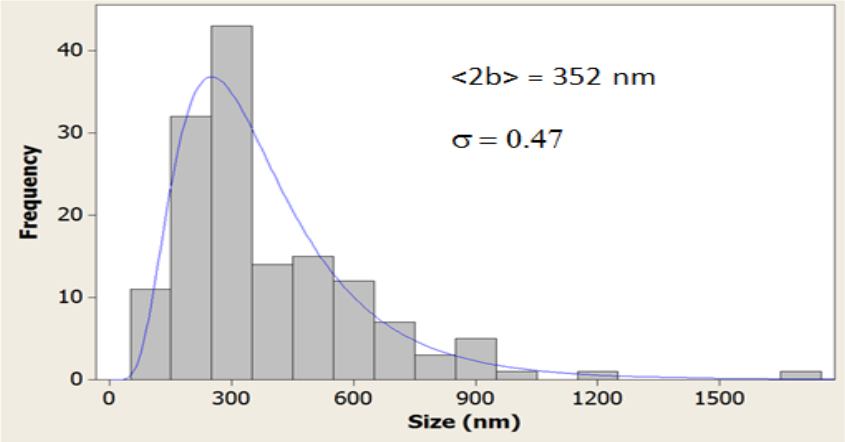

(a)

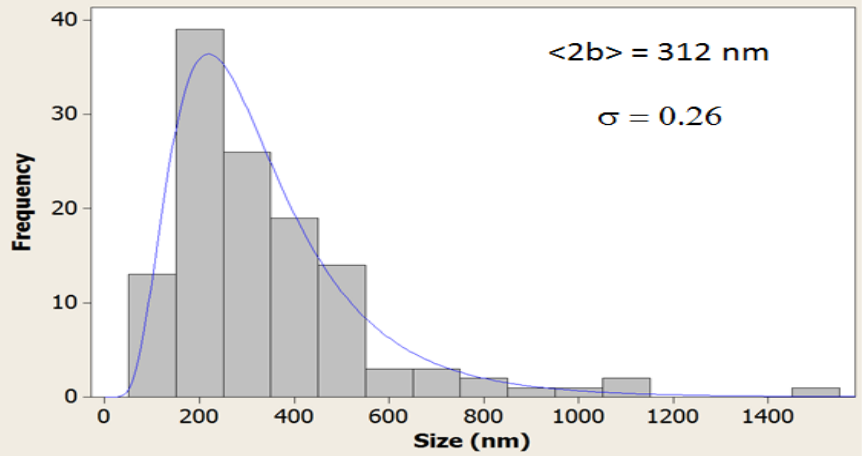

(b)

Figure 4-12. Distribution of commercial GO particles fit to a lognormal distribution as imaged by non-contact AFM (a) before and (b) after 6 min sonication

Furthermore, the histograms were fit well by a lognormal distribution, indicating that such a distribution is successful in describing such GO systems.

$$\Omega(D) = \frac{1}{D\sigma\sqrt{2\pi}} \exp\left(-\frac{(\ln D - \mu)^2}{2\sigma^2}\right) \quad (4\text{-}1)$$

Where, $\Omega(D)$ is the probability distribution function of particle diameter D, while μ and σ^2 are the mean and variance of ln(D) respectively, not to be confused with the true mean <D> and standard deviation s for a given distribution (the latter two can be obtained from the former two via a simple interconversion).

This lognormality is also observed for MTD GO in section 4.2.4 below and is expected, given that one tail of the GO population might be removed by a size-selective mechanism, which can be a separation process (e.g.: centrifugation, filtration or sonication any or all of which might have been used to purify the GO) or it might be dictated during the synthesis by the starting graphite flake/crystallite size, which then gets broken down via a top-down oxidative route. An additional reason that motivated us to suggest the lognormal distribution is that it is simply a variation of the normal distribution, meaning it is relatively easy to describe, and using fewer parameters, than other commonly-used distributions. Hence, it represents one of the simplest possible ways of realistically representing the size distribution data while minimizing the number of parametric descriptors.

Additional work to verify the lognormality of size distribution data was conducted via the Anderson-Darling normality test, described by Stephens (1974), whereby size distribution data of the commercial GO (**Figure 4-12(a))** was plotted in the statistics software package Minitab and fit using the test (**Figure 4-13**) to confirm whether or not the particle size followed a lognormal distribution. The test calculates a parameteric quantity called the p-value based on goodness of fit. This value is then compared to a value called the level of significance (or α), usually chosen to be a value of 0.05 or 0.10; for $p < \alpha$ it is concluded that the data does not follow the proposed distribution. Conversely for $p > \alpha$, it is concluded that the data can be fit by the model under scrutiny. In **Figure 4-13**, the calculated p-value of 0.909 indicates that the data can indeed be considered to follow a lognormal distribution.

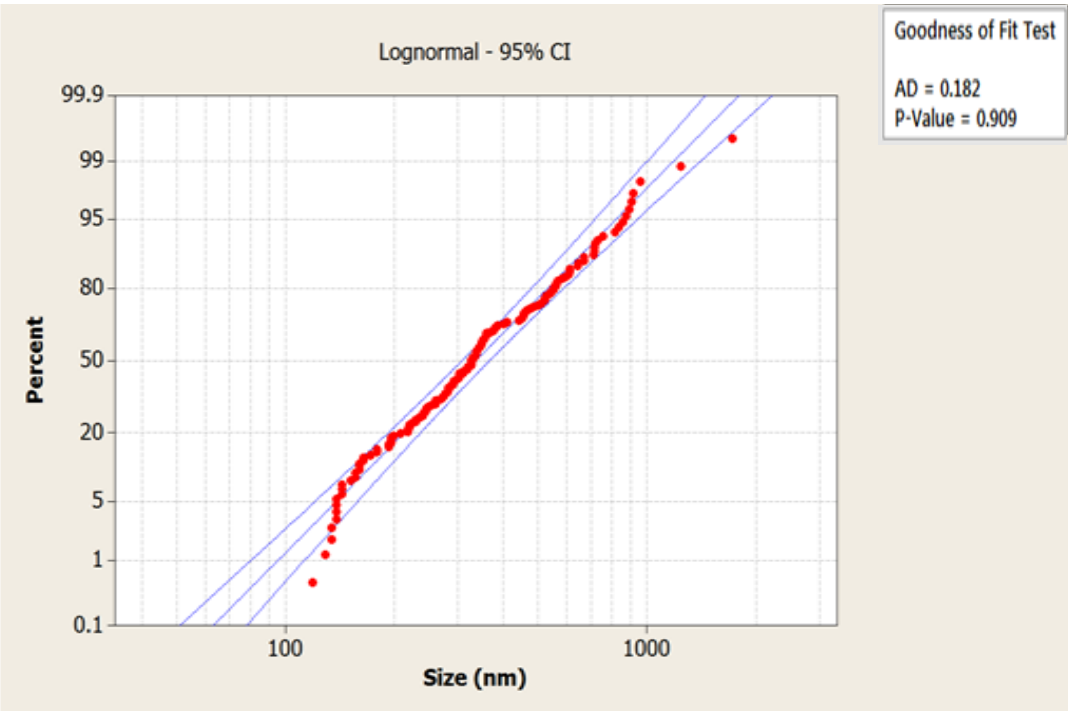

Figure 4-13. Anderson-Darling normality test to determine whether commercial GO size-distribution data obtained via AFM follows a lognormal distribution. Calculated p-value = 0.909 > 0.05, which indicates that the data passes the test for lognormality.

To demonstrate that a lognormal distribution is a better model for the data than the simpler normal distribution, we conducted the A-D test on all of our GO samples, testing both for normality and lognormality. In all such comparisons, it was found that the normal distribution does not fit the data well, while the lognormal distribution succeeds at doing so, thus justifying our use of it as a sample-representative simple size distribution model. One such comparison is shown in **Figure 4-14** for the 6-min probe-sonicated commercial GO. Several interesting observations can be made:

1)- the calculated AD metric is lower for the lognormality test than that calculated for the normality test, indicating that lognormal is a better fit for the data than normal.

2)- the p-value estimated for the normality test is small (~0.05) indicating that the normal distribution fails the hypothesis test for representing the data (i.e.: it is statistically highly unlikely to be the corrrect descriptive model), while the corresponding value is high at 0.697, indicating the lognormal distribution to pass the hypothesis test.

3)- It is noteworthy that the calculated test parameters (A-D metric and p-value) for the lognormal distribution are similar after and before sonication, indicating that our sonication process acted rather uniformly over the different sheet size bins within the commercial GO sample. This is useful to note because it provides supporting evidence of lognormality, and seems to indicate that the sample is made of sheets that are relatively homogeneous in terms of chemical nature, surface defects and overall morphology, which would explain why the characteristic form and descriptive parameters of the lognormal distribution are largely retained after the sonication.

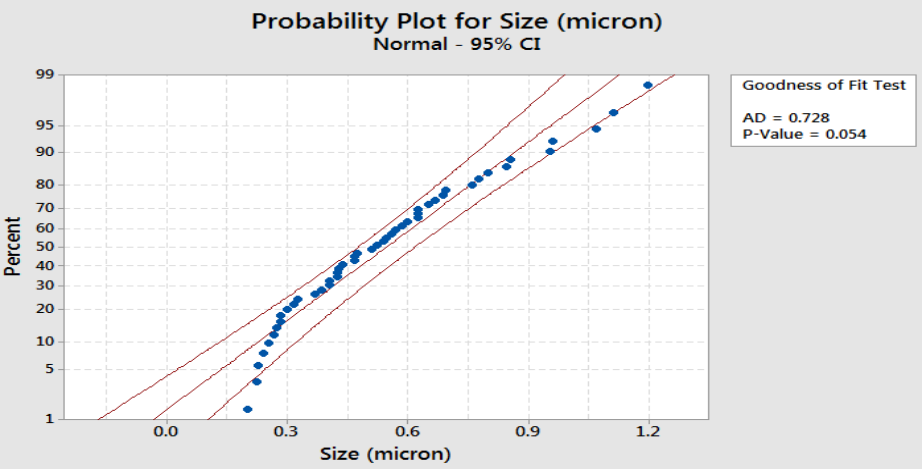

(a)

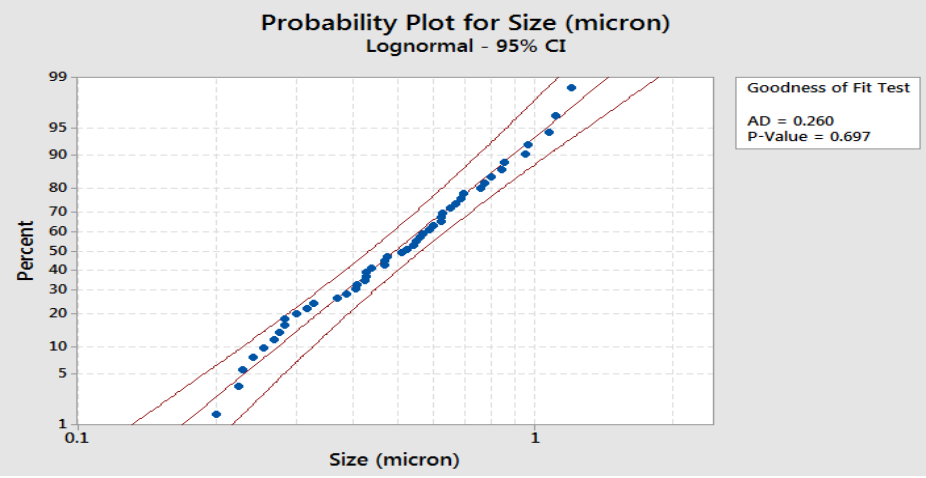

(b)

Figure 4-14. A-D normality test to determine whether 6-min probe sonicated commercial GO size-distribution data obtained via AFM to (a) normal and (b) lognormal distribution. The data passes the test for lognormality but fails that for normality.

4.2.2 Thickness Distribution

We once again attempted to test the ability of the normal and lognormal models at representing the thickness data (**Figure 4-13**). These two distributions were chosen to model thickness for two reasons:

1) - their relative parametric simplicity in describing the data compared to other distribution functions, and

2) - GO thickness is physically limited at the low end of the distribution by the thickness of a carbon monolayer (0.335 nm), while at the high end, most of the thick sheets we typically run into in a well-exfoliated sample are ~2.0 nm (which might be taken to indicate a bilayer); monolayers can vary in the degree of surface oxygenation, thickness of the surrounding hydration shell (if present), and a given distribution can contain monolayers and bilayers of varying thickness. Considering that the mean of such a sample is typically ~0.6-1.2 nm (which is usually taken to indicate a monolayer, as shown by Stankovich et al. (2007)), this is indicative of a symmetric (possibly slightly asymmetric) distribution.

In the case of thickness, the data was found to be fit well by the normal distribution and poorly by the lognormal distribution, as shown by the p-values and AD metric estimates in **Figure 4-15**, which indicate the viability of the former model to describe GO thickness if and when required. The histograms of thickness with the corresponding lognormal fits are presented for MTD-GO and commercial GO in **Figure 4-16** and **Figure 4-18**. Particularly noteworthy is the apparent drop in sheet thickness of commercial GO post-sonication. Considering that sonication is capable of raising local temperature in the vicinity of GO sheets to ~5000 K, this observed decrease in sheet thickness could be because probe-sonication supplies the sheets with sufficient energy to cause some of the physisorbed (and possibly even the chemisorbed) OH and epoxy groups to detach, leading to an overall reduction in thickness. A decrease in surface concentration of oxygen-containing groups could potentially also lead to a weaker and thinner hydration layer surrounding the GO sheets as a result of decrease in hydrophilicity, which would

further explain the observed thickness dropped. Finally, and perhaps most plausibly, this observed drop could be the simple result of sonication-induced sheet exfoliation.

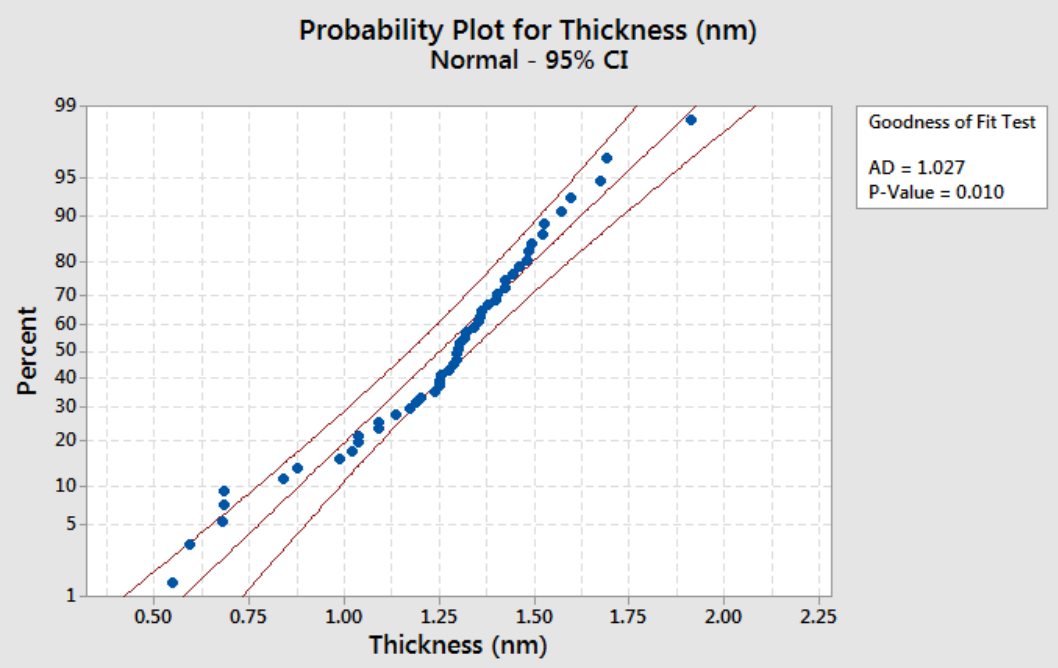

(a)

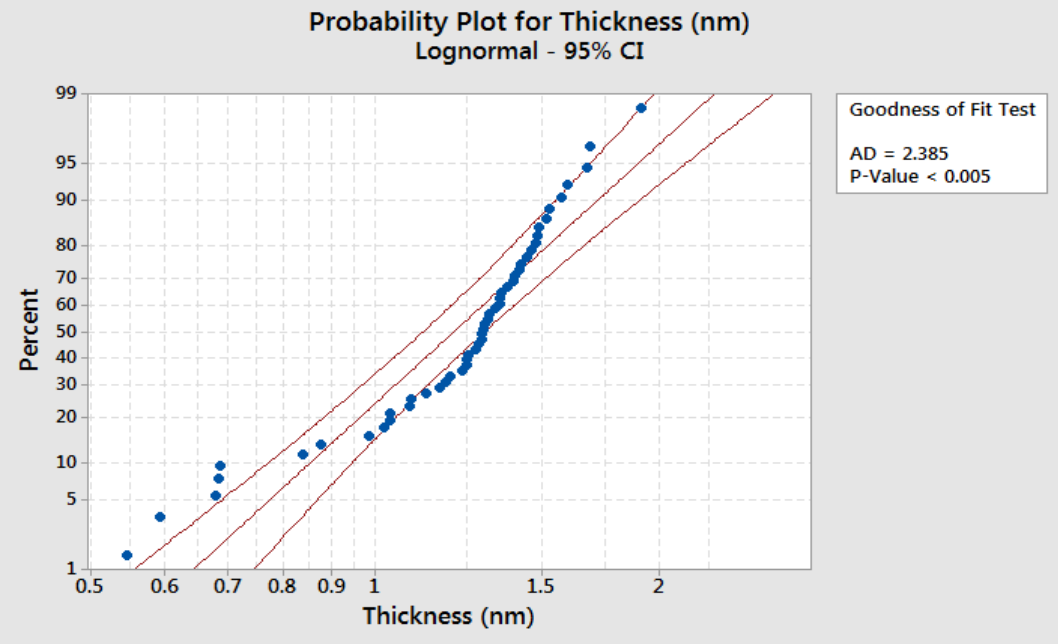

(b)

Figure 4-15. A-D normality test to determine whether commercial GO thickness-distribution data obtained via AFM belongs to (a) normal, or (b) lognormal distribution. The data passes the test for normality but fails that for lognormality.

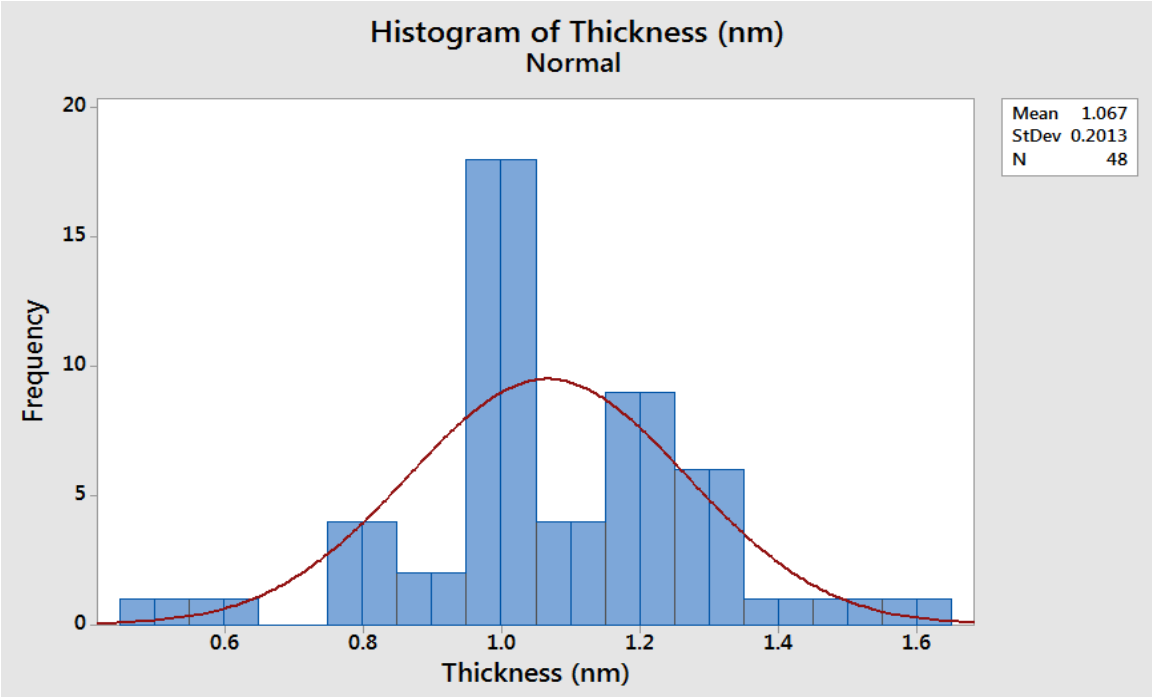

(a)

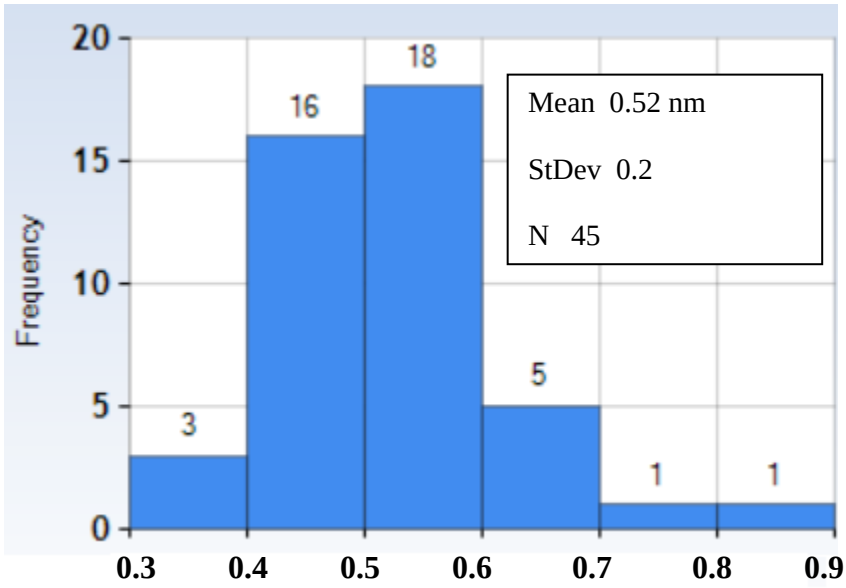

Thickness (nm)

(b)

Figure 4-16. Lognormal distribution fits to sheet thickness data for commercial GO (a) before and (b) after sonication.

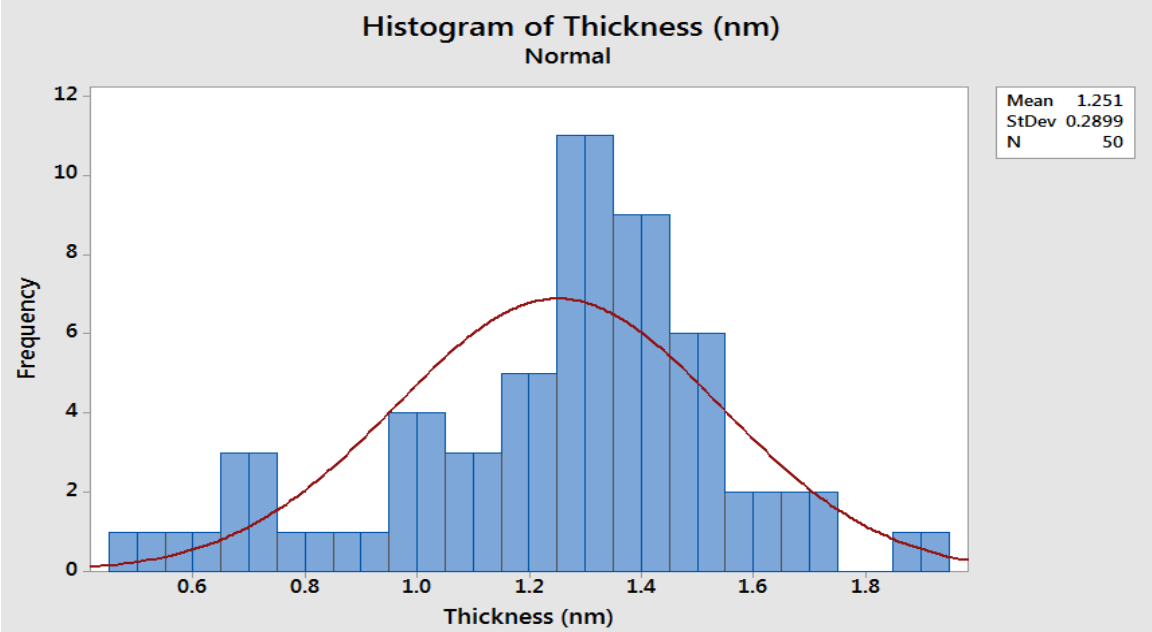

Figure 4-17. Lognormal distribution fits to sheet thickness data for MTD GO.

It must be pointed out that in all these studied cases, the distribution of thickness is narrow (σ_t = 0.29 for MTD-GO, only slightly higher than that for commercial GO, σ_t = 0.20). This indicates that it might not be as important to model the thickness polydispersity of these sheets compared to their size polydispersity, since most of them appear to be monolayers or bilayers. In terms of lateral size, by contrast, the MTD GO and commercial GO have polydispersities σ of 0.92 and 0.47 respectively, significantly higher than for thickness.

4.2.3 Lateral Size and Thickness Correlation

A question to address regarding any population of aspherical particles is that of whether a correlation exists between major and minor dimensions. A Spearman's product-moment correlation, described by Lehman (2005), was run to assess this potential relationship in 50 GO particles for the MTD GO sample for which lateral size and thickness was simultaneously measured using matlab and gwyddion respectively (**Figure 4-18)**. The Spearman correlation is used to assess the strength and direction of association between

two continuous variables that are monotonically related, as shown in the same Figure. Its coefficient, r, indicates the strength and direction of this relationship and can range in value from -1 to +1; the sign of the coefficient is an indicator of direction, i.e.: if both variables tend to increase/decrease together, the coefficient is positive, and the line that represents the correlation slopes upward. The larger the absolute value of r, the stronger is the relationship.

$$\rho = \frac{\sum_{i=1}^{n}(x_i - \bar{x})(y_i - \bar{y})}{(n-1)\ s_x s_y}$$

Notation:

Term	Description
$\bar{x}$	sample mean for the first variable
s_x	standard deviation for the first variable
$\bar{y}$	sample mean for the second variable
s_y	standard deviation for the second variable
N	column length

According to Cohen (1998):

Coefficient Value	**Strength of Association**
$0.1 < \| r \| < 0.3$	Weak correlation
$0.5 < \| r \| < 0.7$	Moderate correlation
$\| r \| > 0.7$	Strong correlation

p-values, as discussed before, are often used in hypothesis tests to determine whether the null hypothesis can be rejected or not. The p-value represents the probability of making a type I error, which is rejecting the null hypothesis when it is true. The smaller the p-value, the smaller is the probability (P) of making a mistake by rejecting the null hypothesis. The p-value for Spearman's correlation coefficient uses the t-distribution, given by:

$$t = \frac{r\sqrt{n-2}}{\sqrt{1-r^2}}$$

where, r is the correlation coefficient, and n the number of observations. The p-value is thus $2 \times P(T > t)$ where variable T follows a t-distribution with $n - 2$ degrees of freedom. In correlation analysis, the null hypothesis is that there is no correlation between the variables, while the alternate hypothesis is there is correlation between the variables. While performing correlation analysis, in order to determine whether the correlation between variables is significant, p-value is compared to the significance level. Usually, a significance level (denoted as α) of 0.05 is assigned, which indicates that the risk of concluding that a correlation exists when no correlation actually exists (type 1 error) is, say, 5%. Thus, $p \leq \alpha$ is taken to indicate that the correlation is statistically significant, while $p > \alpha$ is taken to mean that the correlation is not statistically significant.

Upon generating the t-D scatter plot for the Pearson correlation test in **Figure 4-18**, it is once again observed in that the majority of particles thicknesses lie between 0.8 and 1.8 nm, indicating that the GO for the most part consists of monolayers and bilayers, and showing little spread in the GO thickness to begin with.

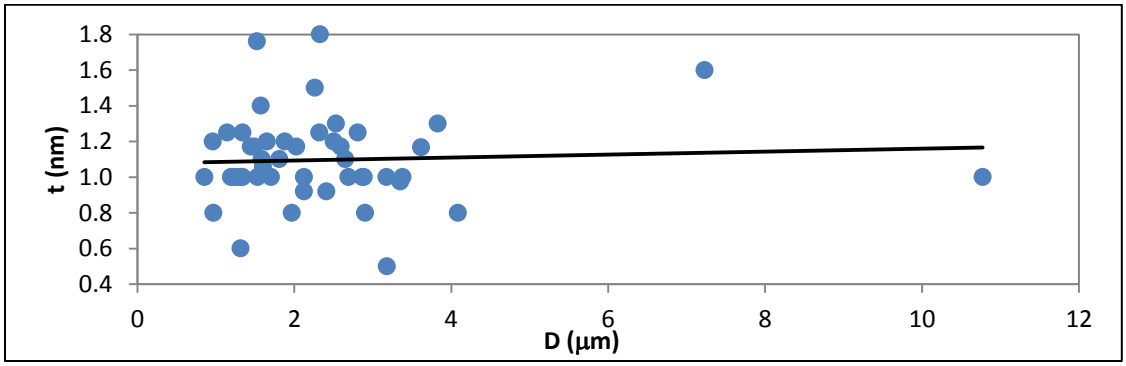

Figure 4-18. Scatter plot of 100 randomly-chosen MTD GO particles for which lateral size and thickness were measured via AFM.

The Spearman correlation between thickness and lateral size is 0.06 based on **Figure 4-18**, which indicates that there is an extremely weak positive correlation between the two variables under study. The relationship between these variables is positive, which indicates that, as lateral size increases, thickness might tends to increase slightly. This is intuitively sensible; it is expected that smaller graphite oxide particle might be easier to exfoliate than bigger particles, albeit slightly so. It must also be noted that the p-value for this case study is 0.42, which is greater than a significance level of 0.05. This indicates

that there is no evidence against the null hypothesis, and it can thus be said with reasonable confidence than no significant correlation exists. The same result of no correlation was observed for all the other analyzed GO samples.

4.2.4 Splicing

The problem with using imaging to describe the statistics of a highly polydisperse system of particles is potential bias due to the resolution limits of the technique(s) used to image the system of interest. We can use AFM without problem to image particles on the scale of 30 μm x 30 μm, but beyond that limit, we start to face problems with the quality of obtained images, and some particles are simply too big to be captured completely by AFM, as in the case of MTD GO (see **Figure 3-7**(c), (d) and **Figure 4-1**). FQM on the other hand, has a lower resolution limit of 350 nm, so small particles cannot be effectively captured by this technique for e.g.: commercial GO as shown via FQM and AFM in **Figure 4-3** and **Figure 4-5** respectively. In the FQM images of this GO (**Figure 4-3**), the sheets are visible, but their morphology is not well-discernible and we cannot see particles <500 nm clearly, so these images are not ideally suited for particle size image analysis by imageJ or MATLAB.

A simple solution to this problem is to use AFM to image GO batches for which a certain percentage of the particle population (say, 90%) is smaller than an arbitrary cut-off size based on the AFM resolution limits (say, 5 μm), while FQM can be used to image GO batches for which the majority of the population is above the lower resolution limit for the technique (say, 350 nm or 1 μm). However, while this approach succeeds for generally small-sized GO samples using AFM (**Figure 4-11**), the potential problem is when the distribution contains a statistically significant number of particles both below the minimum resolution limit of FQM and above the resolution limit for AFM. We use the lab-synthesized MTD GO as a case study. Based on FQM and AFM images, the size distributions obtained on this GO are shown in **Figure 4-19** and **Figure 4-20** respectively.

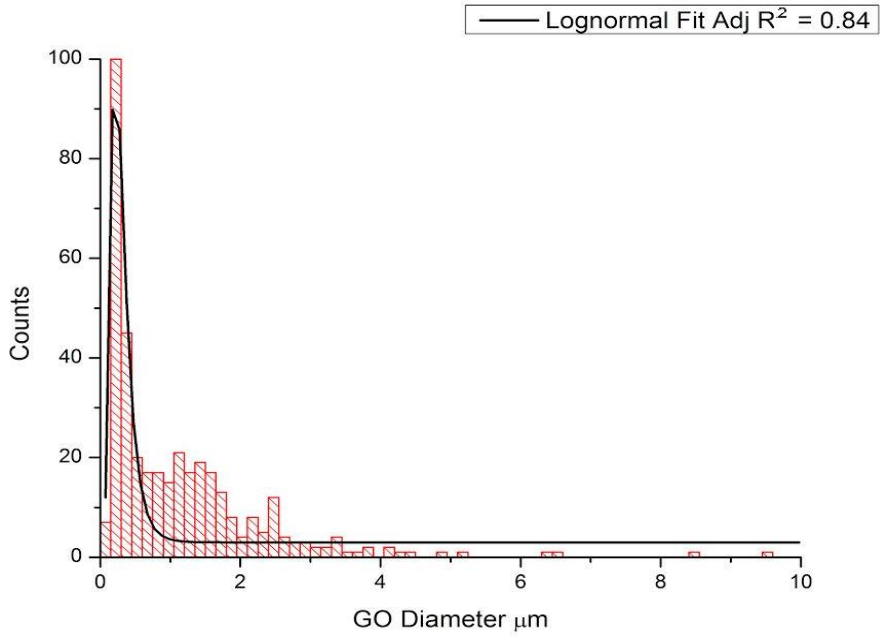

Figure 4-19. Size distribution obtained on MTD GO from AFM images. The histogram poorly fits a lognormal distribution because the bigger particles are harder to discern in AFM images.

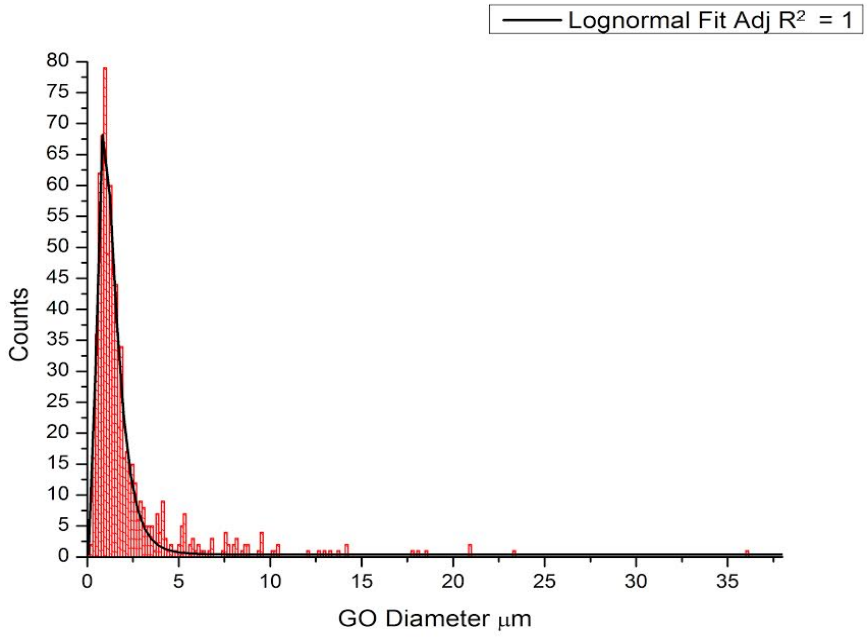

Figure 4-20. Size distribution obtained on MTD GO from FQM images. The histogram is well-fit by a lognormal distribution because bigger particles are easy to discern in FQM (lower resolution limit = 350 nm) and most observed particles are bigger than the resolution limit for FQM.

It can be observed that the AFM histogram from poorly fits a lognormal distribution **(Figure 4-19)**, possibly because the bigger particles are harder to complete image in AFM

images while the FQM histogram from **Figure 4-20** is well-fit by a lognormal distribution because the bigger particles are easy to discern in FQM (lower res limit = 350 nm) and because most particle observed are bigger than the resolution limit for FQM. This indicates that FQM is preferable to AFM in getting size distribution from the larger-than-average Tour GO, just as AFM is better-suited to particle size estimation for the smaller commercial GO.

With that being said, we do not wish to lose the high resolution offered at small sizes by AFM over FQM for the Tour GO. Hence, it is desirable to combine the results from both techniques for such a system to form a distribution that best represents the full range of particle sizes generated by the Tour synthesis. Our suggestion was thus to simply nominate a certain size bin (say 1-2 μm) which is commonly well-detected by both FQM and AFM and to use it as a "normalization bin" between the two distributions. In other words, the data from all size bins smaller than or equal to this selected bin was ignored for the FQM distribution (**Figure 4-20**), while the data from all bins less than or equal to this selected bin was ignored from AFM distribution (**Figure 4-19**). Then, by ratios, and using the selected bin as a common factor, the two parts of the distribution were linked at the size bin of selected (1-2 micron) using data from both the FQM and AFM distributions respectively. In order to get the best possible results from this splicing technique, AFM and FQM images were obtained from the same mica-coated wafer; AFM measurements were obtained first, followed by application of the fluorescent coating and a round of FQM imaging.

While the fit in **Figure 4-21** is not as good as it is for **Figure 4-20**, it is better than that obtained in **Figure 4-19** as a result of using both of the latter Figures to yield the distribution in the former Figure. An R^2 value of 0.88 is also acceptable for experimental purposes and indicates that the data is still reasonably fit by a lognormal distribution. Most importantly, **Figure 4-21** is thought to be a better representation of the Tour GO population than either of **Figure 4-19** or **Figure 4-20**, since the data resolution in **Figure 4-21** is consistently good across size bins; with the smaller particles well-captured by AFM and the big particle by FQM. As before, the lognormality of the spliced data was tested and verified using the A-D normality test, as shown in **Figure 4-22**.

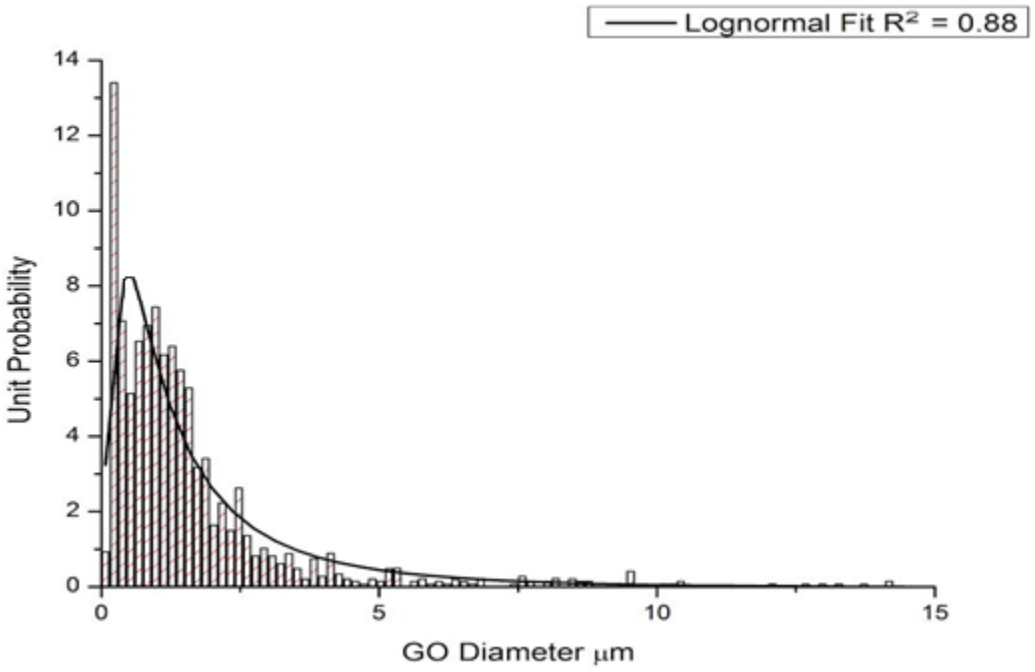

Figure 4-21. Distribution data from FQM and AFM for Tour GO using the splicing approach**.**

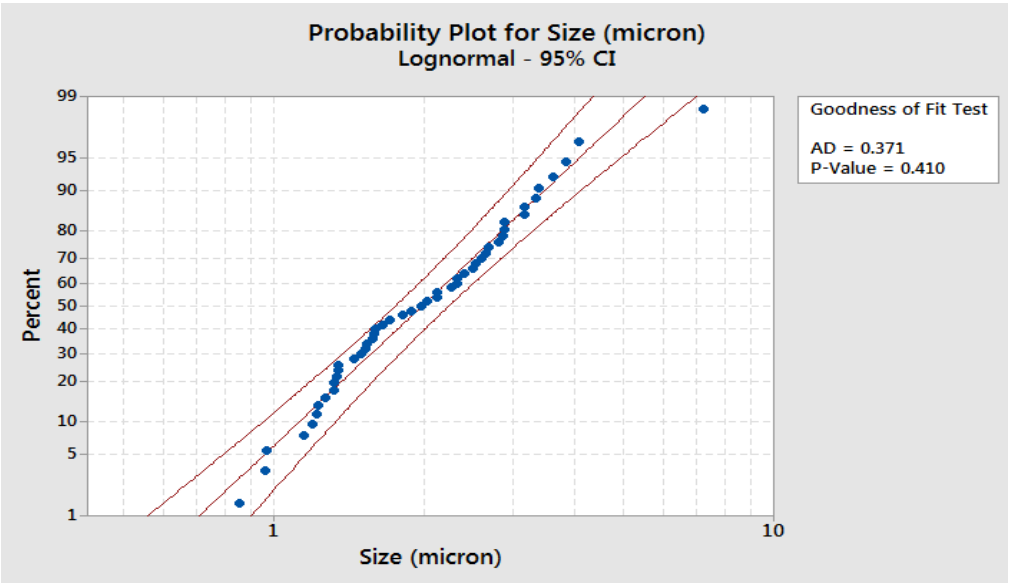

Figure 4-22. A-D normality test to determine if MTD-GO size follows a lognormal distribution. The data passes the test.

4.3 Conclusion

In this chapter, we reviewed the major issues encountered with FQM and AFM imaging of the highly polydisperse polygonal GO sheets. Most of the problems were encountered with FQM imaging, and were attributed to lack of resolution for size-scales < 350 nm, staining problems with the fluorescent-coating quality and issues with uniformity of brightness and edge detection on some of the particles. These problems have been addressed by relying on the combination of FQM and AFM images in our analysis, and by comparing the standard image analysis software ImageJ with MATLAB in terms of the analytical capability for our particle systems, while introducing a number of subroutines that we used in MATLAB to mitigate the issues previously experienced during image analysis.

Based on our analysis we find that Matlab is much more flexible than imageJ for our purposes in analyzing GO particle size distributions MATLAB contains convenient subroutines that can be employed for filtering the images, and ignoring the brightness and staining features of the images. For these two reasons, we recommend the use of Matlab for interpreting FQM images of GO for characterization and we introduce the subroutines used both in the body of the chapter and in the Appendix, where we provide the coding used for image analysis and improvements introduced.

We also use the methods of this chapter to image commercial and lab-synthesized Tour GO. We use our results to conclude that lateral assize and thickness for the GO are weakly correlated and that such a correlation, if it existed, can be safely ignored from a statistical standpoint. We also conclude that GO lateral size follows a lognormal distribution, while thickness follows a narrow normal distribution. We also use our methods to discern changes in the population of the GO before and after sonication, specifically, that sonication leads to a shift in the particle distribution to smaller sizers as expected. Furthermore, we demonstrate that AFM is ideally suited to image GO where the majority of particle are below 5 μm in size, while we find FQM to be better-suited for imaging Tour GO. Finally, we propose a splicing technique to combine the high resolution of AFM at smaller particle sizes (< 1 μm) with that of FQM at large particle

sizes (> 5 μm) to obtain a complete picture of the size distribution of the highly polydisperse Tour GO. The results of this chapter will be drawn upon in Chapter 6, where comparison will be conducted with results from rheology.

Chapter 5: Theory of Dilute Dispersion Rheology of Discs

Colloidal and nanoparticles such as graphene oxide (GO) are not novel substances; however, in recent years, we have developed the necessary tools to not only produce such new materials but also characterize their physico-chemical properties. Morphology and size characteristics of these particles constitute one such set of physical properties which is as important as their respective chemical properties in determining the behavior and practical usage of these materials. Taking GO as an example, it has already been elucidated in previous chapters that nanoparticle size is directly linked to performance in polymer nanocomposites, optoelectronic and barrier films, and we thus need quick and efficient ways of capturing size characteristics for colloidal and nanoparticle systems like GO. Conventional techniques used to characterize the size of disc-shaped nanoparticles, while immensely useful in the direct characterization of particle distributions, suffer a few drawbacks: 1)- microscopy-based techniques such as fluorescence-quenching microscopy (FQM) and atomic force microscopy (AFM) sample a relatively moderate fraction (say, 100-500 particles) of the overall colloidal population at a significant cost in terms of image acquisition, processing and analysis (following optimization, it typically takes 24-48 hrs to conduct all these stages), 2)- optical-based techniques like dynamic light scattering (DLS) and laser diffraction (LD) are highly sensitive to outlier particles, such as synthetic debris Aragon and Pecora (1976).

The measurement of viscosity of dilute disc dispersions and its subsequent correlation to particle morphology is a particularly attractive technique by comparison. The advantages of this technique lie in its simplicity of operation, speed, magnitude of sampling, relative insensitivity to particulate outliers (the results are not strongly skewed by outliers) coupled with sensitivity to variations in particle size distribution parameters such as mean and standard deviation. In this chapter, we review theories of simple shear, uniaxial and biaxial extension rheology for dilute dispersions of oblate spheroidal particles, and suggest modifications to the existing theories that enable us to extend the applicability of these models to polydisperse particle dispersions at practically any rotary Peclet number (Pe) of interest, for applications to disc-like morphologies of interest, such as GO.

5.1 Oblate Spheroids

The classical approaches to model the dilute suspension rheology of flaky structures typically approximate the latter as oblate spheroids in the limit of high aspect ratio, i.e.: b >> a. Such systems have been pioneered by Kuhn and Kuhn (1945), van der Kooij (2001) and Brenner (1974). Most models thus yield the parameters b and a, major and minor axes of an oblate spheroid respectively, and these values are taken to correspond to the lateral dimension and thickness estimates for the nanosheet as illustrated in **Figure** 5-1. It must be noted that these dimensions can be converted to an equivalent circular diameter (D) and thickness (t) respectively, by using a simple variable transformation from (a, b) to (t, D), based on the ideas of conservation of volume and aspect ratio. This yields D = 1.747b = 0.874(2b) and t = 1.747a = 0.874(2a), a difference of ~13% between the estimates for oblate spheroids and equivalent circular discs.

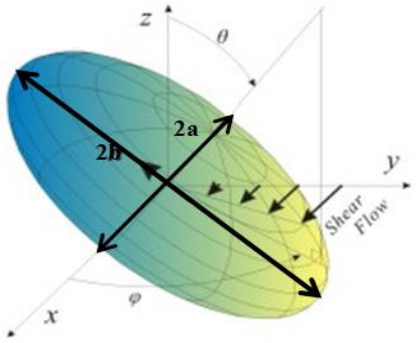

Figure 5-1. Schematic representation of oblate spheroid with polar and equatorial radii a and b respectively. θ and ψ are the azimuthal and zenithal angles respectively, emerging as a consequence of setting up the system in spherical coordinates

5.2 Inter-particle Interaction Limit

In order to enable correlation to particle morphology, the viscosity of the suspension must be measured below the inter-particle interaction limit (**Figure** 5-2); this allows us to later make two simplifying assumptions to model polydisperse nanoparticles at all practically accessible shear-rates. Determination of this limit will be discussed next.

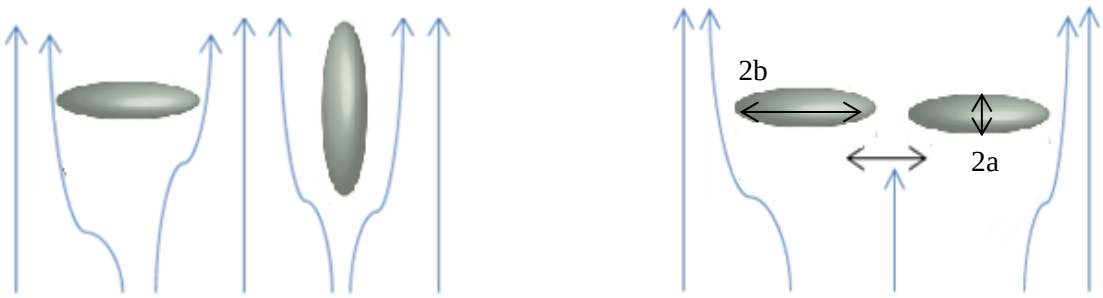

Figure 5-2. (a) for $\phi < \phi^*$, each nanoparticle blocks/diverts streamlines independently of its neighbors, thus explaining why the addition of nanoparticles within this limit simply results in a linear rise in the viscosity, (b) above the interaction limit ($\phi > \phi^*$), there is an added nonlinear contribution from the interparticular interaction which contributes to the impedance of momentum transport

For a dispersion of monodisperse oblate spheroids or circular discs, ϕ^* can be visualized by imagining the spheroid in 3D space and the spherical space enclosing it (

Figure 5-3).

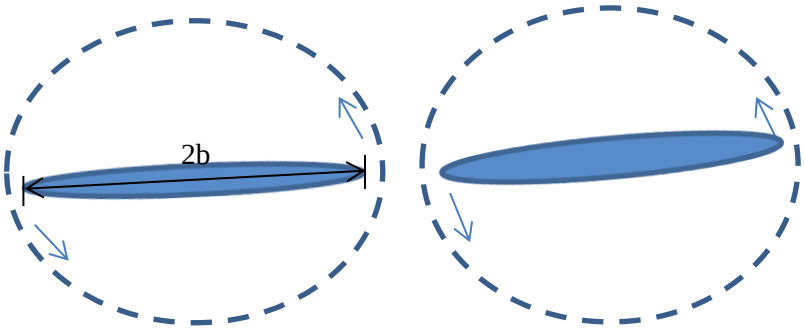

Figure 5-3. Circular discs dispersed in a liquid (with dominant dimension 2b highlighted), with each disc depicted in an enclosure of solvent isolating it from its neighbors during free rotation

It follows then that the threshold volume fraction ϕ^* can be estimated as a state where the nanoparticle volume contained within the enclosure belongs solely to the particle and none other, the remainder of the volume being made up of solvent; analogous to the pervaded volume concept for polymeric chains in a solution or melt. Hence, if the disc

was left to rotationally fan out a spherical volume of length scale equivalent to its own diameter in the space surrounding it in the dispersion; it would remain solely in contact with liquid throughout the rotation, never physically coming into contact with any other particles of the same size. This yields the approximations $\phi^* = \text{disk} = \frac{\frac{4}{3}\pi b^2 a}{\frac{4}{3}\pi b^3} = O\left(\frac{a}{b}\right)$ for oblate spheroids and $\phi^* = \frac{\pi r^2 t}{\frac{4}{3}\pi r^3} = \frac{3t}{2D} \sim O\left(\frac{t}{D}\right)$ for discs.

The main criterion for studying the rheology of a dispersion of discs at the zero-shear limit would then be that $\phi_{max} < \phi^*$, where ϕ_{max} is the maximum particle concentration under rheological study. The above expressions, arrived at through a purely geometrical simplification, make the intuitively reasonable suggestions that particles of higher aspect ratio are expected to begin interacting at lower concentration than their lower aspect counterparts as ϕ^* is linearly dependent on the aspect ratio. Moreover, this linear dependence happens to be consistent with Onsager's thermodynamic prediction (Onsager (1949)) of the onset of isotropic-nematic (I-N) transition for discs in dispersion (based on their so-called critical volume fraction ϕ_c for circular discs, which also scales as $\frac{a}{b}$). Onsager's threshold is predicted from free energy minimization considerations of discs, to which entropy is the dominant factor, such that the energy minimum is then based on a tradeoff of conformational entropy for free-volume entropy.

Furthermore, our prediction of $\phi^* \propto \frac{a}{b}$ is consistent with more recent theoretical predictions of I-N transition Jalili et al. (2014) for aqueous dispersions of narrowly polydisperse discs, of which we present a slightly modified version, Equation 5-(5-1. This equation has been modified to reflect the differences due to different cross-sections (the original work treated hexagons) and Jalili's assumption of limited polydipsersity ($\sigma << 1$) was relaxed here to account for systems of general σ.

$$\phi_{I-N} = f\frac{t}{D}\frac{1+\sigma^2}{1+3\sigma^2+\sigma^3} < nD^3 > \tag{5-1}$$

Where, σ is standard deviation of D, $< nD^3 >$ is dimensionless number density of particles, D is the cross-sectional diameter of a circular disc, square or hexagon (**Figure**

5-4), while f is a shape factor, f = { $\frac{\pi}{4}$, 1, $\frac{3\sqrt{3}}{8}$ } for the aforementioned geometries. In the original work, $< nD^3 >$ was also estimated using Monte Carlo simulation of hexagonal discs to be 2.7 for the transition from the isotropic into the I-N coexistence region, so this value is used as a general working estimate for (5-1 for all cross-sectional geometries.

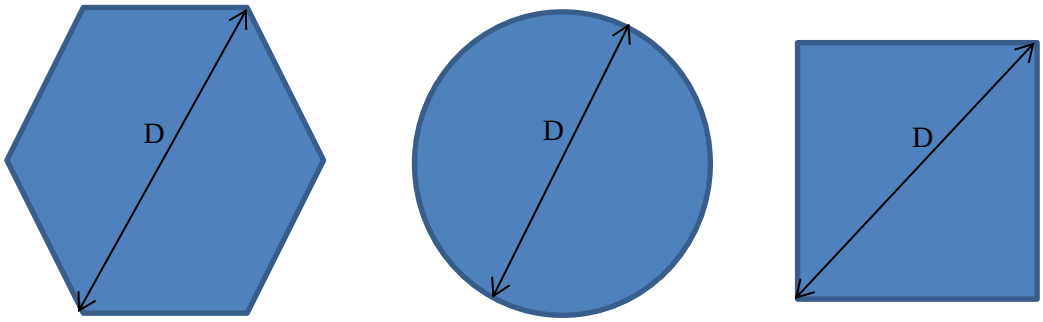

Figure 5-4. Different cross-sections used to obtain f in Equation (5-1)

Since the I-N transition marks the concentration at which the onset of particle-particle orientational influence in dispersion is experienced, it might be reasonable to approximate ϕ^* as being equivalent to ϕ_{I-N}, determined by (5-1). Alternatively, we could approximate ϕ^*, for e.g., by determining an arbitrary particle size beneath which the majority of the particle population (say, ~90%) lies, calculating the corresponding aspect ratio and estimating ϕ^* based on that aspect ratio (i.e.: calling ϕ^* for the polydisperse dispersion as being approximately equal to ϕ^* for the 90th percentile particle size), using either of the preceding geometric or thermodynamic arguments.

5.3 Modeling Disc Rheology

5.3.1 Monodisperse Viscosity in Shearing Flow

The work of Kuhn and Kuhn (1945) is among the first known attempts to capture the viscous morphology-dependence for suspensions of oblate spheroids in shearing flow. They performed scalar energy dissipation calculations to derive the following model:

$$[\eta] = \frac{5}{2} + \frac{32}{15\pi}\left(\frac{D}{t} - 1\right) - 0.628\left(\frac{1 - \frac{t}{D}}{1 - 0.075\frac{t}{D}}\right) \quad (5\text{-}2)$$

where [η] is intrinsic viscosity, defined as $[\eta] = \lim_{\phi \to 0} \frac{\eta - \eta_0}{\phi \eta_0}$, η is suspension viscosity, η_0 is solvent viscosity and ϕ is particle volume fraction. For high aspect ratio (D>>t), this model simplifies to the linear dependence $[\eta] = \frac{32}{15\pi}\left(\frac{D}{t}\right)$. While estimates from this relation are questionable since (5-2) is limited in applicability to monodisperse systems in the zero-shear limit, there may be value in using it to qualitatively compare samples. Van der Kooij attempted to model polydispersity independently and build (5-2) into it; his approach will be reviewed later. An added disadvantage of (5-2) is that it lumps the size information in the aspect ratio and cannot be decoupled into size parameters t and D.

Generalizing the solution for arbitrary shear-rates, Leal and Hinch (1972), Stewart and Sorenson (1972) and Brenner (1974) solved for the simple shear flow field over a system of monodisperse axisymmetric particles in suspension. In the low-shear limit, we simplified the most recent results of Brenner to yield the following correlation:

$$[\eta] = \frac{2}{15\pi}\left(\frac{D}{t}\right)\left[16 - \frac{19}{105}Pe^2 + O(Pe^4)\right] \quad (5\text{-}3)$$

where, Pe is the rotary Peclet number, defined as, $\dot{\gamma}$ is the shear rate, D_r is the rotary diffusion coefficient for oblate spheroids (b>>a), k is the Boltzmann constant, T is the absolute temperature, and η_0 is as the solvent viscosity.

It is important to note that this model is valid for low Pe (~0.1-1), and fails for Pe >> 1 as the higher-order error terms dominate the equation. Within the domain of validity, it is possible to ignore both the O (Pe^2) and O (Pe^4), reducing (5-2) to the same limiting case as that for (5-2) and validating both equations. In (5-3), we thus now have an equation which accounts for shear-thinning in a dilute dispersion of oblate spheroids in the form of the O(Pe^2) and O(Pe^4) terms, even if the influence of these terms is limited.

The limitations of (5-3) are more or less the same as those of (5-2), and we need a more general correlation that models [η] and the shear-thinning experienced by a suspension of oblate spheroids at arbitrary Pe. To this end, Brenner suggests the following correlation for modeling a system of thin spheroids (described by Brenner as "circular discs") which is valid for two dimensional shear flow:

$$\frac{\eta-\eta_0}{\eta_0 n D^3}=\frac{8}{9}\left[4-\frac{3}{2}\langle sin^2\theta\rangle+\frac{5}{2}\,\langle sin^2\theta\, cos\,2\psi\rangle+\frac{3}{Pe}\langle sin^2\theta\, sin\,2\psi\rangle\right] \tag{5-4}$$

where θ and ψ are introduced in **Figure** 5-1, while n is the number concentration of nanoparticles in the dispersion. Brenner expressed the dimensionless viscosity in the unconventional form shown on the LHS of (5-4) rather than in terms of [η] because he treats oblate spheroids in the limit where the diameter of the spheroids is much larger than the thickness. He then moves from an (a, b) to an (n, b^3) parameter space in (5-4); presumably because he considers it might be experimentally easier to count a number of nearly two-dimensional objects in a dispersion rather than to measure the thickness t of these objects. This model is the only known closed-end model to-date describing shear-thinning of dilute disc suspensions over arbitrary Pe. n can be measured using techniques such as nanoparticle tracking analysis (NTA), but such techniques are typically limited in particle detection by a maximum size of 1-2 μm. For this reason, we moving back to an (a, b) description by use of the conversion $\phi = n\,V_p = n\frac{4}{3}\pi ab^2 = n\frac{1}{4}\pi tD^2$, yielding:

$$[\eta]=\frac{2}{3\pi}\left(\frac{D}{t}\right)\left[4-\frac{3}{2}\langle sin^2\theta\rangle+\frac{5}{2}\,\langle sin^2\theta\, cos\,2\psi\rangle+\frac{3}{Pe}\langle sin^2\theta\, sin\,2\psi\rangle\right] \tag{5-5}$$

Equation (5-5), in turn, being in terms of [η], requires knowledge of the nanoparticle density in order to enable the calculation of ϕ. The reliance of the model on ϕ can introduce a significant margin of inaccuracy into the rheo-morphological characterization since the model is based on ϕ-sensitive equations, and especially

considering that density (needed to calculate ϕ) can vary significantly across different batches of colloidal sheets produced depending on the method of preparation, and potentially even from one batch to the next using the same method.

Equations (5-4) and (5-5) contain three geometric factors which result from averaging over the different orientational states accessible to the spheroidal particles in the shear field. The values of these geometric averages change with Pe because increasing shear rate graduating restricts the accessible orientations to the particles. Hence, modeling these factors is a pre-requisite to modeling the shear-thinning of these suspensions. Stewart and Sorenson (1973) were able to indirectly obtain numerical solutions for these geometric factors by solving the equations for [η] as well as the first and second normal stresses in the suspension. The solutions were obtained for two limiting cases: 1) - no particles in the suspension, and 2) - touching particles. Brenner (1974) re-presented the results of Stewart and Sorenson in the form of a tabulation which directly correlates the three geometric factors to Pe. Furthermore, Brenner noticed that the solutions at high Pe for all three factors take the form $n + m\ Pe^{-1/3}$, estimating and reporting coefficients n and m for each factor. These solutions are applicable at $Pe^{-1/3} << (a/b) \sim (t/D)$; the limit of touching discs.

We were able to fit all the tabulated values for the three geometric factors by introducing fitting terms of order $Pe^{-2/3}$ as shown in Figure 5-5 (a-c). We fit the computational data presented by Stewart and Sorenson (1973) and Brenner (1974) by taking the simulation data from **Figure 5-5**, adding the simulation results for each of the three geometric factors to generate a curve of [η] vs Pe and fitting this simulation curve to closed-ended functional forms in Pe at the low and high limits. This proposed approach results in piecewise model 6), which represents the data over the entire range of Pe, thus helping minimize the computational time involved during the fitting of experimental data.

$$[\eta] = \frac{D}{t}\frac{2}{3\pi}\begin{cases} 1.733 \times 10^{-3} Pe^{3} - 2.335 \times 10^{-2} Pe^{2} - 2.377 \times 10^{-2} Pe + 3.2 & Pe < 9 \\ -2.357(Pe)^{-\frac{2}{3}} + 6.014(Pe)^{-\frac{1}{3}} & Pe > 9 \end{cases} \quad (5\text{-}6)$$

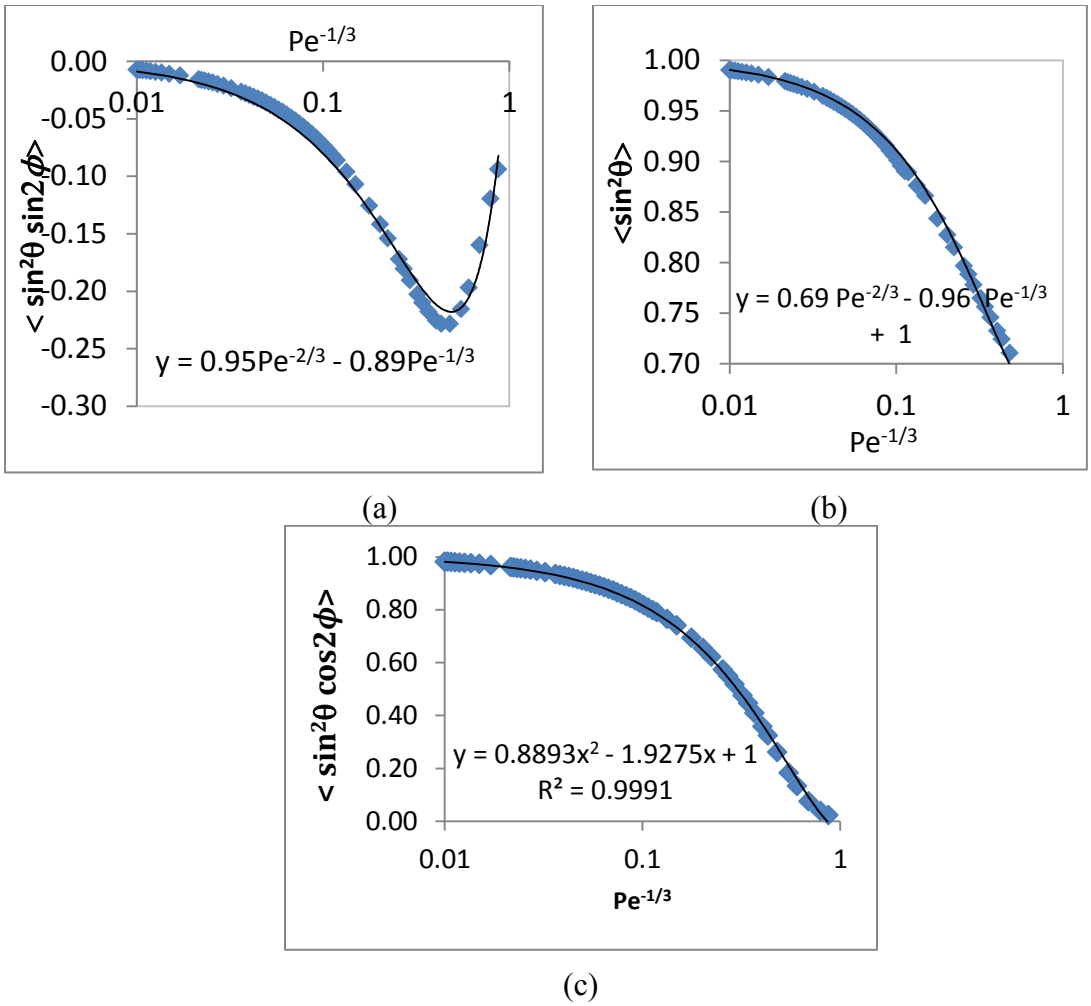

Figure 5-5. Term-by-term fitting we did on the simulation data reported by Brenner (1974) based on Stewart and Sorenson (1973) for the three geometric factors in Equations (5-4) and (5-5) to 2nd-order polynomials in $Pe^{-1/3}$

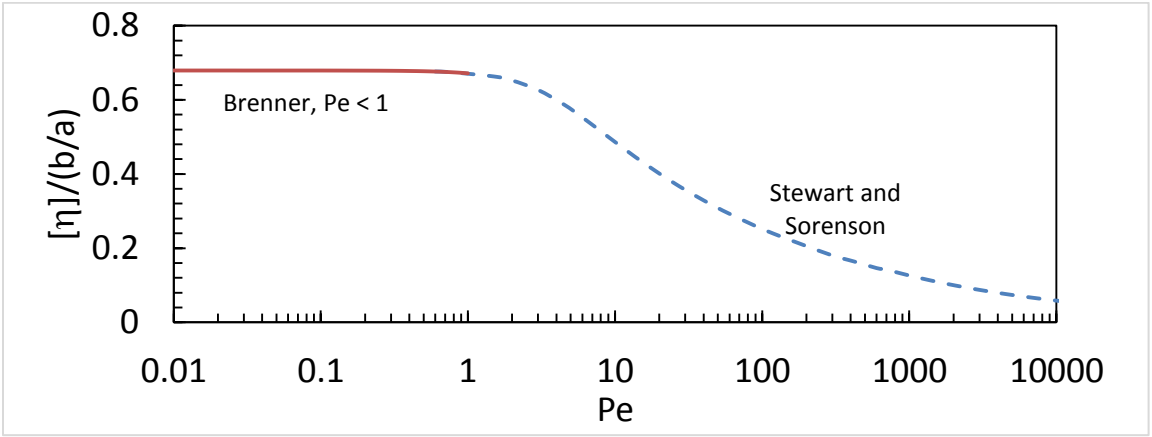

Figure 5-6. Simulated [η] based on the Stewart and Sorenson (1973) estimates of the geometric factors for arbitrary Pe (5-6) and comparison to Pe < 1 result (5-3)

5.3.2 Polydispersity

The only known attempt to account for polydispersity in a dilute suspension of oblate spheroids and to build it into a viscosity-morphology correlation comes from the work of van der Kooij et al. (2001) who modeled a narrowly distributed dispersion of gibbsite platelets. They assumed that $[\eta]$a volume-fraction average, yielding:

$$[\eta] \ = \frac{\sum_i \phi_i \, [\eta]_i}{\sum_i \phi_i} \ = (1 + 2\sigma^2).\frac{32}{15\pi}.\frac{\langle D \rangle}{\langle t \rangle} \qquad (5\text{-}7)$$

In (5-7), $[\eta]_i$ for each individual fraction i of nanoparticles was taken to be given by (5-2) in the limit of b >> a ($[\eta]_i = \frac{32}{15\pi}\left(\frac{D_i}{t_i}\right)$). Equation (5-7) represents an improvement over both (5-2) and (5-3) as the former uses standard deviation σ to account for polydispersity in a narrowly-disperse system (i.e.: for small σ). Using the same approach as van der Kooij and generalizing the result to a system of arbitrary σ, we obtain:

$$[\eta] = \ \frac{(1 + 3\sigma^2 + \sigma^3)}{1 + \ \sigma^2} \cdot \frac{32}{15\pi} \ \cdot \frac{\langle D \rangle}{\langle t \rangle} \qquad (5\text{-}8)$$

Equation (5-8) reduces to the more special form for small σ (5-7). Like its predecessors, this model still valid only at low Pe, and does not account for Pe dependence of [η]. We should also note that the model development shown in (5-7) assumes linear weighing of $[\eta]_i$ with ϕ_i over the entire Pe range. This has the following consequences:

1) assuming the $[\eta]_i$ contributions to be linearly additive is equivalent to stating that no inter-particle interaction exists between any pair of particles, which might be a sensible assumption, given that [η] is being measured at $\phi < \phi^*$.
2) using ϕ_i as the weighting factor is equivalent to stating that bigger particles are expected to contribute more to [η] than the smaller ones, since ϕ_i is sized-biased ($\phi_i = \ n_i \frac{1}{4}\pi t_i D_i^2 \propto D_i^2$).

This assumption of linear additivity must be validated; in spite of operating beneath the geometric or thermodynamic ϕ^* for the dispersion, the only fact that can be stated with reasonable confidence is that no interactions exist between identically-sized particles. By contrast, interactions might occur between different-sized particles. To investigate the

linearity claim, we thus invoke the classical derivation of the Kreiger-Dougherty relation (Kreiger (1972)), which claims for a binary system of dispersed particles:

$$\begin{aligned}\eta(\phi_1+\phi_2) &\approx \eta_0[1+\phi_1\eta(D_1)]\,[1+\phi_2\eta(D_2)] \\ &= \eta_0\,[1+\phi_1[\eta(D_1)]+\phi_2[\eta(D_2)]+\phi_1\phi_2[\eta(D_1)][\eta(D_2)]\end{aligned} \tag{5-9}$$

By operating in the dilute limit, the problem remains simple since we can continue to ignore excluded volume effects that result from each particle size bin taking up its own volume in dispersion (originally accounted for by Kreiger and Dougherty). This allows us to work with (5-9) as it is without having to account for excluded volumes.

Inspection of (5-9) for the binary colloidal system shows that of the four terms on the RHS: the 1st term corresponds to η_{solv}, the 2nd and 3rd terms to the linearly independent contributions to the suspension by each of the two particle fractions, while the 4th and highest order terms can be thought of as an approximation of the composite interactive effect of the binary fractions with the solvent in shear flow. While we realize that such a composite interaction need not be necessarily represented as a geometric combination of the individual ϕ contributions, we will adopt Krieger and Dougherty's coupling term as an approximation and use it to lay down the remainder of the argument. By demonstrating that this composite term is negligible in the expansion of $[\eta]$, this would mean by extension that all higher-order interaction terms with the solvent are also negligible, thus enabling us to retain the linear terms only. It must be noted that the following argument uses the relation $\phi = \sum_{i=1}^{k}\phi_i$, which is once again based on the assumption of negligible excluded volume effects, thus enabling us to treat individual ϕ_i as though they were linearly additive. The foregoing assumption holds well for $\sum_{i=1}^{k}\phi_i \ll \phi_{solv}$ (where the latter is the volume fraction belonging to the solvent), an excellent approximation under the dilute conditions we are working at, especially since $\phi \ll \phi^*$ is a necessary theoretical condition in order to enable analysis of experimental data using the $[\eta]$ approach. Inspection of (5-1) reveals that $\phi^* \ll 0.01$ even for the biggest size fractions in a given particle distribution. Hence, the assumption $\phi = \sum_{i=1}^{k}\phi_i$ can be satisfied via the simple expedient of operating within the window $\phi \ll \phi^*$. Farris (1968) has a more rigorous treatment that models ϕ as $\ln(1-\phi) = \sum_{i=1}^{k}\ln(1-\phi_i)$ for

general ϕ. His expression reduces to $\phi = \sum_{i=1}^{k} \phi_i$ for $\phi << \phi_{solv}$. Applying the preceding set of simplifications, we can represent $[\eta]$ for the bimodal system as follows:

$$[\eta] = \lim_{\phi \to 0} \frac{\eta(\phi_1 + \phi_2) - \eta_0}{\phi\, \eta_0}$$

$$= \lim_{\phi_1,\, \phi_2 \to 0} \left[\frac{\phi_1}{\phi_1 + \phi_2} [\eta(D_1)] + \frac{\phi_2}{\phi_1 + \phi_2} [\eta(D_2)] + \frac{\phi_1 \phi_2}{\phi_1 + \phi_2} [\eta(D_1)][\eta(D_2)] \right]$$

$$= \frac{\sum_{i=1}^{2} \phi_i\, [\eta]_i}{\sum_{i=1}^{2} \phi_i} \qquad (5\text{-}10)$$

As seen in (5-10), the cross-term drops in the limit, leaving behind the linear terms in ϕ_i. The preceding argument is immediately generalizable to a discrete system containing k fractions of dispersed particles, thus recovering the middle expression in (5-7) which claims that measured $[\eta]_{measured}$ is a ϕ -average $[\eta]$. Having established the validity of the discrete polydispersity modeling approach of van der Kooij, we will now proceed with a brief discussion of the limitations of applicability of this technique to the shear flow equations (5-6), thus justifying our use of a continuum modeling approach instead (next subsection).

Applying the discrete polydisperse modeling result of (5-10) with (5-6), we end up with the set of equations (5-11) which contain higher order moments of <D> (e.g.: $<D>^{12}$), and we would thus need to invoke the concept of moments of a distribution in order to convert these higher order moments into useful lower order counterparts; this is what was done by van der Kooij to enable the development of model (5-7):

$$[\eta] = \frac{2}{3\pi} \begin{cases} \dfrac{\sum_i n_i (1.734 \times 10^{-3} D_i^{12} \delta^3 - 2.335 \times 10^{-2} D_i^9 \delta^2 - 2.377 \times 10^{-2} D_i^6 \delta + 3.192\, D_i^3)}{\sum_i n_i\, D_i^2 t_i} & \{Pe_i < 9\} \\ \dfrac{\sum_i n_i \left(-2.357\, D_i (\delta)^{-\frac{2}{3}} + 6.014 D_i^2\, (\delta)^{-\frac{1}{3}} \right)}{\sum_i n_i\, D_i^2 t_i} & \{Pe_i > 9\} \end{cases}$$

$$= \frac{2}{3\pi <D^2><t>} \begin{cases} c_1 < D^{12} > \delta^3 + c_2 < D^9 > \delta^2 + c_3 b_i^6 \delta + c_4\, b_i^3 & \{Pe < 9\} \\ c_5 < D > (\delta)^{-\frac{2}{3}} + c_5 < D^2 >\, (\delta)^{-\frac{1}{3}} & \{Pe\ > 9\} \end{cases} \qquad (5\text{-}11)$$

The problems with using this approach to model experimental rheological data are the following:

1) - to begin with, the limits of applicability of the two pieces of (5-12) become blurry after the discrete modeling. The best we can do is to assume that the limits $Pe_i < 9$ and $Pe_i > 9$ are defined for the discrete distribution such that $Pe \sim Pe(< D >)$. This is a problematic statement to make since particles of different D generate different Pe, so a quantity like $Pe(< D >)$ is misleading because it does not allow domains of applicability to be calculated for every particle at ever shear rate, and we thus have no mechanism of differentiating between particles in our experimentally-measured dispersion for which Pe < 9 versus the rest (Pe > 9). The domain of applicability for each of the two pieces of (5-13) thus becomes impossible to compute.

2) - A moment is a higher-order average that spans an entire distribution, while (5-14) is a piecewise function separated by a transition Pe. This approach of using the moments of a discrete distribution is thus impossible to employ from the fitting perspective for an experimental dataset, because neither of the two pieces of (5-15) can take the moment for an entire distribution as a parameter in its argument. Rather, it is a part of the particle size distribution that is contributing to each of the two functional pieces in (5-16); such a part of a distribution (e.g.: a tail) is impossible to represent using the idea of moments and moment conversions, since the latter are a property of an entire distribution.

3) – This discrete modeling approach is limited in applicability to models of [η] which are polynomial functions of D, because it is for such models that we can apply the idea of the moments of a distribution. As the functional form for [η] becomes more complicated e.g.: fractional polynomials as seen in (5-17), or modified Bessel functions as we will observe later for extensional flows, it becomes difficult and outright impossible to use the moment conversions to obtain a closed-ended polydisperse functional form relating [η] to discrete distribution parameters (μ and σ).

For the reasons discussed above, we realize that discrete distributions are a poor approach towards representing the rheology of dilute polydisperse particle systems and we switch instead to a continuous polydisperse expression which overcomes all of the aforementioned issues with discrete modeling, as discussed below. Finally, it is

noteworthy that with the exception of the 3rd point on the preceding list, all the issues with discrete modeling are strictly from the analytical perspective when we attempt to fit experimental [η] data for a dispersion, but not from the modeling perspective, i.e.: a simulated discrete particle distribution can be used with (5-18) to model the rheological behavior of such a distribution. We use this idea with MTD-GO in Chapter 6 to validate the results of continuum modeling of experimental [η] data by taking the image-analyzed discrete particle size distributions of Chapter 4 and substituting them in (5-19) to simulate [η] for the discrete distribution. These image-simulated mock [η] data are then compared to the experimental [η] data and the fitting thereof by the continuum rheological polydisperse model (discussed below).

5.3.3 Modeling Polydispersity: Continuum Approach

Among the few literature attempts where polydispersity was analytically accounted for in a model to correlate [η] and shear-thinning to particle morphology comes from the work of Parra-Vasquez et al. (2014). In this work, the authors treated single-walled carbon nanotubes (SWCNTs) as polydisperse, prolate spheroids and integrated over a predetermined distribution function. The drawback of this method is that prior knowledge of the nature of the distribution function is a pre-requisite. Applying this method to (5-4) generates the following equation:

$$\frac{\eta - \eta_0}{\eta_0} = n \int_0^\infty \Omega(D)\ b^3\, f(D)\, dD \tag{5-20}$$

where, $\frac{\eta - \eta_0}{\eta_0}$ can be referred to as the incremental (η_{inc}) viscosity. f(D) is given by (5-6) and $\Omega(D)$ is the diameter distribution function, assumed to be lognormal based on the results and discussions of Chapter 4:

$$\Omega(D) = \frac{1}{D\sigma\sqrt{2\pi}} \exp\left(-\frac{(\ln D - \mu)^2}{2\sigma^2}\right) \tag{5-21}$$

μ and σ^2 are the mean and variance of ln(D) respectively. Alternatively, when we once again invoke the conversion $n = \phi V_p$ and relax the assumption of infinitesimal thickness a on the discs, this yields the following expression:

$$[\eta] = \int_0^\infty \Omega(D)\ [\eta](D)\, dD \qquad (5\text{-}22)$$

5.4 Model Predictions

5.4.1 Shear Flow

Choosing Equation (5-22), we present a series of model predictions (**Figure 5-7**, Figure **5-8** and **Figure 5-9**) for different values of simulated parameters <t>, <D> and σ respectively. In all of these Figs, we notice a number of common features: 1)- shear-thinning behavior, 2)- increasing [η] as a function of <D>, <t> and σ, coupled with a preservation of the overall trend, and 3)- plateau (shear-independent) behavior at low Pe(~1), 4)-sensitivity to all simulation parameters decreases with increasing shear-rate.

These observations are consistent with our expectations; bigger particles experience slower rotary diffusivities than smaller particles, and hence will begin to align with the shear field quicker than the smaller particles. An alternative way of understanding this observation is that bigger particles, being more flow-resistive than smaller particles, are the quickest to get streamlined to the flow and so experience shear-thinning first. This explains the lower onset of shear-thinning for particles of bigger D as well as the higher viscosity observed for bigger particles (**Figure 5-7**). This is an important observation for practical purposes; it means that our chances of extracting complete and accurate details about a given particle distribution are higher if we are able to experimentally measure the onset of shear-thinning. It also means though that data is needed from the low shear rate regime. At lower shear rates instrument error starts to influence the torque measurements made by a rheometer. A dataset which clearly displays the initial plateau, followed by the onset of shear-thinning and transition region, followed by behavior at high shear-rates (where [η] starts to level off); such a dataset would contain complete details about the morphology distribution of a given particle dispersion. Using such a dataset, the theory here can be used effectively to model particle size distribution. We show some examples of this in the next Chapter.

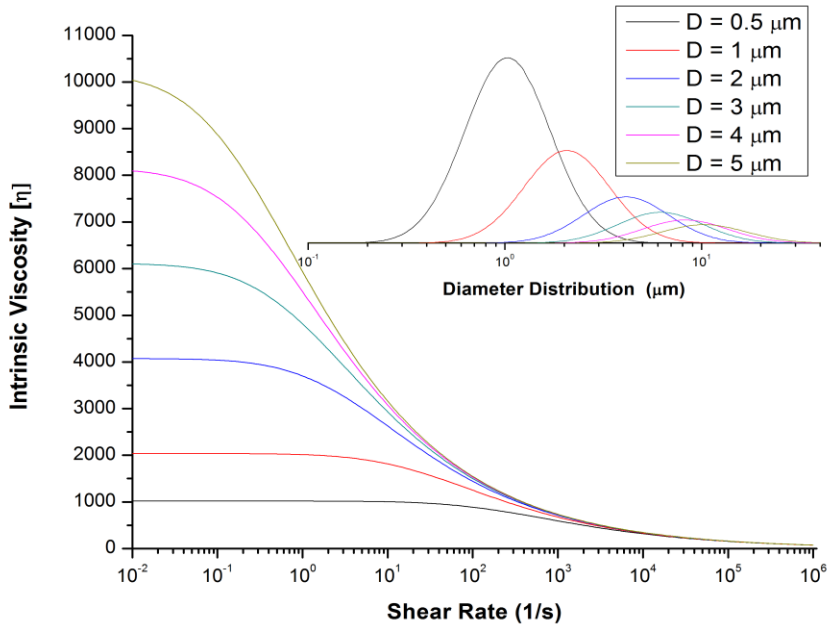

Figure 5-7. Influence of particle diameter D on [η] as per Equation 15 (t = 1.00 nm, σ =1.00)

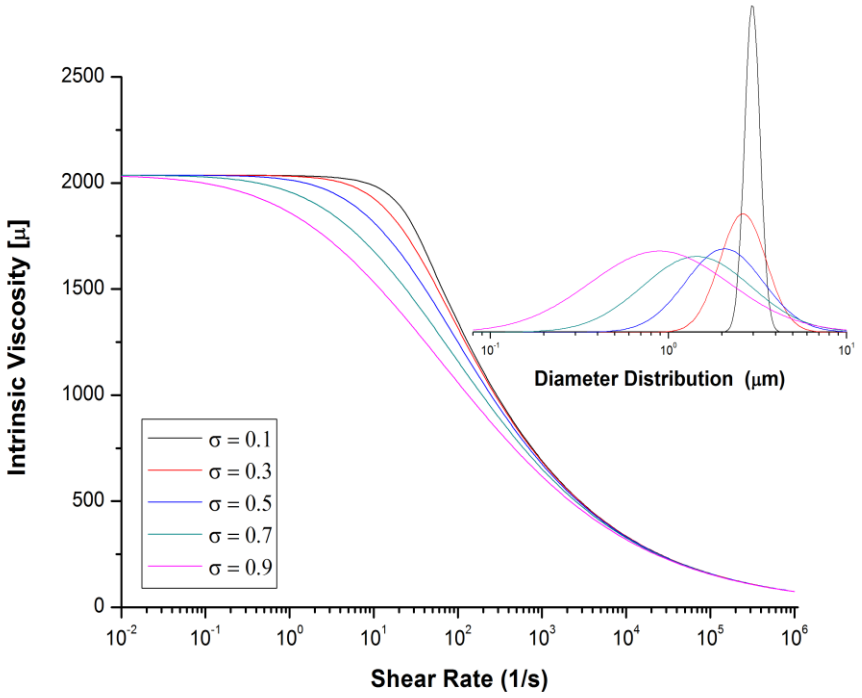

Figure 5-8. Influence of standard deviation σ on [η] in Equation 15 (D = 1.00 μm, σ =1.00)

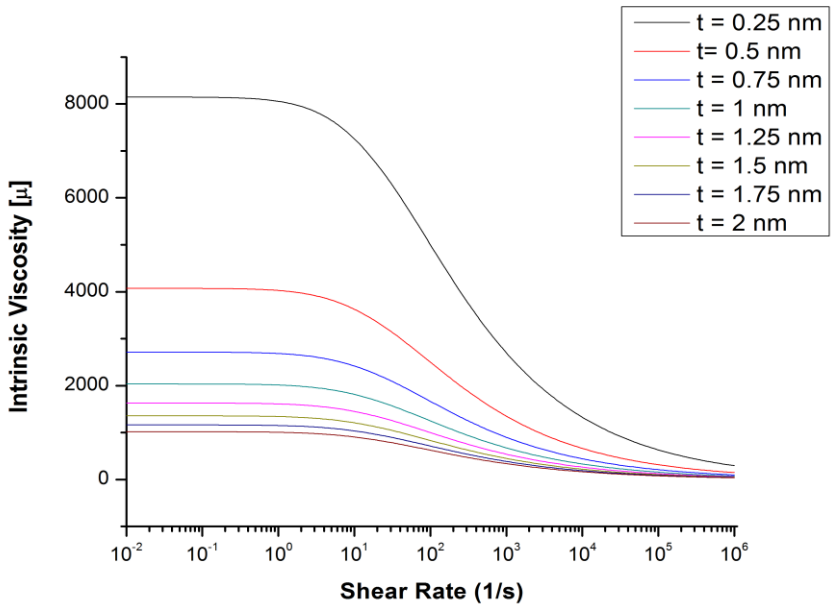

Figure 5-9. Influence of particle thickness t on [η] in Equation 15 (D = 1.00 μm, σ =1.00)

Secondly, the fact that the onset of shear-thinning is experienced sooner for samples of higher σ (**Figure** 5-8) is consistent with our formulation which poses that larger particles are expected to have a stronger influence than smaller ones in contributing to [η]. Hence, in comparing two samples with similar <D> but different σ, the one with higher σ is expected to possess a longer tail of larger particles (especially considering the lognormal distribution used to model our particle systems). These bigger particles will begin aligning sooner, causing a sooner onset of shear-thinning as discussed previously.

Finally, the effect of increasing particle thickness t in reducing [η] (**Figure** 5-9) can be explained by the role played by t in calculating ϕ; as t decreases with respect to D, we get similar obstruction of fluid flow (due to the dominant effect of large D) while reducing the volume occupied by each particle in the suspension, thus reducing ϕ. Increasing t, on the other hand, loads the dispersion more in terms of particle volume and ϕ, while it does not significantly elevate η. This, of course, has the net effect of reducing [η] as t increases.

It is noteworthy that the influence of the simulation parameters on [η] decreases greatly as shear-rate rises. This is also a physically reasonable simulation result; as particles line up with the shear-field, the differences between big and small particles in terms of obstruction to fluid flow gradually decrease until they almost vanish (a big and a small particle perfectly aligned with the circular shear-field are expected to offer similar shear resistance to flow). A similar argument can be made for thick versus thin particles.

5.4.2 Uniaxial Extensional Flow

In efforts to develop more user friendly characterization techniques, we will also examine the uniaxial extensional flow of oblate spheroids in dilute dispersion; the equations governing this type of flow are actually simpler than for shear. Following Brenner (1974), the equation for intrinsic viscosity of uniaxial extensional flow of a monodisperse system is:

$$[\eta]_{mono} = \frac{5}{2}\left[2Q_1 - \frac{3}{2}\left(F + \frac{1}{3}\right)Q_2 + \frac{3}{\lambda}\left(F - \frac{1}{3}\right)(3Q_2 + 4Q_3)\right] \tag{5-23}$$

Q_1,Q_2 and Q_3, are structural factors dependent on the aspect ratio of a spheroid. In this work, these parameters were calculated employing a custom Matlab routine. They are complicated derived values. The factors are material constants that are general to any spheroid, and their formulation is laid below as per Brenner (1974):

$$Q_1 = \frac{1}{5\alpha_{\parallel}'} \tag{5-24}$$

$$Q_2 = \frac{2}{3}Q_1\left(1 - \frac{\alpha_{\parallel}''}{\alpha_{\perp}''}\right) \tag{5-25}$$

$$Q_3 = Q_1\left[\frac{r_p(\alpha_{\parallel} + \alpha_{\perp})}{r_p^2\alpha_{\parallel} + \alpha_{\perp}}\left(\frac{\alpha_{\parallel}'}{\alpha_{\perp}'}\right) - 1\right] \tag{5-26}$$

$$\alpha_{\parallel} = \frac{2}{r_p^2 - 1}(r_p^2\beta - 1) \tag{5-27}$$

$$\alpha_{\perp} = \frac{r_p^2}{r_p^2 - 1}(1 - \beta) \tag{5-28}$$

$$\alpha'_{\parallel} = \frac{r_p^2}{4\left(r_p^2 - 1\right)^2}(3\beta + 2r_p^2 - 5) \tag{5-29}$$

$$\alpha'_{\perp} = \frac{r_p}{\left(r_p^2 - 1\right)^2}(r_p^2 + 2 - 3r_p^2\beta) \tag{5-30}$$

$$\alpha''_{\parallel} = \frac{r_p^2}{4\left(r_p^2 - 1\right)^2}\left[2r_p^2 + 1 - \left(4r_p^2 - 1\right)\beta\right] \tag{5-31}$$

$$\alpha''_{\perp} = \frac{r_p^2}{\left(r_p^2 - 1\right)^2}\left[\left(2r_p^2 + 1\right)\beta - 3\right] \tag{5-32}$$

$$\beta = \frac{\cosh^{-1} r_p}{r_p\left(r_p^2 - 1\right)^{\frac{1}{2}}} \tag{5-33}$$

F is the rotary distribution function describing the state of the particles as they align with the extensional flow. F is a function of the peclet number and material properties where:

$$B = \frac{(a^2 - b^2)}{a^2 + b^2} \tag{5-34}$$

$$\lambda = B.Pe \tag{5-35}$$

$$\xi = \left(\frac{3}{4}\lambda\right)^{0.5} \tag{5-36}$$

$$F(\xi) = \frac{1}{2\xi D(\xi)} - \frac{1}{2\xi^2} \tag{5-37}$$

The function $D(\xi)$ is Dawson's integral defined by:

$$D(\xi) = \exp(-\xi^2)\int_0^{\xi} \exp(z^2)\, dz \tag{5-38}$$

Since this is an exact solution, no interpolation was required to create the following graphs. We did, however, find that it was computationally more efficient to interpolate F

instead of recalculating it for every iteration of the function. Employing (5-22) we can extend our mono-disperse equation to model a polydisperse system.

5.4.2.1 Model Predictions:

Figure 5-10 depicts the [η] behavior of a lognormal polydisperse system of discs in uniaxial extensional flow. Unlike shear flow, extensional flow is expected to result in shear-thickening of these particles in dispersion. It can be observed from **Figure 5-10** is that for extensional flow, the difference in [η] between the high and low extrema is not as large as for the shear flow system; in the latter, [η] tends to one as the shear rate goes to infinity, resulting in an acute net change in the thousands over the complete range of shear rates. In uniaxial extension, [η] only changes by a few hundred units.

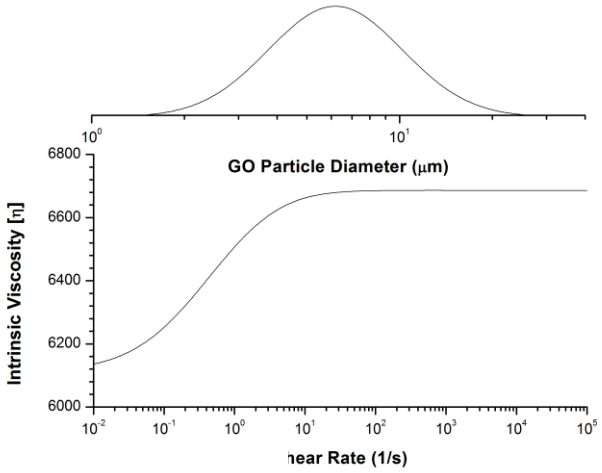

Figure 5-10. [η] behavior of a polydisperse colloidal oblate spheroid system (D = 3 μm, t = 1 nm) in uniaxial extensional flow. The polydisperse diameters are described by a lognormal distribution with a standard deviation of 0.5.

Figure 5-11 illustrates that a change in mean diameter (D) of our system can be determined by two specific properties of the curve: the location of the transition period shifts to lower shear rates as D increases, and [η] is proportional to D. The effect of D on [η] will be explained in more detail in the section below on biaxial extension. For now, we point out that: 1)- uniaxial extension, unlike simple shear and biaxial extension, displays show shear-thickening behavior, and 2)- the proportionality of [η] with D is a

property shared between simple shear, uniaxial and biaxial extension. Both of these observations will be explained in additional detail later.

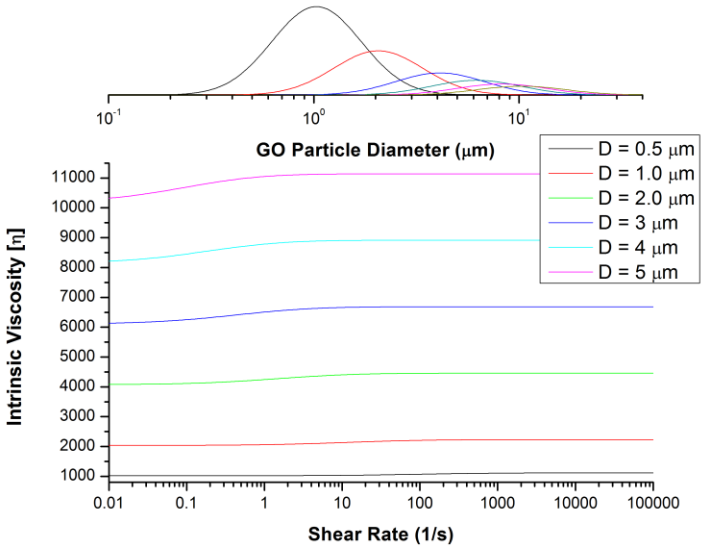

Figure 5-11. Effect of mean diameter D on [η] of dilute oblate spheroids in uniaxial extension

Figure 5-12 depicts the influence of σ on [η] in polydisperse systems under uniaxial extension. The [η] curves broaden with the distribution for the same reason as in shear flow; a broader distribution means we have both smaller and larger dispersed particles than before. Smaller particle begin to respond to the flow sooner and larger particles later, so the domain of the [η] thinning response broadens with the distribution.

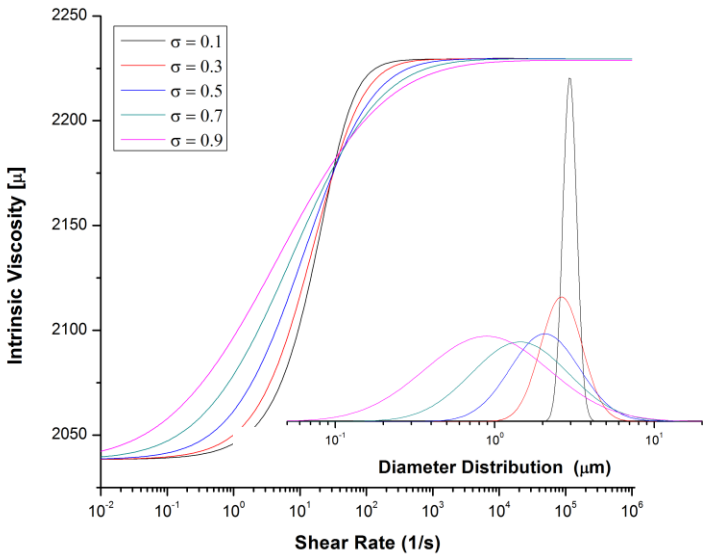

Figure 5-12. Effect of σ on [η] in dilute systmems of polydisperse oblate spheroids

Similar to shear flow, t is inversely proportional to the [η] as observed from **Figure** 5-13. This is thought to be the result of increase in the hydrodynamic resistance per unit volume of oblate spheroids that results from decreasing t for the same D. This is the same reason thought to be behind the proportionality of [η] with D, and both of these are explained in additional detail in the biaxial extension section as well as in conclusions.

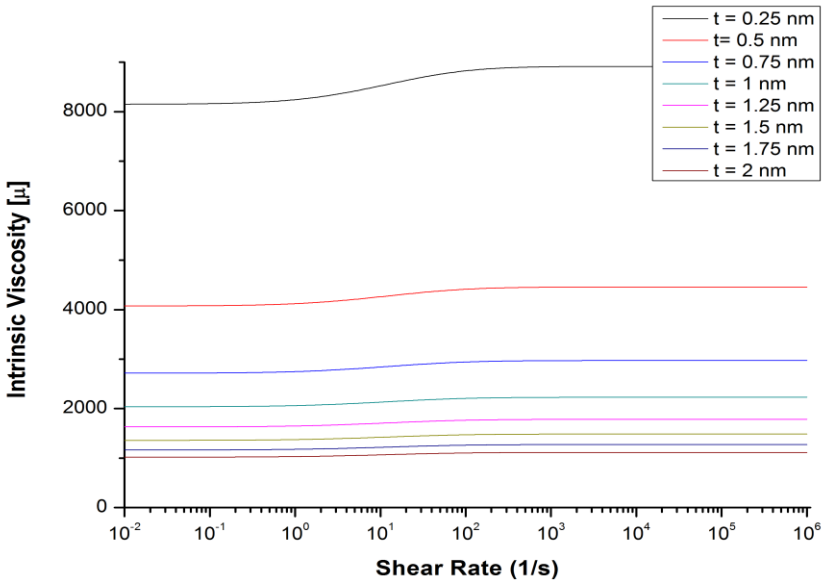

Figure 5-13. Effect of t on [η] of a polydisperse oblate spheroidal system in uniaxial extensional flow.

From the preceding sensitivity analysis, it appears that we should also be able to employ uniaxial extensional rheology to characterize oblate spheroidal particles. This allows for flexibility in our capabilities as the extensional flow data can help validate shear flow information. It might also allow us to use different equipment that may be at our disposal to gather information across a broad spectrum of shear rates.

5.4.3 Biaxial Extensional Flow

In compliment to the uniaxial extensional flow model we also present a polydisperse biaxial extensional flow. Although the motion is similar between the two Brenner (1974) shows that the biaxial extensional flow is shear thinning, in contrast with the shear thickening uniaxial flow. Brenner (1974) solves the differential equation for the intrinsic viscosity of a monodisperse oblate spheroids as:

$$[\eta]_{mono} = \frac{5}{8}[8Q_1 - 3(h(\lambda)Q_2 + \frac{6}{\lambda}g(\lambda)(3Q_2 + 4Q_3)] \tag{5-39}$$

Where $h(\lambda)$ and $g(\lambda)$ are linear combinations of the rotational distribution functions defined by :

$$h(\lambda) = \frac{I_{\frac{1}{4}}\left(\frac{1}{8}|\lambda|\right) I_{\frac{-1}{4}}\left(\frac{1}{8}|\lambda|\right) + I_{\frac{3}{4}}(\frac{1}{8}|\lambda|) I_{\frac{-3}{4}}(\frac{1}{8}|\lambda|)}{I_{\frac{1}{4}}(\frac{1}{8}|\lambda|) I_{\frac{-1}{4}}(\frac{1}{8}|\lambda|)} \tag{5-40}$$

$$g(\lambda) = \frac{I_{\frac{1}{4}}\left(\frac{1}{8}|\lambda|\right) I'_{\frac{-1}{4}}\left(\frac{1}{8}|\lambda|\right) + I_{\frac{-1}{4}}\left(\frac{1}{8}|\lambda|\right) I'_{\frac{1}{4}}(\frac{1}{8}|\lambda|)}{I_{\frac{1}{4}}(\frac{1}{8}|\lambda|) I_{\frac{-1}{4}}(\frac{1}{8}|\lambda|)} \tag{5-41}$$

I is the modified Bessel function of the first kind. The derivatives were calculated using centered finite difference. These rotary distribution factors can be performed with sufficient computational efficiency that the exact answers have been used in the following calculations. Q_1,Q_2 and Q_3 are the same shape factors presented in the uniaxial extension case. This is not surprising because the nature of the nanoparticles is the same in both systems. The only things that change are how the particles align with the flow field and how that interacts with the surrounding fluid environment.

5.4.3.1 Biaxial Extensional Flow Model Predictions

With the monodisperse [η] formulas in place we may employ (5-22) to properly formulate a polydisperse system. We use a base case of a distribution of oblate spheroids with a mean D of 3 μm, t of 1 nm and σ of 0.5 for comparison purposes. **Figure** 5-14 illustrates the behavior of a typical biaxial extensional system: [η] decreases from a Brownian state as the particles align with the flow field; however at high extension rates, [η] does not decrease towards unity as in the shear case. This behavior limits the biaxial model since a lower difference between the Brownian and high extension rate limits means a lower amplitude signal for fitting purposes. That being said, this model adds to the toolbox of potential characterization techniques for these particle systems.

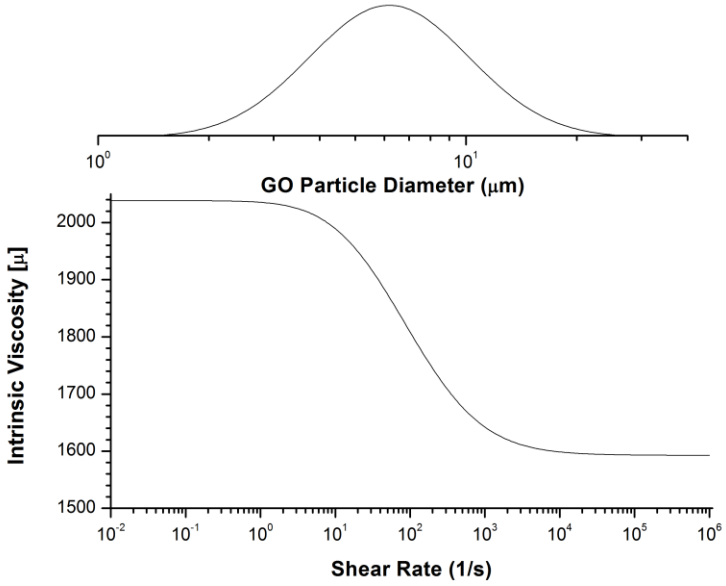

Figure 5-14. Biaxial extensional flow for a system of polydisperse discs.

Figure 5-15 displays the effect of thickness on [η]. Although the direct effect of t is not appearent in our models, t affects [η] in exactly the same manner of inverse proportionality across the three models, biaxial extensional flow not being an exception.

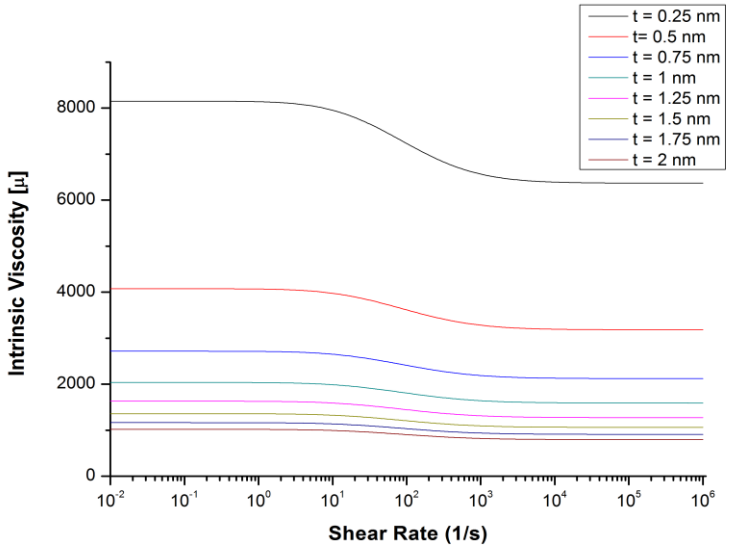

Figure 5-15. Effect of t on [η]of dilute polydisperse oblate spheroids in biaxial extension.

Figure 5-16 reinforces the previously observed behavior of [η] as a function of D in a dilute dispersion of polydisperse oblate spheroids; D shifts the transitional region, while [η] remains proportional to D. We can explain the common trends across all three types of flow reviewed in this section by reducing all the relationships to the rotational distribution function D_r: particles with lower D_r have a lower angular inertia, thus enabling them to align sooner and more easily with the flow, resulting in little shear-thinning, while the biggest particles with the highest D_r (and angular inertia) experience the biggest change in [η] as they align with the flow. The proportionality effect of D on [η] is due to the increased hydrodynamic resistance offered by big particles compared to smaller ones.

Figure 5-17 highlights the effect of σ of a polydisperse sample on [η]. Similar to previous models, a broadening of the distribution allows for an increase in the range of shear-rate over which onset of shear-thinning is experienced, depending on the Brownian motion at each particle D, thus resulting in a characteristic broadening of the shear-thinning regime, a broadening significant enough to provide distinct data about the system polydispersity. This can be employed when we characterize GO particles using our rheological methods.

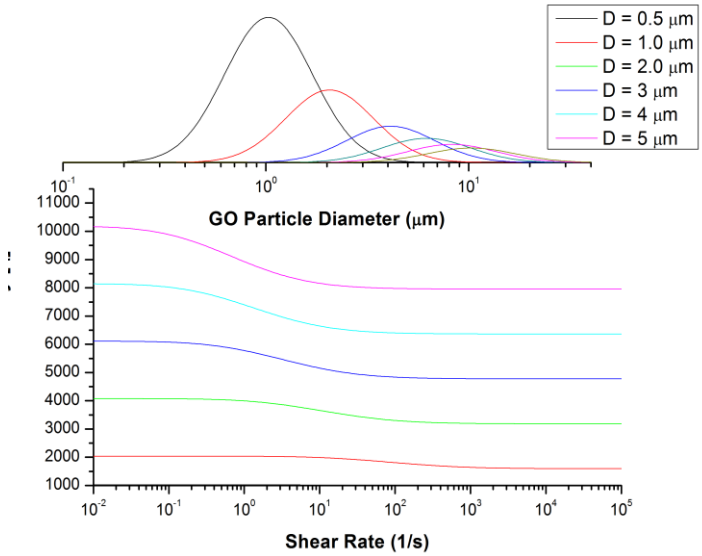

Figure 5-16. Effect of D on [η] of dilute polydisperse discs in biaxial extension.

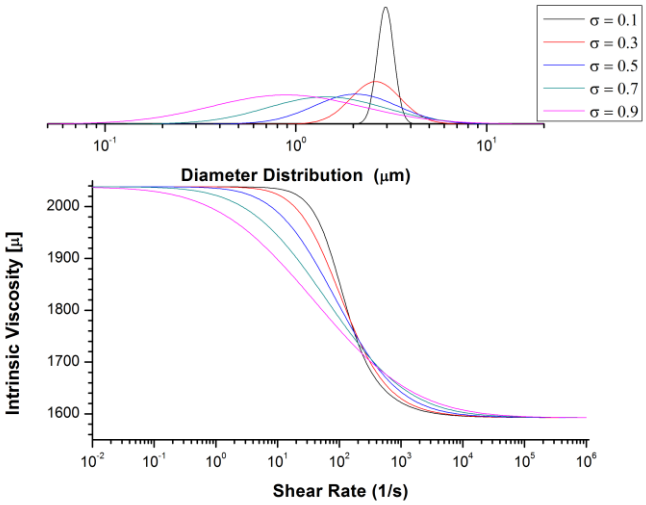

Figure 5-17. Effect of σ on [η] of dilute polydisperse oblate spheroids in biaxial extension.

5.4.4 Other distributions: Bimodal and Gaussian

We demonstrate the versatility of our modeling approach to any general distribution (other than lognormal) by simulating a dilute bimodal colloidal distribution of Gaussian modes in 50%:50% proportion under shear flow, as shown in **Figure 5-18**.

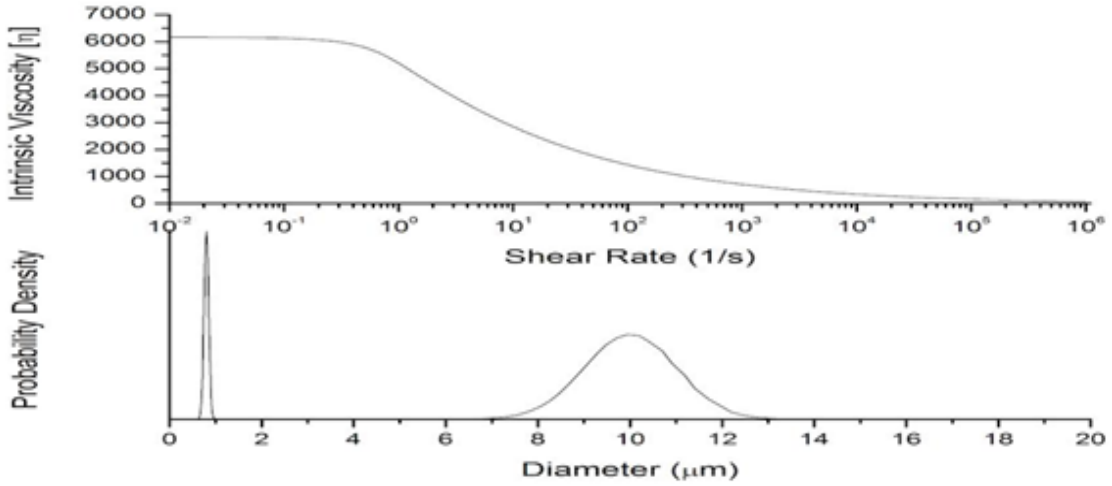

Figure 5-18. Shear results for a dilute 50%:50% bimodally-distributed colloidal dispersion of Gaussian modes centered at ~1 μm and 10 μm, with $\sigma = 0.50$ and t = 1 nm.

It is noted from **Figure 5-18** that the behavior of the bimodal distribution is qualitatively similar to that shown by the lognormal distributions of previous sections. In order to highlight the effect of the bimodal distribution, we thus varied the proportion of big: small particles in the distribution as shown in **Figure 5-19**. This reveals an interesting result; when we introduce a few big particles into a sea of small particle in dispersion (e.g.: 90%:10%), our results predict that we should see a large jump in [η], coupled with the appearance of two distinct regions of shear-thinning: one at low shear-rates, corresponding to the fraction of smaller particles, and other at higher shear-rates, corresponding to the complementary fraction of bigger particles. These results imply that a dilute bimodally-distributed colloidal system is rheologically insensitive to the bimodality of the distribution at low relative concentrations of small particles, but conversely sensitive to low relative concentrations of big particles. This observation can be explained in a simple manner based on the preceding discussion in section 5.3.2 that the modeling approach used is biased towards big particles (with higher volume fraction ϕ_i) at the expense of the smaller ones. Since the modeling approach was rigorously shown to be sound in section 5.3.2, this bias is also expected to be genuine and experimentally observable upon measuring [η] for such systems.

The simulation results also imply from a practical standpoint that a bimodal distribution consisting primarily of small particles and a small percent (~5-25%) of big particles should show two characteristic onsets of shear-thinning, thus enabling us to experimentally detect the bimodality of such a system through rheological measurements of shear-thinning without needing to know any additional experimental data (e.g.: from images) about the system under study. For a bimodal system consisting dominantly of big particles, however, our results imply that we need to have apriori knowledge about the bimodal nature of the system under study from other non-rheological techniques such as imaging and light scattering in order to model the system as such.

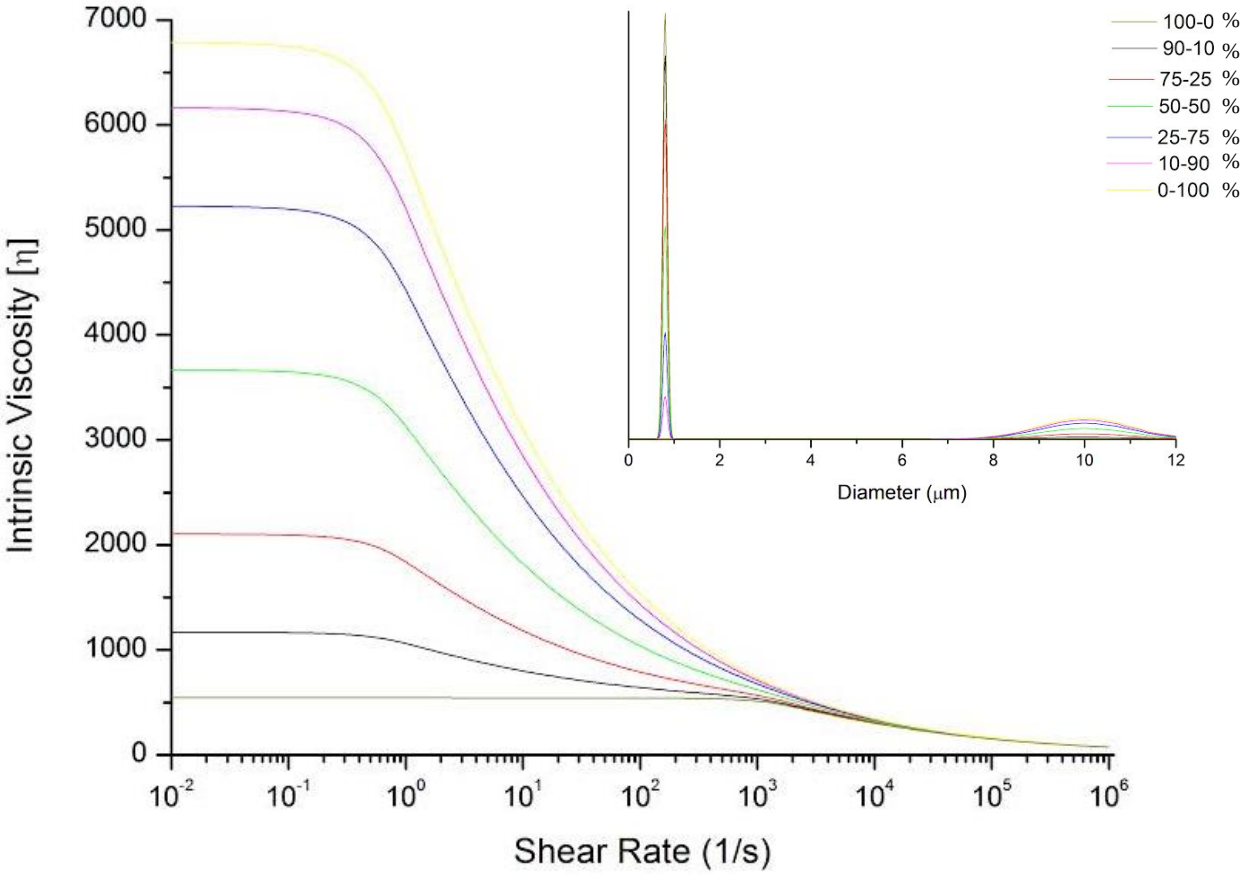

Figure 5-19. Shear results for a dilute bimodally-distributed colloidal dispersion of Gaussian modes centered at ~1 μm and 10 μm, and the response of such a system to variations in the relative % of small-big particles (inset).

5.4.5 Modeling Thickness and Thickness Distribution

Until now, our modeling approach has assumed that the thin oblate spheroids (or sheets) are monodisperse in thickness. In this subsection, we relax this condition to investigate the properties of a system polydisperse in both lateral size and thickness. This will be accomplished by making two assumptions:

1) The particle thickness exists on a continuous distribution. This is a reasonable assumption, given uncertainties in thickness measurement, as well as variations in the degree of surface chemistry and hydration layer thicknesses, if any, between particles within the same sample. This is shown to be true for GO in Chapter 4, for instance, where we do not see a set of discrete multiples of a single monolayer thickness (e.g.: 0.335 nm for single-layer grapheme), but rather a complete spectrum of values ranging from ~0.4 nm to ~2.0 nm, and hence it justifies representing the system as a continuous distribution when needed.
2) The thickness of a given nanoparticle is statistically uncorrelated to the particle diameter, or it is weakly correlated such that said correlation can be safely ignored. This was shown to be the case for GO in Chapter 4, and it helps simplify the modeling problem at hand. In any case, making this assumption helps us avoid the problem of having to measure the distribution via other non-rheological means (to determine such a correlation, that is, where it to exist) before using our rheological method to measure and model the system.

A polydisperse thickness in the case of GO, for example, would then be the result of multiple sheets stacking on top of each other to create thicker particles, i.e.: particles that have not been fully exfoliated. We denote the number of monolayer sheets in a stack as l, and apply this method to Equation (5-15) to yield the following Equation:

$$[\eta] = \frac{3}{2\pi}\int_{t_{min}}^{\infty}\frac{1}{t}\Omega(t)\int_{Di}^{\infty}\Omega(D)\ D\ f(D)\,dD\,dt \tag{5-42}$$

where, t_{min} is the minimum physical thickness for the system under study (0.335 nm for a graphene monolayer), $\Omega(t)$ is the t distribution function represented as a normal distribution, and f(D) comes from (5-6).

$$\Omega(l) = \frac{1}{\sigma\sqrt{2\pi}} \exp\left(-\frac{(t-\mu)^2}{2\sigma^2}\right) \tag{5-43}$$

We shall be using the normal distribution as a model thickness distribution, because we were able to show in Chapter 4 that it accurately describes a distribution of GO sheets. **Figure 5-20** shows the effect of polydisperse thickness on 2-D extensional rheology of a system of suspended oblate spheroids. Given a σ_t of 0.5, we see a marked increase in [η]. This can be explained by considering the effect of thickness on the monodisperse model; in our formulation (5-42) where [η] is inversely proportional to thickness t. Hence, when we attempt to account for polydispersity, the tail of smaller-than-average particles tends to dominate the equation, raising [η] on average. For example if one third of the particles in a suspension are 1 nm thick and the remaining two-thirds are 2 nm thick, then due to the inverse relationship, the "effective thickness" present in dispersion would be a harmonic mean of these two modes, yielding a halfway value of 1.5 nm, even though there are more of the 2 nm than the 1 nm particles in dispersion. The resultant [η] would thus also be a simple average value between [η] for the 1 nm monodisperse model and that for the 2 nm monodisperse model, even though the dispersion is concentration-dominated by the latter. This is what causes the effect simulated in **Figure 5-20**.

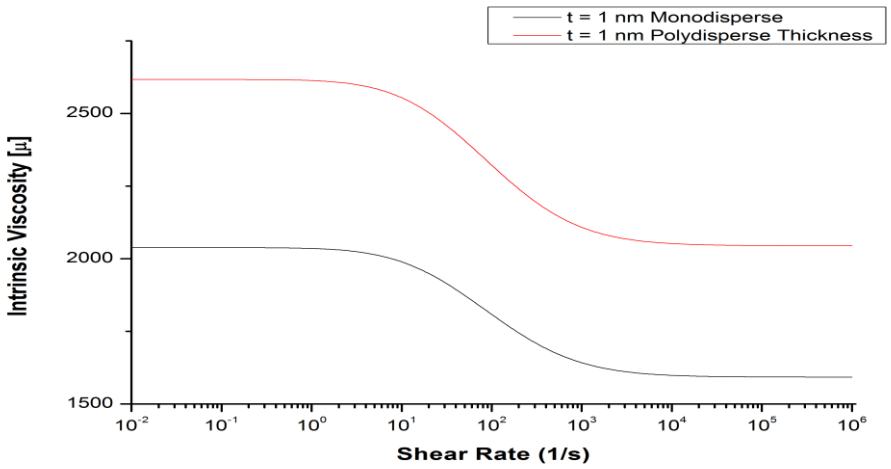

Figure 5-20. Effect of a polydisperse thickness on 2-D extensional rheology**.**

The preceding example highlights a limitation of our modelling approach regarding thickness determination: since the model is biased towards the thinner particles in the system, the value estimated in this way for t will be unrepresentative of the population. Moreover, this means the model is not sensitive to thick outlier particles that may exist in dispersion. In other words, our model is able to selectively capture the behaviour of the thinner particle in dispersion at the cost of sensitivity towards thicker particles and outliers in the data (which may be foreign or incompletely-exfoliated particulates). While this enables us to predict the thickness of the thin sheets in dispersion, the estimate we will obtain in this way is unlikely to be sample representative.

Figure 5-21, which we include for completeness, illustrates that the effect of changing the mean thickness on [η] for the same system depicted above. The increase in mean thickness causes a rise in [η], qualitatively similar to the effect of increasing the monodisperse thickness on [η] for a monodisperse sample.

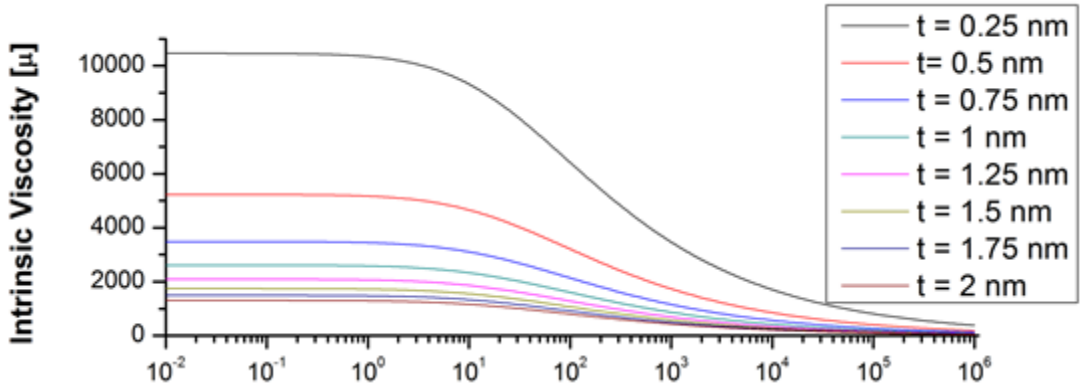

Figure 5-21. Effect of changing the thickness polydispersity on [η] in a system under shear flow.

Yet another complication is introduced by comparing **Figure 5-20** and **Figure 5-21**; the effect of changing the mean thickness on [η] is qualitatively very similar to that of changing the polydispersity. This means that in interpreting a given set of experimental rheological data, it is not possible to decouple the effects of mean and standard deviation of thickness from each other and make accurate estimates of these two quantities for a particular sample. This problem was not encountered with modelling polydispersity in lateral dimension, because each of the modelling parameters in the latter case led to unique effects on [η] and could be decoupled from the rest of the parameters in the equation. Thickness, on the other hand, appears in only one place in the denominator of all of the preceding equations and so it is difficult to break it down into informative constituent parameters such as mean and standard deviation.

Based on the preceding discussion, our attempt to model polydispersity in thickness has afforded us significant insight into how our model responds to changes in the particle thickness, and it can thus be recommended to keep thickness a single parameter in the model without attempting to account for polydispersity (which will keep the model parameters at an acceptable number of three: μ, σ and t) and to interpret this estimate of t as being biased to the thinner sheets in dispersion.

5.4.6 An Alternative Formulation of Intrinsic Viscosity

The classical formulation of $[\eta]$ assumes that η can be expanded in terms of a power series in ϕ, with higher order terms corresponding to particle contributions adding to the solvent viscosity η_0:

$$\eta = \eta_0 + \eta_0[\eta]\phi + \eta_0 B\phi^2 + O(\phi^3) \tag{5-44}$$

However, the form of Brenner's equation (5-4) suggests an alternative formulation where η might be expanded as a power series in terms of number concentration *n* instead of ϕ:

$$\eta = \eta_0 + \eta_0(\eta)n + O(n^2)$$

$$(\eta) = \lim_{n \to 0} \frac{\eta - \eta_0}{\eta_0 n} \tag{5-45}$$

where, (η) can be called the innate viscosity. All the conditions and derivations applicable to $[\eta]$ are applicable to (η) (i.e.: all conditions in terms of ϕ become conditions in terms of *n* instead). Now, from Brenner (1974), we can make the following statement for a particle fraction i in a distribution:

$$\frac{\eta - \eta_0}{\eta_0 n b^3} = f(D_i)$$

$$\frac{\eta_i - \eta_0}{\eta_0 n_i} = {D_i}^3 f(D_i)$$

$$(\eta)_i = \lim_{n_i \to 0} \frac{\eta_i - \eta_0}{\eta_0 n_i} = {D_i}^3 f(D_i) \tag{5-46}$$

Then, for a discrete polydisperse distribution, we arrive at the following expression which is analogous to (5-10):

$$(\eta) = \frac{\sum_{n=1}^{j} n_i (\eta)_i}{\sum_{n=1}^{j} n_i} \tag{5-47}$$

Switching to a continuum model yields the following equation:

$$(\eta) = \int_0^\infty \Omega(D)\ D^3\ f(D)\ dD \tag{5-48}$$

The advantages of this model (5-48) are the following:

1) - (η) requires measurement of number concentration n and not volume fraction ϕ. Number concentration can be tracked using techniques such as nanoparticle tracking analysis (NTA), flow cytometry, dynamic light scattering (DLS), laser diffraction, etc and requires less sample by mass on a per measurement basis than ϕ; the latter requires measurement of density (ρ), which can be both time-consuming and introduce significant inaccuracies to calculations since ϕ, and [η] by extension, are ρ–sensitive and ρ can vary significantly on a sample-to-sample basis.

2) – Secondly and more importantly, the continuous polydisperse model has been reduced from three to two parameters, μ and σ. t has been eliminated from the model, since its information is contained in the combination nD^3, where n is a measurable quantity and was re-shuffled to the LHS of (5-48) into (η), while D^3 was moved to RHS, where it already appears as a parameter in several locations.

Thus, (η) provides an alternative formulation for the analysis of experimental rheological data. In Chapter 6 on experimental rheology, we rely exclusively on [η] and (5-14) to model η, simply because we were able to experimentally measure ρ but not n.

5.5 General Comments and Conclusions

To summarize, we were able to model polydisperse dilute dispersions of oblate spheroids and discs in shear, uniaxial and biaxial extension. Generally, it was observed that shear and biaxial extension both result in shear-thinning, while uniaxial extension results in shear-thickneing. This is understandable; an oblate spheroid or a sheet (unlike a prolate one or a fiber) has a morphology closer to 2D than 1D. Shear and biaxial extension are, by their nature 2D flows, and so oblate spheroids will tend to line up parallel to these flows in suspension. Uniaxial extension, on the other hand, is a 1D flow. Unable to line up parallel to the flow, oblate spheroids and sheets will tend to line up orthonormally, resulting in high drag on the particles and the simulated shear-thickening effect.

A common phenomenon observed across all flows is proportionality of [η] to D, coupled with inverse proportionality to t (i.e.: proportionality to aspect ratio a). This was

commented on and explained in the sections above; the higher the aspect ratio, the greater the influence of the particles in obstructing these three flow systems per particle, and hence the higher [η]. Secondly, more shear-thinning/thickening is observed for bigger particles than smaller ones, because the former align from a state of greater Brownian angular inertia to/against the flow field in place. Finally, a signature broadening of the [η] response was observed in response to increasing polydispersity σ, an expected phenomenon whose explanation follows immediately from the preceding observation on response of [η] to D. This signature broadening in [η] can thus, in turn, be used to try and capture the polydispersity of a distribution of oblate spheroids or discs.

Our modeling approach was shown to be versatile by using it to simulate lognormal, Gaussian and bimodal distributions of particles. By modeling a bimodal distribution, it was demonstrated that the presence of a small fraction of big particles increases [η] for a dilute dispersion of small spheroids significantly and introduces two distinct regions of shear-thinning corresponding to the two modes; this is justified by the model being more sensitive to big particles. Finally, an attempt was made at modeling thickness, but it was shown that it was practically not useful to model polydispersity of thickness because it is not possible to decouple the qualitatively similar effects of mean and standard deviation of thickness on [η]. It was also shown that the value of t estimated by the model is biased towards the thin particles in dispersion. It was thus recommended to leave t in the model without attempting to model polydispersity, thus maintaining the number of model parameters as three, while the estimated t is taken to be representative of the thinner particles in dispersion rather than being globally sample-representative.

Building on these simulation results, we will be using (5-22 to model experimental shear rheology data on a number of samples, and this will be the subject of the next Chapter. The choice of shear rheology was made based on the availability of equipment and the ability to conduct experiments, but in principle, uniaxial and biaxial extensional experiments could also be performed on dispersions to augment shear rheology results.

Chapter 6: Dispersion Rheology application to sheets

6.1 Introduction and Method

As discussed in Chapter 5, the problems with classical particle size characterization techniques stem from several reasons, some of which are summarized below:

1) - the inability of some of these techniques to handle the entire range of a size distribution e.g.: nanoparticle tracking analysis, fluorescence quenching microscopy, etc.

2) - sensitivity to particle outliers; especially light scattering-based techniques.

3)- high cost-to-sampling ratio on some techniques e.g.: atomic force microscopy (AFM), where it takes around 18 working hours to coat, image, analyze and extract size data on a sample of 50-100 nanoparticles, which might arguably be sample unrepresentative).

In this chapter, we use Equation 15 from Chapter 5 to model shear rheology data from four nanosheet systems to demonstrate the advantages offered by rheology to conventional size estimate techniques in the three areas mentioned above:

1) Commercial Graphene Oxide (GO), ~500 nm in size
2) Comparison of commercial GO before and after sonication
3) Measurement on GO synthesized by the Tour method (~1 μm in size)
4) Literature case: layered double-hydroxides dissolved in water with polyacrylamide.

Regression was conducted using a MATLAB-assisted numerical method, an approach commonly used for the calculation of a minimum for an objective function (algorithm shown in **Figure 6-1**, MATLAB code included in Appendix). The algorithm relies on submitting an initial guess of number-average particle diameter (D), standard deviation in D (σ) and number-average thickness (t). The initial guesses of D, t and σ are then used to generate an estimation of [η] against shear-rate. The estimate is used to evaluate a sum of squared errors (SSE), which is used as a cost function in the fitting algorithm. We have chosen to adopt the Nelder-Mead method to fitting due to its simplicity of

implementation in Matlab's environment. This algorithm updates our initial guesses and runs until a minimized SSE is obtained.

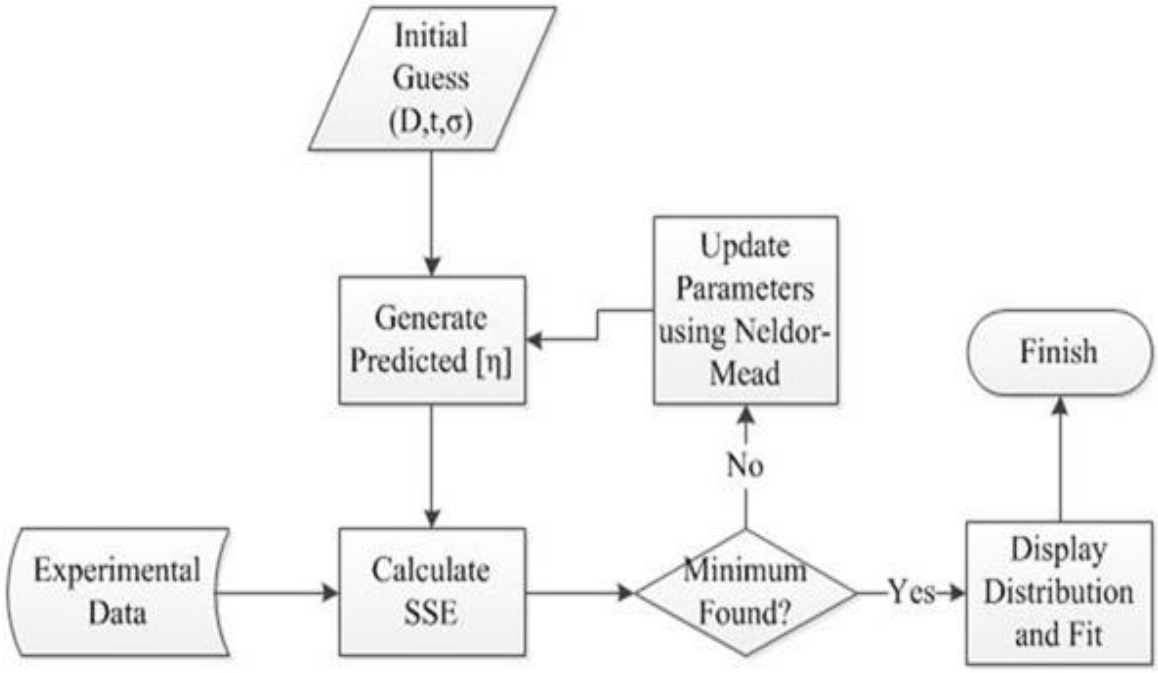

Figure 6-1. Regression analysis algorithm using Nelder-Mead numerical method used to infer distribution parameters from [η] shear rheology data for a given dilute disc dispersion.

The regression approach described above was tested using an experimental dataset of aqueous GO synthesized using the modified Tour-Dimiev (MTD) method, described in Chapter 3. The results obtained from this sample will be presented and discussed at length in following sections, but for now, we point out that the model was found to converge on the dataset in spite using a number of different initial guesses of D, t and σ. The results of this analysis are shown in Appendix B. This consistency of fit regardless of initial guesses used provides good evidence supporting the validity of the regression method used to obtain the results in the following subsections.

6.2 Experimental Section

Materials

Commercial 0.50 wt% aqueous GO dispersion (N002-PS) was purchased from Angstron Materials (Angstron Materials, 2015). The concentration was verified by drying-and weighing. Angstron reported a lateral dimension of 0-1100 nm (number-averaging 550 nm) and thickness 1.0-1.2 nm based on laser diffraction and AFM data respectively. Lab-synthesized GO was made using Tour's synthesis – the procedure for synthesis was discussed in Chapter 3.

Rheology

GO concentrations for the rheology experiments was selected such that the suspension viscosity is ranged from about 10-20% above the solvent viscosity to roughly twice the solvent viscosity. The lower end of the range was selected to minimize the influence of the subtraction error with the solvent viscosity when calculating the inherent viscosity. The higher end of the range corresponds to the volume fraction threshold for inter-particle interaction $\phi*$ and can be estimated more rigorously using the simple correlation $\phi* = \frac{t}{D}$ (van der Koiij et al., 2001) based on reasonable initial guesses for a and b respectively.

A serial dilution scheme was followed, starting with the highest concentration and moving down to the lowest one. Moreover, to prevent GO morphological changes and shear-induced aggregation from introducing significant measurement errors to viscosity and concentration, each of the more dilute dispersions was sheared once and not used to make further dilutions (see Appendix A for additional detail).

At each concentration, the shear viscosity of the dispersion was measured using DHR3 strain-controlled rheometer (TA Instruments) by carrying flow-sweep experiments over shear rate range of 1-100 s^{-1} in a DIN Couette fixture (Titanium bob and 316 stainless steel cup, height 42 mm, cup diameter 30 mm, bob diameter 28 mm, torque sensitivity 5 nN.m). The shear-rate range was chosen based on the torque sensitivity limit of the

instrument at the low end and the onset of Taylor instabilities and GO aggregation at the high end (see Appendix B). The use of a vapor trap helped maintain a saturated environment within the test fixture thus preventing evaporation-induced solvent losses. The bob was used with three iterations of rotational precision mapping (10 min each) at the start of a typical measurement. To minimize errors introduced by the operator's sample-loading technique, the sample was loaded to 22 mL each time using a mass balance rather than a measuring cylinder to ensure the highest possible degree of consistency, since the balance gives more precision in measurement.

AFM

GO dispersions (unsonicated and sonicated) were spin-coated at 3000 rpm for 30s onto freshly-cleaved mica (Electron Microscopy Science) followed by overnight vacuum drying at 50^{o}C. AFM images were obtained in AC mode using a Digital Instrument Nanoscope III Multimode AFM at a scan rate of 1.00 Hz over areas of 1-10 μm. Cantilevers were z-calibrated prior to scanning each sample by using them first to scan HF-etched mica (see Chapter 4).

Images were post-processed and used to estimate the lateral dimension and thickness using image analysis softwares: ImageJ and Gwyddion respectively. Image digitization in ImageJ and a MATLAB code was used to measure the areas (A) of the GO sheets and estimate equivalent circular diameter D_{eq} ($D_{eq} = 2\sqrt{A/\pi}$, which will simply be referred to as D in the sections that follow) in order to enable systematic comparisons of lateral size with the characterization results from other techniques, such as AFM. Experimental details on the coating and image analysis routines are discussed in Chapter 4. The thickness was estimated by taking line traces of the GO nanosheets along the longest dimension versus the surrounding mica background and considering the difference between the two to correspond to the layer thickness.

6.3 Results

Case Study A: Commercial GO

Figure 6-22 shows the η of aqueous commercial GO as function of shear-rate and ϕ. The higher ϕ display significant shear-thinning, as expected for systems above the interaction threshold ϕ^*, estimated to be at 2.00 mg/mL based on the GO size reported by the manufacturer (D = 550 nm, t = 1.1 nm). This is consistent with the observation that samples at lower concentrations (going up to 1.25 mg/mL) show limited shear-thinning (**Figure 6-22** inset) as a result of particle alignment with the shear flow, with a large amount of shear-thinning observed at 2.50 mg/mL.

As a result, the lower concentrations in **Figure 6-22** were exclusively used to estimate the specific viscosity (η_{sp}), which is defined as $(\eta-\eta_s)/\eta_s\,\phi$, and can be thought of as a measure of the incremental change of dimensionless viscosity (i.e.: the relative viscosity, $\eta_{rel} = (\eta-\eta_s)/\eta_s$) with nanoparticle loading ϕ. This gradient-like nature of η_{inh} makes it a more sensitive function of shear-rate than η. Thus based on the inset of **Figure 6-22**, we generated a set of curves of η_{sp} versus ϕ in **Figure 6-23**(a) corresponding to behavior at different $\dot{\gamma}$. The linearity of these curves in the inset of Figure 6 indicates that the chosen ϕ are indeed all well within ϕ *. It is also noted that the results from the two trials performed on this GO sample give very similar results, as shown by the error bars in **Figure 6-22**, indicating success of the serial dilution scheme used to measure replicates.

Neldor-Mead regression was performed on the [η] versus shear-rate data using model (5-14), enabling estimation of the sizing parameters (**Figure 6-23**(b)). **Figure 6-24**, in turn, shows the AFM and size distribution results for the spin-coated GO, indicating an average size and thickness of 352 nm and 1.1 nm respectively, with polydispersity σ of 0.47. The lateral size data were fit with a lognormal distribution, and when goodness of the fit was tested using the normality test of Anderson and Darling (1954), the data was seen to obey a lognormal distribution (as shown in Chapter 4).

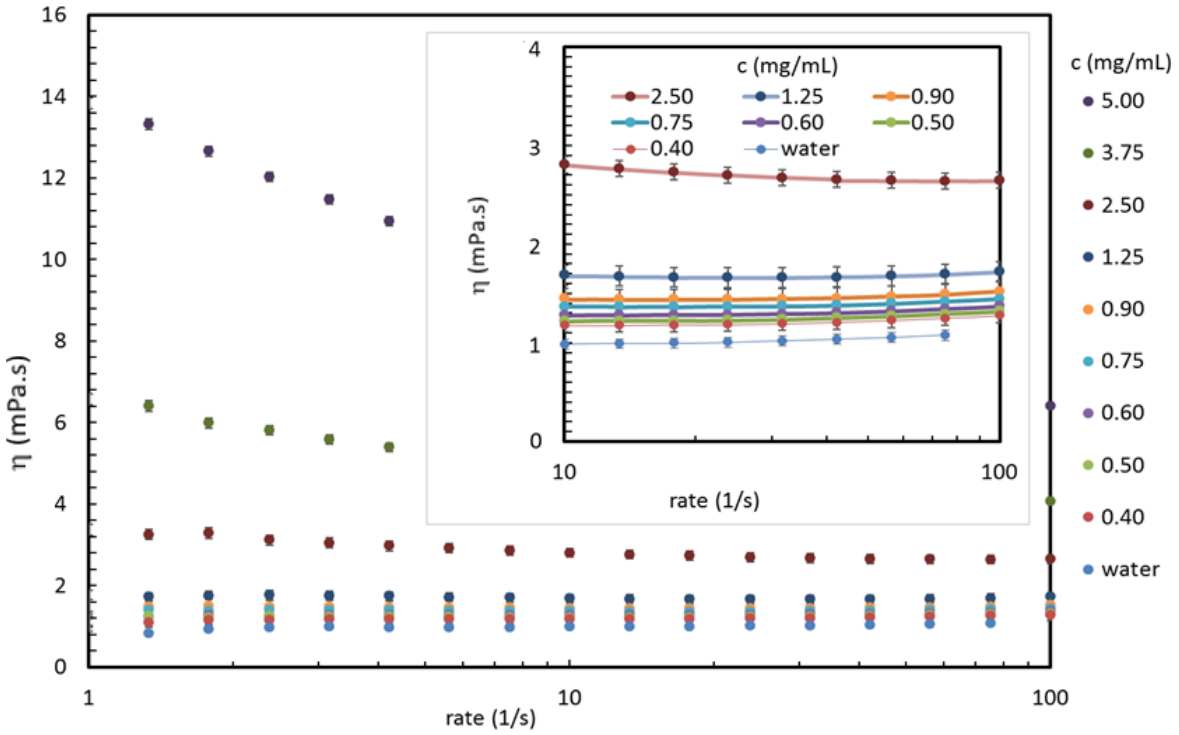

Figure 6-22. η vs shear-rate for commercial GO dispersed in water at various c (mg/mL). Two replicates were obtained at each c, following the serial dilution scheme method described in the experimental section and detailed in Appendix B, yielding consistent results, as seen by the error bars. This higher c show shear-thinning due to inter-particle interaction, while the lower c (inset) displays limited shear-thinning, due to GO alignment to shear flow.

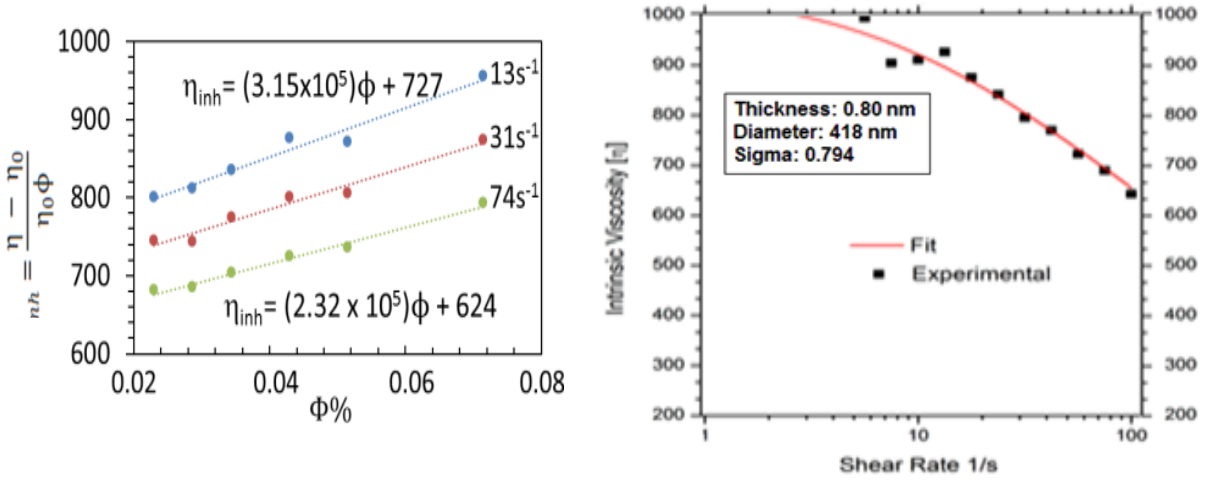

(a) (b)

Figure 6-23. (a) Specific viscosity (η_{sp}) plotted against ϕ for commercial GO at three shear-rates; the intercepts correspond to [η] at each shear-rate, which were in turn plotted in (b), which also shows the fit using regression analysis to Equation 15.

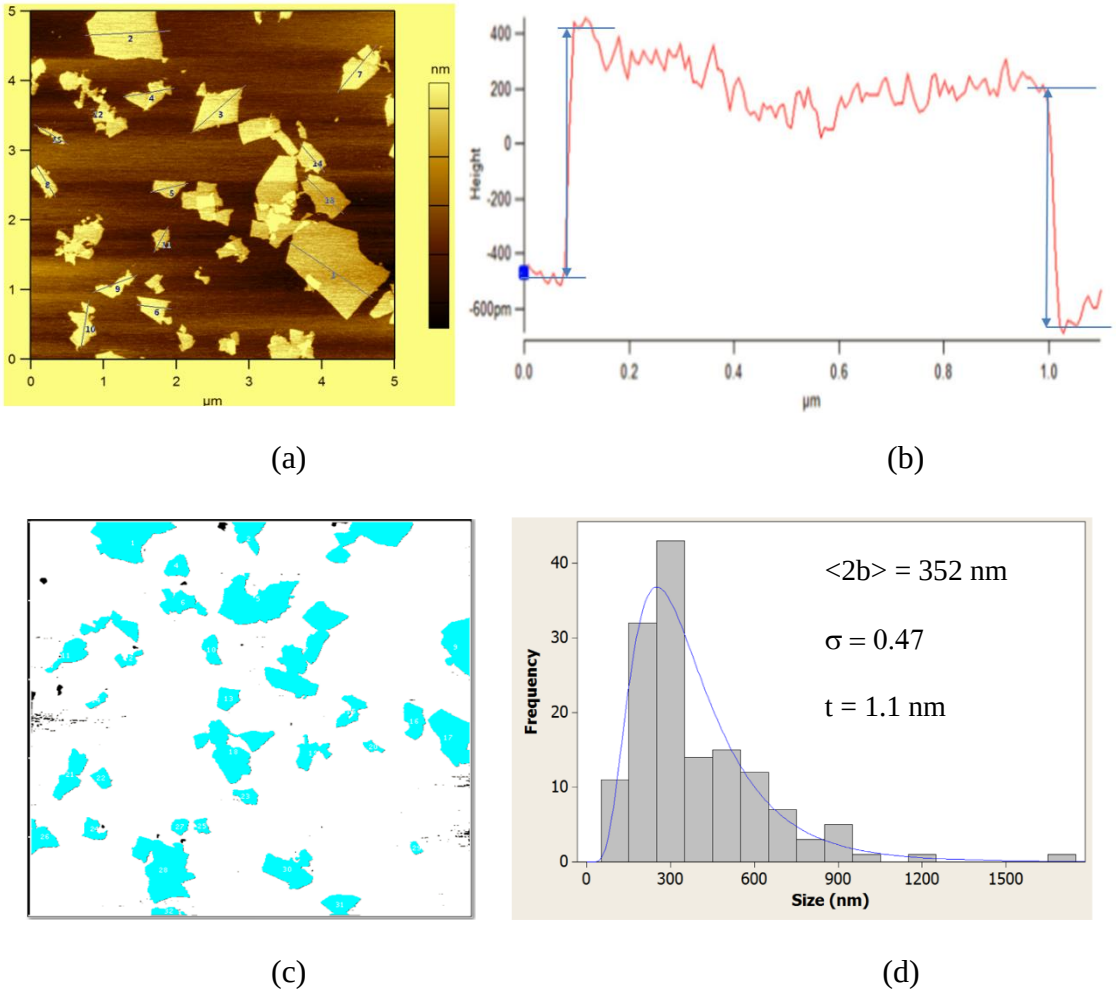

Figure 6-24. AC mode AFM of GO on freshly-cleaved mica with line traces across for thickness estimation (shown in (b)). Images were digitized using ImageJ analysis software (c) and used to estimate a distribution of equivalent diameters, shown and fitted to lognormal distribution in (d).

Case Study B: Unsonicated vs Sonicated Commercial GO

In this case study, particle dimensions were estimated from rheology and compared to AFM image analysis results for unsonicated and sonicated commercial GO samples. The AFM results (**Figure 6-25**) do not show a marked qualitative difference between the two samples. A quantitative analysis of about 100 imaged particles per sample using ImageJ indicates that the GO size distribution was changed, albeit not very significantly, by sonication. Rheology, on the other hand, reveals significant qualitative sample variation due to sonication, with η at 5 mg/mL dropping threefold after sonication (**Figure 6-26**(a),

inset). Although it lies above ϕ^* of unsonicated GO, a concentration of 5 mg/mL was chosen for the comparison because it highlights the effect of sonication, a process expected to shift in nanoparticle distribution to lower sizes. It is notable that **Figure 6-26**(a) shows deviation from linearity in η at higher concentrations as expected due to the onset of interparticle interactions. This behavior was consistently observed across samples, and these high ϕ at which the curve becomes non-linear were ignored in the estimation of $[\eta]$, where we typically used the first 3-4 linear points to calculate intercepts.

The regression analysis (**Figure 6-26**(b)) yields $\langle 2b \rangle \simeq 305$ nm and $\sigma = 0.45$ post-sonication, consistent with our expectation of size reduction. $< t >$ was estimated to be 0.49 nm, indicating what appears to be a reduction in thickness post-sonication. Considering that sonication is capable of raising local temperature in the vicinity of GO sheets to ~5000 K, this observed decrease in sheet thickness could be because probe-sonication supplies the sheets with sufficient energy to cause some of the physisorbed (and possibly even the chemisorbed) OH and epoxy groups to detach, leading to an overall reduction in thickness. A decrease in surface concentration of oxygen-containing groups could potentially also lead to a weaker and thinner hydration layer surrounding the GO sheets as a result of decrease in hydrophilicity, which would further explain the observed thickness dropped. Finally, and perhaps most plausibly, this observed drop could be the simple result of sonication-induced sheet exfoliation. It is noteworthy that this reduction in sheet thickness was observed in the results of the AFM image analysis as well, which was shown in Chapter 4.

The conclusions from this case study are: 1) - shear-rheology can be used to qualitatively detect size changes to GO after sonication similarly to AFM, 2)- shear rheology also allows for quantitative comparison of the GO before and after sonication. Both of these are useful features both for GO quality control as rheology thus provides characterization of size for an application of interest following sonication.

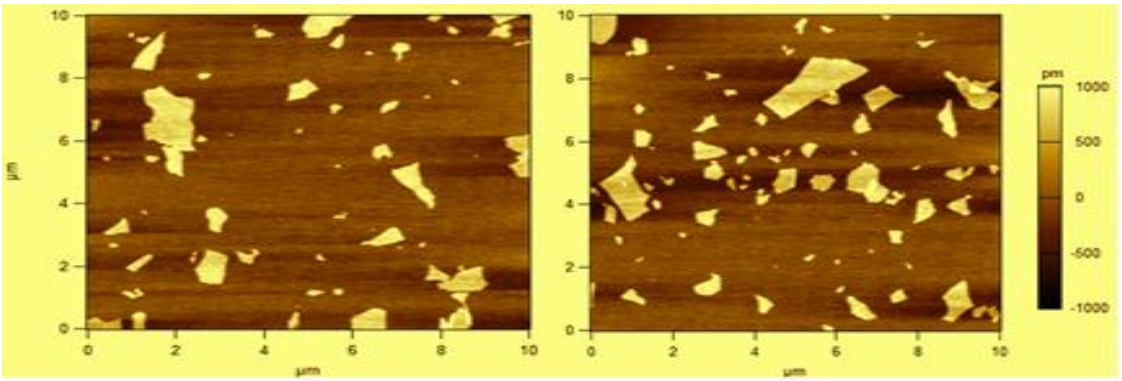

(a)

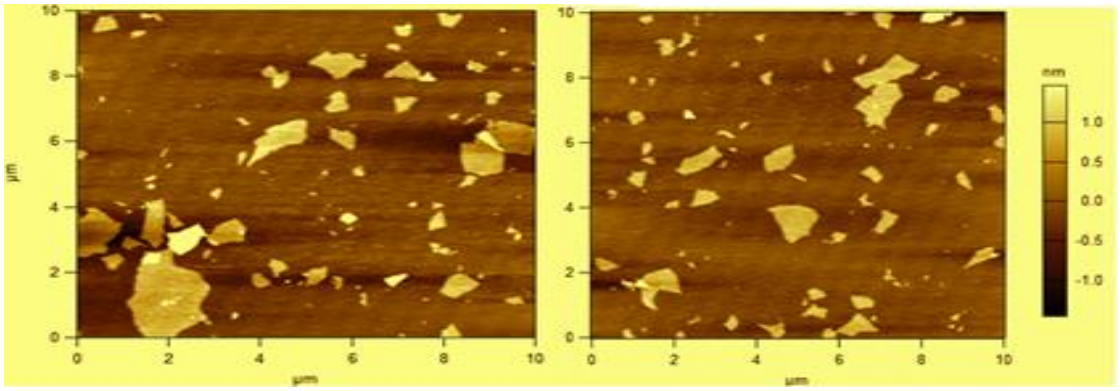

(b)

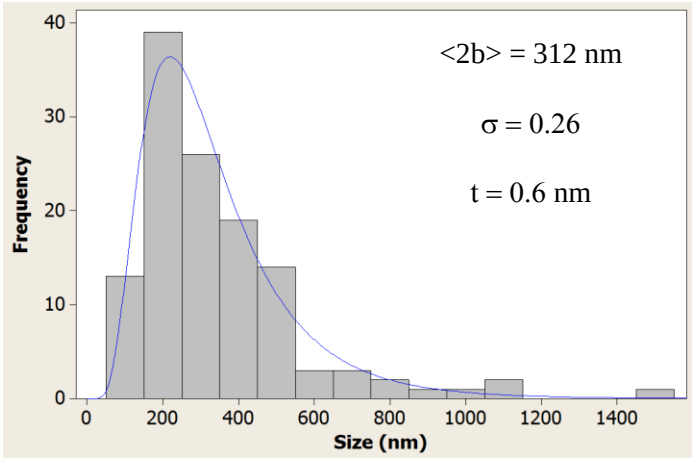

(c)

Figure 6-25. GO before (a) and after (b) sonication on freshly-cleaved mica, showing little discernible morphological variation and size reduction. This is confirmed quantitatively by obtaining particle distributions and fitting them to lognormal distributions (c), indicating a shift to lower particle sizes.

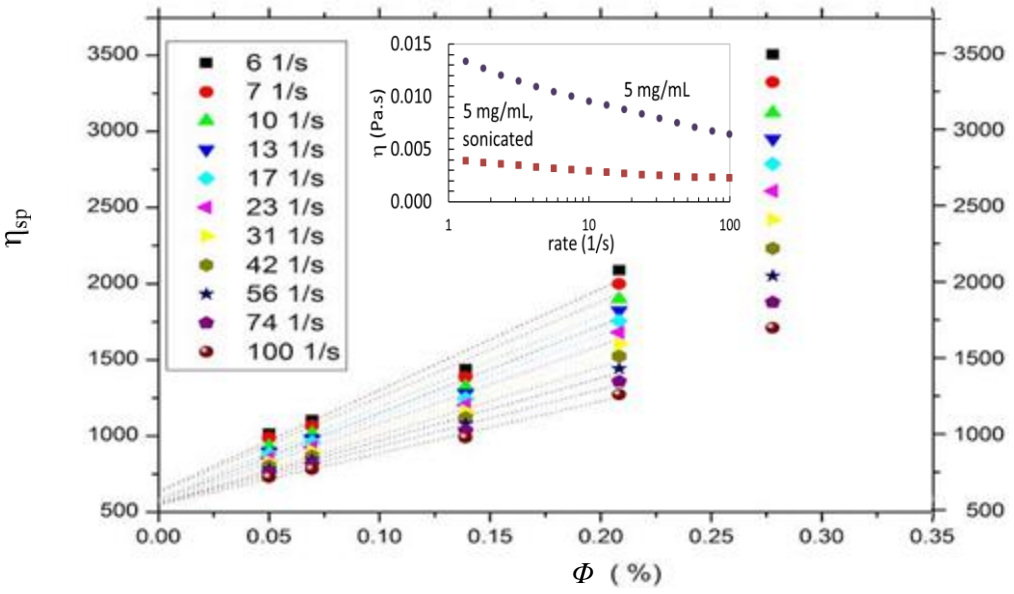

(a)

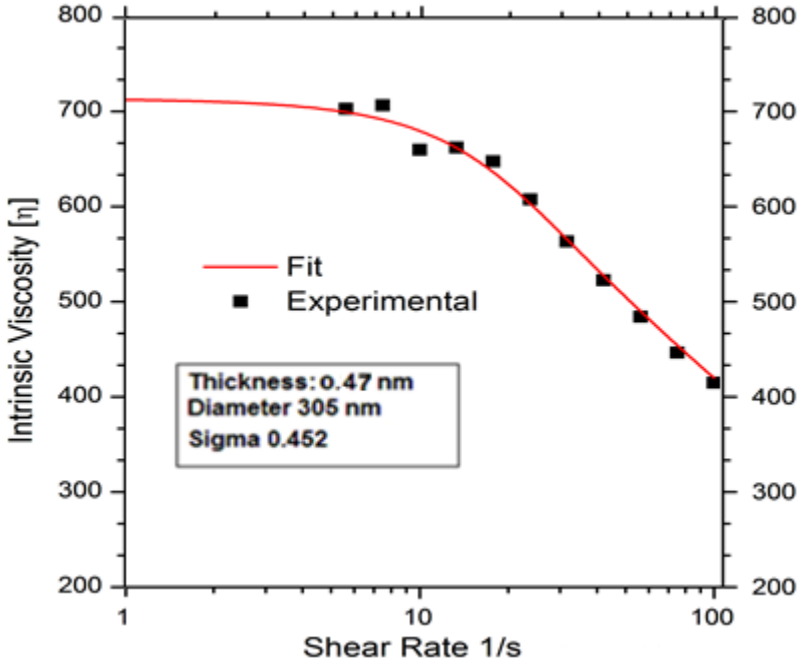

(b)

Figure 6-26 (a)-Inset compares η for commercial GO at 5 mg/mL before/after sonication showing a threefold drop in η, which corresponds to a shift in nanoparticle distribution towards smaller sizes. The main Figure shows the η_{sp} results for the sonicated sample, while shows (b) fitting results for [η].

Case Study C: Lab-Synthesized GO

To further demonstrate the versatility of our rheology technique, we used it to analyze lab-synthesized modified Tour-Dimiev (MTD) GO (**Figure 6-27**) and compared these results to sizing from FQM and AFM image analysis (**Figure 6-28**(a) and (b)), combined to yield particle statistics on the entire distribution (**Figure 6-28**(c)). Details of how FQM and AFM were used to independently obtain and later splice size distribution data for this GO sample were presented in Chapter 4. The comparison of rheology to imaging results yielded <D> = 738 nm for rheology compared to <D> = 1.34 μm for imaging. The big polydispersities calculated using these two techniques (σ = 0.81 and σ = 0.91 respectively) mean that these estimates are overlapping.

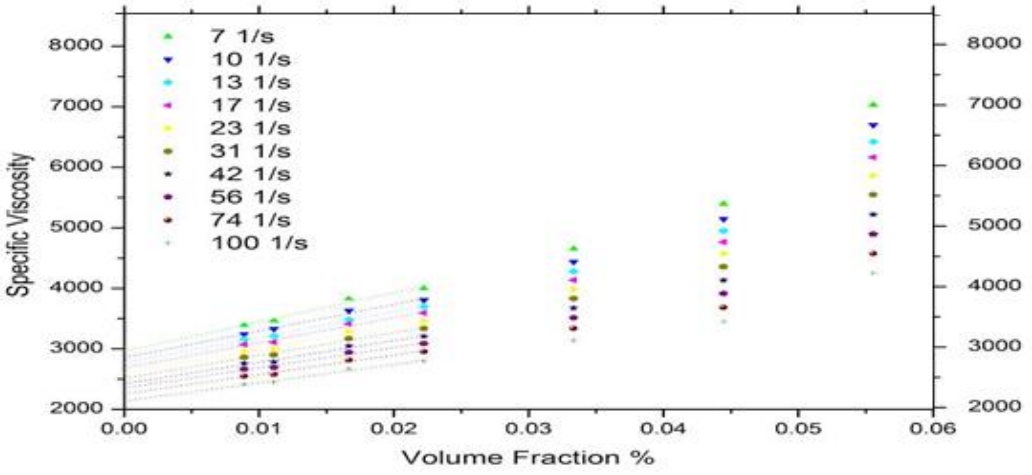

(a)

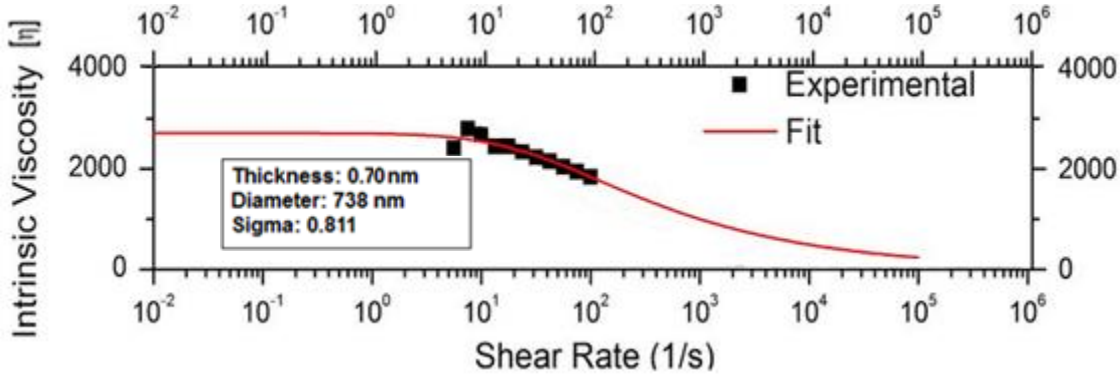

(b)

Figure 6-27. Shear rheology data for MTD GO. The η_{sp} data in (a) is used to construct the [η] vs shear-rate plot in (b), which is then fit to yield nanoparticle statistics.

This case study highlights the main issue typically encountered in the imaging and image of polydisperse particles, namely the inability to capture all particle sizes using FQM or AFM alone; FQM is limited in terms of optical resolution (>350 nm) and magnification (100x in our case) and is as such unable to resolve smaller particles, while AFM on the other hand can resolve particles on the length scale of nm, but is limited at the high end because image resolution and contrast can drop if the scan area is more than 30 μm x 30 μm, which means it is cumbersome to obtain a statistically representative size distribution for the population under study (especially since some particles may be too big to fit within a given AFM area scan, as previously argued in Chapter 4).

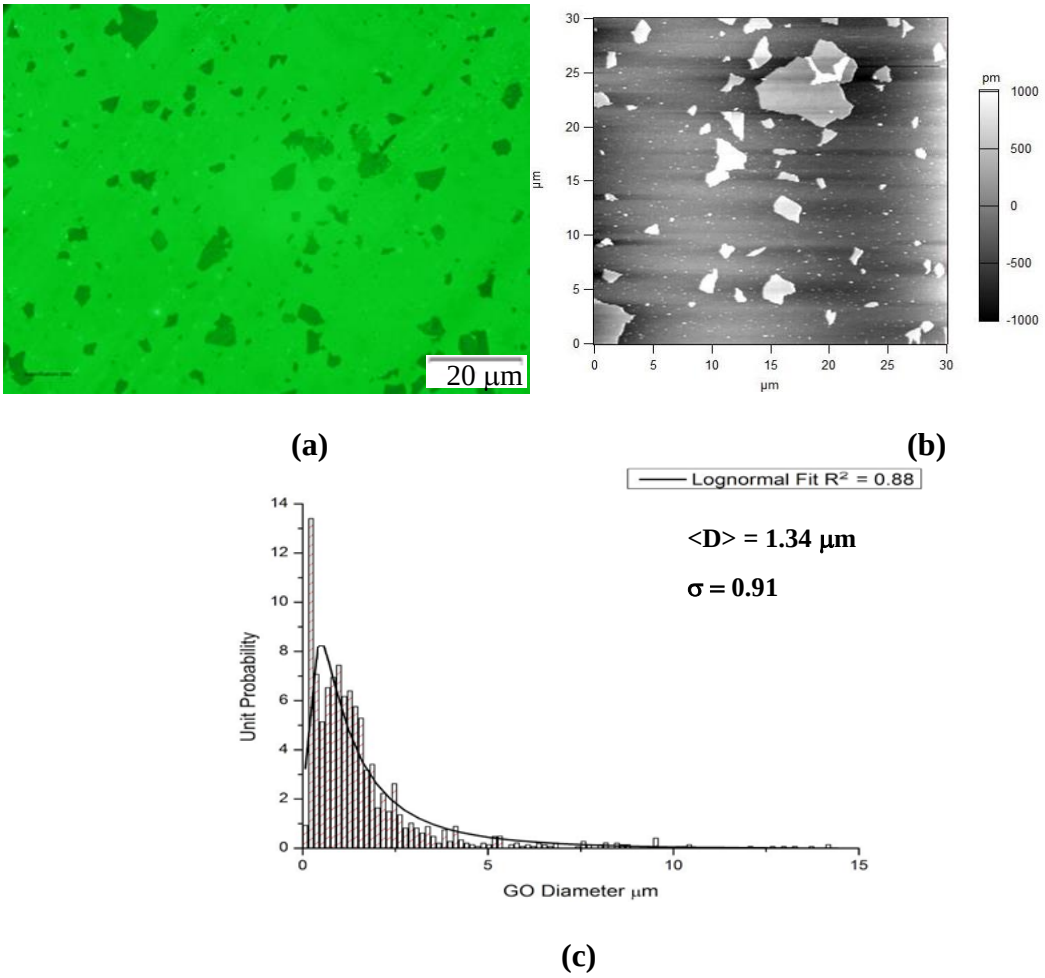

Figure 6-28. (a) Size statistics on MTD GO coated on freshly-cleaved mica. Statistics on the big particles were provided by FQM in (a), for which resolution level is >350 nm (scale bar = 20 μm), while smaller particles were counted via AFM (b). This data was integrated to create the size histogram shown in (c), with< D > = 1.34 μm, σ = 0.91.

For this reason, we recommend performing both FQM and AFM in-parallel to capture both big and small particles respectively, then combining these results into a representative distribution as we did in **Figure 6-28**(c). This process can be time-consuming, both from the acquisition and analytical perspectives, taking ~24-48 hrs of analysis time per sample, and it serves to highlight the need for techniques like shear rheology to quickly characterize the size distribution parameters for an entire population of GO and similar sheet systems (the next case study shows an example of the latter).

It is worth commenting that this data set was used as an internal consistency check of sorts to verify the validity of the model (5-14) used to represent the rheological data. This was done by taking the discrete size distributions from Chapter 4 (**Figure 4-19**, **Figure 4-20**, and **Figure 4-21**) and using them to generate simulation curves of [η] against shear-rate via a combination of the monodisperse shear rheology model (5-6) and the discrete polydisperse model (5-12). This was used to generate the set of curves shown in **Figure 6-29**. To enable comparison, the rheology data and regression analysis performed using Equation (5-14) were re-plotted in **Figure 6-29**. Examining **Figure 6-29** reveals a number of interesting observations:

1) The FQM-simulated rheology curve (**Figure 6-29**(a)) is higher than the all of the other simulation curves and real rheology data. This is expected since FQM is successful at visualizing all the big GO particles, while being limited in resolution at the low end to ~350 nm. Moreover, we have already established that the rheology model is biased in lateral size to big particles. Both of these factors contribute to this elevated curve.
2) The AFM-simulated rheology curve (**Figure 6-29**(b)) tracks the experimental data more closely than the FQM curve, possibly because the GO population is dominated by the smaller AFM-detectible sheets, so AFM could be providing a more realistic statistical representation of the population. In other words, it might be that the number of big sheets undetected by AFM is too small to significantly skew sample rheology.
3) The splice-simulated rheology curve (**Figure 6-29**(c)) provides the best tracking of the experimental data. This might be the result of the spliced distribution being more realistic than either of the FQM and AFM distributions at representing data, which could be taken to indicate the success of our splicing approach to imaging MTD GO.

4) It seems that the splice-simulated curve (**Figure 6-29**(c)) appears to be displaced an axis-shift from the experimental data, but otherwise tracks the data well. This axis-shift could be attributed to one or both of the following two reasons:

   (a)- It could be an artifact resulting from the acircularity of real GO sheets, while the rheology models used assume circular discs. The presence of sharp corners and edges on GO sheets could confer something akin to a modified diameter on the sheets, or change the nature of the solution to the governing model (Equation 5-8) altogether; Brenner (1974) warns of potential issues resulting from treating sharp-edged objects in dispersion as if they were as flow-disruptive as regular, blunt-edged particles (e.g.: spheroids). However, it is interesting to note that except for this observed axis-shift, even an acircular system as GO is still closely mimicked by Brenner's solution for thin hard oblate spheroids.

   (b)- This apparent axis-shift could also be caused by issues in modeling GO as hard discs in dispersion; by accounting for a soft hydration shell adhering to the sheet surface, this might change the density value inputted into the model sufficiently to account for the axis-shift (density influences volume fraction φ and so would manifest as a y-shift).

5) Finally, it is interesting to note that all the image-simulated rheology curves either intersect with or closely follow the rheology data. This indicates a consistency between the results obtained from rheology and those obtained from image analysis, and gives us confidence in the all-round validity of both sets of results at describing GO size statistics.

Finally, to underscore the ability of our proposed rheology technique at estimating particle size for quality control purposes, we include a case-study in Appendix B for an identically synthesized MTD GO sample which yielded very similar results to those obtained from the first batch, producing $\langle D \rangle$ = 674 nm, σ = 0.86 and t = 0.82 nm. This replicate experiment demonstrates simultaneously the viability of our proposed rheology technique at QC characterization, as well as batch-to-batch rheological consistency for replicates of the same synthesis protocol. The entire data acquisition and analysis process for each of these batches takes around 8-12 hrs to measure 3-4 sample concentrations.

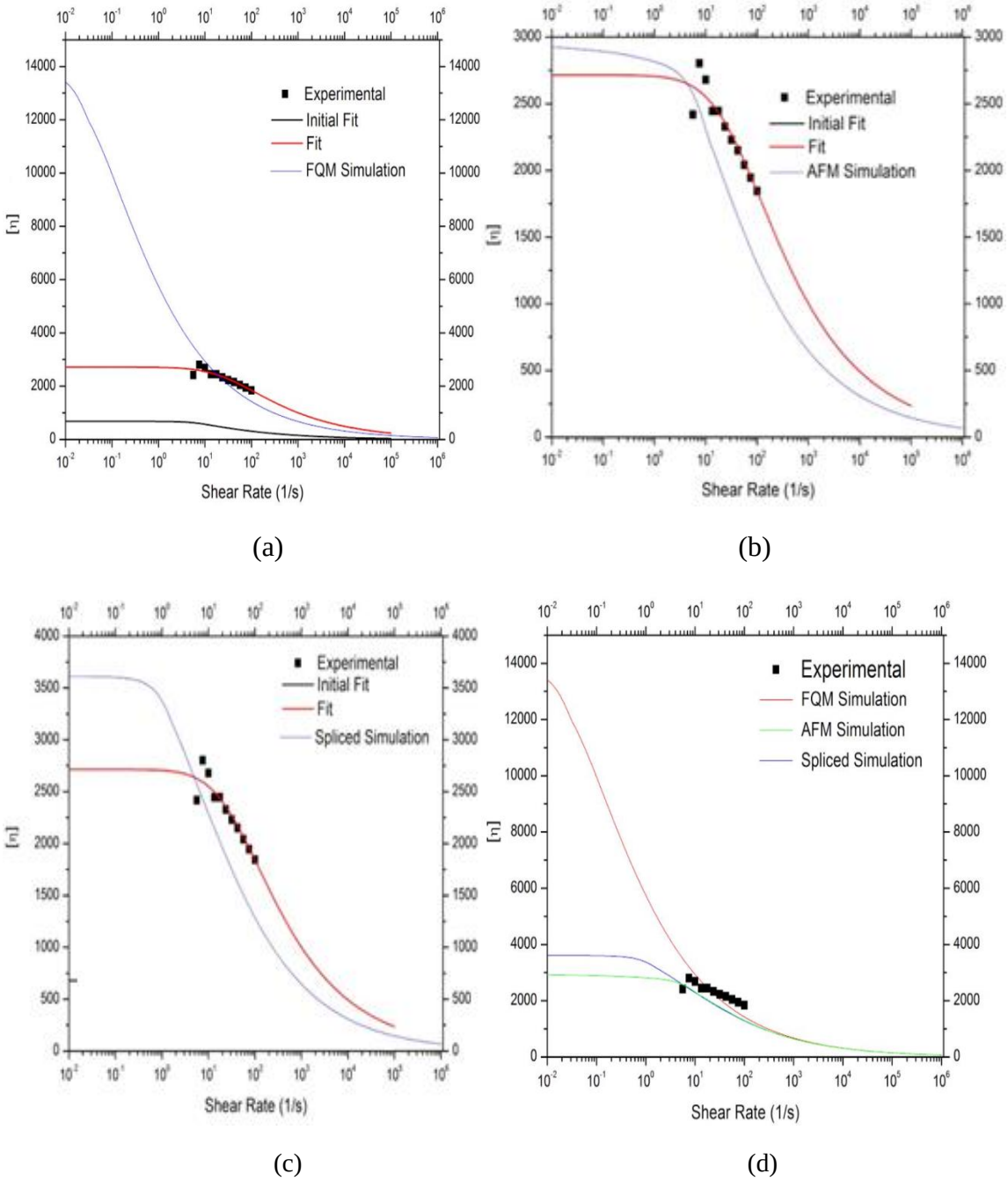

Figure 6-29. Simulated rheology curves of [η] vs shear-rate obtained using image-analysis data on MTD GO (Figures 4-16, 4-17 and 4-18), the shear model equation (5-8), and the discrete polydisperse model equation (5-12). Rheology data and regression curves obtained using equation (5-15) are also shown in Figure (6-11) for comparison. (a)- FQM-simulated curve (based on Figure 4-16), (b) - AFM-simulated curve (based on Figure 4-17), (c) - spliced-simulation curve (based on Figure 4-17), (d)- summary plot.

Case Study D: Double-layered Hydroxides and polyacrylamide in water

To investigate the ability of the model to describe the behavior of general sheet systems, we considered a paper by Hu and Chen (2014) on the rheology of double-layered hydroxides in dispersion in water. The experiment was performed by the authors using the parallel-plate geometry of an AR-2000 rheometer. Polyacrylamide was used to increase sample viscosity. This helped increase the torque for accurate sensing by the AR-2000 force transducer. The data is presented in **Figure 6-30**(a), while **Figure 6-30**(b) shows the results of extracting [η] from **Figure 6-30**(a) and subsequent regression, which yields D = 128 nm, σ = 0.60 and t = 0.55 nm. The diameter estimate compares favorably to the size distribution statistics measured by the authors for the nanoparticles using DLS and SEM respectively, which gave D estimates of 40-60 nm and 20-180 nm, respectively (DLS size lognormal distribution results from the study are shown in **Figure 6-31**, based on which an average size of 50 nm and σ = 0.82 were estimated for the sample). Even though the authors do not expressly measure t for their system, they do demonstrate using XRD data that their layered system has been delaminated prior to rheological analysis, and it was recorded in the literature by Ali et al. (2012) that the thickness for delaminated double-layered Mg/Al-NO_3 hydroxides (the system under study) is typically around 0.48 nm, consistent with the prediction by rheology.

This simultaneously demonstrates the versatility of our technique to measure the particle size distribution of a system analyzed in a different geometry (parallel plates, as opposed to the couette cell) and containing a non-Newtonian matrix in the form of the polyacrylamide polymer. We attempted to subtract out the non-linear influence of the polymer from η for each dispersion in the η_{sp} calculation by subtracting the black curve in **Figure 6-30** from each of the colored curves to obtain results that are consistent with the size characteristics for the sheets under study. Inherent to this analysis is the assumption that the polymer does not introduce a high enough level of interaction with the sheets to significantly and non-linearly change the mechanism of shear-thinning experienced by the system due to particle alignment in shear flow. The parallel-plate geometry is also not ideal for making such measurements because it introduces the risk of

particles gradually settling and thus migrating away from the shearing surface. These might be the issues behind the difference in estimate between rheology and DLS results. It is worth mentioning that even considering the above issues and in spite of the observed difference from DLS results, the size parameters estimate from rheology for the layered double hydroxide system are physically realistic by comparison with DLS. However, it is recommended for best results to use this approach only with particle dispersions in Newtonian media and to perform the measurements in a couette cell.

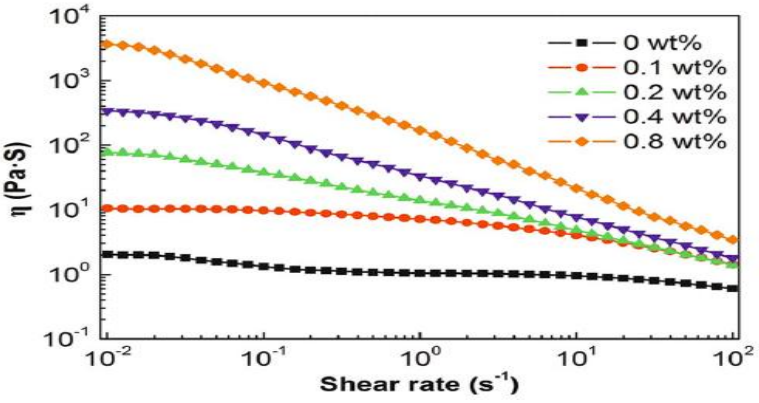

(a)

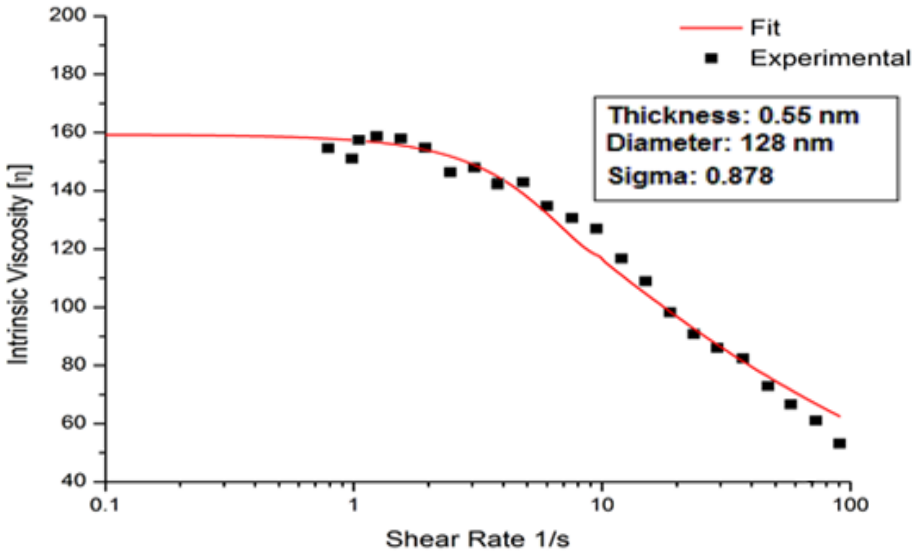

(b)

Figure 6-30. (a) Figure excerpt from Hu and Chen (2014) for shear data on layered double-hydroxides and polyacrylamide dissolved in water, (b) [η] extracted and analysed.

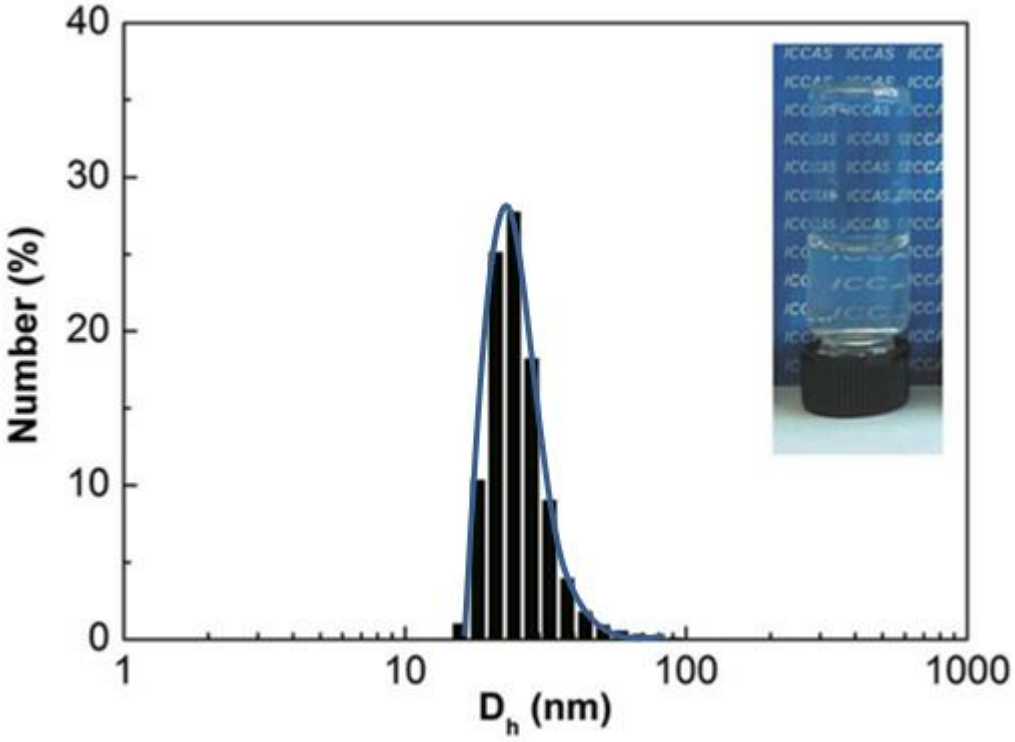

Figure 6-31. DLS size distribution from Hu and Chen (2014) on double-layered hydroxides dispersed in water. Data is fit to a lognormal distribution (blue line).

Summary of Results and Comments

The key results of this chapter for the four analyzed samples (commercial unsonicated and probe-sonicated GO, MTD GO are summarized in **Table 6-1**, with the corresponding microscopy results presented in (**Table 6-2**).

Table 6-1: Summary of shear rheology and microscopy/DLS results for the four samples (GO-C: commercial, GO-C-P: probe-sonicated, GO-MTD: modified Tour-Dimiev GO, Double-OH: layered double hydroxides (DLS results were used in the case of double hydroxides). The result in parenthesis is not explicitly measured but deduced based on literature estimates from Ali et al. (2012), as explained in case study D.

Sample	<D> (nm)		σ		t (nm)	
	Rheology	Imaging/DLS	Rheology	Imaging/DLS	Rheology	Imaging/DLS
GO-C	418	352	0.79	0.47	0.80	1.1
GO-C-P	305	312	0.45	0.26	0.38	0.50
GO-MTD	738	1343	0.81	0.91	0.70	1.3
Double-OH	128	50	0.88	0.82	0.55	(0.48)

It can be seen that there is a good degree of consistency between shear rheology and microscopy for all the systems under investigation which is a good indication for the potential of rheology as a quick and versatile quality control GO characterization method. It is noticed that our rheological technique consistently yields smaller particle thickness results than the corresponding microscopy results; this is not only true for all the GO samples, but also for the literature-reviewed layered double-hydroxide sample, for which we estimated from shear rheology data a thickness (0.55 nm) comparable to the smallest possible thickness found in the literature for delaminated monolayers of this material (~0.48 nm). This underestimation of thickness by rheology was attributed to a number of reasons: 1)- most importantly, we think based on a discussion in section (5.4.5) that our rheological model is biased towards the thinner sheets in a given dispersion, and 2)- for GO sheets, the smallest possible thickness is that of a graphene monolayer (0.335 nm) which, being suspended in aqueous medium for the duration of a rheology experiment, might be surrounded by a hydration layer, thus increasing this minimum sheet thickness to the 0.70-0.80 nm observed in rheological measurements (a similar argument can be made for delaminated and hydrated layered double-hydroxides, resulting in the t estimate of 0.55 nm). The consistently low t estimates for the sonicated commercial GO sample from both rheology and AFM were attributed to the possibility of sheets partially losing their surface oxygen groups (and consequently losing part of the attached hydration layers, if any).

On the other hand, there could be inaccuracy in the AFM measurements of GO layer thickness. The calibration of AFM cantilevers for z-dimensional measurements was described in Chapter 4, and it was found out that there is an inherent uncertainty of at least 0.2-0.3 nm in these measurements even under controlled conditions (this was shown by measuring 1 nm steps on an HF-etched mica wafer, as per the procedure described by Nagahara et al. (1994)). It could thus be the AFM measurements that are responsible for the observed discrepancy with the rheology estimates.

Another observation in the results is that the rheology-measured polydispersity is generally higher for all the samples than its image-measured counterpart, except for the MTD GO, where rheology and imaging yield polydispersities of 0.81 and 0.91

respectively. This is thought to be due to a simple reason; the average size and polydispersity of the MTD GO, as indicated by the image analysis, are thought to be high enough that the shear-thinning transition region is not captured as adequately by the rheology data as it is for the smaller sized commercial samples. In other words, it may be that the shear-thinning onset (which corresponds to the alignment for the smallest sheets in dispersion) might be masked by the presence of significantly bigger sheets, given the higher polydispersity of such a system. Since we know that the rheology measurements are likely biased towards the big sheets in dispersion, this might be a reasonable assumption to make. In the measurement of big-sized, highly polydisperse samples, it might thus be advisable to work on improving the experimental resolution especially at lower shear-rates e.g.: collecting more data at lower shear-rates, using double-couette geometry to attain higher sensitivity. This will enable the collection of good quality data at lower shear-rates and will help resolve the issue described above.

6.4 Conclusions

In this work, we were able to successfully demonstrate the use of rheology to characterize the aspect ratio of a number of nanosheet systems (GO and layered double hydroxides) using simple shear flow sweep experiments on serially-diluted samples. This technique used a shear-thinning model for oblate spheroids obtained based on the literature to represent the particle dispersions under study, and accounting for polydispersity of the dispersed particles in this model. It was possible to infer a number of size and distribution properties on the nanoparticle population via application of regression analysis to the theoretical models to fit the experimental shear data, yielding physically realistic fitting parameters. The entire data acquisition and analysis process for each of these batches takes around 8-12 hrs to measure 3-4 sample concentrations; three points would be sufficient to construct a straight line of credible fit, while a fourth point would help verify linearity or reveal non-linearity due to onset of particle interactions, if existent.

As a proof of concept, results from this approach were compared to those obtained via AFM for size distribution for a commercial GO sample before and after probe-sonication.

Before and after sonication, the two techniques yielded comparable estimates of the GO lateral size, with both methods yielding yielding statistics that reflect a shift in particle size towards smaller sizes. This indicates the potential of rheology as a quality-control technique that is suitably sensitive to particle size variation.

The technique was also shown to be effective in estimating the size on a challenging, highly-polydisperse lab-synthesized modified Tour-Dimiev (MTD) GO sample, yielding ~738 nm, which was shown to be consistent with the estimate from FQM and AFM images. A similar estimate was obtained for a batch synthesized under identical conditions, once again demonstrating the quality-control potential for this proposed rheological method. Finally, we used our rheology technique to estimate size characteristics based on rheological data found in the literature on a more complex system consisting of layered double-hydroxide (sheets) dissolved with polyacrylamide in water. The estimate obtained was ~128 nm, consistent with TEM and DLS characterizations done by the authors on their sample, and thus further asserting the versatility of our propsed technique for experimental characterization and quality control. The experimental drawback of this technique is our current difficulties in sensitively measuring and interpreting shear rheology data at low ($< 1s^{-1}$) shear-rates. These obstacles are by no means insurmountable, however, and we suggest some ways of dealing with them at the end of the previous section without adding significant cost in terms of data acquisition and analysis times. The theoretical drawback of our approach is its reliance on a piecewise function as the model to represent shear rheology data, which can generate computational errors in fitting experimental data while trying to patch two pieces of a function, and can thus also lead to a higher computational time than if the representation was by a single continuous function. A more accurate closed-ended equation from fluid mechanics relating viscosity to the dimensions of an oblate spheroid is expected to improve the accuracy of the distribution estimates obtained from this method, which already shows a good level of promise in its current form.

Chapter 7: New Insights into the Interfacial Assembly of Graphene Oxide Films

7.1 Introduction

Graphene's excellent combination of physical properties, such as its high mechanical strength shown by Lee et al.. (2008), 97.7% optical transparency shown by Sheehy and Schmalian (2009), and high charge carrier mobility as shown by Bolotin et al.. (2008) give graphene-based materials a wide array of applications and uses in electronics, energy storage, and polymer composites as described by Stankovich et al.. (2006). A potential application of graphene oxide (GO) is for thin films of transparent conductors made from reduced GO; therefore an overarching goal of this project is the production of film coatings from GO nanosheets. These exfoliated GO sheets are dispersion-processable in water and a fundamental property of GO nanosheets is their ability to float at the air-water interface, described as "amphiphilicity" by Cote et al.. (2009); the basal plane primarily consists of polyaromatic islands of unoxidized domains giving a hydrophobic contribution, whereas the hydrophilicity is given by the carboxylic rich edge groups. Greater electrical conductance can potentially be attained in part through the production of large GO nanosheets on the order of tens to hundreds of microns, with Zheng et al.. (2011) showing that large GO nanosheets reduce the amount of inter-sheet contact resistance. We can produce large-sized nanosheets through modifications in the chemical synthesis (discussed in Chapter 3) and the literature suggests that control of the film structure and packing can be achieved through manipulation of the Langmuir monolayer at the air-water interface. The controlled packing of GO nanosheets affects both conductive properties and the processability of films for industrial applications. Therefore, this chapter will focus on the assembly of controlled GO structures packed at the air-water interface. We present a detailed investigation of the behavior of these sheets at the air-water interface, as well as their potential for coating applications based on the Langmuir-Blodgett technique. In order to better present and discuss the details and implications of our Langmuir-Blodgett (LB) work, a brief summary of influential research pertinent to the interfacial assembly of GO films as measured through pressure-area isotherms is presented.

7.1.1 Literature Review

Cote et al.. (2009) demonstrated the assembly of single layers of chemically exfoliated graphite at the air-water interface. This was shown through correlations between pressure-area isotherms and film morphology (5-20 μm). These correlations are inferred through careful study of supported films fabricated through the Langmuir-Blodgett technique. Pressure-area compression/expansion curves express a high degree of 'surface activity', which is partially explained by looking at the fundamental interacting geometries and assessing colloidal stability according to the classical DLVO theory. Cote also provides a traditional Langmuir physical description and vocabulary involving the transition from a gas, condensed liquid, to a solid film. Furthermore, upon multiple compressions, percolation onset has a gradual transition to lower surface areas, which is attributed to material overlap. Isotherm hysteresis is observed at higher monolayer compression, however, a possible explanation is not provided.

Imperiali et al.. (2012) in an assessment of GO film stability has shown that during isotherm cycling, material is rearranged at the surface much like tiles at a liquid interface. This is contrary to previous studies as described by Cote et al.. (2009) and Zheng et al.. (2011), which state that material is lost through partial overlap. Nevertheless, once GO sheets are at the interface, they are irreversibly trapped according to an estimate on the energy of detachment, $E_{det} \sim (10^5 - 10^7)k_BT$ calculation for GO sheets of lateral dimensions ranging from 100nn to 1μm. They also argue that due to the relative acidic conditions of the subphase, low dissociation of functional groups is expected. Therefore, film formation at the interface is primarily due to interface-specific forces such as lateral capillary waves or line tension effects. A variety of isotherms are presented and in an effort to characterize pressure-area isotherms, they have fitted the Volmer equation of state for particles at interfaces for liquid-expanded states ($\Pi < 22$ mN/m)

Botcha et al.. (2014) show that pressure-area curves are highly sensitive to acidic conditions of the subphase. They show that percolation onset in negatively correlated to pH subphase conditions. In support to the initial claims by Cote et al.. (2011) they attribute the differences in the pressure-area curves for the various levels of pH to variations in sheet size, which is directly related to the level of sheet ionization. Two

main assertions are employed to explain the progression in the pressure-area isotherms: (a) acidic subphase results in "large densities of unionized GO sheets of low hydrophilicity at the surface", meaning that larger GO sheets would tend to remain at the interface. (b) Basic subphase conditions allow for partial overlapping among GO sheets aided by water-molecule lubrication; however, due to the enhanced ionization, there is a stronger repulsive interaction upon monolayer compression.

7.1.2 Contributions

A review of the literature reveals that questions remain about the fundamental mechanisms of GO nanosheet assembly at the air-water interface. In this chapter we focus on two important considerations in the use of GO nanosheet Langmuir monolayers for the preparation of thin films on solid substrates. 1) We will assess how films pack along different directions due to uniaxial deformation of a conventional Langmuir trough. 2) We will analyze the "intrinsic" surface activity of GO nanosheets. Our experimental approach employs a conventional Langmuir trough outfitted with two surface pressure sensors (tensiometers) to assess the anisotropic and inhomogeneous nature of GO nanosheet surface packing as well as the process of loading the air-water interface with GO and the impact of pH concentration. Additionally, our studies will utilize *in situ* Brewster Angle Microscopy (BAM) and Fluorescence Quenching Microscopy (FQM) *ex situ* to understand and correlate film packing and morphology with pressure area-isotherms.

7.2 Experimental

7.2.1 Materials

GO synthesized by the modified Tour-Dimiev (MTD) method and characterized in Chapters 3, 4 and 6 was used to generate the Langmuir monolayers for all the experiments that follow.

7.2.2 Characterization

7.2.2.1 Langmuir-Blodgett Assembly

Π-A isotherms were obtained using a NIMA Langmuir trough (Coventry, England) with dual barriers for symmetric compression (schematic shown in **Figure 7-1**). To reduce contamination and spurious results due to air-flow the Langmuir system is placed in a small enclosure. It was reported by Imperiali et al.. (2012) that trough geometry contributes to the shape of the Π–A isotherms. Therefore, we note that with barriers fully open the maximum trough area is ~65 cm^2 and the trough width is 7 cm. All experiments were done using a subphase of 18 MΩ·cm and pH of 6.7 from water prepared using a Direct Q3 filtration system (EMD Millipore Corporation, Billerica, MA). Prior to GO deposition at the air-water interface, the trough was cleaned with an Alconox solution, followed with careful chloroform treatment. To ensure cleanliness, barriers were compressed, and did not rise above 0.1 mN/m for pure water. GO was deposited as described in Cote et al.. (2009) using a Hamilton syringe (Reno, Nevada). All experiments were carried out using two NIMA PS/4 surface pressure sensors (filter paper Wilhelmy plates) positioned at the center of the trough. A compression speed of 20 cm^2/min was used and GO depositions of 0.313 mg from a stock sample of initial concentration 2.67 mg/mL diluted in methanol to 0.125 mg/mL.

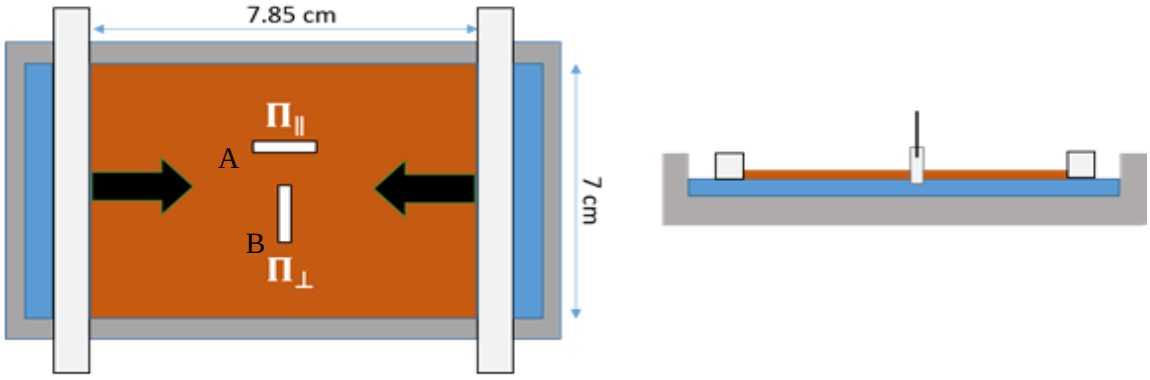

Figure 7-1. Schematic of Langmuir trough setup. Top-down view shows the two simultaneous Wilhelmy plates recording surface pressure in perpendicular orientations. Plate orientation is in respect to the direction of compression, or long trough axis. Tensiometers are referred to as A and B based on their locations in the trough.

7.2.3 Imaging

Brewster Angle Microscopy (BAM) images were taken with an Accurion EP3 BAM coupled to a NIMA BAM Langmuir trough. The quoted resolution of the BAM is ~ 1 micron. As above, this entire system is enclosed in a Faraday cage. Fluorescence Quenching Microscopy (FQM) images were taken with a Fluorescence microscope (Olympus IX-71 microscope and Retiga EXi cooled ccd camera). Experimental procedure is the same as described by Kim et al.. (2009) and is briefly summarized. Typically, 1 mg of green fluorescent dye and 1 mg of PVP is added to 10 mL of ethanol solution. Magnetic stirring can be used to keep solution homogeneous. A coating deposition of 100 microliters of solution per 0.5 inches squared of substrate area. A spin coater is used with rotation speeds ranging from 400 – 4000 rpm.

7.3 Results and Discussion

7.3.1 Langmuir Films

GO films at the air-water interface have been characterized through the standard surface chemistry technique of Langmuir films, but there are still questions about the basic characteristics of their pressure-area isotherms. Langmuir troughs have traditionally been used to study lipid, protein and polymer films as discussed by Zasadzinski et al. (1994) and Stottrup et al. (2014). In such systems, thermal energy plays an essential role in describing the behavior of the films during isothermal compression. A standard interpretation involves describing the compression in terms of phases: gaseous, liquid-expanded, and solid. As an example, and for verification of a fully functional Langmuir system,

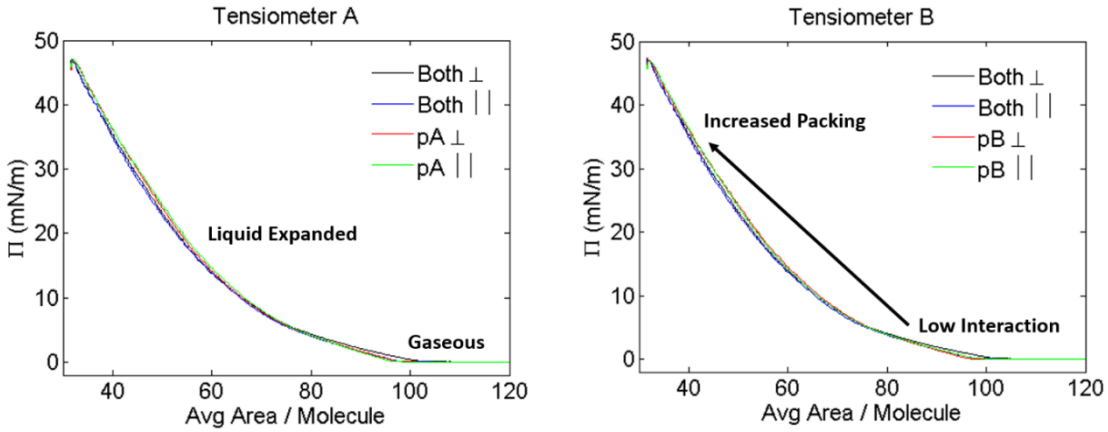

Figure 7-2 presents a series of pressure-area curves for the well-characterized lipid monolayer of DMPC. In the experiment, we record surface pressure using two identical tensiometers oriented orthogonally to each other. To minimize the uncertainty in using two sensors, we tested all possible perpendicular/parallel combinations. The high consistency exhibited by the tensiometers is indicative of controlled and trustworthy apparatus. The surface pressure readings are experimentally identical regardless of the Wilhelmy plate orientation. This is expected since lipids films of molecular thickness are isotropic. It is generally safe to utilize a Langmuir trough without particular attention to the orientation of the Wilhelmy plate, much less use two tensiometers simultaneously.

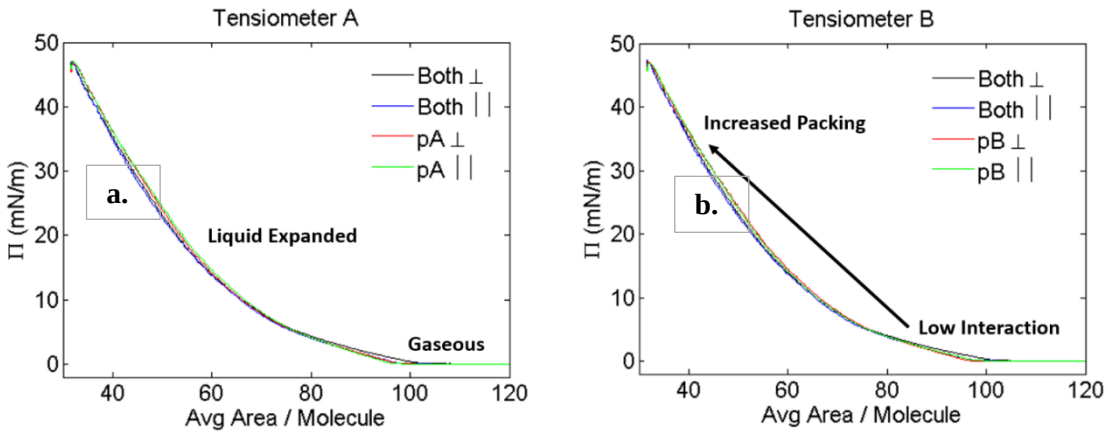

Figure 7-2. 10 µL deposition of 0.5 mg/mL DMPC lipid in chloroform. Pressure-area isotherms are all identical within experimental error regardless of Wilhelmy plate orientation. (a) tensiometer A; (b) tensiometer B according to experimental set up.

7.3.1.1 Anisotropic Surface Pressure Dependence

The literature presents many pressure-area isotherms for GO nanosheet films. [Cote et al.. 2009, Imperiali et al.. 2012, Botcha et al.. 2014] While these isotherms have some general points of agreement there are also significant differences. These differences arise due to variations in nanosheets size, chemical synthesis, or deposition/subphase conditions. Additionally, experimental considerations of the Langmuir system also may create significant discrepancies to pressure area isotherms. GO nanosheets are on the order of many microns and form highly elastic films as shown by Imperiali et al.. (2012), therefore uniaxial deformation will induce differences in film packing along the two axis: perpendicular and parallel to the direction of compression. Anisotropic differences in nanosheet packing may result in differences in surface pressure measurements using the Wilhelmy plate method. To test this hypothesis, we arranged our experimental setup to measure both parallel and perpendicular surface pressure readings simultaneously. **Figure 7-3** shows that upon monolayer compression/expansion, pressure-area isotherms reveal significant anisotropic behavior. Using DMPC we tested our experimental approach and found as expected, no difference between the parallel and perpendicular measurement of the isotherms.

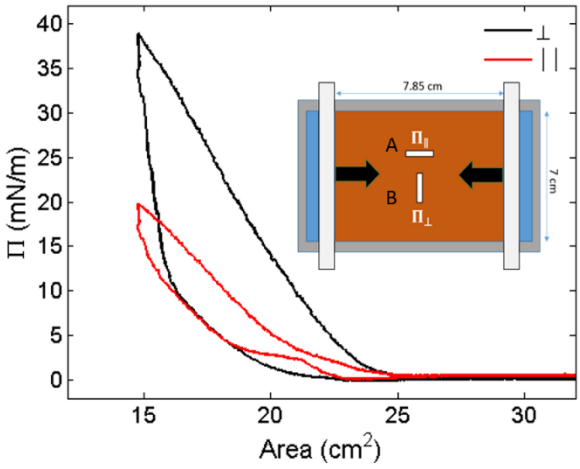

Figure 7-3 Pressure-area isotherm cycle. Surface pressure is directly dependent on the Wilhelmy plate orientation. Two simultaneous Wilhelmy plates: black is ($\mathbf{\Pi}_{\perp}$) and red curve is ($\mathbf{\Pi}_{\parallel}$). Inset: Schematic of Langmuir trough setup. Top-down view shows the two simultaneous Wilhelmy plates recording surface pressure in perpendicular orientations. Plate orientation is in respect to the direction of compression, or long trough axis. Tensiometers are referred to as A and B based on their locations in the trough.

If we think of the surface pressure as a tensorial quantity, then let us describe the perpendicular pressure readings as $\mathbf{\Pi}_{\perp}$ and the parallel as $\mathbf{\Pi}_{\parallel}$. It was found (data not shown) that a range of isothermal curves can be obtained by varying the angle of the Wilhelmy plate in relation to the compression direction. It is therefore expected that if one is not careful with the plate orientation, isotherm curves will vary widely and lead to inconsistent isotherm curves. However, the perpendicular and parallel orientations offer the maximum and minimum surface pressures respectively (shown in **Figure 7-3**). The fact that the $\mathbf{\Pi}_{\perp}$ component of the surface pressure is consistently greater than $\mathbf{\Pi}_{\parallel}$ sheds light on a systematic way of obtaining reproducible pressure-area isotherms.

A canonical Langmuir experiment is to examine hysteresis in isotherms through several expansion and compression cycles at constant speed. For our experiments the peak pressures obtained during the $\mathbf{\Pi}_{\perp}$ and $\mathbf{\Pi}_{\parallel}$ cycles are 40 mN/m and 20 mN/m respectively. In all of these experiments, compression was stopped at minimum trough area of 15 cm^2. Previous work by Cote et al.. 2009 and Imperiali et al.. 2012 have shown that isotherm compressions performed in series are repeatable with a small leftward shift in the surface pressure percolation onset. The perpendicular orientation completely reproduces these results; however, the parallel orientation does not demonstrate a percolation onset

translation. We demonstrate two additional points: first, the anisotropy noted in **Figure 7-3** is repeated upon multiple cycles and second, the isotherms cycles show significant hysteresis and recovery (**Figure 7-4**).

Significant hysteresis is observed during film expansion. We do not credit the hysteresis loop to nanosheet leakage; the barriers held at constant position only result in a small surface pressure decrease. The $\boldsymbol{\Pi}_{\perp}$ component records a more severe change in surface pressure. In **Figure 7-4**, we can see that a small degree of area expansion ($\sim 2\ \mathrm{cm}^2$) after maximum compression, results in an immediate drop in surface pressure. This is most noticeable in the perpendicular orientation, as compared to the parallel orientation. Furthermore, we notice that during expansion, the parallel orientation records a surface pressure plateau between 18 and 22 cm^2. This we attribute to mechanical film packing and will be discussed in light of real-time imaging. It is important to notice that except for the initial slope of the expansion curves, the rest of the isotherm expansions appear very similar between the two plate orientations. This indicates that the initial stages of film expansion are important in understanding the observed anisotropy.

The explanation we suggest for this observed anisotropy is as follows: after the monolayer has been compressed GO nanosheets are packed tightly and buckled at the air-water interface. Upon expansion the stress within the monolayer is relieved and the monolayer may relax. The relaxation process may take longer than the expansion speed of the barriers and cracks or fissures might start to appear perpendicular to the motion of the barriers. This would result in a quick drop in the surface pressure for a Wilhelmy plate in the perpendicular orientation. For a Wilhelmy plate in an orientation parallel to the motion of the trough, no such cracks in the film are expected and the pressure area isotherm would be expected to fall following the contours of the original isotherm. This is generally what we observe in the isotherm. Such a physical mechanism provides a reasonable explanation based on the nanosheet packing for the difference in surface pressure sensor readings across orientations, and would be interesting to independently investigate as a working hypothesis.

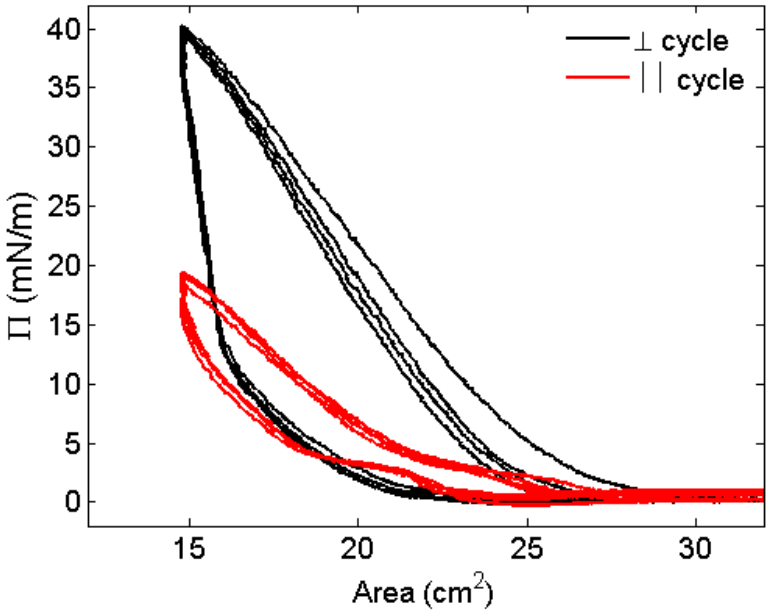

Figure 7-4. Anisotropic pressure dependency is maintained throughout a series of pressure-area isotherm cycles. $\mathbf{\Pi}_{\perp}$ shows significant reduction in the percolation onset, whereas $\mathbf{\Pi}_{\parallel}$ shows higher stability. Maximum pressure is independent of the number of compressions for both orientations. Hysteresis loop is observed, most prominent in the $\mathbf{\Pi}_{\perp}$ orientation.

In the following section we provide morphological evidence of film packing as described through Brewster Angle Microscopy (**Figure 7-5**). We note that we are able to obtain good quality images of film morphology during the early stages of film compression, however, during high compression we lose resolution because the interface is completely covered with GO sheets (**Figure 7-6**). It therefore is an experimental challenge to image the film *in situ* during high film compression and obtain quantitative information regarding any sort of film breakage immediately after film expansion. On the other hand, we do note that film morphology is highly distorted for surface pressures above 3 mN/m as recorded by the parallel orientation. Visually with BAM we do not see any change for higher surface pressures, and therefore we can preliminarily conclude with the aid of Imperiali et al..'s (2012) work with *in situ* bright field microscopy that during high compression, the GO film is wrinkling and folding. In light of this description of the film at the interface, the wrinkle and folding of the GO nanosheets are due to the uniaxial stress deformation, however, once the stress is removed, it would be expected that the GO nanosheets would immediate tend to relax from their buckled state because of their

mechanical properties. This would be especially expected since the barriers are expanding at a high speed. We can partially support this reasoning through Imperiali et al..'s (2012) claim regarding GO's high elastic properties at the air-water interface along with data from Lee et al.. (2008) regarding monolayer graphene's high inplane Young's modulus and sheet stiffness.

7.3.1.2 *In Situ* Film Morphology: Correlation to Surface Pressure

Another method of characterizing film assembly is through the use of *in situ* Brewster Angle Microscope (BAM) to monitor film morphology. **Figure 7-5** is a schematic showing the basic characteristics of the BAM along with an image of a clean water surface. Previously published BAM images lack distinguishable GO nanosheet morphology because of resolution limitations and small nanosheets on the order of a few microns.

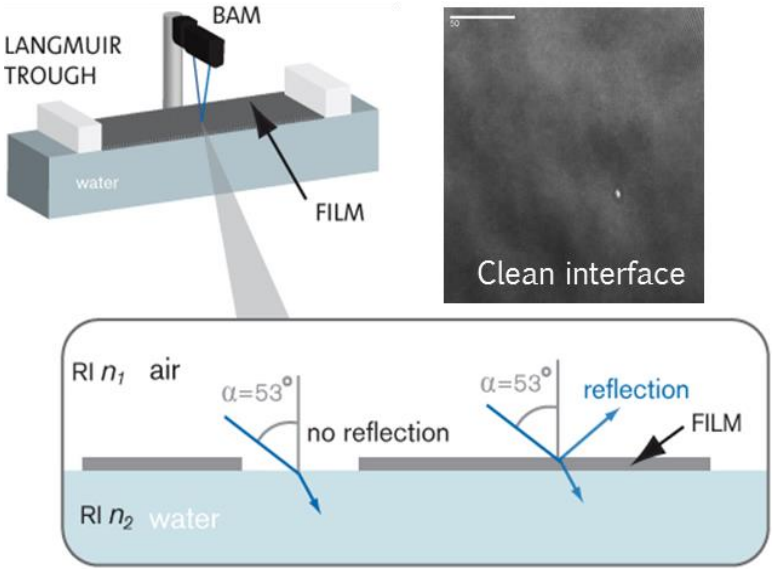

Figure 7-5. BAM set up under Langmuir-trough. Adapted from Bolin Scientific. Image of a clean water surface, Π ~ 0.0 mN/m**.**

BAM images are obtained by directing a laser of *p-polarized* light at the air-water interface of a Langmuir trough. At the Brewster angle (**53**° for air-water) all the light is refracted, however, when a film comes into view, some light is reflected into a CCD camera and the film morphology is therefore imaged. By using this technique, we can

simultaneously look at the film morphology while also recording interfacial tension measurements using the parallel orientation since it allows for optimal placement of all the experimental apparatus. **Figure 7-6** shows the assembly of GO nanosheets using clear *in situ* morphological images. It is expected that surface pressure would be a measure of the macroscopic interactions among the many GO nanosheets. BAM images show that increase in surface pressure is indeed related to film packing. Interestingly, in contrast to previous reports regarding the assembly of GO nanosheets, full coverage seems to occur at relatively low surface pressures ($\mathbf{3.5-5.0}\frac{\boldsymbol{mN}}{\boldsymbol{m}} \rightarrow \boldsymbol{\Pi}_{\parallel}; \mathbf{9-13}\frac{\boldsymbol{mN}}{\boldsymbol{m}} \rightarrow \boldsymbol{\Pi}_{\perp}$). To provide a more comprehensive view, **Figure 7-7** shows film morphology at the same surface pressures, but lower magnification. It must be noted that the **Figure 7-6**(a) and **Figure 7-7**(a) correspond to the reading at maximum trough surface area, rather than right before percolation onset.

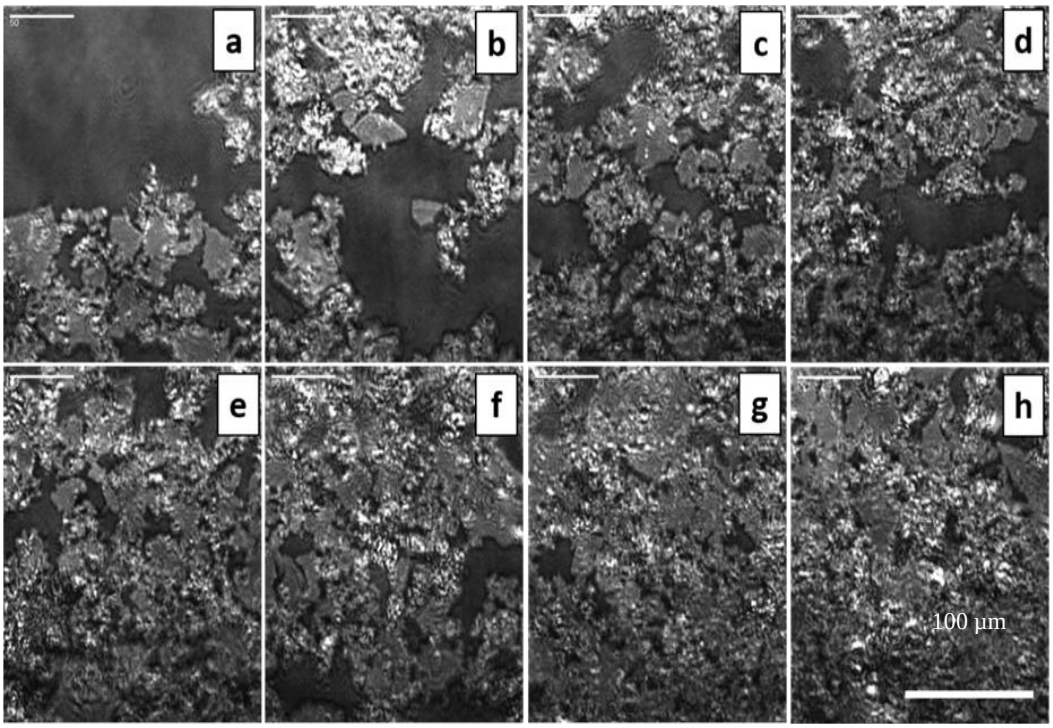

Image	a	b	c	d	e	f	g	h
$\Pi_{\parallel}$ (mN/m)	0.0	0.2	0.4	1.2	1.5	2.5	3.5	5.0

Figure 7-6. Direct correlation between surface pressure $\Pi_{\parallel}$ and film morphology obtained with BAM. Complete coverage at low surface pressures. Scale bar is 100 µm.

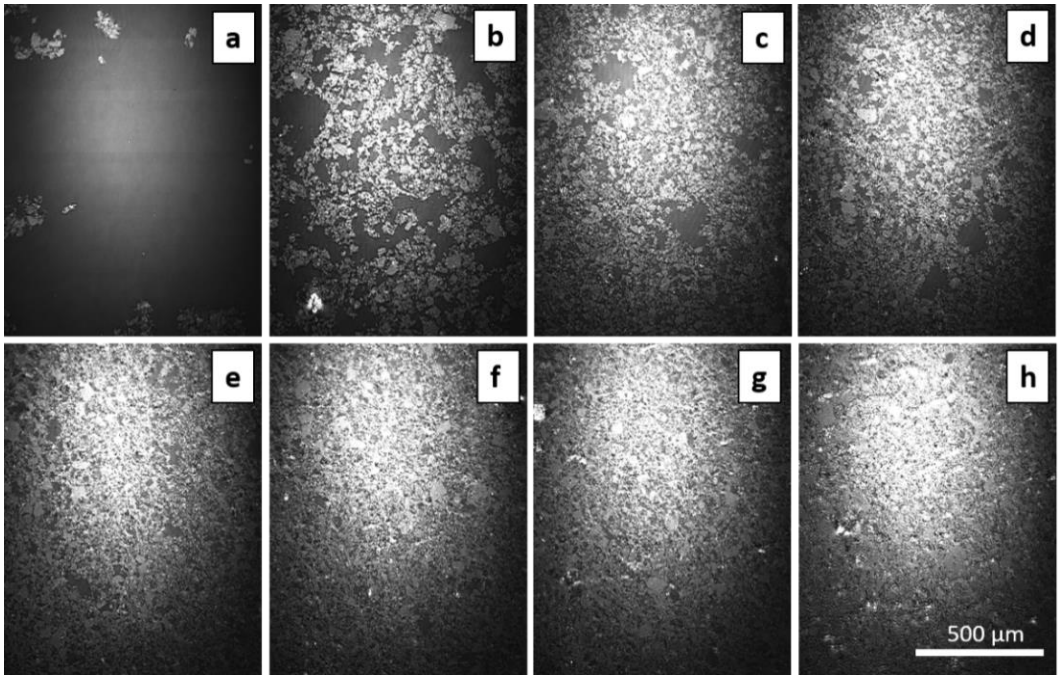

Figure 7-7. Lower Magnification images BAM images of MTD GO. The global film morphology at each Π is consistent with the images at higher magnification.

We have related the early stages of the compressional isotherm to film morphology. However, we are not able to distinguish fine details of the film morphology for high packing on account of the low resolution offered by BAM. Nevertheless, we can conclude that for GO sheets of large lateral dimensions, high compression is not required since this would induce wrinkling and folding as shown by Cote et al.. (2010), unwanted for major applications such as coatings for transparent conductive thin films.

Returning to the plateau observed during isotherm expansion as recorded by the parallel orientation, it was thus found that this corresponds to a particular form of film unpacking. BAM allows for real time observations, which means we can take movies of the pressure-area isotherms. We found that the plateau observed with the parallel orientation corresponds to the presence of interlocked GO sheets jammed together. The movies revealed that during isotherm expansion, GO sheets do not relax in the reverse way to how they pack during compression. Instead of expanding to fill new area, GO sheets are observed to remain interlocked in their precompressed state along the parallel axis until a given point at which they release from this interlocked state, as marked by the downward slope in the isotherm and sudden film movement in the BAM movie. This indicates that

the film experiences breakage during expansion as a result of release from a buckled pre-compressed state; an intuitively sensible physical mechanism. It also seems to indicate that surface pressure measurements are correlated to overall film packing rather than just the local interactions between the Wilhelmy plate and GO sheets, which gives us confidence in the validity of the measured surface pressure at gauging overall film behavior.

7.3.1.3 Loading Experiments

We now investigate the effect of linear mass loading of GO. This experiment probes the GO deposition technique using successive Π-A and Π-c isotherms (c – mass loading). The question of material loading is of practical importance since during any deposition, material is continuously loaded drop-by-drop onto the interface. Loading experiments monitor shifts in the pressure-area with successive deposition increments of 0.0625 mg of material every two hours until a total of 0.313 mg. To provide the most representative and accurate results, we set the orientation of the Wilhemly plates to be the same for both barriers in order to see the effect of surface saturation of GO or surface concentration inhomogeneity. This is shown in **Figure 7-8**.

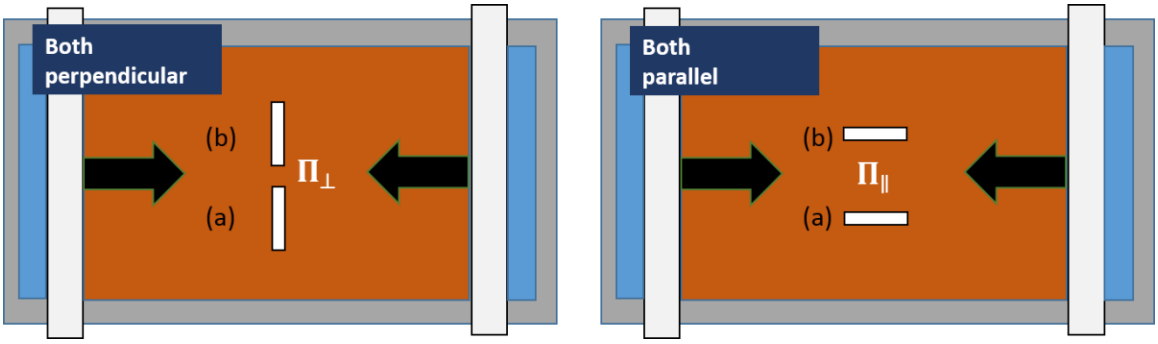

Figure 7-8. Experiments were performed with both tensiometers in either perpendicular or parallel orientation in order to examine the homogeneity of the strain field.

We will present the results of experiments done with tensiometers both in the perpendicular orientation. Results obtained from the parallel orientation gave similar results, with an observed quantitative difference in the maximum surface pressure identical to the experiments performed with the perpendicular orientation.

It was found that for loadings of 0.0625 the surface pressure barely rose above minimum following a full compression. For a deposition of 0.125 mg (not shown) the variations between the tensiometers of the same orientation were significant. This is an indication that the strain field, that is to say the homogeneity of GO concentration as measured by the two tensiometers in different locations of the trough is not constant. We have previously seen the effect of sheets interlocking at the interface as shown in the expansion cycle, and also reproduced in the literature, to be responsible for differences in the isotherm curves. A possible explanation is that for low surface loadings, GO sheets become interlocked in a specific overall configuration, which could yield slightly different forces on the Wilhemly plates, and therefore different pressure-area isotherms. The reason this could hold true is because for low surface loadings, the surface is not entirely saturated with GO nanosheets therefore heightening any differences in surface concentrations that originate due to the drop-wise deposition method.

Deposition amounts of 0.188, 0.25, and 0.313 mg show consistent results. At a loading of 0.188 mg and above on a trough 55 cm^2 at maximum area, we can say the system is fully saturated with GO to the point where GO is spatially distributed in a rather uniform manner. **Figure 7-9** shows two sets of plots with the results for the linear mass loading experiment as measured by tensiometer A, black curves, and tensiometer B, red curves by the perpendicular orientation. The first set of curves is pressure-area curves and the second set are pressure-surface concentration curves. The pressure-area curves show that tensiometer B consistently records a higher surface pressure for all loading units and that as the loading units increase, the curves shift towards larger percolation onsets and reach a higher maximum surface pressure upon maximum compression. The fact that we consistently obtain a higher surface pressure from one tensiometer B is an indication that our deposition method is consistent throughout the entire deposition.

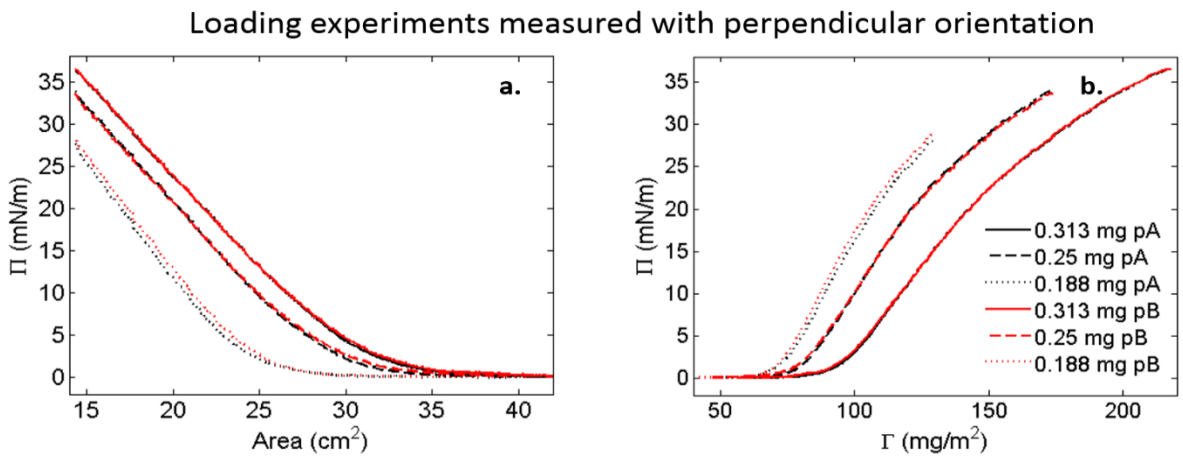

Figure 7-9. Effect of linear mass loading as recorded by $\mathbf{\Pi}_{\perp}$. Black and red curves correspond tensiometer (a) and (b) respectively. a. Pressure-area shows an increase in area percolation onset. b. When rescaled to surface concentration, there is an inefficiency during linear mass deposition.

The more interesting observation is that both tensiometers exhibit the behavior that from the lowest unit of loading (dotted line) to the next (dashed line) there is a shift, which is reproduced over the next stage of loading (solid line). The interpretation is simple: this is saying that upon higher loading units, more material is left on the air-water interface. This is as expected, however, we can make this claim more quantitative by looking at the theoretical surface concentration. Since we know the exact amount of material deposited on the surface, we can then calculate the surface concentration which is another measure of film assembly. In theory, it would be expected that if twice as much material gets deposited on the surface, one would obtain an identical pressure-surface concentration curve since the x-axis would be rescaled accordingly. However, this is assuming that there is a direct and linear relationship between surface material loading and surface concentration. In the case of GO films, it turns out to be a non-linear relationship. The pressure-surface concentration curves show overall transition towards higher surface concentrations, an indication that not all the GO deposited is staying at the interface. Specifically, at a surface pressure of 15 mN/m the corresponding surface concentrations are ~96, 109, and 127 mg/m^2 corresponding to 0.188, 0.25, and 0.313 mg respectively. This indicates differences of ~13 and 18 mg/m^2 in loading concentration with the addition of 0.625 mg of GO. The corresponding loading efficiency is approximate 50% between 0.188 and 025 mgs and 30% for the loading process between 0.25 and 0.313 mg.

The reason is again related to material saturation at the interface; that is to say that there is a deposition inefficiency once the interface is saturated with GO nanosheets.

7.4 Langmuir-Blodgett Deposition onto Solid Substrates

An alternative form of characterizing film morphology is through Langmuir-Blodgett depositions onto supported substrates, but beyond being a GO interfacial characterization method, the LB technique can be used to generate monolayer films of GO for applications such as transparent conductors. To characterize such films, Kim et al.. (2010) developed of the novel technique of Fluorescence Quenching Microscopy (FQM), which provides an alternative in nanoparticle visualization. Their method was based on the observation by Nakayama et al.. (2007) that graphitic systems such as graphite and carbon nanotubes have been shown to be efficient fluorescence quenchers. Unlike sophisticated techniques such as Scanning Electron Microscope (SEM) and Atomic Force Microscopy (AFM), FQM is efficient and relatively inexpensive in the characterization of GO films. Contrast in brightness is what allows for GO sheet visualization. Through the process of quenching, a contrast difference occurs between GO nanosheets and background substrate, furthermore, not only are we allowed to see the GO film, but also able to quantify the relative number of layers as shown by Kyle et al.. (2011). Contrast is given by the following equation: $C = (I_b - I_g)/I_b$, where I_b is the brightness of background and I_g is the brightness of GO sheets based on an FQM image. Due to GO's high quenching effect, a spacer may be used to provide practical contrast.

We have performed a Langmuir-Blodgett deposition on RCA-1 treated glass slides and then imaged using FQM. In agreement with the literature, surface treatment of glass slides allows for a better film transfer. **Figure 7-10** shows our results for different LB depositions at relatively low surface pressures. The reason we chose low surface packing is because with FQM we obtain high-quality images for film morphologies that are clearly outlined. We found that upon high compression (not shown), we are not able to clearly distinguish film morphology. We compare the FQM images to those obtained from BAM. Our GO LB coated film show large nanosheets on the order of 10-50 μm in

lateral size, which is highly consistent with BAM images. Film is mostly composed of single layer material as seen by the overall uniformity in contrast. Through BAM images, we were able to show a nice progression for increasing surface pressures. It was found that surface pressures start to increase as GO sheets start to get closer together, however, GO sheets were in full contact for surface pressures of around 3-5 mN/m as measured by the parallel orientation. We could not distinguish with BAM the level of wrinkling/folding or overlap, however, FQM images provides better individual nanosheet visualization.

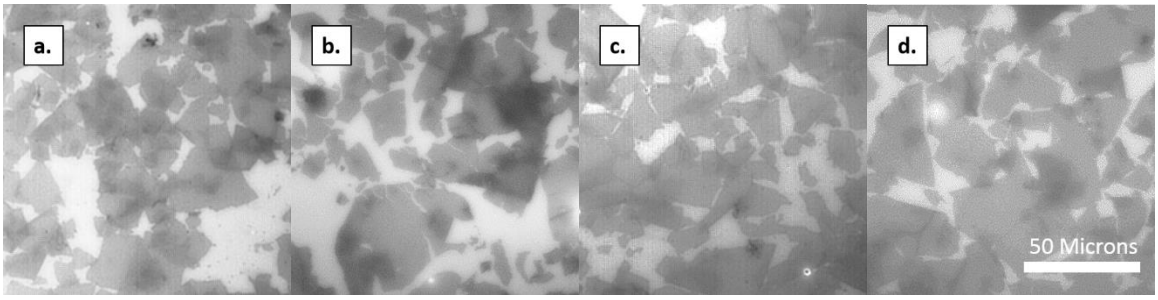

Figure 7-10. FQM images of a LB deposition on RCA-1 treated glass slides. GO film shows consistent packing and large GO nanosheets. Images (a)-(d) reveal consistency in the observed morphology across coatings. $\Pi_{\parallel} = 1.5\ \mathrm{mN/m}$.

If we take a look at **Figure 7-10**(a) and (b), there are regions where small GO nanosheets are trapped on top of larger nanosheets. This is something we primarily attribute to the polydispersity of the GO as produced by the synthesis, but could also be a result of repeated film compression. In contrast to the polydispersity of the sample, which ranges from hundreds of nanometers to tens of microns; our images, as shown through BAM and FQM, show a much more homogenous distribution of nanosheet sizes. This we attribute to small sheets potentially falling into the subphase due to the neutral pH of the subphase, leaving only sheets on the micron scale (we plan to measure subphase retention in the future using techniques such as in-situ or ex-situ UV-Visible spectrophotometry). **Figure 7-10**(c) and (d) show a more homogenous distribution of single layered material, and if we look close we can see that partial overlap occurs among the assembly of sheets. Based on these images we can conclude that we can successfully transfer our film from the air-water interface onto a simple and versatile substrate such as surface-treated glass.

We can easily imagine compressing the film to a higher extent in order to fully fill the available space, much like in the BAM images at higher surface pressure, and then perform the same LB deposition. A fully-compressed yet flat film would be obtained, which would serve as an ideal film for various applications. It is possible to further enhance these films by electrochemically reducing them to restore their electrical conductivity. Overall, we have shown how control of the structure and stability of GO films can be utilized to produce high-quality GO coatings.

7.5 An Investigation of GO Inherent Surface Activity

We conclude with an analysis of the surface activity of GO films. Unlike surfactants, phospholipids, or other amphiphilic molecules which through various mechanisms self-assembly into the interface to form Langmuir films, it remains uncertain if GO nanosheets also self-assemble and exhibit "intrinsic" surface activity. A key consideration is the method of deposition onto the interface. Usually, a volatile organic solvent such is IPA or methanol is used to disperse and dilute the exfoliated GO, which are then deposited onto the air-water interface drop-wise using a microsyringe. This allows the nanosheets to be more evenly dispersed on the interface. There are experimental results along with some thermodynamic approximations that show that once GO nanosheets are at the interface, they are irreversibly pinned (Imperiali et al.. 2012). This brings the question if GO's claimed surface activity is simply a result of the water-solvent interaction through a mechanism that would yield some nanosheets to lie flat and remained pinned at the interface.

Results from Li et al.. (2013) show that depositions of GO into the subphase have produced no signs of "surface activity" as measured through a pressure-area isotherms and LB coatings on silicon substrates. However, these results are inconclusive since only lipid-GO interactions resulted in GO nanosheets to the interface. However, others have shown that surface activity can be induced by lowering subphase pH. Cote et al.. (2011) and Botcha et al.. (2014) have explained this stating that the level of GO activity at the interface is a function of GO nanosheet ionization; sheets in the presence of an acidic subphase might tend to remain at the interface because of the carboxylic acid groups at

the GO sheet edges getting re-protonated at lower pH, thus simultaneously reducing their colloidal stability in dispersion, while allowing them to laterally sit beside each other at the air-water interface without experiencing mutual repulsions that might drive their desorption or pose an enthalpy barrier to their adsorption to begin with.

Figure 7-11 shows the effect of subphase pH on the intrinsic surface activity of GO nanosheets. We find through pressure-area isotherms that GO diluted in water and inserted into the subphase under neutral pH is not surface active. When the pH of the system is lowered, GO sheets are observed at the interface. Magnetic stirring is required since the diffusion of GO in water is extremely slow and thus this would be an impractical experiment. It must be noted that even at our lowest tested subphase pH of 1, the isotherms are about four times lower than those obtained through the drop-wise deposition using an organic volatile solvent (**Figure 7-3** for instance). This result generates interest to further investigate the mechanism that results in the irreversible pinning of GO nanosheets at the interface during drop-wise deposition using an organic volatile solvent, especially because in these latter experiments, sheets that fall into the subphase do not naturally come back to the surface at neutral pH. We note that it is better to perform depositions under acidic subphase to maximize deposition efficiency. It would then be expected to have smaller nanosheets at the interface, which as previously stated, would yield higher interface polydispersity and potentially unwanted for electronic-based applications. In future work, it is envisioned to perform this experiment under the use of BAM to observe the change in film morphology at the interface. We then would be able to be quantitative about the intrinsic surface activity of GO.

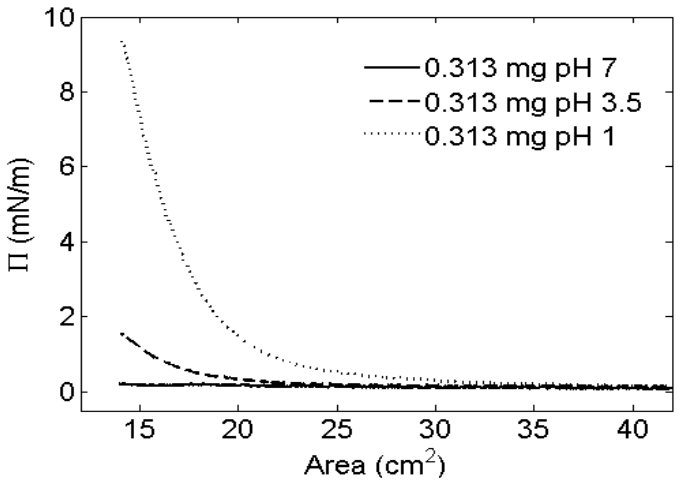

Figure 7-11. GO was dispersed in water and slowly injected into the subphase of different pH. Several hours wait along with magnetic stirring was allowed for good subphase mixing. Π-A isotherms collected with Wilhelmy in perpendicular orientation GO's intrinsic surface activity is seen to be pH-dependent.

7.6 Conclusions and Implications

In conclusion, we have explored a range of established and novel Langmuir-based experiments with our large-sized GO nanosheets. We address some of the fundamental mechanisms surrounding the assembly of GO nanosheets at the air-water interface. Our findings on the surface pressure anisotropic dependence shed light on how to obtain reproducible pressure-area isotherms. We provide a potential explanation for the differences observed in pressure-area isotherms in the literature. This suggests a physical interpretation of how the Wilhelmy plate method might be inadequate in separating the various parameters surrounding film interfacial assembly such as local interactions between GO nanosheets and Wilhelmy plate, or other components such as elastic film properties or breaking of the GO film upon stress.

Moreover, we were able to successfully transfer our film from the air-water interface onto a simple and versatile substrate such as surface-treated glass. We successfully correlate film morphology as measured *in situ* through the use of Brewster Angle Microscopy and *ex situ* through Langmuir-Blodgett depositions on supported substrates imaged with Fluorescence Quenching Microscopy, to the corresponding pressure-area isotherm. We

find consistency in our imaging techniques, and establish that film packing occurs at relatively low surface pressures, such that we do not need to reach high pressures to coat GO films using this approach. We plan to quantitatively measure the subphase retention of small sheets and interfacial selectivity towards big sheets in the future using techniques such as in-/ex-situ UV-Visible spectrophotometry and FQM.

Finally, there has been an ambiguous use of the term surface activity when describing GO sheets as "amphiphilic". We show that GO is not intrinsically surface active for neutral pH but exhibits surface activity under acidic subphase. Overall, we have provided a coherent set of experiments to provide novel insights into the interfacial assembly of GO films, all in an effort to better use Langmuir monolayers as a template for film coatings.

Chapter 8: Conclusions and Future Work

8.1 Conclusions

Following a comprehensive literature review, it was discovered that there is an increasing frequency of citations for both the Hummers oxidation method and the MTD method for graphite oxidation to obtain graphene oxide (GO). It was also shown that the Tour method is gaining attention compared to the other methods used in this area, and is potentially able to become the method of choice over the coming years for making GO. This was shown to be due to a combination of factors: the low overall metal content used and generated by the Tour's synthesis compared to the Hummers' method (especially potassium and manganese), the ability of the Tour method to generate larger sheets than any of the other oxidative methods – which makes it suitable for optoelectronics and a number of other applications which utilize this property - due to its protective chelation mechanism using agents such as phosphoric acid, as well as its simultaneous ability to relatively protect the graphitic surface from defect formation via the same mechanism

Based on the preceding review, the Tour method was singled out as the method of choice for making GO, with the introduction of a few modifications tailored towards producing large sheets by starting with a large graphite size and tuning the oxidation conditions (graphite: oxidant amount and reaction time) to 1:4.5 (compared to 1:6 using the Tour method) and 72 hrs respectively, by visually inspecting the disappearance of dark flakes in the product. Temperature control was used to ensure result reproducibility and avoid unintentional reduction of the GO product. This method was called the modified Tour-Dimiev (MTD) method. The product GO was characterized using a number of techniques: XPS revealed a higher than normal O content (expected for Tour GO), an observation supported by elemental analysis. FT-IR qualitatively revealed the same functionalities that were discerned by XPS, indicating consistency of results. Raman spectroscopy revealed a comparable degree of surface defects to GO synthesized by similar techniques in the literature, an indication that the long oxidation time we used did not significantly increase the level of surface defects introduced to the graphite beyond

what is expected following oxidation, and is something that might be attributed to our minimization of the oxidant amount used.

The next step was to introduce a coherent scheme towards the coating, visualization via fluorescence quenching microscopy (FQM) and atomic force microscopy (AFM), and image analysis of polydisperse, polygonal and polymorphic GO sheets using flexible Matlab routines that are ideally suited to this purpose and offer a higher degree of control. First, we reviewed the major issues encountered with FQM and AFM imaging GO, most of which were encountered with FQM imaging and were attributed to lack of resolution for size-scales < 350 nm, staining problems with the fluorescent-coating quality and issues with uniformity of brightness and edge detection on some of the particles. These problems have been addressed by relying on the combination of FQM and AFM images in our analysis, and by comparing the standard image analysis software ImageJ with MATLAB in terms of the analytical capability for our particle systems, while introducing a number of subroutines that we used in MATLAB to mitigate the issues previously experienced during image analysis. We also used our analytical methods to image commercial and lab-synthesized MTD GO, using the results to conclude that lateral assize and thickness for the GO are weakly correlated and that such a correlation, if it existed, can be safely ignored from a statistical standpoint. We also concluded that GO can be successfully described by a lognormal distribution. Moreover, we used our methods to quantitatively discern the shift to lower sizes in commercial GO due to sonication, demonstrating technique sensitivity. Furthermore, we demonstrate that AFM is ideally suited to image GO where the majority of particle are below 5 μm in size, while we find FQM to be better-suited for imaging GO > 1 μm (such as MTD GO). Finally, we propose a splicing technique to combine the high resolution of AFM at smaller particle sizes (< 1 μm) with that of FQM at large sizes (> 5 μm) to obtain a complete picture of the distribution of the polydisperse MTD GO.

Next, we were able to model polydisperse dilute dispersions of oblate spheroids and discs in shear, uniaxial and biaxial extension using a set of microhydrodynamic models found in the literature and (in the case of shear flow) adapted for use as closed-ended models.

By assuming and validating linear additivity of particle fractions, these originally monodisperse models were generalized for us to any polydisperse suspended particle system of interest. Generally, it was observed that shear and biaxial extension both result in shear-thinning, while uniaxial extension results in shear-thickening. This was justified by an oblate spheroid or a sheet (unlike a prolate one or a fiber) having morphology closer to 2D than 1D, thus causing these 2D disc-like spheroids to line up parallel to shear and biaxial extensional flows in suspension, which are, in turn, 2D flows by nature 2D flows. Uniaxial extension, on the other hand, is a 1D flow. Unable to line up parallel to the flow, oblate spheroids and sheets will tend to line up orthonormally to the flow, resulting in high drag on the particles and the simulated shear-thickening effect. A common phenomenon observed across all flows is proportionality of suspension intrinsic viscosity to diameter and inverse proportionality to particle thickness (i.e.: proportionality to aspect ratio). This was explained by noting that the higher the aspect ratio, the greater the influence of the particles in obstructing these three flow systems per particle, and hence the higher the intrinsic viscosity, which is a rate of change of viscosity per unit volume loading of sheets in the dilute limit. Secondly, more shear-thinning/thickening was observed for bigger particles than smaller ones, because the former align from a state of greater Brownian angular inertia to/against the flow field in place. Following from the preceding argument, a signature broadening of the intrinsic viscosity response was observed in response to increasing polydispersity.

Building on these simulation results, we used the shear rheology model to fit experimental data on a number of nanosheet systems (GO and layered double hydroxides) using shear flow sweep experiments on serially-diluted samples to obtain the dimensions and distributions thereof. As proof of concept, this approach was compared to AFM for measuring size distribution of a commercial GO sample before and after sonication. Before sonication, the two techniques yielded comparable estimates of the GO lateral size. After sonication, AFM was shown to be relatively less sensitive to changes in the overall distribution, compared to rheology, with the latter method yielding statistics that reflect a bigger shift in the distribution towards smaller sizes. This indicates the potential of rheology as a quick, qualitatively and quantitatively sensitive quality-

control technique which is not skewed by sample impurities, thus simultaneously giving it advantages over AFM and DLS for this line of work. It also has the advantages of being non-destructive and sampling over the entire population of GO, regardless of population or particle size considerations which might need to be accounted for in other particle morphology characterization techniques. The technique was also shown to be effective in estimating the size on a challenging, highly-polydisperse lab-synthesized GO sample as per MTD's method, yielding consistent estimates with those from FQM and AFM images. Finally, the rheology technique was used to estimate size characteristics based on rheological data found in the literature on a more complex system consisting of layered double-hydroxide nanosheets dispersed with polyacrylamide in water, yielding consistent results with TEM and DLS characterizations done by the authors on their sample, and thus further asserting the versatility of our proposed technique for experimental characterization and quality control.

Finally, we explored a range of established and novel Langmuir-based experiments with our large-sized MTD GO, in the process addressing some caveats pertaining to the understanding of certain fundamental mechanisms surrounding the air-water interfacial assembly of GO nanosheets. Our findings on the surface pressure anisotropic dependence shed light on how to obtain reproducible pressure-area compression behavior. Moreover, we were able to successfully transfer our film from the air-water interface onto a simple and versatile substrate such as surface-treated glass. We successfully correlated film morphology as measured *in situ* through the use of Brewster Angle Microscopy and *ex situ* through Langmuir-Blodgett depositions on supported substrates imaged with FQM, to the a particular pressure-area isotherm. We find consistency in our imaging techniques, and establish that film packing occurs at relatively low surface pressures, such that we do not need to reach high pressures to coat GO films using this approach. Finally, there has been an ambiguous use of the term surface activity when describing GO sheets as "amphiphilic". We show that GO is not intrinsically surface active for neutral pH but exhibits activity under acidic subphase. We were thus able to provide a coherent set of experiments to provide novel insights into the interfacial assembly of GO films, all in an effort to better use Langmuir monolayers as a template for film coatings.

8.2 Future Work

8.2.1 Synthesis

Following initial success with modifying the Tour method for large GO production, we plan to target the following areas for further improvement:

1) - graphite pre-expansion: such a step is expected to increase the graphite (002) spacing sufficiently to minimize diffusion limitations of oxidant species. This is thought to offer a double advantage: a)- it might enable us to minimize the time and/or oxidant amount required for the Tour oxidation step, and b)- as a result of this, both sheet size and sp^2 graphitic domains are maximized in the product GO, since the expanded graphite is not overly exposed to oxidant species. Coupling such a pre-expansion step to the Tour method is also expected to add synergistic value beyond each of these two independent techniques; the pre-expansion step prepares the graphite ideally for the oxidation (as discussed above), while the Tour step (as opposed to Hummers oxidation or any of the other synthetic routes) protects the surface from excessive hole formation and fragmentation. This experiment was tried out by carrying out the MTD synthesis on a batch of Alfa Aesar graphite pre-expanded for 1 min at 1050^{o}C, following intercalation with sulphuric acid. A preliminary result is shown in **Figure 8-1** below, showing that the sheets produced from such a process are 10-50 μm, and this was achieved using a graphite:oxidant ratio of 1:2 i.e.: we were able to reduce the oxidant amount by >50% compared to the MTD method used to make GO in Chapter 3.

2) - Taylor-Couette flow reactor: the use of such a reactor introduces cylindrical symmetry which allows good mixing of the reactants, thus potentially resulting in a reduction of the required oxidation time (and thus the same advantages as those discussed above). Results from our rheology section indicate that such a cylindrical shear system causes the graphitic sheets to line with the circular flow field in a shear-thinning fashion which minimizes hydrodynamic drag on particles. Such a reduction in system viscosity can contribute towards reducing diffusion limitations in the reaction mixture.

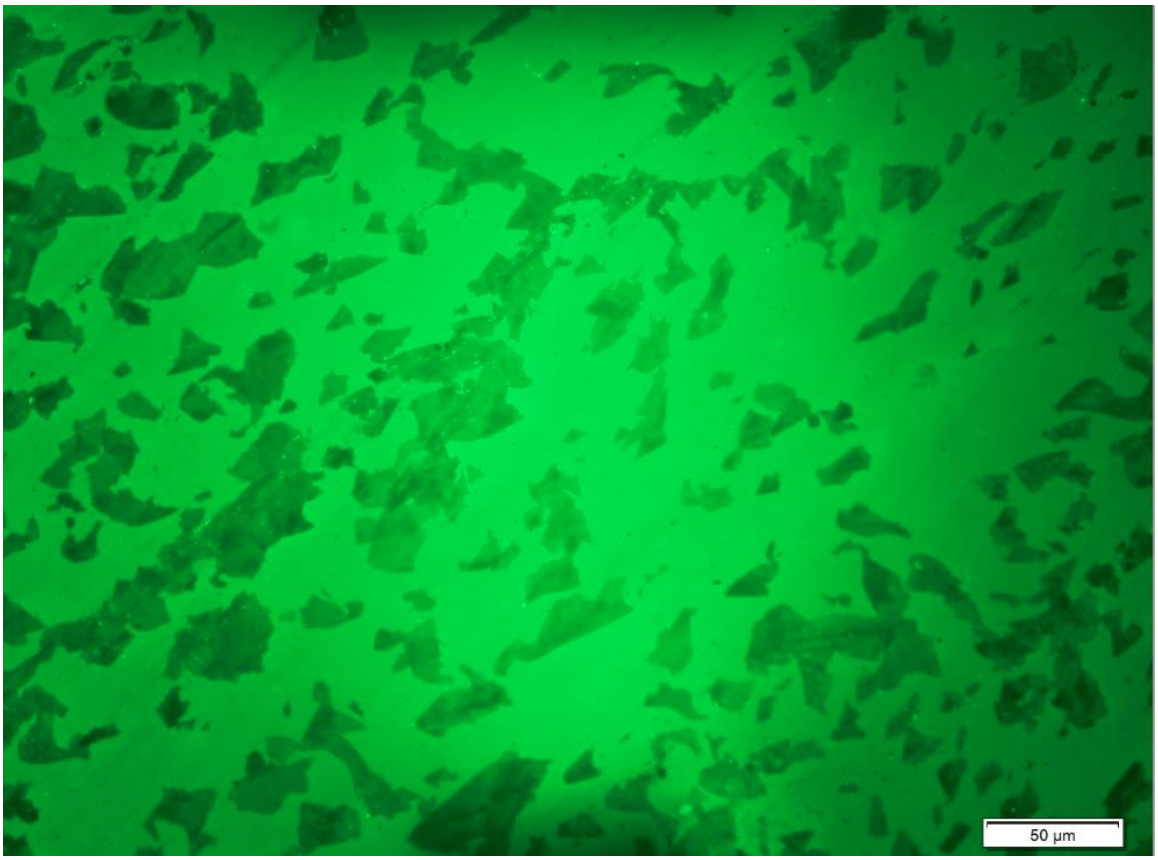

Figure 8-1. FQM image of MTD GO produced using pre-expanded graphite.

3) - Graphite Choice: as discussed previously in Chapter 3 on GO synthesis, the typical oxidative routes followed to arrive at GO all rely on a top-down approach starting from graphite, hence it makes sense to start from a graphite as large as possible in order to maximize the sheet size of the product. To this end, a systematic study spanning a few types of graphite of large flake and crystallite size might help us identify suitable candidates for ultralarge GO production.

8.2.2 Size-separation

Among the primary hurdles facing any size-separation attempt on GO is a fundamental lack of sufficient literature on the hydrodynamics of such separation phenomena for sheet-based colloidal systems. We will thus undertake a survey of literature to locate

correlations linking hydrodynamic friction factors to sheet dimensions, based on work by Perrin (1934) for polymers and Kim for hard oblate spheroids (2005), and adapting both sets of correlations to circular discs by taking the limit of b >> a. The correlations might require coupling to electrostatic phenomena based on potential edge-charging of GO carboxylic groups upon deprotonation (especially in basic media), in order for them to be practically usable. These correlations can then be used to model the centrifugation of GO, whether via differential ultracentrifugation, or density-gradient ultracentrifugation (DGU), thus enabling us to predict the centrifugation time-scales and positions along the centrifuge tube at which we expect to find GO sheets of a certain size cut. We plan to do this in the future, with the theory informing our centrifugation experiments, in an attempt to separate GO sheets of maximum possible size and minimum thickness (i.e.: maximum aspect ratio).

Another size-separation technique that seems viable for GO is that of using interfaces (especially the one between air and water) to isolate big sheets for the applications of interest, as seen in Chapter 7. This can be achieved via the simple expedient of running Langmuir experiments on GO in an LB trough. The larger the area of interface created per unit volume, as in emulsions and fluid drops/vesicles for instance, the higher the expected ability to isolate cuts of large GO sheets. Generating GO aqueous sprays or aerosols, for instance could constitute a viable means of generating such fluid vesicles.

8.2.3 Uniaxial Extension Experiments

In chapter 5, we introduced correlations to model shear, uniaxial and biaxial extension of dilute dispersions of discs. In chapter 6, we went ahead to test the correlations for shear flow using experiments involving GO dispersions and a single dataset from aqueous dispersions of double-layered hydroxide sheets. While the model proved useful in extracting physically realistic descriptive parameters for the systems under study, it suffers from the problem of being a piecewise function over the experimentally accessible shear-rates of interest (and Peclet numbers), and this can make convergence simultaneously a difficult and time-consuming process. For this reason, we plan to conduct uniaxial extension experiments relying on capillary flow of GO aqueous

dispersion through a narrow channel in a CaBER extensional rheometer. The correlations for uniaxial extension are continuous over the entire domain of interest and so expected to be easier to use for modeling of experimental data. Moreover, this will provide us with a different approach to characterizing particle size characteristics for a dispersion of discs, enabling comparison with the same information extracted from the shear rheology experiments.

8.2.4 Optoelectronic Films

One of the primary motivations behind this thesis is the synthesis and characterization of GO for applications such as optoelectronic films. We claim to have reached a stage (through Chapter 10) at which we are able to understand the behavior of our GO in Langmuir monolayers at the air-water interface, and at which we are also able to deposit LB films on substrates such as glass slides for optoelectronic testing. This would involve the following steps such as suitable substrate choice, testing of Langmuir-Blodgett deposition, choosing a suitable approach to reduce the resulting films, measurement of conductivity and optical transmittance of the films produced in this way.

8.2.5 Graphene-zeolite Hybrids

In parallel to the work we did on LB of GO, we also did work on zeolite MFI nanosheets, proving that they can be deposited at the air-water interface, transferred to silicon wafers using the LB method and even used as a seed layer to grow minimal-defect MFI films of tunable thickness. One idea we have is to study the potential of GO and MFI for use in hybrids, which can later be annealed to reduce the GO and yield grapheme-zeolite hybrids. Such hybrids might possess interesting properties for catalytic applications, especially for electrochemical and photochemical reactions, with the grapheme acting as an electron-scavenger of sorts, and the MFI acting as the catalyst for the reaction. Thus, the potential of LB for layer-by-layer deposition of alternate layers of GO and MFI will be examined. In addition, we will study the behavior of a binary 2D interfacial system consisting of both GO and MFI, the mixing of these two potential phases and the potential to deposit a homogenous mixture of the two components directly onto substrates such as Silicon wafer.

References

Adams, J., and D. Pendelbury, "Global Research Report," *Thomson Reuters*: (2011).

Allen, M. J., V. C Tung, and R. B. Kaner, "Honeycomb Carbon: A Review of Graphene," *Chem. Rev*. **110**, 132-146 (2010).

Al Ali, S. H., M. Al Qubaisi, M. Z. Hussein, M. Ismail, Z. Zainal, and M. N. Hakim, "Comparative study of Mg/Al- and Zn/Al-layered double hydroxide-pendropil erbumine nanocomposites for inhibition of angisotensin-converting enzyme" *Int J Nanomed*. **7**, 4251 (2012).

Angstron Materials, N002-PS, http://www.angstronmaterials.com/, (accessed July 2015).

Aragon, S. R., and R. Pecora, "Theory of dynamic light scattering from polydisperse systems," *J. Chem. Phys.* **64**, 2395 (1976).

Brenner, H., "Rheology of a Dilute Suspension of Axisymmetric Brownian Particles," *Int. J. Multiphase Flow*. **1**, 195-341 (1974).

Bae, S., H. Kim, Y. Lee, X. Xu, J. Park, Y. Zheng, J. Balakrishnan, H. Kim, Y. Song, Y. Kim, K. S. Kim, B. Özyilmaz, J. Ahn, B. H. Hong, and S. Iijima, "Roll-to-roll production of 20-inch graphene films for transparent electrodes," *Nature Nanotech.* **5**, 574-578 (2010).

"Basic Image Enhancement and Analysis Techniques." *MathWorks*. The MathWorks, Inc., 1 Jan. 2014. Web. 2 Feb. 2015.

Bing-Bing, F., H. Guo, R. Zhang, Y. Jia, and S. Chun-Yah, "Structural Evolution during the Oxidation Process of Graphie," *Chin. Phys. Lett.*, **31**, 1-4 (2014).

Bolotin, K. I., K. J. Sikes, Z. Jiang, M. Klima, G. Fudenberg, J. Hone, P. Kim, and H. L. Stormer, "Ultrahigh Electron Mobility in Suspended Graphene," *Solid State Communications*. **146,** 351–355 (2008).

Botcha, V. D., P. K. Narayanam, G. Singh, S. S. Talwar, R. S. Srinivasa, and S. S. Major, "Effect of Substrate and Subphase Conditions on the Surface Morphology of Graphene Oxide Sheets Prepared by Langmuir–Blodgett Technique," *Colloids and Surfaces A: Physicochemical and Engineering Aspects.* **452,** 65–72 (2014).

Boukhvalov, D. W., and M. I. Katsnelson, "Modeling of Graphite Oxide," *Journal of the American Chemical Society*. **130**, 10697-10701, (2008).

Briggs, D., and G. Beamson, “High resolution XPS of organic polymers: The scienta ESCA300 database,” New York: John Wiley and Sons, (1992).

Brodie, B.C., “Sur le poids atomique du graphite,” *Ann Chim Phys.* **59**, 466-472 (1859).

Bunch, J. S., “Mechanical and Electrical Properties of Graphene Sheets,” *Cornell*. (2008).

Chua, C. K., A. Ambrosi, Z. Sofer, A. Mackova, V. Havranek, I. Tomandl, and M. Pumera, "Chemical Preparation of Graphene Materials Results in Extensive Unintentional Doping with Heteroatoms and Metals," *Chem. Eur. J.*, **20**, 15760-15767 (2014).

Cote, L. J., F. Kim, and J. Huang, “Langmuir−Blodgett Assembly of Graphite Oxide Single Layers,” *J. Am. Chem. Soc*. **131,** 1043–1049 (2009).

Cote, L. J., J. Kim, V. C. Tung, J. Luo, F. Kim, and J. Huang, “Graphene Oxide as Surfactant Sheets,” *Pure and Applied Chemistry*. **83**, 95-110 (2011).

Taha-Tijerina, J., D. Venkataramani, C. P. Aichele, C. S. Tiwary, J. E. Smay, A. Mathkar, P. Chang, and P. M. Ajayan, "Quantification of the Particle Size and Stability of Graphne Oxide in a Variety of Solvents," *Particle System Characterization*. **32**, 334-339 (2015).

Dikin, D. A., “Preparation and characterization of graphene oxide paper,” *Nature Letters*. **448**, 457-460 (2007).

Dimiev, A. M., and J. M. Tour, “Mechanism of GOFormation,” *ACS Nano*. **8,** (2014).

Dimiev, A. M., and T. A. Polson, “Contesting the two-component structural model of GO and re-examining the chemistry of GO in basic media,” *Carbon*. **92**, 544-554 (2015).

Eigler, S., M. Enzelberger-Heim, S. Grimm, P. Hofmann, W. Kroener, A. Geworski, C. Dotzer, M. Rockert, J. Xiao, C. Papp, O. Lytken, H. Steinruck, P. Muller and A. Hirsch, "Wet Chemical Synthesis of Graphene," *Advanced Materials*. **25**, 3583-3587 (2013).

Garg, B., T. Bisht, and Y. Ling, “Graphene-Based Nanomaterials as Heterogeneous Acid Catalysts: A Comprehensive Perspective,” *Molecules*. **19**, 14582-14614 (2014).

Geim, A. K., and K. S. Novoselov, “The Rise of Graphene,” *Nature Materials*. **6**, 183–191 (2007).

Geim, A. K., “Graphene: Status and Prospects,” *Science*. **324**, 1530-1534 (2009).

Goh, M. S., A. Bonanni, A. Ambrosi, Z. Sofer and M. Pumera, "Chemically-modified graphenes for oxidation of DNA bases: analytical parameters," *R. Soc. Chem*. **136**, 4738-4744 (2011).

Shi, G., Y. Tu, H. Fang and J. Yang, "High Correlation between Oxidation Loci on GO," *Angewandte Communcations*. **53**, 10190-10194 (2014).

Huang, J., J. Kim, L. J. Cote and F. Kim, "Visualizing Graphene Based Sheets by Fluroescence Quenching Microscopy," *J. Am. Chem. Soc*. **132** (1), pp 260-267 (2010).

Hummers, W. S. and R. E. Offeman, "Preparation of Graphitic Oxide," *J. Am. Chem. Soc.* **80,** 1339–1339 (1958).

Imperiali, L., K. Liao, C. Clasen, J. Fransaer, C. W. Macosko, and J. Vermant, "Interfacial Rheology and Structure of Tiled Graphene Oxide Sheets." *Langmuir*. **28,** 7990–8000 (2012).

"Identifying Round Objects." *MathWorks*. The MathWorks, Inc., 1 Jan. 2014. Web. 2 Feb. 2015.

Jalili, R., S. H. Aboutalebi, D. Esrafilzadeh, K. Konstantinov, J. M. Razal, S. E. Moulton, and G. G. Wallice, "Formation and processability of liquid crystalline dispersions of GO", *Mater. Horiz.* **1**, 87-90 (2014).

Jia, J., K. Jingjing, C. Kan, X. Lin, and X. Shen, "Effects of processing and material parameters on synthesis of monolayer ultralarge graphene oxdie sheets," *Carbon*. **77**, 244-254 (2014).

Johnson, N. L., S. Kotz, and N. Balakrishnan, "14: Lognormal Distributions", *Continuous univariate distributions. **1***, (1994), Wiley Series in Probability and Mathematical Statistics: Applied Probability and Statistics (2nd ed.), New York: John Wiley & Sons, ISBN 978-0-471-58495-7.

Kooij, F. M., E. S. Boak, and A. P. Philipse, "Rheology of Dilute Suspensions of Hard Platelike Colloids," *J. Coll Interface Sci*. **235**, 344–349 (2001).

Kreiger, I. M. "Rheology of monodisperse lattices", *Adv. Colloid Interface Sci*. **3**, 111-136 (1972).

Kuhn, W., and H. Kuhn, "The dependence of the viscosity on velocity gradient in suspensions and solutions of fibrous macromolecules," *Helv. Chim. Acta*. **28**, 97-127 (1945).

Kim, F., J. Luo, R. Cruz-Silva, L J. Cote, K. Sohn, and J. Huang, "Self Propagating Domino-like Reactions in Oxidized Graphite", *Adv. Func. Mat*. **20**, 2867-2873 (2010).

Kim, H., J. Sung, H. Chung, Y. J. Choi, D. Y. Kim, and D. Kim, "Covalently Functionalized Graphene Composites: Mechanistic Study of Interfacial Fluorescence Quenching and Recovery Processes," *J. Phys. Chem*. **119**, 11327-11336 (2015).

Koch, K. R., "Oxidation by Mn_2O_7: An impressive demonstration of the powerful oxidizing property of dimanganeseheptoxide," *J. Chem. Educ*. **11**, 973 (1982).

Kosynkin, D. V., A. L. Higginbotham, A. Sinitskii, J. R. Lomeda, A. Dimiev, B. K. Price and J. M. Tour, "Longitudinal unzipping of carbon nanotubes to form graphene nanoribbons," *Nature*. **458**, 872-876, (2009).

Kumar, S. C., S. Naqvi, N. Gupta, K. Gaurav, S. Khan, P. Kumar, A. Rana, R. K. Singh and R. Bharadwaj, "Bulk synthesis of highly conducting GO with long range ordering," *RSC Adv*, **5**, 35893-35898 (2015).

Kaner, R. B. and J. K. Wassei, "Graphene, a promising transparent conductor," *Materials Today*. **13** (3), 52-59 (2010) .

Kim, H., A. A. Abdulla, and C. W. Macosko, "Graphene/Polymer Nanocomposites," *Macromolecules*. **43**, 6515-6530 (2010).

Kim, J., L. J. Cote, F. Kim, and J. Huang, "Visualizing Graphene Based Sheets by Fluorescence Quenching Microscopy," *J. Am. Chem. Soc.* **132,** 260–267 (2010).

Kim, K. S., Y. Zhao, H. Jang, S. Yoon Lee, J. M. Kim, K. S. Kim, J. Ahn, P. Kim, J. Choi, and B. H. Hong, "Large-Scale Pattern Growth of Graphene Films for Stretchable Transparent Electrodes," *Nature*. **457,** 706–710 (2009).

Kyle, J. R, A. Guvenc, W. Wang, M. Ghazinejad, J. Lin, S. Guo, C. S. Ozkan, and M. Ozkan, "Centimeter-Scale High-Resolution Metrology of Entire CVD-Grown Graphene Sheets," *Small*. **7**, 2598–2606 (2011).

Marcano, D. C., D. V. Kosynkin, J. M. Berlin, A. Sinitskii, Z. Sun, A. Slesarev, L. B. Alemany, W. Lu, and James M. Tour, "Improved Synthesis of Graphene Oxide," *ACS Nano*. **4**, 4806-4814 (2010).

Leal, L. G., and E. J. Hinch, "The effect of weak Brownian rotations on particles inshear flow," *J. Fluid Mech*. **46**, 685-703 (1971).

Leal, L. G., and E. J. Hinch, "The rheology of a suspension of nearly spherical particles subject to Brownian rotations," *J. Fluid Mech*. **55**(4), 745-765 (1972).

Lee, C., X. Wei, J. W. Kysar, and J. Hone, “Measurement of the Elastic Properties and Intrinsic Strength of Monolayer Graphene,” *Science*. **321,** 385–388 (2008).

De, S., P. J. King, M. Lotya, A. O’Neill, E. M. Doherty, Y. Hernandez, G. S. Duesberg, and J. N. Coleman, “Flexible, Transparent, Conducting Films of Randomly Stacked Graphene from Surfactant-Stabilized, Oxide-Free Graphene Dispersions,” *Small*. **6,** 458–464 (2010).

Li, J., K. N., Nudin, M. J. McAllister, R. K. Prud'homme, I. A. Aksay, and R. Car, “Oxygen-Driven Unzipping of Graphitic Materials,” *Physical Review Letters*. **96**, 1-4 (2006).

Li, X., Y. Zhu, W. Cai, H. Borysiak, B. Han, D. Chen, R. D. Piner, L. Colombo, and R. S. Ruoff, “Transfer of Large-Area Graphene Films for High- Performance Transparent Conductive Electrodes,” *Nanoletters*. **9**, 4359-4363 (2009) .

Lifshitz, L. D., and E. M. Lifshitz, *Statistical Physics*. **Part I**. Pergamon Press: Oxford, (1980).

Moghaddam, S., and A. Paneri, "Impact of synthesis conditions on physicochemical and transport characteristics of GO laminates," *Carbon*. **86**, 245-255 (2015).

Moo, J. G., B. Khezri, R. D. Webster, and M. Pumera, "Graphene Oxides Prepared by Hummers', Hofmann', and Staudenmaier's Methods: Dramatic Influences on Heavy Metal-Ion Adsorption," *Chem. Phys. Chem*. **15**, 2922-2929 (2014).

Sharma, M., D. Mondal, C. Mukesh, and K. Prasad, “Studies on the effect of bio-ionic liquid structures on the spontaneous reduction and dispersion stability of GO in aquesous media,” *RSC Adv*. **4**, 42197-42201 (2013).

Nair, R. R., P. Blake, A. N. Grigorenko, K. S. Novoselov, T. J. Booth, T. Stauber, N. M. R. Peres, and A. K. Geim, “Fine Structure Constant Defines Visual Transparency of Graphene,” *Science*. **320**, 1308 (2008).

Nagahara, L. A., K. Hashimoto, A. Fujishima, D. Snowden-lfft, and P.B. Price, “Mica etch pits as a height calibration source for atomic force microscopy,” *J. Vac. Sci. Technol. B*. **12**, 1694-1697 (1994).

Novoselov, K. S., A. K. Geim, S. V. Morozov, D. Jiang, Y. Zhang, S. V. Dubonos, I. V. Grigorieva, and A. A. Firsov, “Electric field effect in atomically thin carbon films,” *Science*. **306**, 666-669 (2004).

Onsager, L., "The Effects of Shapes on the Interaction of Colloidal Particles,” *Ann. N. Y. Acad. Sci*. **51**, 627–659 (1949)

Ortega, A., and J. G. de la Torre, "Hydrodynamic properties of rodlike and disklike particles in dilute solution," *J. Chem. Phys*. **119**, 9914 (2003).

Pumera, M., "Graphene-based nanomaterials and their electrochemistry," *Chemical Society Reviews*. **39**, 4146-4157 (2010)

Rao, C. N. R., A. K. Sood, K. S. Subrahmanyam and A. Govindaraj, "Graphene: The New Two-Dimensional Nanomaterial," *Angew. Chem. Int. Ed*. **48**, 7552-7777 (2009)

Ren, Z., E. Kim, S. W. Pattinson, K. S. Subrahmanyam, C. N. R. Rao, A. K. Cheetham, and D. Eder, "Hybridizing photoactive zeolites with graphene: a powerful strategy to superior photocatalytic properties," *Chemical Science*. **3**, 209-216 (2012).

Schwarz, G., "Zur theorie der Leitfahigkeitsanisotropie von Polyelektrolyten in losung", *Z. Physik*. **145**, 563 (1956).

Stewart, W. E., and J. P. Sorenson,"Hydrodynamic interaction effects in rigid dumbbell suspensions. II. Computations for steady shear flow", *Trans. Soc. Rheol.* **16**, 1-13 (1972).

Stankovich, S., D. A. Dikin, R. D. Piner, K. A. Kohlhaas, A. Kleinhammes, A., Y. Jia, W. Wu, S. T. Nguyen, and R. Ruoff, "Synthesis of graphene-based nanosheets via chemical reduction of exfoliated graphite oxide", *Carbon*. **45**, 1558- 1565 (2007).

Staudenmaier, J. "Verfahren zur darstellung der graphitsaure", *Ber. Dtsch. Chem. Ges.* **31**, 1481-1487 (1898).

Szabó, T., O. Berkesi, and I. Dékány, "DRIFT study of deuterium-exchanged graphite oxide," *Carbon*. **43**(15), 3186-3189 (2005).

Taylor, G. I., "Stability of a viscous liquid contained between two rotating cylinders," *Phil. Trans. Roy. Soc.* **223**, 289 (1923).

Timofeeva, A. A., V. V. Shinkarev, K.D. Dyukova, A.V. Ukhina, E.A. Maksimovskii, S.I. Yusin, and A. G. Bannov, "Syntheiss and Studies of Properties of Graphite Oxide and Thermally Expanded Graphite," *Protection of Metals and Physical Chemistry of Surfaces*. **50**, 183-190 (2014).

Tour, J. M. and D V. Kosynkin, "Highly oxidized grapheme oxide and methods for production thereof", *US 20120129736 A1*. (2012).

Wang, G., X. Shen, B. Wang, J. Yao and J. Park, "Synthesis and characterization of hydrophilic and organophilic graphene nanosheets," *Carbon*. **47**, 1359-1364 (2009).

Waltman, R. J., J. Pacansky, C. W. Bates Jr., "X-ray photoelectron spectroscopic studies on organic photoconductors: Evaluation of atomic charges on chlorodiane blue and p-(diethylamino)benzaldehyde diphenylhydrazone", *Chem Mater*. **5**(12), 1799–804 (1993).

Xiang, C., C. C. Young, X. Wang, G. Cerioti, J. Lin, J. Kono, X. Wang, Z. Yan, C. Hwang, M. Pasquali and J. M. Tour, "Large Flake GO Fibers with Unconventional 100% Knot Efficiency and Highly Aligned Small Flake GO Fibers," *Adv. Mat.* **25**, 4592-4597 (2013).

Zhang, Y. B., Y. W. Tan, H. L. Stormer, and P. Kim, "Experimental Observation of the Quantum Hall Effect and Berry's Phase in Graphene," *Nature*. **438**, 201-204 (2005).

Zhou, X. and Z. Liu, "A scalable, solution-phase processing route to Graphene Oxide and graphene ultralarge sheets," *Chemical Communications*. **46**, 2611-2613 (2010).

Zhu, Y.G., Y. Wang, I. J. Xie, G. Cao, and T. Zhu, "Effects of Graphene Oxide Function Groups on SnO2/Graphene Nanocomposites for Lithium Storage Application", *Electrochimica Acta.* **154**, 338-344 (2015).

Zuo, P., H. Feng, Z. Xu, L. Zhang, Y. Zhang, W. Xia, and W. Zhang, "Fabrication of biocompatible and mechanically reinforced GO-chitosan nanocomposite films," *Chem. Central Journal*. **7**, (2013).

Appendix A MATLAB Image Analysis

A.1 Proposed MATLAB method

The matlab method we use generates total surface area data for objects with holes. This method consists of various subroutines which we outline here. Firstly, a certain threshold contrast value is set to obtain a binary image. The binary image consists of pixels which can be "particle" or "non-particle" pixels. Then default functions 'imfill' and 'imclose' are used to fill gaps and holes and to obtain even surfaces to correct for any errors in the binary image processing. The 'bwboundaries' function can be used to trace and label boundaries of particles and holes. The 'Regionprop' function output area and centroid data for particles in the image, and metric data are calculated to identify round objects. Matlab built-in functions and custom-defined function are used for image analysis. Matlab contains a powerful suite of algorithms to aid in this task. The algorithms and effects of these functions are discussed as follows as they are implemented in our code.

A.1.1 graythresh and im2bw

The first step in image processing is choosing the appropriate settings to interpret the image. The graythresh function computes a global threshold contrast value for an image. This program optimizes the threshold contrast level that differentiates between the particle and the backround. The threshold contrast level is passed to im2bw which then converts the image into binary pixels where each pixel can be in a non-particle or particle state.

The graythresh function uses the Otsu Method. The Otsu Method assumes the image only contains two classes of pixels, foreground pixels and background pixels, which are separated by a threshold contrast value. Assuming a threshold value, the method calculates weight, mean and variance of the intensity of the foreground pixels and background pixels. An optimization protocol is invoked to reduce the variance in intensity within the different classes of pixels. Iterating through all the possible threshold

values, threshold value with the lowest within-class variance is selected as a global threshold value.

By using 'im2bw', all pixels in the input image with luminance greater than the threshold value passed by ‘graythresh’ will be replaced by the value 1 (white), and other pixels are replaced by 0 (black). This results in a binary image that can be passed to other algorithms. It should be noted that each of the binary values in Matlab are stored in the memory as double-class variables, increasing the amount of memory used when compared to other languages such as C.

A.1.2 bwconncomp and regionprops

The binary image is passed to the networking subroutines defined by ‘bwconncomp’. The subroutine ‘bwconncomp’ can find connected components in a binary image by solving for the network formed by each pixel to surrounding pixels. The network of pixels defines the particle in the image. ‘Regionprops’ starts to solve for information from the networked data. The latter subroutine returns measurements for each of the networked components (i.e.: particles) for properties such as area and perimeter. For area, ‘regionprops’ returns the actual number of pixels in each networked component. For perimeter, ‘regionprops’ computes the distance between each adjoining pair of pixels around the border of the networked components.

A.1.3 Imcomplement

Sometimes, it is necessary to invert the values assigned to each pixel. The subroutine ‘imcomplement’ does that for us. The function computes the complement of the image. In the complement of a binary image, 0 (black) becomes 1(white) and ones become zeros. This is analogous to the negation command in binary logic.

A.1.4 imclearborder

The next steps are to remove particles that may skew the sample sizes from the population. The easiest particles to identify and remove are the ones connected to the edges. Ths process is similar to the deconstruction of a jigsaw puzzle; the connected pictures to the edges are the easiest to identify. Using the imclearborder function, pixels

and connected pixels on the border of the image are cleared. This exists because the particles that are cropped by the edges are not true representations of the imaged particles. This may result in a malrepresentation of particle size in the sample. This function eliminates that error.

A.1.5 bwareaopen

This function filters out any pixels that are defined as small particles based on particle size. This allows us to sift the puzzle pieces so that any dust and grim that may have fallen on the coating and is showing up on the image is removed from the final product. The filter removes fine particulates that we know that the optical imaging cannot resolve. In our case, any particle less than 350 nm would be filtered by this function. It determines the connected components by 'bwconncomp', computes area of each of the components using 'regionprops', and clears components that have fewer than certain pixels.

A.1.6 edge

The 'edge' function can find edges of components in the image using the 'canny' method. The function looks for local maxima of the gradient of the image and uses two thresholds to detect strong and weak edges. If weak edges are connected to strong edges, the former are also shown in the output.

A.1.7 filledgegaps

The filledgegaps function is the creation of Peter Kovesi (2013) from the University of Western Australia. The filledgegaps solves current issues that we were experiencing with the small holes that were appearing in our previous images. After edge detection, there are small gaps between edge fragments of components. 'filledgegaps' function can fill the gaps by algorithm as follows:

1. Input the gapsize, an arbitrary value corresponding to a pixel size, e.g. gapsize=7
2. Generate binary circles with the gapsize's radius
3. Find endpoints of edges and isolated pixels
4. Place circles at endpoint and isolated pixels
5. Thin the image. Overlapping circles become lines.

6. Find remaining circles (not connected fragment), fill and re-thin until there is no endpoint of edges.

A.2 AFM and FQM Image Analysis

A.2.8 Introduction and Current Problems

Acquiring defect free and images of dispersed nanoparticles is only half the challenge presented in optically characterizing polydispersity of nanoparticles. The other half is designing a software package to analyze these particles, which is a must for acquiring significant sample sizes to characterize the population because of the nature of the simple and repetitious nature of such an analysis. Refining this technique would significantly reduce the man hours currently being assigned to such endeavours. Current problems in the field include particle edge detection and detecting particles on the edges of images.

A.2.9 Method and example

A.2.9.1 AFM images with uniform background.

Now we shall illustrate what each of the subroutines is doing to an actual image. In our proposed Matlab method (see code in **Appendix A.4**), first, a grayscale AFM image is converted to a binary one by setting a threshold value. The Matlab function ‘greythresh’ is used to automatically compute an optimal global threshold contrast value, and the ‘im2bw’ function is used to convert grayscale image to a binary one. Automatically determining threshold value avoids checking and adjusting threshold according to various images thereby leading to more accurate results.

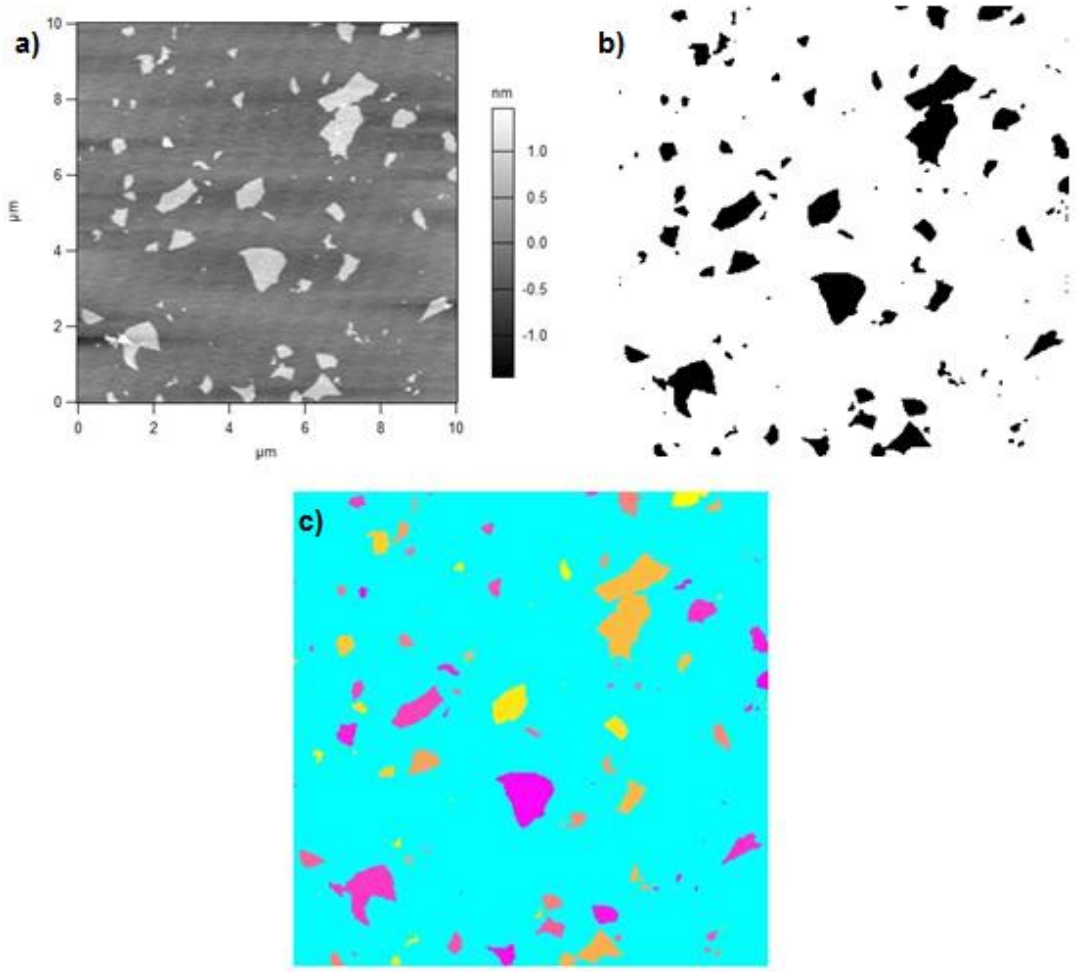

Figure A2-1. (a) The original AFM image, b) the binary image processed by Matlab, and c) an RBG image produced from the post-processed image in b).

Secondly, since the desired GO particles are separated and have connected boundaries, the function ‘bwconncomp’ can be used to find connected components in the image. Each nanoparticle consists of multiple connected components that the algorithm recognizes and groups together. Once organized in such a manner, the particle is labeled in RBG color (Figure c). Color labels show shapes of each nanoparticle, which makes it easier for researchers to observe major morphological characteristics of particles through images. This is what we refer to as poymorphicity of GO, as shown by the use of at least three colors to identify the particle in Figure 7c). Lastly, area and perimeters of particles in the image are estimated using ‘regionprops’ function. The function uses the networked data to draw pixel density for each particle.

In order to verify our results, we employ the commonly used imageJ software. imageJ can automatically adjust threshold, convert greyscale image to a binary one and analyze particles' areas and perimeters. Therefore, imageJ is used to verify the accuracy of Matlab method by testing consistency between the results obtained from imageJ and Matlab.

A.2.9.2 FQM images with even background and particles with yellow borders

During image analysis using Matlab and imageJ, both programs use colour definitions to store information. Small particles, defined as particles fewer than 5 pixels in size, are tagged as yellow particles. These are, in all likelihood, debris on the surface of the coating, and so should be discared from our size analysis. Even if these small particles were genuine GO particles, we are unable to visualize them appropriately using FQM and so we are unable to get accurate sizing data. In either case, it is difficult to discern the true nature of these particles from FQM alone and AFM images would need to be invoked to augment the particle distribution by accounting for small particles, distinguishing them from surrounding debris, and adding that tail to the distribution. In Matlab, 'bwareaopen' function is used to remove these yellow-tagged particles from the FQM images. In imageJ, when analyzing particles, size is input as 5 to infinity in order to exclude the border of particles.

The Matlab default setting for image analysis is 'bright particles on dark background' and brighter parts are traced. Since particles on the given images can be darker than the surrounding background (this is unanimously true for FQM images), the 'imcomplement' function is used to invert the color of the binary image to fit the default setting.

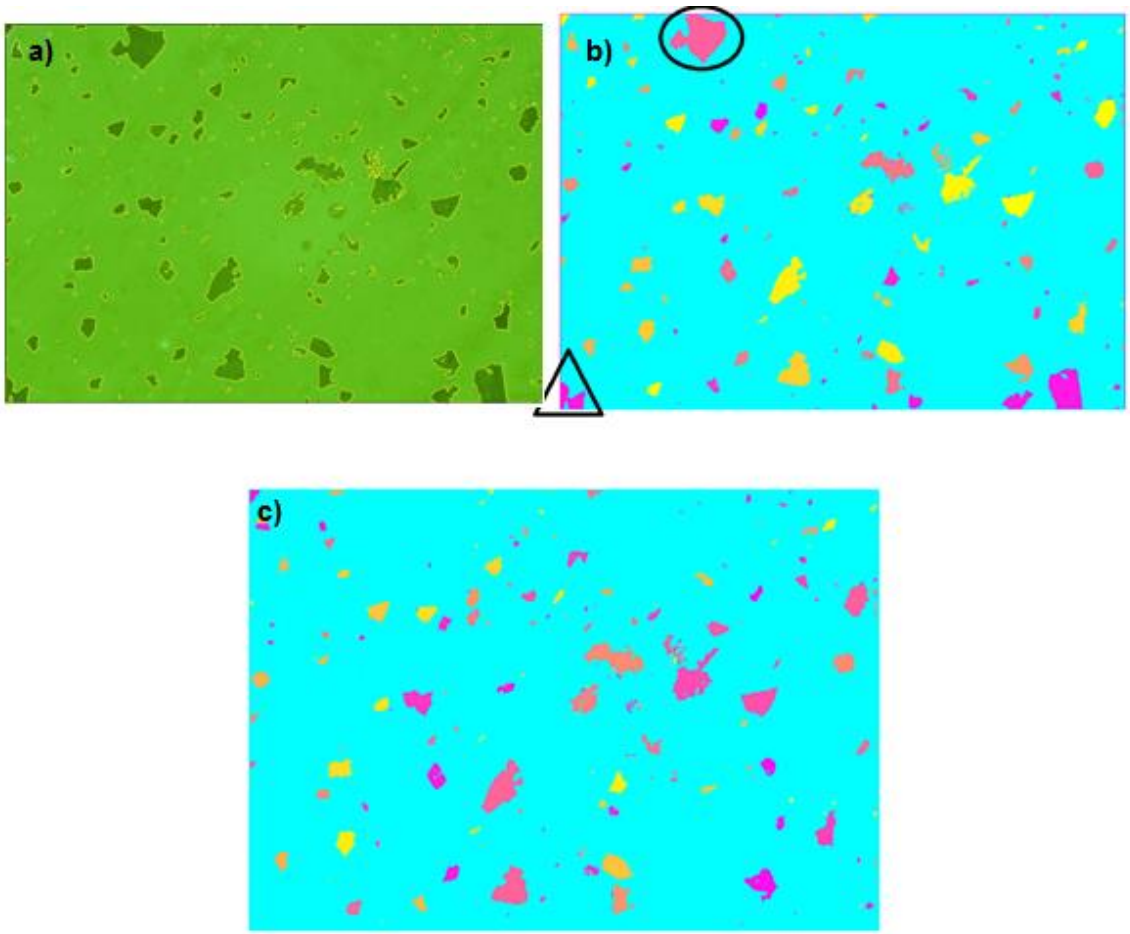

Figure A2-2. The edge problem: a) The original picture b) Matlab's interpretation c) ImageJ's interpretation, depicting the loss of at least two particles due to the edge-detection problem

A.2.9.3 FQM images with uneven background

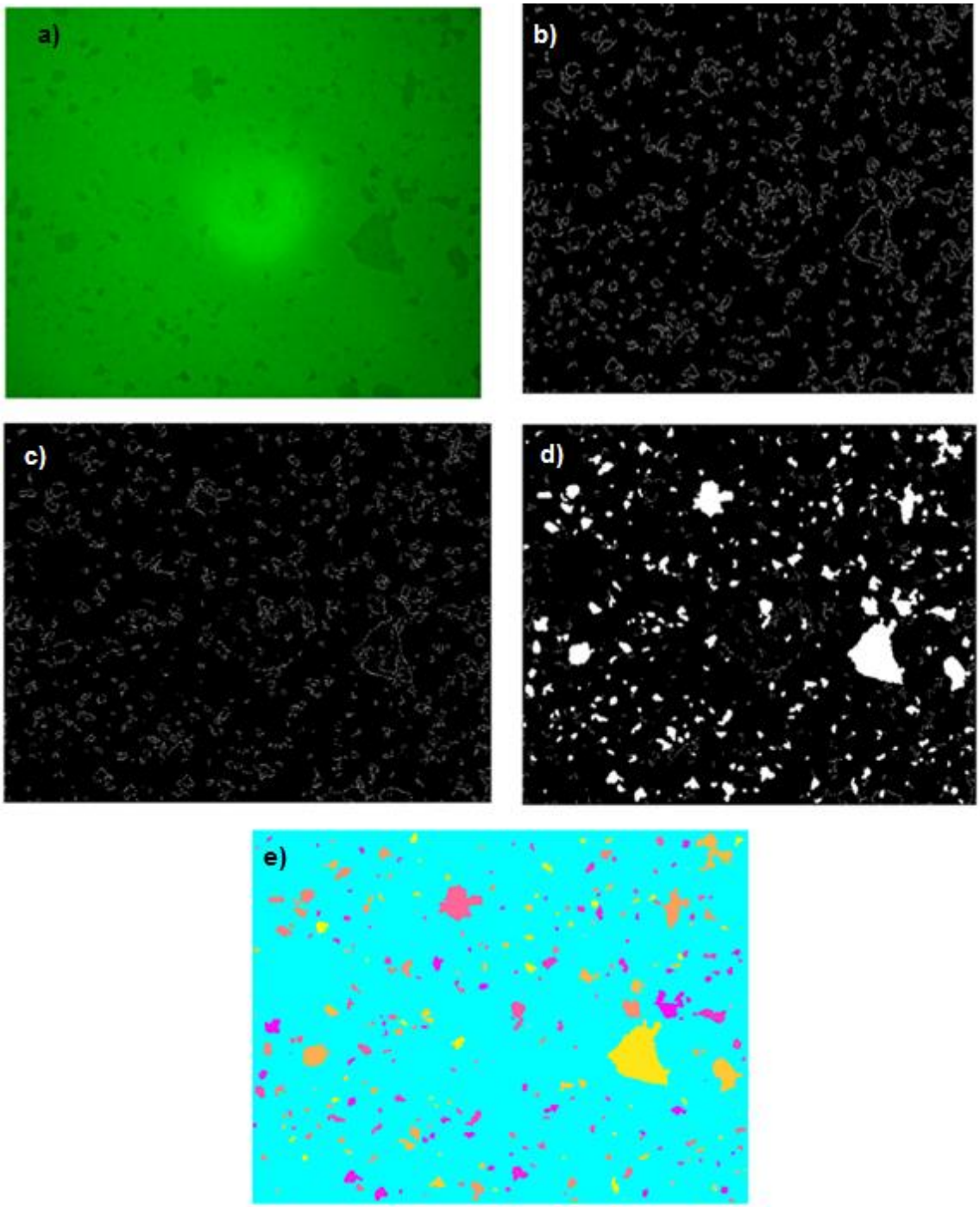

Figure A2-3. a) Original image, b) edges identified by Matlab, c) corrected edges by Matlab post processing, d) holes corrected for and the network for each particle is formed, e) The final colour image produced by Matlab.

Original FQM images are colored images with uneven colored background and darker colored particles (See Figure). Adjusting threshold value and converting images into binary form can separate particles and background, however, as background color is uneven, and contrast between background and particles is low, a clear image visualizing all particles with background removed cannot be obtained through previous method.

To separate background and visualize particles, the 'edge' function is used to trace edges of particles and visualize on a blank background. The edge function increases the contrast between the edges of the particles and the background pictures. Holes inside of edges are filled using 'imfill' function. These edges cannot form continuous boundaries for Matlab to detect a particle. Therefore, 'filledgegaps' function, written by Peter Kovesi (2013), is used to fill gaps in edge.

We employ the matlab function 'filledgegaps' to fill gaps in edges (See **Appendix A.4**). The strategy used here is, firstly a binary circular blob of radius = gapsize/2 is placed at the end of every edge segment to connect two ends. Gapsize=7 was found to be optimal.

After finding edges, holes with solid edges are filled using 'imfill' and 'bwareaopen' function is used to exclude objects <10 pixels. Particles are labeled in color and are analyzed using similar method as analyzing AFM images.

A.3 Sample comparison of matlab and imageJ for commercial GO

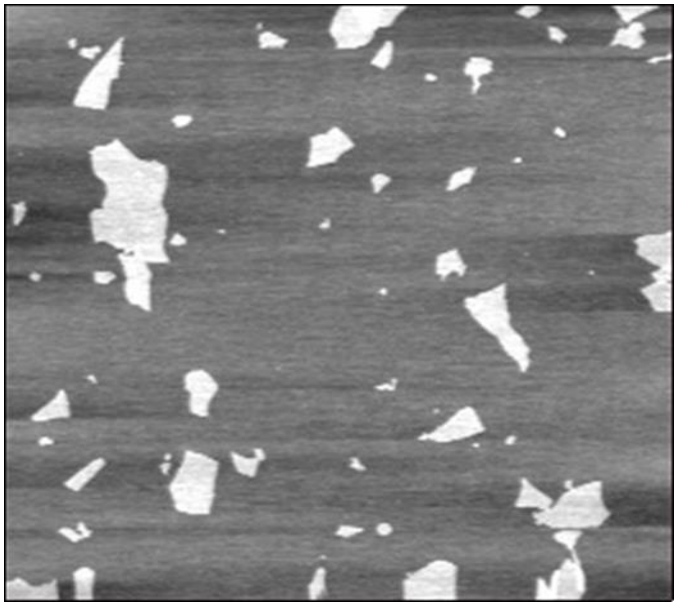

Figure A3-1: Cropped image of commercial GO

Figure A3-2: Binary image of commercial GO

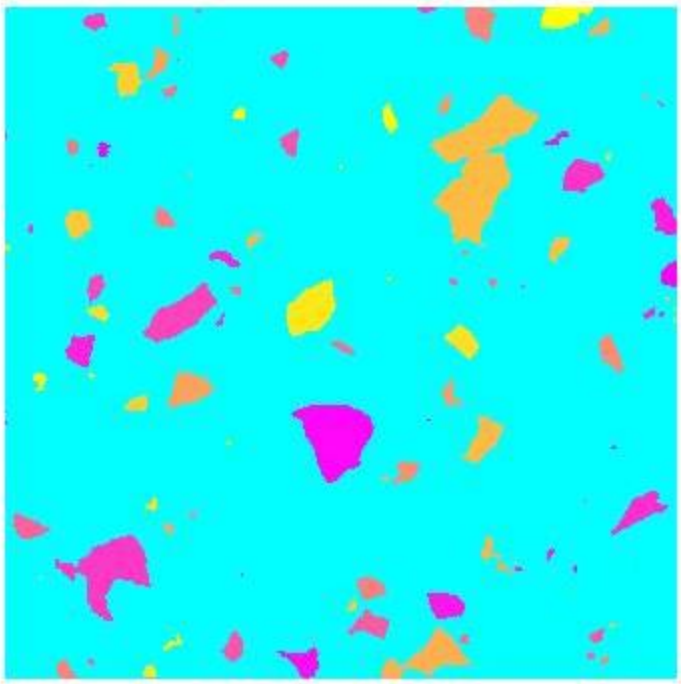

Figure A3-3. Commercial GO image, nanoparticles are color labeled by Matlab

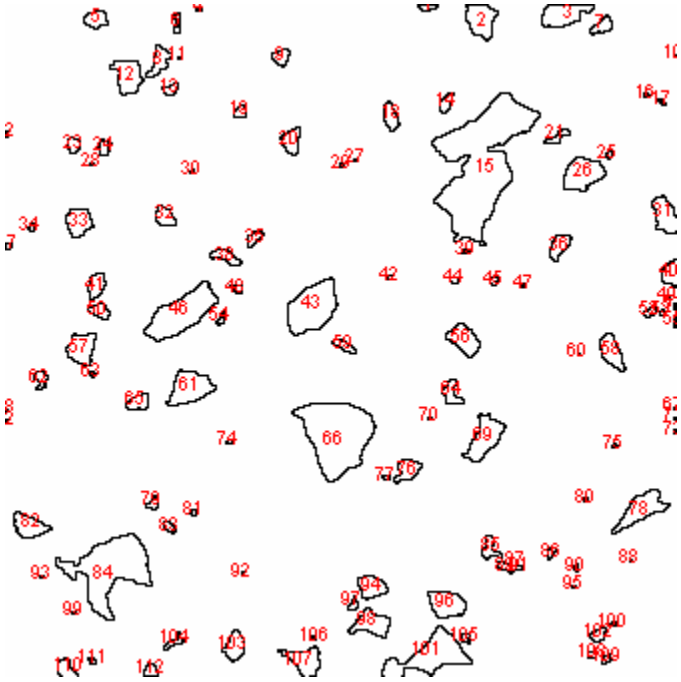

Figure A3-4. commercial GO image, nanoparticles are labeled by imageJ

Table A3-1. Comparison between imageJ and matlab results for AFM of commercial GO. Sample results shown for 75 particles, with the average for all analyzed particles reported at the bottom of the table

	ImageJ		MATLAB Method			
	Area	Perim.	Area	Perim.	area diff%	peri diff%
1	1835	268.434	1835	274.3919	0%	2%
2	981	134.125	981	133.0538	0%	1%
3	875	175.581	875	178.6102	0%	2%
4	508	104.368	508	103.2965	0%	1%
5	470	123.196	470	124.468	0%	1%
6	465	87.497	465	85.8406	0%	2%
7	265	70.77	265	69.6985	0%	2%
8	245	63.355	245	62.2843	0%	2%
9	240	74.912	240	74.4264	0%	1%
10	236	82.326	236	80.669	0%	2%
11	205	67.456	205	66.3848	0%	2%
12	193	57.113	193	56.0416	0%	2%
13	189	54.284	189	53.2132	0%	2%
14	181	58.284	181	57.799	0%	1%
15	166	54.284	166	52.6274	0%	3%
16	166	62.77	166	61.6985	0%	2%
17	164	60.184	164	59.6985	0%	1%
18	162	53.698	162	52.0416	0%	3%
19	161	50.426	161	49.3553	0%	2%
20	143	53.355	143	51.6985	0%	3%
21	140	46.042	140	44.9706	0%	2%
22	134	50.527	134	48.8701	0%	3%
23	122	43.456	122	42.3848	0%	2%
24	106	41.113	106	40.6274	0%	1%
25	96	42.527	96	42.0416	0%	1%
26	93	46.527	93	47.2132	0%	1%
27	88	38.627	88	36.9706	0%	4%
28	83	38.042	83	36.3848	0%	4%
29	83	36.385	82	33.8995	1%	7%
30	81	37.213	81	35.5563	0%	4%
31	75	33.799	75	32.1421	0%	5%
32	71	36.627	71	31.3137	0%	15%
33	71	32.385	71	34.3848	0%	6%
34	68	39.213	68	38.1421	0%	3%

35	66	38.87	66	30.7279	0%	21%
36	66	32.385	66	37.799	0%	17%
37	65	31.799	65	30.7279	0%	3%
38	58	38.042	58	37.5563	0%	1%
39	57	32.87	57	31.2132	0%	5%
40	55	29.799	55	28.1421	0%	6%
41	51	27.799	51	26.1421	0%	6%
42	42	26.385	42	24.7279	0%	6%
43	40	29.213	40	27.5563	0%	6%
44	40	28.627	40	27.5563	0%	4%
45	38	21.556	38	20.4853	0%	5%
46	37	32.385	37	22.7279	0%	30%
47	37	24.385	37	31.3137	0%	28%
48	37	23.556	37	21.8995	0%	7%
49	35	22.142	34	22.7279	3%	3%
50	34	24.385	34	19.6569	0%	19%
51	30	22.142	30	20.4853	0%	7%
52	29	19.314	29	28.9706	0%	50%
53	29	30.627	29	17.6569	0%	42%
54	24	24.728	24	18.4853	0%	25%
55	24	20.142	24	23.0711	0%	15%
56	23	20.971	23	19.8995	0%	5%
57	22	21.899	22	19.6569	0%	10%
58	21	18.142	21	15.8995	0%	12%
59	21	17.556	21	16.4853	0%	6%
60	20	19.314	20	17.0711	0%	12%
61	18	16.485	18	14.2426	0%	14%
62	17	16.728	17	15.0711	0%	10%
63	15	15.899	15	13.6569	0%	14%
64	15	14.728	15	13.0711	0%	11%
65	14	18.142	14	15.8995	0%	12%
66	13	12.485	13	10.8284	0%	13%
67	12	11.657	12	10	0%	14%
68	11	11.071	11	9.4142	0%	15%
69	9	10.485	9	8.8284	0%	16%
70	9	10.485	9	8.8284	0%	16%
				Avg	1%	14%

Table A3-2. Difference between data obtained from Matlab and imageJ for a number of AFM images of unsonicated (A3) and probe-sonicated (A3P) GO samples. Sample results are shown for 50 particles, with the average difference for all analyzed particles shown at the bottom.

	A3_1		A3_2		A3P_1		A3P_2	s	A3P_3	
	area diff%	peri diff%	area diff%	peri diff%	area diff%	peri diff%	area diff%	peri diff%	area diff%	peri diff%
1	0%	1%	0%	1%	0%	1%	0%	1%	0%	2%
2	3%	16%	0%	1%	0%	2%	0%	1%	0%	1%
3	0%	0%	0%	1%	1%	11%	0%	0%	0%	1%
4	0%	3%	0%	0%	0%	1%	0%	1%	0%	1%
5	1%	3%	0%	1%	1%	1%	0%	0%	0%	2%
6	0%	1%	0%	2%	1%	0%	0%	1%	0%	2%
7	1%	1%	0%	1%	0%	1%	0%	1%	0%	2%
8	1%	1%	0%	1%	0%	2%	0%	0%	0%	1%
9	1%	2%	0%	3%	0%	0%	0%	1%	0%	2%
10	1%	1%	0%	2%	2%	1%	0%	1%	0%	2%
11	2%	1%	1%	1%	1%	1%	0%	1%	0%	2%
12	3%	49%	0%	1%	0%	0%	19%	41%	0%	2%
13	3%	33%	1%	1%	0%	2%	33%	26%	0%	1%
14	1%	3%	1%	1%	12%	98%	5%	10%	0%	3%
15	3%	2%	0%	1%	2%	16%	1%	1%	0%	2%
16	2%	2%	1%	3%	1%	29%	0%	0%	0%	1%
17	0%	3%	0%	0%	0%	2%	0%	2%	0%	3%
18	2%	2%	0%	1%	1%	23%	0%	3%	0%	2%
19	1%	4%	0%	1%	1%	12%	0%	1%	0%	3%
20	1%	2%	0%	2%	0%	0%	5%	13%	0%	2%
21	3%	40%	1%	0%	0%	3%	8%	8%	0%	3%
22	4%	22%	0%	2%	0%	36%	4%	5%	0%	3%
23	0%	2%	1%	2%	0%	22%	1%	11%	0%	1%
24	0%	2%	1%	2%	2%	1%	3%	8%	0%	1%
25	1%	6%	0%	1%	11%	147%	32%	31%	0%	1%
26	1%	2%	1%	6%	5%	5%	3%	4%	0%	4%
27	1%	0%	0%	4%	15%	12%	0%	24%	0%	5%
28	1%	7%	1%	4%	3%	46%	7%	16%	1%	7%
29	1%	4%	0%	1%	2%	3%	11%	4%	0%	5%
30	0%	1%	7%	22%	11%	11%	2%	12%	0%	5%
31	5%	39%	14%	9%	2%	6%	2%	8%	0%	17%
32	5%	1%	3%	26%	2%	11%	2%	20%	0%	6%
33	4%	4%	12%	2%	0%	25%	11%	22%	0%	3%
34	5%	0%	5%	8%	3%	17%	12%	1%	0%	26%
35	3%	10%	1%	18%	3%	1%	3%	40%	0%	14%

36	3%	9%	13%	1%	0%	5%	17%	26%	0%	3%
37	2%	7%	2%	8%	3%	5%	0%	15%	0%	1%
38	1%	16%	0%	4%	6%	12%	7%	44%	0%	5%
39	2%	2%	2%	20%	0%	9%	15%	35%	0%	6%
40	0%	4%	0%	6%	0%	8%	17%	4%	0%	6%
41	0%	4%	2%	19%	0%	13%	5%	6%	0%	7%
42	0%	4%	2%	11%	7%	170%	0%	16%	0%	6%
43	1%	2%	2%	3%	8%	18%	6%	14%	0%	4%
44	1%	12%	4%	9%	18%	26%	0%	13%	0%	5%
45	1%	0%	2%	2%	10%	145%	18%	2%	0%	42%
46	5%	33%	10%	17%	10%	97%	14%	7%	0%	22%
47	9%	7%	2%	5%	11%	11%	17%	2%	0%	8%
48	2%	6%	0%	7%	11%	121%	10%	12%	3%	3%
49	1%	12%	0%	5%	11%	27%	11%	10%	0%	24%
50	1%	11%	3%	2%	0%	27%	25%	22%	0%	8%
	Average Diff %									
	3%	15%	4%	17%	7%	30%	7%	11%	1%	19%

Table A3-3. Comparison of imageJ and matlab results for uneven FQM images of MTD GO. The full comparison was conducted over 250 particles, while we only show sample results for 30 such particles here. The average for the full analysis is shown at the bottom of the table.

Particle #	Matlab Area (μm^2)	ImageJ Area (μm^2)	Perim. (μm)	% Area
1	5368	6821	2568.127	21%
2	4997	6609	1628.802	24%
3	4838	3529	1461.866	37%
4	4805	3412	1121.592	41%
5	4252	3148	905.828	35%
6	3772	3002	1408.452	26%
7	3325	2968	664.649	12%
8	3146	2880	1235.817	9%
9	2750	2631	501.512	5%
10	2486	2111	597.938	18%
11	1760	2077	639.98	15%
12	1653	2040	325.404	19%
13	1562	1819	553.938	14%
14	1531	1786	583.352	14%
15	1482	1726	471.47	14%
16	1465	1722	933.786	15%
17	1465	1621	572.181	10%
18	1444	1598	610.666	10%
19	1326	1422	569.394	7%
20	1296	1401	394.316	7%
21	1210	1344	315.546	10%
22	1189	1283	601.394	7%
23	1176	1278	471.813	8%
24	1169	1237	475.955	5%
25	1157	1172	417.387	1%
26	1130	1151	329.061	2%
27	1112	1143	454.357	3%
28	1103	1117	393.345	1%
29	1065	1116	374.659	5%
30	1065	1103	330.475	3%
31	956	1075	300.09	11%
32	952	1065	362.801	11%
33	938	1054	353.688	11%
34	927	1035	346.132	10%
35	890	1026	258.392	13%
			Average	34%

A.4 Matlab Code

For purposes of completeness we include the code used to analyze AFM images, even-background and uneven-background FQM images.

A.4-1 Code for AFM Images

```
%show original image
IMG = imread('4.tif','tiff');
figure(1);
imshow(IMG);
%1%
%autoselect threshold:
threshold = graythresh(IMG);
%Convert greyscale img to binary
bw = im2bw(IMG,threshold);
figure(2);
%2%
%Find all connected objects in the binary image
%Connectivity parameter is 4
cc = bwconncomp(bw, 4)
cc.NumObjects
%Visualize all connected components in the image
labeled = labelmatrix(cc);
RGB_label = label2rgb(labeled, @spring, 'c', 'shuffle');
imshow(RGB_label)
%3%
%Compute the area of each object in the image using regionprops
```

```
imgdata = regionprops(cc,'Perimeter','Area')
%Create a vector grain_areas to hold the area measurement of each object.
img_areas = [imgdata.Area];
%Perimeter
img_peri = [imgdata.Perimeter];
disp(img_areas')
disp(img_peri')
```

A.4-2. Code for even-background FQM images (finding connected objects)

```
%show original image
IMG = imread('a1.png','png');
figure(1);
imshow(IMG);


%1%
%autoselect threshold:
threshold = graythresh(IMG);
%Convert greyscale img to binary
bw = im2bw(IMG,threshold);
figure(2);
%2%
%inverting the color of image
figure(3);
bwi=imcomplement(bw);
imshow(bwi);
%Find all connected objects in the binary image
%Connectivity parameter is 4
cc = bwconncomp(bw, 4)
```

```
cc.NumObjects
%Visualize all connected components in the image
labeled = labelmatrix(cc);
RGB_label = label2rgb(labeled, @spring, 'c', 'shuffle');
figure(4);
imshow(RGB_label)
%Compute the area of each object in the image using regionprops
imgdata = regionprops(cc, 'Perimeter','Area')
%Create a vector grain_areas to hold the area measurement of each object.
img_areas = [imgdata.Area];
img_peri = [imgdata.Perimeter];
```

A.4-3. Matlab code for uneven FQM images (edge detection method)

```
%show original image
IMG = imread('rsz_after3.png','png');
figure(1);
imshow(IMG);
Igray = rgb2gray(IMG);
Iedge = im2uint8(edge(Igray,'canny',0.2));
figure(2);
imshow(Iedge)
bw = Iedge;
gapsize=3;
bw2 = filledgegaps(bw, gapsize);
figure(4);
imshow(bw2)
bwi=bw2;
```

```
% fill any holes, so that regionprops can be used to estimate
% the area enclosed by each of the boundaries
bwi = imfill(bwi,'holes');
figure(5);
imshow(bwi)
bw=bwi;
bw2=bwareaopen(bw,30,4);
bw= imclearborder(bw2);
bw=bw2;
%Find all connected objects in the binary image
%Connectivity parameter is 4
cc = bwconncomp(bw, 4)
cc.NumObjects
%Visualize all connected components in the image
labeled = labelmatrix(cc);
RGB_label = label2rgb(labeled, @spring, 'c', 'shuffle');
figure(6);
imshow(RGB_label)
%Compute the area of each object in the image using regionprops
imgdata = regionprops(cc,'Perimeter','Area')
%Create a vector grain_areas to hold the area measurement of each object.
img_areas = [imgdata.Area];
%Perimeter
img_peri = [imgdata.Perimeter];
A1=sort(img_areas,'descend');
P=sort(img_peri,'descend');
```

```
A2 = A1*((10/288)^2);

P=P*(10/288);

A=sqrt((4*A2)/pi);

disp(A')

disp(P')

mu = mean(log(A));

sigma = std(log(A));

pmu = mean(log(P));

psigma = std(log(P));

stravgdia=['average=',num2str(mu)];

strstddia=['std=',num2str(sigma)];

stravgperi=['average=',num2str(pmu)];

strstdperi=['std=',num2str(psigma)];

figure(7);

nbins = 25;

hist(A,nbins)

title(['\fontsize{14}  histogram for equivalent diameter', ...

      '\newline \fontsize{10} \color{red} \it ',stravgdia,...

       '\newline \fontsize{10} \color{red} \it ',strstddia]);

xlabel('equivalent diameter in micron')

ylabel('number of particles')

figure(8);

nbins = 25;

hist(P,nbins)

title(['\fontsize{14}  histogram for perimeter', ...

      '\newline \fontsize{10} \color{red} \it ',stravgperi,...
```

```
        '\newline \fontsize{10} \color{red} \it ',strstdperi]);
xlabel('perimeter in micron')
ylabel('number of particles')
Y = lognpdf(A,mu,sigma);
figure(9);
plot(A,Y); grid;
xlabel('Area in micron^2'); ylabel('Lognormal probability')
title('Area lognormal distribution')
Z = lognpdf(P,pmu,psigma);
figure(11);
plot(P,Z); grid;
xlabel('Perimeter in micron'); ylabel('Lognormal probability')
title('Perimeter lognormal distribution')
```

Functions for edge detections:

1) Junction.m

```
function b = junction(x)
   a = [x(1) x(2) x(3) x(6) x(9) x(8) x(7) x(4)]';
   b = [x(2) x(3) x(6) x(9) x(8) x(7) x(4) x(1)]';
   crossings = sum(abs(a-b));
   b = x(5) && crossings >= 6;
```

2) Isolated.m

```
function b = isolated(x)
   b = x(5) && sum(x(:)) == 1;
```

3) findisolatedpixels.m

```
function [r, c] = findisolatedpixels(b)
   lut = makelut(@isolated, 3);
```

```
    isolated = applylut(b, lut);
    [r, c] = find(isolated);
```

4) findendsjunctions.m

```
function [rj, cj, re, ce] = findendsjunctions(b, disp)
    if nargin == 1
        disp = 0;
    end
    % Set up look up table to find junctions.  To do this we use the function
    % defined at the end of this file to test that the centre pixel within a 3x3
    % neighbourhood is a junction.
    lut = makelut(@junction, 3);
    junctions = applylut(b, lut);
    [rj,cj] = find(junctions);
    % Set up a look up table to find endings.
    lut = makelut(@ending, 3);
    ends = applylut(b, lut);
    [re,ce] = find(ends);
    if disp
        show(edgeim,1), hold on
        plot(cj,rj,'r+')
        plot(ce,re,'g+')
    end
```

5) ending.m

```
function b = ending(x)
    a = [x(1) x(2) x(3) x(6) x(9) x(8) x(7) x(4)]';
    b = [x(2) x(3) x(6) x(9) x(8) x(7) x(4) x(1)]';
```

```
    crossings = sum(abs(a-b));
    b = x(5) && crossings == 2;
```

6) circularstruct.m

```
function strel = circularstruct(radius)
if radius < 1
  error('radius must be >= 1');
end
dia = ceil(2*radius);  % Diameter of structuring element
if mod(dia,2) == 0     % If diameter is a odd value
 dia = dia + 1;        % add 1 to generate a `centre pixel'
end
r = fix(dia/2);
[x,y] = meshgrid(-r:r);
rad = sqrt(x.^2 + y.^2);
strel = rad <= radius;
```

7) filledgegaps.m

```
function bw = filledgegaps(bw, gapsize)
    [rows, cols] = size(bw);
    % Generate a binary circle with radius gapsize/2 (but not less than 1)
    blob = circularstruct(max(gapsize/2, 1));
    rad = (size(blob,1)-1)/2;  % Radius of resulting blob matrix. Note
                               % circularstruct returns an odd sized matrix
  % Get coordinates of end points and of isolated pixels
    [~, ~, re, ce] = findendsjunctions(bw);
    [ri, ci] = findisolatedpixels(bw);
    re = [re;ri];
```

```
ce = [ce;ci]
% Place a circular blob at every endpoint and isolated pixel
for n = 1:length(re)
   if (re(n) > rad) && (re(n) < rows-rad) && ...
         (ce(n) > rad) && (ce(n) < cols-rad)
      bw(re(n)-rad:re(n)+rad, ce(n)-rad:ce(n)+rad) = ...
         bw(re(n)-rad:re(n)+rad, ce(n)-rad:ce(n)+rad) | blob;
   end
end
bw = bwmorph(bw, 'thin', inf);  % Finally thin
% At this point, while we may have joined endpoints that were close together
% we typically have also generated a number of small loops where there were
% more than one endpoint close to an edge.  To address this, we identfy the
% loops by finding 4-connected blobs in the inverted image.  Blobs that are
% less than or equal to the size of the blobs we used to link edges are
% filled in, the image reinverted and then rethinned.
L = bwlabel(~bw,4);
stats = regionprops(L, 'Area');
  % Get blobs with areas <= pi* (gapsize/2)^2
ar = cat(1,stats.Area);
ind = find(ar <= pi*(gapsize/2)^2);
% Fill these blobs in image bw
for n = ind'
   bw(L==n) = 1;
end
       bw = bwmorph(bw, 'thin', inf);  % thin again
```

Appendix B Experimental Rheology

B.1 Goodness and Consistency of model convergence

The results of this analysis (Figures **B1-1**, **B1-2** and **B1-3**) show that the fit is consistently good with the regression curves lying on top of each other regardless of initial estimate which was increased by over three orders of magnitude in D and by an order of magnitude for each of σ and t. It is worth noting that in **Figure B1-3**, the initial guess of 0.1 nm provided to the algorithm generates an initial curve which lies above the experimental data, but the fitting results in the regression curve closely following the data and coinciding with those from the other two initial guesses.

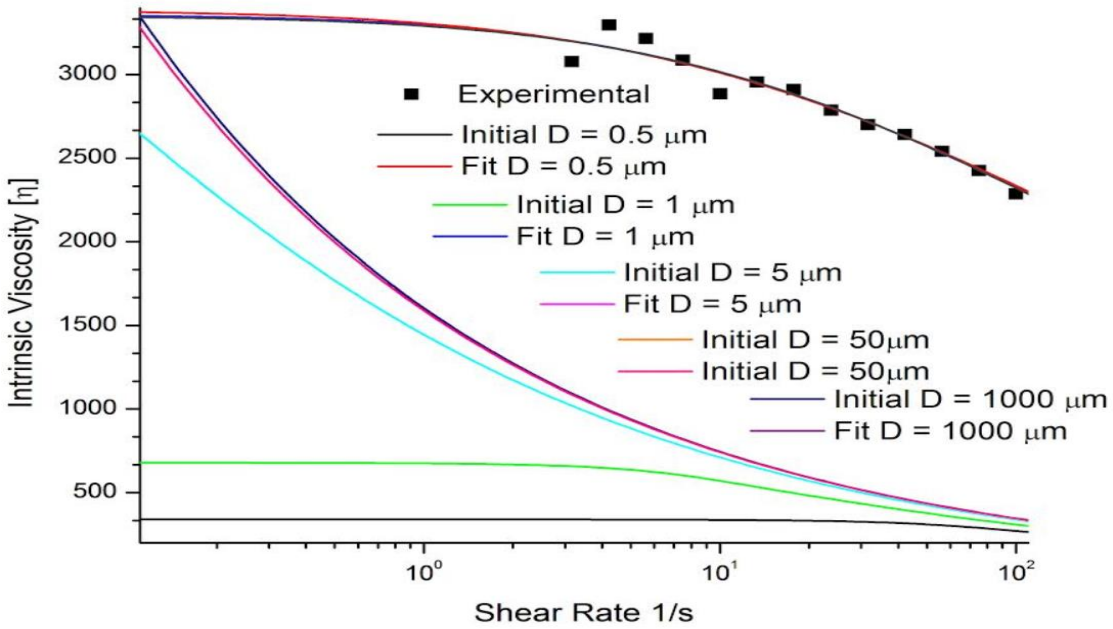

Figure B1-1. Regression performed on an experimental shear rheology dataset on MTD GO using several initial guesses of D, with initial guesses of t = 1 nm, σ = 0.1 used for all attempts.

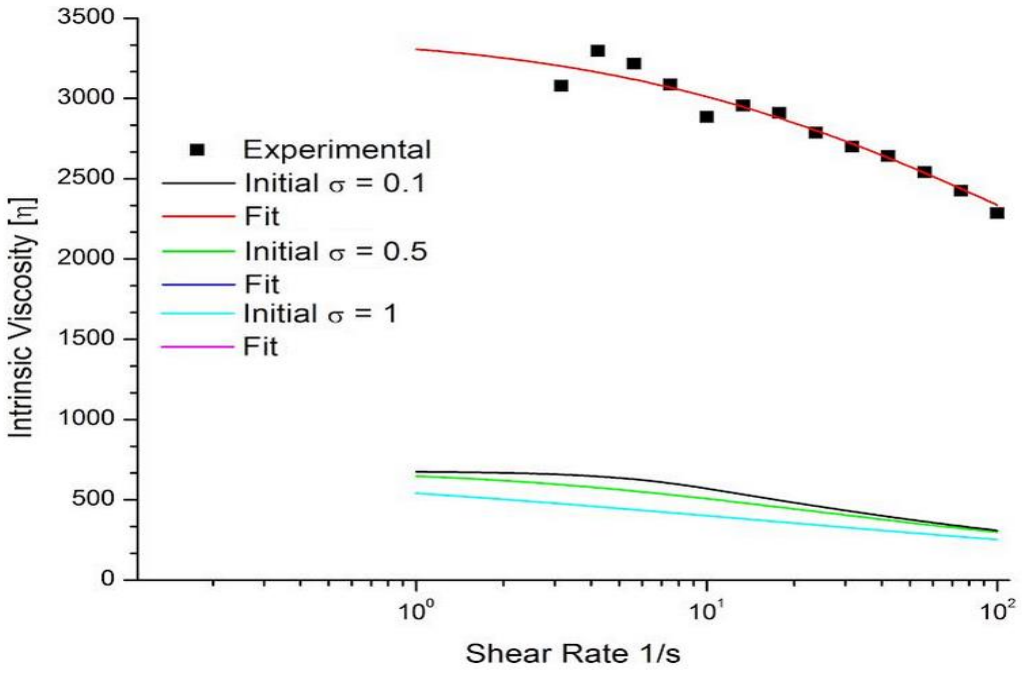

Figure B1-2. Regression analysis results on MTD GO shear rheology data using three initial guesses of σ, with initial guesses of D = 1 μm and t = 1 nm for all 3 attempts.

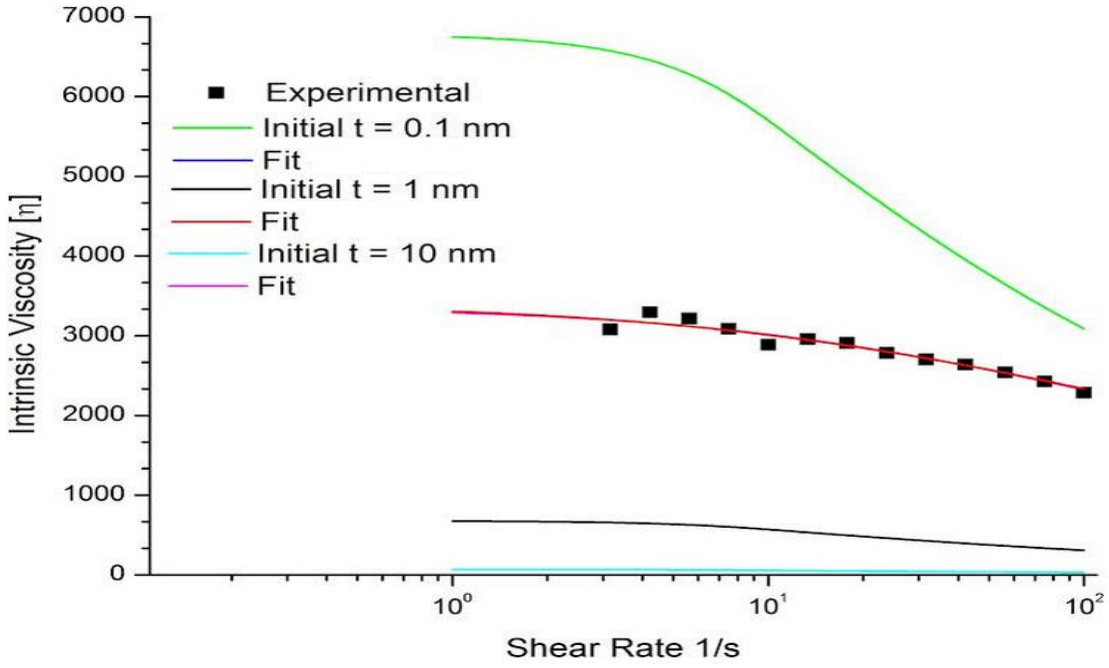

Figure B1-3. Regression analysis results on MTD GO shear rheology data using three initial guesses of t, with initial guesses of D = 1 μm, σ = 0.1 for all three attempts.

B.2 GO Agglomeration

Fig 9 shows the agglomeration at the end of a typical flow-sweep experiment on the concentric cylinders of the DHR3. Severity of agglomeration indicates that the concentration of the suspension becomes suspect at the end of the run, meaning that a fresh dispersion needs to be tested every time a replicate measurement needs to be taken at the concentration of interest. The tested dispersion can be recycled as a "new concentration", provided that one keeps quantitative measure of agglomeration-induced reduction in concentration (e.g.: using UV-Vis spectrophotometry). We did not attempt to do this in our study. Instead, we followed a serial dilution scheme (Fig. B2-2) which ensured that no single dispersion was sheared more than once. The amount of dispersion masterbatch needed was precalculated using Equation (B-1):

$$V_i = \sum_{C_i}^{C_n} V_R \frac{C_i}{C_1} \tag{B-1}$$

Figure B2-1. GO agglomerates at the cup bottom of the DHR3 DIN concentric cylinders at the end of a flow-sweep 1-100 1/s

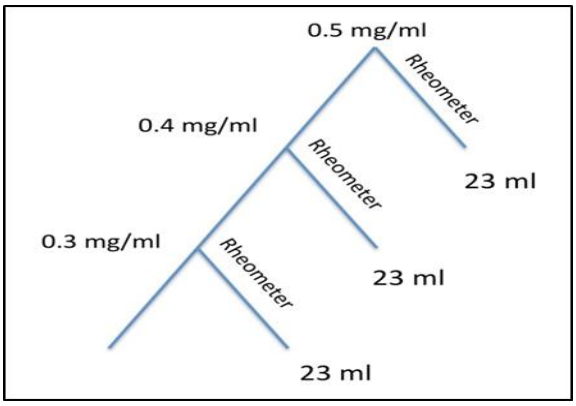

Figure B2-2. Serial dilution scheme followed for the rheology experiments. A masterbatch dispersion (e.g.: 0.5 mg/mL) is split into two portions, one which undergoes shear-testing (~23 mL) and another which gets diluted in turn to the next concentration (0.4 mg/mL)

B.3 Rheometry sensitivity limits

The torque sensitivity limit ($M_{d,min}$) is 5 nN.m for the DHR3. Following Equation (B-2) (where η, R_i and L are the system viscosity, bob inner radius and length respectively), it was this possible to calculate a lower boundary of sensitivity shear-rate for our system as a function of η.

$$\dot{\gamma_{sens}} = \frac{M}{2\pi\eta R^2 L} \simeq \frac{10^{-4}}{\eta}\left(\frac{1}{s}\right) \tag{B-2}$$

Moreover, based on the anticipated onset of Taylor instabilities (Equation B-3, where T_a is Taylor number, ω is angular rotation rate, R_a is outer annular radius, and ν is kinematic viscosity), it was possible to calculate an upper boundary of shear-rate (Equation B-4):

$$T_a = \frac{\Omega^2 R_1 (R_2 - R_1)^3}{\nu^2} = \frac{\dot{\gamma}^2 \bar{R}^6 (R_2 - R_1)^5}{{R_1}^3 {R_2}^4 \nu^2} < 1700 \tag{B-3}$$

$$\dot{\gamma_{turb}} \simeq (1.6 \times 10^5)\eta \tag{B-4}$$

Based on Equations (B-2) and (B-4), it was possible to construct a theoretical envelope of operation for our rheology experiments on GO aqueous dispersion, as shown in **Figure B2-1**.

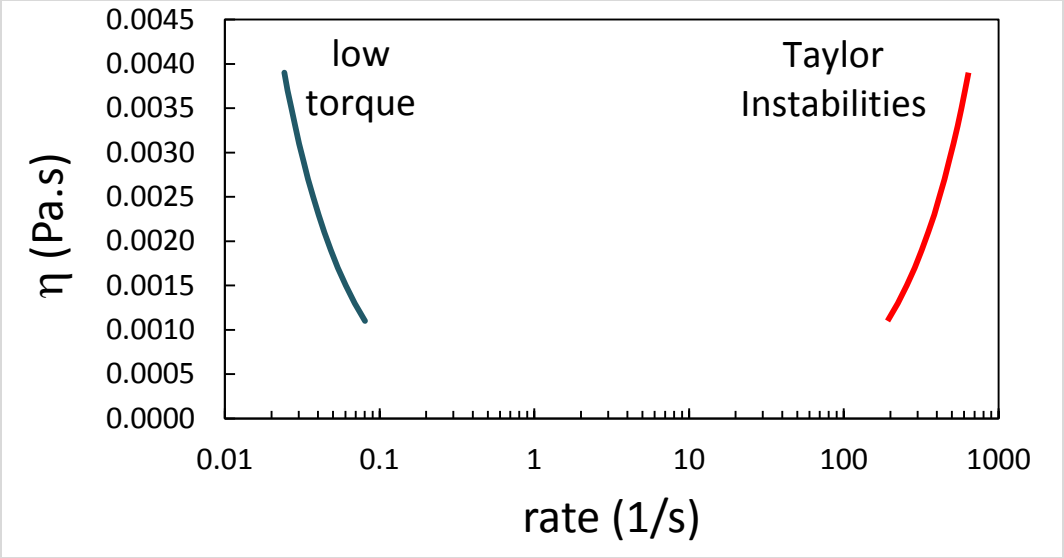

Figure B2-1. Theoretical envelope of operation for rheology experiments on GO dispersions, bounded at the low extreme by the DHR3 torque sensitivity limit (Equation 2) and at the high by the predicted onset of Taylor instabilities (Equations 3-4).

B.4 MTD GO Replicate

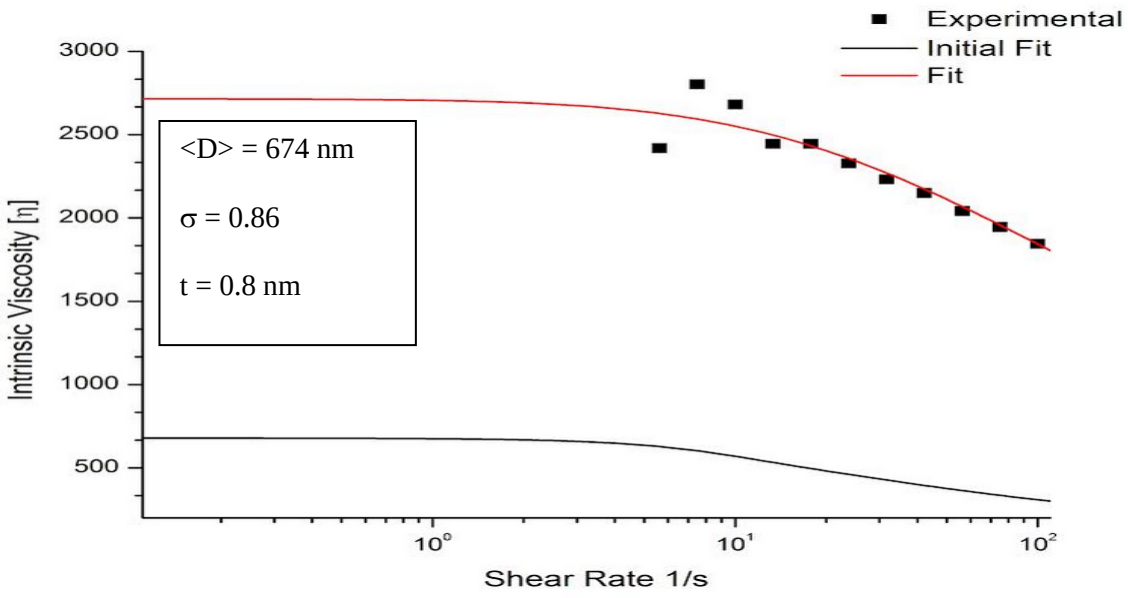

Figure B4-1. Fitting results on MTD GO replicate. Results similar in absolute values and shear-thinning trend, as well as fitting parameters to the first batch.

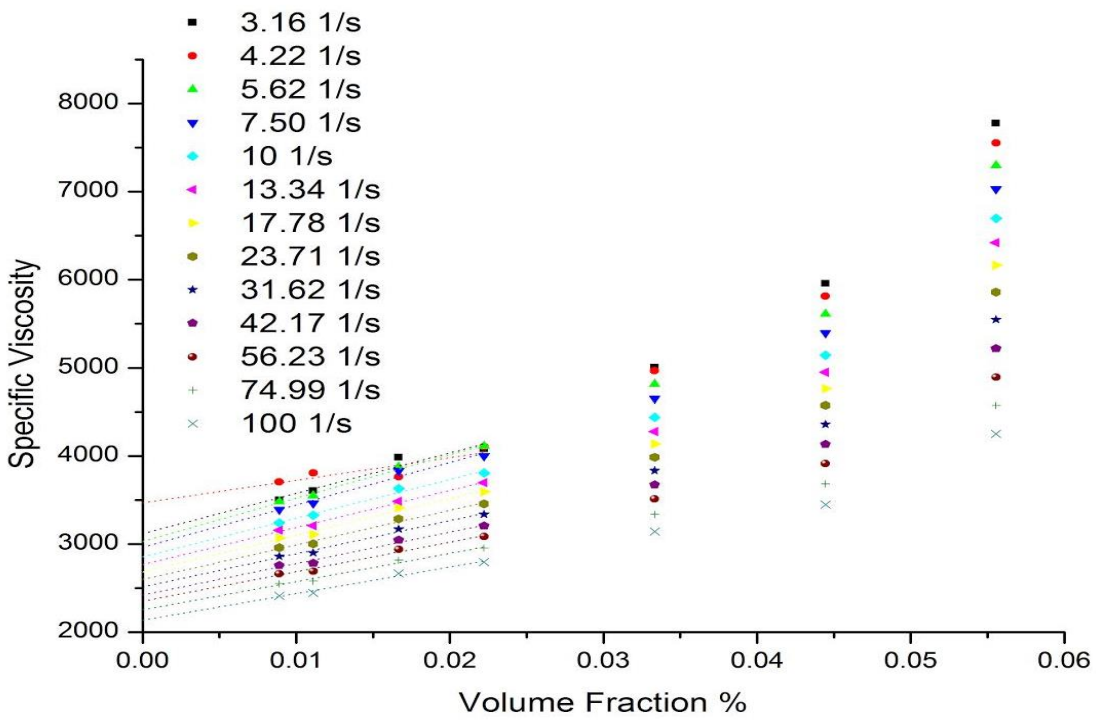

Figure B4-2. η_{sp} data used to extract [η] for the MTD GO replicate sample, depicting non-linearity at high concs. First 4 (linear) datapoints were used to obtain [η] intercepts.

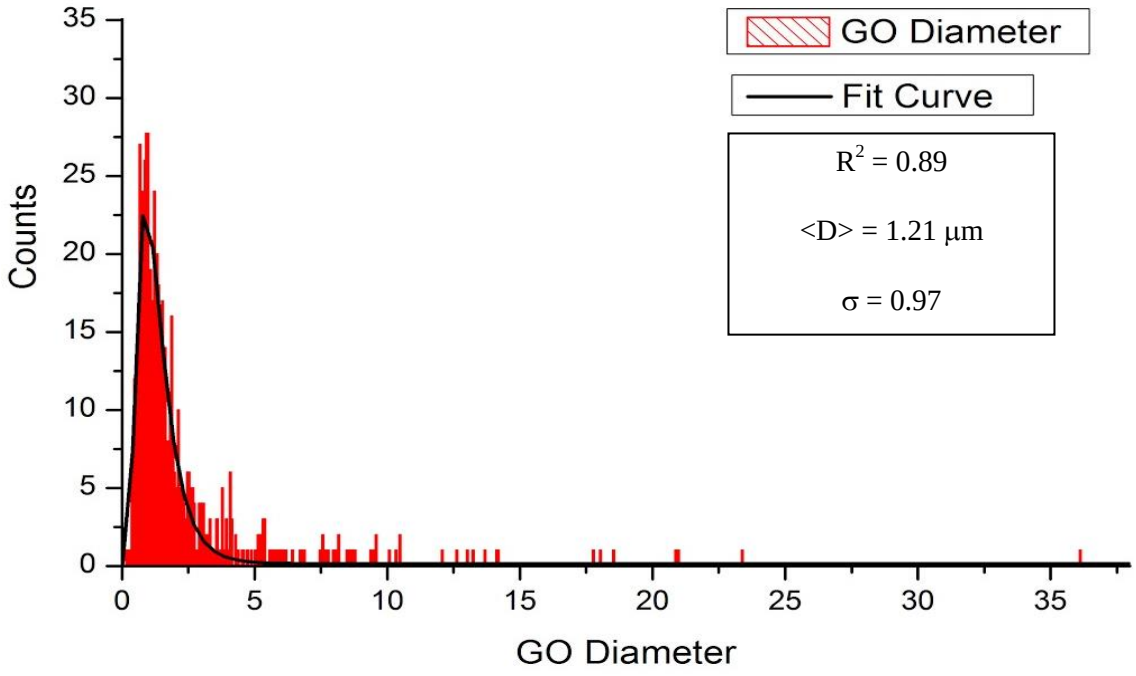

Figure B4-3. Spliced distribution obtained from FQM and AFM-splicing for MTD GO replicate.